Karla Marina Jaimes Merazzo

ORDERED MAGNETIC ANTIDOT ARRAYS

Supervisors:
Prof. Manuel Vázquez Villalabeitia
Dr. Rafael Pérez del Real

Tutor:
Dr. Julio Camarero de Diego

Study submitted to the Department of Condensed Matter Physics and Nanotechnology in partial fulfillment of the requirements for the degree of Doctor in Physics

Consejo Superior de Investigaciones Científicas
Instituto de Ciencia de Materiales de Madrid

Departamento de Física de la Materia Condensada y Nanotecnología
Universidad Autónoma de Madrid
Julio 2012

A mi madre
A mi familia
A Edu

AGRADECIMIENTOS

Este trabajo no hubiera sido posible sin la colaboración de todo nuestro grupo, ni el apoyo de muchas personas. Es posible que me deje a alguien por fuera, pero por favor no lo tomen como una falta de agradecimiento, sino de un agujero espacio-temporal en mi memoria…cosa que sucede muy a menudo últimamente.

Primero que todo, me gustaría agradecerle a mis directores, a Manuel por todo su apoyo y por darme la oportunidad de realizar este trabajo y permitirme aprender todo lo que he aprendido durante estos cuatro años. A Rafa por apoyarme y por las discusiones sobre los fenómenos magnéticos. Gracias a ambos por todo el trabajo involucrado en esta tesis.

A todos los adultos del grupo. Agustina, gracias porque siempre me has ayudado con una sonrisa, y por tenerme paciencia con las dudas sobre AFM y MFM. Además de escuchar tantas tonterías mías. Paco, siempre dispuesto a hablar de neutrones o sincrotrones, gracias por tus comentarios del XPEEM. Alfredo (el Chuck Norris, el MacGyver del grupo), el alma de la fiesta, gracias por ayudarnos siempre SIEMPRE!!! Que sería de nosotros sin ti Alfredo?

A Giovanni, muchas gracias por poner la cordura en el laboratorio y el digestivo para después de comer. Eres un gran maestro y una indudable fuente de sabiduría, gracias porque nunca te has negado a darnos una mano. Di, no tengo palabras para agradecerte todo lo que me has enseñado. Sabes que gran parte de esta tesis no hubiera sido posible sin ti!!! Gracias por ser una maestra y una amiga.

A mis compis de laboratorio, mi segunda familia, las personas con las que he compartido estos casi 5 años!!! Ruy, Wagner, gracias por haberme enseñado todos los procesos del laboratorio con paciencia y buena disposición. Jacob, Germán, he aprendido mucho de ustedes, y nos hemos reído mucho, espero no ser más ruido de fondo Germán!!! Kleber y David, que aunque no pude compartir mucho tiempo con ustedes, sus huellas en el laboratorio perduran por siempre, y aún aprendemos de su trabajo. Miriam, la más conocedora de los deportes que conozco, y de mangas y de películas frikis….gracias por ayudarme en tantas cosas con una gran sonrisa, y ser compañera de cotilleo cuando nos aburríamos; ha sido divertido ser población femenina en aumento en el grupo. Lauris, mi gran amiga y compañera de despacho/laboratorio, sé que estás un poco loca, pero has sido un gran apoyo, y como persona eres muy grande. Nunca nadie me ha hecho reír tanto con una foto tan comprometedora. Nacho, cuando vuelvas a ordenar el laboratorio nos avisas vale? Suerte también con tus proyectos futuros.

Mariana, ha sido un placer trabajar contigo, aunque no haya sido en el mismo tema, siempre nos hemos compartido experiencia y datos, y muchas risas!!! Oscarrrrr: —•—• ——— •—•• •—. Sabes que has perdido la cordura por el camino verdad? Sonia, la química que nos ha sacado de apuros con cálculos estequiométricos, gracias por todo. Rimhou, gracias por compartir con nosotros. Ale, compi de despacho/laboratorio, suerte con tu trabajo!!! A los nuevos integrantes, siento no haber compartido más tiempo con ustedes, pero ha sido divertido lo poco que hemos compartido: David, Cristina, Victor.

A los chicos del instituto, María, Fernando, Bernd, Gladys, Rocío. La tesis ha sido más amena gracias a su compañía. Siempre tendremos la tarde de chicas: María, Laura, Mariana, Gladys y Karla!!!

A mis colegas de PEEM, Julia, Celia y Luis Miguel, gracias por darme la oportunidad de trabajar con ustedes, ha sido un gran placer y he aprendido mucho. Este trabajo ha sido más interesante gracias a estos experimentos.

Erika, gracias por ayudarme con el MOKE, por enseñarme todo lo que sabías al respecto. Julio, gracias por abrirme las puertas de tu laboratorio como si fuera mi propia casa. He aprendido mucho gracias a la colaboración de ambos.

A mis compañeros de máster, y mis nos compañeros, pero mis amigos de vida. Bruno, fuiste mi primer trauma en España, pero con el tiempo lo has sabido compensar…y con creces. Es genial tener con quien frikiar en las comidas, y haber soñado con hacer una tesis en conjunto…"haremos el estudio por STM, AFM de muestras crecidas por SPUTTERING y le mediremos MAGNETISMO y propiedades QUIMICAS, y para MUSEOS de ARTE….era algo así no?? Sarita, gracias por darme más de dos "asucarillos" y permitirme compartir tanta ternura!! Eres una gran amiga y lo sabes, es genial tenerte para obligarme a ver las cosas como son….y ayudarme a recuperar el voto de confianza a la humanidad. Miguel el macho, eres un caballero, eres un diamante en bruto y jumao!!!….jajajaja…tenía que decir algo no? Dani, cuidado que estás madurando muy rápido, que luego no sabes qué hacer con tanta seriedad!! Gil y Ana, las partidas de Wii debemos seguirlas alguna vez, ha sido genial tenerlos cerca. Zuri, la loca!!! Vaya que traes música a nuestros oídos…estás loca pero sabes escuchar. Chamo, aunque hayas volado lejos, siempre serás mi mejor amigo, siempre que hable contigo será como si nos hubiéramos visto ayer, eres de verdad un gran amigo!! Cris, fuiste un gran apoyo cuando llegué a España, y siempre lo has sido, gracias por escuchar y aconsejar!!! Zuri, Chamo, Cris, gracias por ser mi familia durante estos últimos 3 años y medio.

A los chicos del no laboratorio: Jaka, pura vida!!! Eres como mi hermano mayor....sí MAYOR!!!!. Palen, ya sabes que cuando tengas la granja "feliz" seremos tus clientes frecuentes, y cuando saques tus genes de marinero nos das un paseo por el mar. Andreas, tendremos que celebrarlo con una pachanga!!!. Pepelu, gracias por todo. Javirán un café?

A todos los demás, la Rubia, Blanca, Pol, Patricia, Puku, Inés, Palen 2, chule, Ayuso, Eoni, y todos lo demás gracias por colaborar en la perversión de mi mente!!! No me olvido de Patri Arcas, mi primera amiga en España!!! Gracias por haber sido mi compi en el Colegio Mayor durante mis primero meses aquí. Te deseo toda la suerte como la próxima presidente de España.

No me podría olvidar tampoco a mis amigos y a los que me apoyaron desde Costa Rica, mi primeros estudiantes y mi posteriores amigos: Naty y Vane; y mis primeras dos generaciones: Mary, Marcia, Eder, Mariam, Tony D., Diego L., Laura, Tony M., Randy, Anthony, Dani, Davis, Pablo, Diego G., Cristian y la siguiente generación. A doña Gretta, Coccio, don Jorge Moya y a toda la Sede de Liberia. Gracias por darme un voto de confianza.

A mi familia le agradezco el apoyo, todo lo bueno y lo malo que hemos pasado juntos como familia. Tío, gracias por estar ahí cuando he necesitado de un apoyo, de unas palabras… lo bueno es que ya no tengo apéndice!!! A papi Carlos y Mami Neni, mis padres, mis abuelos, mis mejores fans!!! Gracias por permitirme realizar mis sueños y con ellos los suyos. A mi tía y a mis primos, muchos éxitos en la vida.

A mis hermanos, chicos, siento que uno de los precios a pagar por realizar este sueño haya sido estar tan lejos de ustedes…espero compensarlo!!! pincho: el hombre con el corazón más grande del mundo, nunca olvides que eres un ser con grandes sentimientos, así que deja que sean estos quienes te guíen, eres mi compañero de juegos y de pleitos..Ojalá fuéramos niños otra vez!!!. Kassi, la mejor mujercita del mundo, la persona más razonable que conozco y aún no eres ni mayor de edad!!! Eres la luz de mis ojos, la canción de mis mañanas, eres una inspiración para mí!!

A mi madre, mi mejor apoyo, mi peor juez y sin duda mi mejor amiga, porque me has heredado la fortaleza y la terquedad, pero me has enseñado a usarla a mi favor, eres la mejor, esta tesis va por ti!!!

Y por último, pero el primero en mi corazón, Edu, gracias por compartir mis locuras, gracias por bajarme los pies a la tierra cuando lo he necesitado, gracias por enseñarme que el mundo es más sencillo de lo que parece en mi cabeza…gracias por ser el rey de mi mundo. La vida no tendría sentido sin ti!! Espero ser siempre tu compañera de batallas…un beso infinito.

SUMMARY

Nanoscale patterned magnetic films are envisaged for technological purposes profiting of the possibility of tuning the local distribution of magnetization in a controlled way. That makes them advantageous in comparison with their continuous thin films counterpart. The applications of the antidot arrays go from magnetic recording media to sensor and magnonic devices.

Antidot arrays have been commonly prepared by different nanolithography techniques with size in the order of few hundred of nm or μm. Recently, an alternative route has been being increasingly employed, which is based on a combination of different techniques of electrochemical processes and physical deposition (e.g. sputtering). The templates are prepared by a controlled double anodization process, whereby self-assembled nanopores grow during the anodization of high purity aluminum films.

Magnetic anisotropy in antidot films, either in-plane or out-of-plane, can be tuned by suitable selection of geometrical parameters. While there is a broad documentation about the magnetic behavior for lithographed antidots, there is still a lack of detailed studies on antidot arrays prepared following the ordering of precursor anodic templates.

Specifically, antidot arrays of Permalloy grown over anodic aluminum templates have shown interesting magnetic properties. They lack crystalline and magnetoelastic anisotropies, and consequently their magnetic behavior are essentially determined by the surface anisotropy modified by the presence of local stray fields induced by the antidots. The discontinuities or periodic defects originate dipoles or charges that change strongly the internal shape effective anisotropy. These properties, such as coercivity, can overcome up to two orders of magnitude that the measured in continuous films or in the bulk of the same composition. This shape anisotropy can conveniently vary with the geometry of the arrays. They can even show biphase magnetic behavior in spite of being constituted by single alloy component.

A study of the magnetic properties of Permalloy antidot thin films was made. These arrays were grown by sputtering onto anodic alumina templates replicating their hexagonal order and the micrometric geometric domains. The study consists in the measurements of magnetic properties with different geometric parameters, such as diameter, separation of the nanoholes and film thickness.

Many techniques were employed in the magnetic study, such as Vibrating Sample Magnetometer, Magneto Optical Kerr Effect Magnetometer, Magnetic Force Microscopy, and a special study was performed using imaging to study the magnetic domain structures using an advanced technique of high spatial sensitivity: X-Ray Photoemission Electron Microscopy.

The soft-magnetic character and the almost cero magnetocrystalline constant of the Permalloy, are reflected in the magnetic behavior of the antidot arrays, thus the magnetization reversal process is a direct result on the geometric dimensions of the nanoholes, and depends strongly in the properties of the thin films, such as the thickness. However, the most interesting result was the biphase behavior shown when the arrays have the largest diameter of nanoholes.

The magnetic behavior on the surface of the arrays is different that the behavior present in the whole system. At the bottom of the films, the topological properties of the membranes and the sputtering conditions cause an extravagant behavior, producing in consequence different magnetic domain structures in the whole array.

Using the results of the Permalloy arrays with different geometrical parameters, antidot arrays of Co were studied. These arrays in principle are expected to exhibit a harder behavior; besides gives a relatively high anisotropy and magnetization saturation. Subsequently, antidots of Co/Py bi-magnetic systems sputtered over anodic alumina membranes were prepared, with the aim to investigate the influence of the presence of antidots in the magnetic behavior. These bi-layer systems show an interesting exchange spring effect.

RESUMEN

Películas magnéticas nano-patronadas están previstas para fines tecnológicos pues tiene la ventaja de ajustar la distribución local de la imanación de una manera controlada. Esto les da una ventaja en comparación con su contraparte películas delgadas continua. Las aplicaciones de las matrices antidot van desde medios de grabación magnética hasta sensores y dispositivos magnónicos.

Las matrices de antidot han sido comúnmente preparadas por diferentes técnicas de nano-litografía con un tamaño del orden de unos pocos cientos de nm o µm. Recientemente, una ruta alternativa ha sido cada vez más empleada, que se basa en una combinación de diferentes técnicas de procesos electroquímicos y deposición física (por ejemplo, pulverización catódica o sputtering). Las plantillas se preparan mediante un proceso controlado de doble anodización, por el cual nanoporos auto-ensambladas crecen durante la anodización de las películas de aluminio de alta pureza.

La anisotropía magnética de las películas de antidot, ya sea en el plano o fuera del plano, se puede ajustar mediante la selección adecuada de los parámetros geométricos. Si bien existe una amplia documentación sobre el comportamiento magnético de antidots litografiados, todavía no hay muchos estudios detallados sobre las matrices de antidot preparadas siguiendo el orden de las membranas porosas de alúmina anódica.

Específicamente, las matrices de antidot de Permalloy crecido sobre plantillas de aluminio anódico han mostrado propiedades magnéticas interesantes. Estas carecen de anisotropías cristalinas y magneto-elásticas, y en consecuencia su comportamiento magnético se determina esencialmente por la anisotropía superficial modificada por la presencia de efectos locales como los “stray fields” inducidas por los antidots. Las discontinuidades o defectos periódicos originan dipolos o cargas que cambian fuertemente la anisotropía magnética interna efectiva de forma. Estas propiedades, tales como coercitividad, pueden superar hasta dos órdenes de magnitud que el medido en las películas continuas de la misma composición. Esta anisotropía de forma puede variar convenientemente con la geometría de las matrices. Incluso pueden mostrar un comportamiento magnético bifásico a pesar de estar constituida por un solo componente.

Se realizó un estudio de las propiedades magnéticas de películas delgadas de antidot de permalloy. Estos arreglos fueron crecidos por sputtering sobre las membranas porosas de alúmina anódica replicando su orden hexagonal y los dominios geométricos micrométricos. El estudio consiste en la medición de las propiedades magnéticas con

diferentes parámetros geométricos, tales como el diámetro, la separación de los nano-agujeros y espesor de película.

Muchas técnicas fueron empleadas en el estudio magnético, tales como Magnetómetro de Muestra Vibrante, magnetómetro Magneto-Óptico por Efecto Kerr, microscopía de fuerza magnética, y un estudio especial por imágenes se realizó con el fin de estudiar las estructuras de los dominios magnéticos, utilizando una avanzada técnica de alta sensibilidad espacial: Microscopía Electrónica de Emisión de Fotones.

El carácter magnético blando y la constante magneto-cristalina casi cero del permalloy, se reflejan en el comportamiento magnético de las matrices antidot, por lo tanto el proceso de inversión de la imanación es un resultado directo de las dimensiones geométricas de los nano-agujeros, y depende en gran medida en las propiedades de las películas delgadas, tales como el espesor. Sin embargo, el resultado más interesante fue el comportamiento bifásico que las matrices muestran cuando tienen el mayor diámetro de nano-agujeros.

El comportamiento magnético en la superficie de las matrices es diferente que el comportamiento presentes en todo el sistema. En la parte inferior de las películas, las propiedades topológicas de las membranas y las condiciones de sputtering causan un comportamiento extravagante, produciendo en consecuencia diferentes estructuras de dominio magnético en toda la matriz.

Utilizando los resultados de las matrices de permalloy con diferentes parámetros geométricos, se estudiaron matrices de antidot de Co. Estas matrices en principio se espera que exhiban un comportamiento más duro, además da una anisotropía y magnetización de saturación relativamente alta. Posteriormente, se prepararon sistemas de antidots bi-magnéticos de Co/Py crecidos sobre membranas porosas de alúmina anódica, con el fin de investigar la influencia de la presencia de antidots en el comportamiento magnético. Estos sistemas bi-capa muestran un interesante “exchange spring effect”.

List of Abbreviation

- A: intrinsic magnetic anisotropy constant
- AAM: anodic alumina membranes
- AFM: Atomic Force Microscopy
- A_h: exchange constant of the hard phase
- $(BH)_{max}$: maximum energy product
- CTF: continuous thin film
- δ_{DW}: DW width
- δ_h: DW width of the hard magnetic phase
- DW: domain wall
- D: center-to-center distance between the holes or lattice parameter
- d: antidot diameter
- d_P: AAM’s pore diameter
- e.a.: magnetization easy axis
- EDS: Energy Dispersive X-Ray Spectroscopy
- FORC: First Order Reversal Curves
- G.S.: grain size
- GOe: gauss oersted
- H_a: anisotropy field
- H_c: coercivity
- H_D: demagnetizing field
- H_{ex}: exchange field
- h.a.: magnetization hard axis
- IP: in-the-plane
- IP-GS: in-plane grain size
- IRM: Isothermal Remanence Measurement
- K: magnetic anisotropy constant
- K_{eff}: effective anisotropy
- K_h: anisotropy constant of the hard phase
- K_{ind}: induced anisotropy constant

- MFM: Magnetic Force Microscopy
- M-H: magnetization versus applied magnetic field – hysteresis loop
- MOKE: Magneto-Optic of Kerr Effect Magnetometry
- M_r: remanent magnetization
- M_s: magnetization of saturation
- N_D: demagnetizing factor or shape factor
- H_N: nucleation field
- OOP: out-of-plane
- OOP-GS: out-of-plane grain size
- P: porosity
- Py: Permalloy
- P_w: work pressure of the sputtering system
- SEM: Scanning Electron Microscope
- SFD: Switching Field Distribution
- T_{Al}: thickness of Al film
- t_{Co}: thickness of Co film
- t_{Py}: thickness of Py film
- r: antidot aspect ratio
- r’: alternative antidot aspect ratio
- virgin: First magnetization curve or Virgin Curve Measurement
- VSM: Vibrating Sample Magnetometer
- XPEEM: Photo-Emission Electron Microscopy
- XRR: X-Ray Reflectivity

Contents

CHAPTER 1

CHAPTER 2

CHAPTER 3

CHAPTER 4

CHAPTER 5

CHAPTER 6

1. CHAPTER 1

INTRODUCTION

1.1 INTRODUCTION

“There's Plenty of Room at the Bottom”. These words pronounced by Richard Feynman in 1959 [1], are the first reference on nanotechnology, and they were an inspiration for searching new dimensions in the physical word. He proposed the fabrication of films with atom by atom control and arrangement; and he was the first scientist in analyzing the possibility of computers using individual atoms.

Since then, the study of new phenomena has compelled to investigate new properties at nano-scales dimensions. During these 53 years, the nanotechnology research has grown, and the frontiers are increasingly far. Several branches have been developed from the new world: nano-medicine, nano-magnetism and spintronics, among others.

Magnetism in thin films has been studied since the ’70, when the high control in the growth conditions, new deposition processes [2] and the characterization with spectroscopy techniques, were possible. Ever since, magnetization in thin films has been an active area in research. In the ’80, with the discovery of the Giant Magnetoresistance effect [3,4] had an important impact in the computer read-head technology. The research is focused in the study of low dimensional and interfacial magnetism, oriented to the development of new devices for technological applications, such as the storage media for reading and storing of information in magnetic RAMs [5].

The spintronics became the cornerstone of new technology [6,7,8,9], and magnetic thin films play an important role in this research; their applications go from tunnel junction [10,11,12], exchange spring or spring magnets [13,14], to the study of switching dynamics [15].

Nano-patterned films, such as the antidot arrays, have shown good magnetic properties thanks to the induced local shape anisotropy, which modify/enhance the magnetic behavior of the continuous thin film. Two-dimensional nanostructures geometrically arranged in arrays of nanoholes or antidots can be described as spatially ordered non-magnetic defects on a continuous thin film or as the counterpart of dot nanostructures [16]. The most important effect is that such holes or antidots modify conveniently the magnetization process of the otherwise continuous film [17] and they avoid the superparamagnetic limit [18]. The applications of the antidot arrays go from magnetic recording media [18,19,20,21,22] to sensor [23] and magnonic devices [24,25].

Specially, the ultrahigh density storage application of the antidot arrays media has been proposed thanks to the stable domain configuration formed around the nanoholes. These configurations are the result of the interplay of the intrinsic uniaxial anisotropy of the magnetic thin film and the demagnetizing fields associated with the antidots, which tend to align the magnetization parallel to the edge of the nanoholes [26], as represented in Figure # 1.1 by a schematic diagram with the ideal remanence of an antidot array.

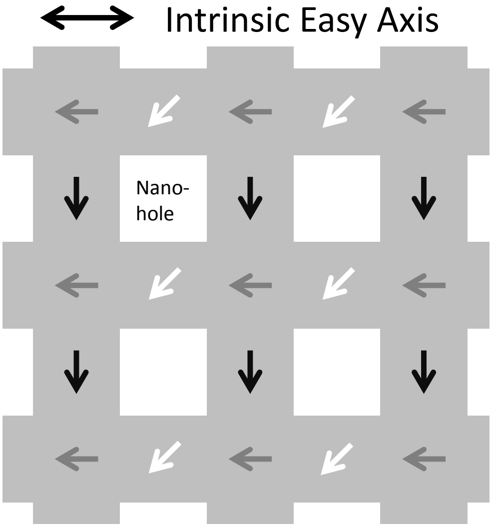

Figure # 1.1. Schematic diagram of an antidot array with ideal remanent state for applying as magnetic storage.

The magnetization of the regions with black arrows is parallel to the intrinsic hard axis and can be used to store bits of information [18,27]. An important work has shown by micromagnetic simulations that such systems can achieve an areal density of 760 Gbits/in^2 [28].

Antidot arrays are commonly prepared by different nanolithography techniques [17,26,27,29,30,31,32] with size in the order of a few hundred nm and μm, as electron beam lithography and lift-off-processes [29, 26,33], focused ion beam [34], interferometric lithography [30], X-Ray lithography [35,36] and using deep ultra-violet lithography [37].

Recently, an alternative route is being increasingly employed based on combined electrochemical and physical deposition (e.g. sputtering) techniques. Templates with the precursor desired ordering of the final antidot array are prepared by controlled double anodization process by which self-assembled nanopores grow during the anodization of high-purity aluminum films [38,39,40,41,42,43].

Specifically, antidot arrays of Permalloy grown onto *anodic aluminum membranes* (AAM) have shown interesting magnetic properties [40]. They lack crystalline and magnetoelastic anisotropies [44], and consequently their magnetic behavior are essentially determined by macroscopic in-plane anisotropy modified by the presence of local stray fields effects induced by the antidots. The intrinsic magnetic properties of the continuous thin film, such as the switching fields and magneto-resistance behavior, can be modified by changing the size, separation and the lattice symmetry and orientation of the nanoholes. They can even show biphase magnetic behavior [45] in spite of being constituted by single alloy component.

1.2 MAGNETIZATION REVERSAL PROCESS IN CONTINUOUS THIN FILMS OF PY

In a uniformly magnetized material, the formation of magnetic domains, separated by *domain walls* (DW), reduces the magnetostatic energy of the system. The DW corresponds to the boundary between magnetic domains of distinct orientations and their size depends on the intrinsic properties of the material and on the competition between anisotropy and exchange energy. If the width of this boundary is comparable to *a* (where *a* is the inter-spin distance), the exchange energy would be very high, so this energy could be reduced by distributing the rotation over several lattice spacing [46].

The expected *magnetization versus applied magnetic field* (M-H) loop in thin films of Py, in-the-plane of the sample, is a square loop with finite coercivity, mainly ascribed to nucleation and propagation of DW; while in the out-of-plane a linear loop is obtained instead, with almost zero coercivity, corresponding to reversible rotations.

According to Ref. 2, in thin films with thickness of the order of microns, the DW width is approximately of 200 nm, while according to the equations in Ref. 2 and 52, and using the intrinsic magnetic values for *Permalloy* (Py) [52], the DW width corresponds to:

$$\delta_{Bl} = \pi\sqrt{\frac{A}{K}} = 730\, nm. \qquad \text{Eq. (1.1)}$$

where K is the magnetic anisotropy constant and A is the is the intrinsic magnetic anisotropy constant

$$A = 1.64 \cdot 10^{-6}\ erg/cm\ ,\ \ K_u = 3 \cdot 10^{3}\ erg/cm^{3}$$

Several works have shown that the wall width depends on the thickness of the film at nano-scales dimensions [47,48]. In references 49 and 50, the films with $t_{Py} > 2500$ nm have Bloch type DWs, with a magnetization distribution along the wall plane. The wall has a big Bloch region in the middle and Néel caps at the bottom and at the surface [47]. As the *thickness of the Py film* (t_{Py}) decreases, for example in samples with $t_{Py} < 35$ nm, the Néel DW appears.

1.3 ANISOTROPY IN CONTINUOUS THIN FILM AND ANTIDOT ARRAYS

Most of the previous works on antidot arrays are made by lithography, and they show homogeneous magnetic domain structures due to the periodicity of the nanoholes. The magnetic behavior demonstrates a great enhancement in comparison with their counter-part *continuous thin film* (CTF).

The anisotropy induced by the lattice symmetry, the growth conditions and the magnetocrystalline properties define the magnetic behavior of the arrays, such as *coercivity* (H_c) and *remanence* (M_r). Many studies have shown that the intrinsic anisotropy of the unpatterned film, or CTF, is still present in the arrays [18,51].

The anisotropies that must be account in the system of antidot arrays are:

1. Magnetocrystalline anisotropy;
2. The shape of the sample – macroscopic scale;
3. The induced field during the growth of the films – macroscopic scale;
4. The lattice ordering of the arrays – local scale.

1.3.1 Magnetocrystalline anisotropy

The magnetocrystalline anisotropy describes the preference for the magnetization to be oriented along certain crystallographic directions [52]. Materials can be characterized by its magnetocrystalline anisotropy. More generally speaking, the magnitude of the ratio *k* characterizes the basic magnetic behavior of the material.

$$\text{Ratio} \qquad k = \frac{2K}{{M_S}^2} \qquad \text{Eq. (1.2)}$$

If k >> 1, the behavior is dominated by magnetocrystalline anisotropy; such materials are called hard magnetic. If k << 1, the behavior is governed by the magnetostatic energy; such materials are called soft magnetic material [53].

Py belongs to the group of soft magnetic materials, with a near zero magnetocrystalline constant, therefore it has not influence on the effective anisotropy of the Py antidot arrays.

1.3.2 Macroscopic Shape of the Sample

The antidot arrays have micrometer sizes, so an appropriated comparison was made with the CTF in order to calculate the effect of the macroscopic shape. The used expressions for the calculus of the demagnetizing fields are expressed in c.g.s. [52,54]:

$$\overrightarrow{H_D} = -N_D\,\vec{M} \qquad \text{Eq. (1.3)}$$

where N_D is the demagnetizing factor, being a tensor function of the sample shape along three principal orthogonal directions: a, b, c; their sum is 4π in cgs units.

For the two-dimensional problem of a thin film, two shapes were used: a rectangular film with dimensions w, t, and h, as we can see in Figure # 1.2, and a circular shape as shown in Figure # 1.3 [52].

In the first case, we can use the general prolate ellipsoid approximation, where the demagnetizing field in a thin film along the w and h directions corresponds to Eq. (1.4), respectively (cgs units) [54,55]:

$$H_D = -4\pi M_s\frac{t}{w} \;\; ; \;\; H_D = -4\pi M_s\frac{t}{h} \qquad \text{Eq. (1.4)}$$

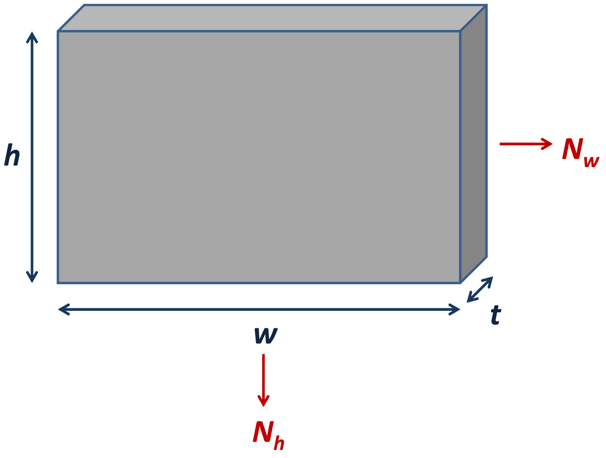

Figure # 1.2. Continuous thin film with rectangular shape and finite dimensions: h, w and t**.**

In the case of thin films with circular shape, the approximation can be made using the oblate spheroid, with two long equal axes *x*, *m* times the length of the axis of symmetry (*t*). In all the cases presented in this work, it follows the relation m (x/t) >> 1.

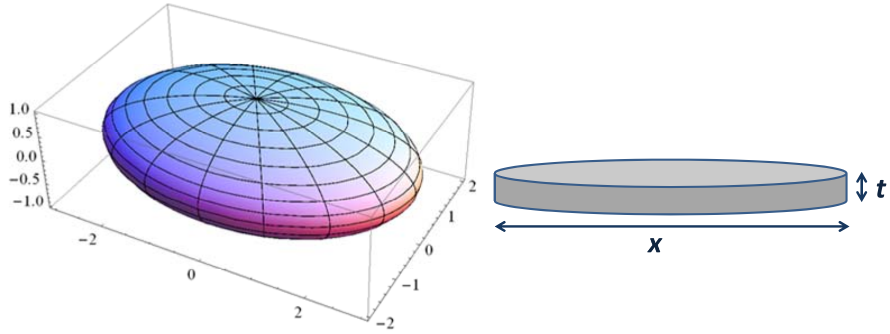

Figure # 1.3. Oblate ellipsoid compare with a thin film with circular shape, x = y.

When the magnetization lies along the long axes, the shape factor is [52]:

$$N_x = \left(\frac{\pi}{4m}\right)\left(1 - \frac{4}{\pi m}\right) \qquad \text{Eq. (1.5)}$$

On the contrary, if magnetized along its short axis:

$$N_t = 1 - \frac{\pi}{2m} + \frac{2}{m^2} \qquad \text{Eq. (1.6)}$$

With the calculated shape factor N, the demagnetizing field can be obtained using Eq. (1.3).

1.3.3 Induced field during the growth of the films

The application of applied magnetic fields during some treatments, as heat-treatment, to induce magnetic anisotropy is commonplace in a variety of soft magnetic material to the performance of certain specifications, as for example, in Co-Cr or Fe-Ni films for magnetic recording media, and thin film heads, respectively [52]. For field annealing to be effective, the field must be applied below the Curie temperature of the material and must saturate the material.

In this study, an analysis of the magnetic response to the application of a magnetic field, without any heat treatment, was made. A weak induced magnetic field of approximately 6-7 Oe was applied parallel to the film plane, along to the sample holder of the sputtering system. This field is enough to saturate the Py films but not as much to alter significantly the antidot arrays. In this way, the application of a field ensures that the magnetization lies IP of the sample, thus any OOP component will become from the geometry of the templates.

1.3.4 Lattice ordering of the arrays

The nano-patterned defects on the CTF, i.e. nanoholes, act as domain nucleation and also as strong pinning centers for the DW, avoiding the fast wall propagation. Locally, these defects produce a spatially dependent dipolar field (depends on the array arrangement and its geometric properties), thus creating magnetic charges around the holes, which anchor DWs and hinder their displacement.

The demagnetizing field introduced by the edges of the holes leads to a spatially variant shape anisotropy fields, which competes with the intrinsic uniaxial anisotropy of the compound, and gives rise to magnetically easy regions with respect to the applied field [43].

Depending on their geometric features, three regimes appear for antidots: diluted, high concentrated and intermediate concentrated [56]. Their classification relies on the relation between the density of holes and the width of the DW: 1) *Diluted*: DW width is much smaller than the *center-to-center distance between the holes* (D); 2) *high-concentrated* regime: *DW* width is much larger than *D* or the *antidot diameter* (*d)*; and c) *intermediate concentrated* regime, in which the DW width is comparable to *D* or *d*, allowing its propagation in between the holes.

Some works [36,57,58] claimed that the shape of the holes and the intrinsic anisotropy of the unpatterned film, and not the symmetry of the lattice, are the responsible of the anisotropy. They found no anisotropy in a circular holes array, while they measured two-fold and four-fold anisotropy in elliptical and square holes arrays in a square lattice, respectively. But more recent works [37,51,59,60] found that the lattice symmetry is as much important as the hole shape.

Different array arrangement can be obtained by lithographic techniques, in which the limitations of having larger dimensions are compensated by the long-range order in the arrays; besides this technique allows designing distinct geometrical configurations. The magnetic domain structures depend on the lattice pattern presented in the film. Different holes geometries have been proposed: square [18], rectangular [29], and circular, the latter showing the lowest anisotropy energy [56].

In the following sub-sections, an overview on the properties of lithographed antidot arrays with different lattice geometry is presented (square, honeycomb, and hexagonal). Each configuration results in different conditions for the minimization of the magnetostatic energy. The dimensions of these arrays are of the order of several hundreds of nanometers of diameter and lattice parameter. Besides, this study is limited by holes with circular geometry, because is the one obtained in the AAM templates.

1.3.4.1. *Square lattice*

The anisotropy in the square lattice is defined as four-fold (biaxial) configuration, with two easy axes along the diagonals of the square and the hard axes parallel to the edges of the array [61]. Figure # 1.4, displays the square lattice and the corresponding schematic magnetic domain structure. The spin configuration in the remanent state of the square lattice is divided into five domains: four domains in between the holes, with spins oriented along the hard axis (Figure # 1.4b), decreasing the high magnetostatic interactions within the holes; and one larger domain in the center of the lattice pointing along the easy axis [37].

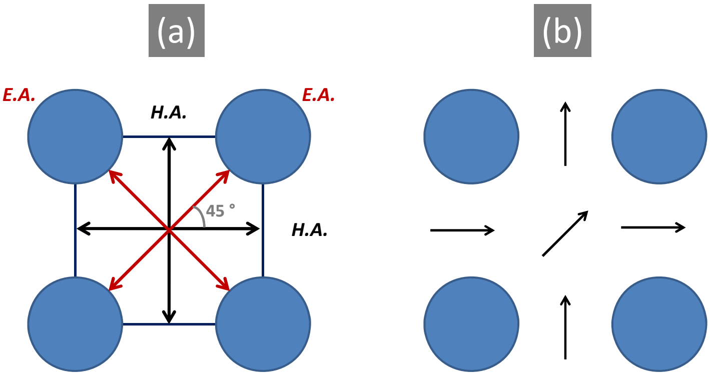

Figure # 1.4. (a) Square lattice, and (b) it corresponding spin configuration.

1.3.4.2. *Honeycomb lattice*

The anisotropy in the honeycomb lattice is a six-fold (three easy axis) configuration. The hard axis still remains parallel to the edges of the lattice. Figure # 1.5 shows the geometry and the orientations of the easy and hard axis of the honeycomb lattice. The spin configuration in the honeycomb lattice can be divided into nine domains, with a more intricate structure [37].

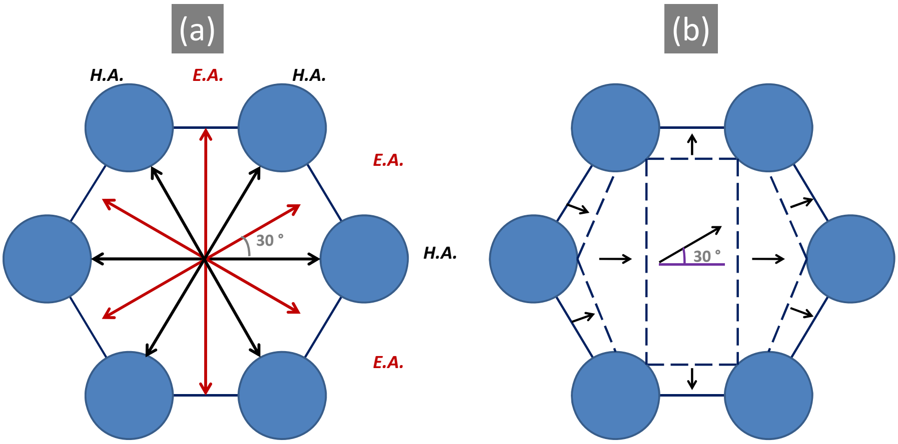

Figure # 1.5. (a) Honeycomb lattice; and (b) it corresponding magnetic domain structure.

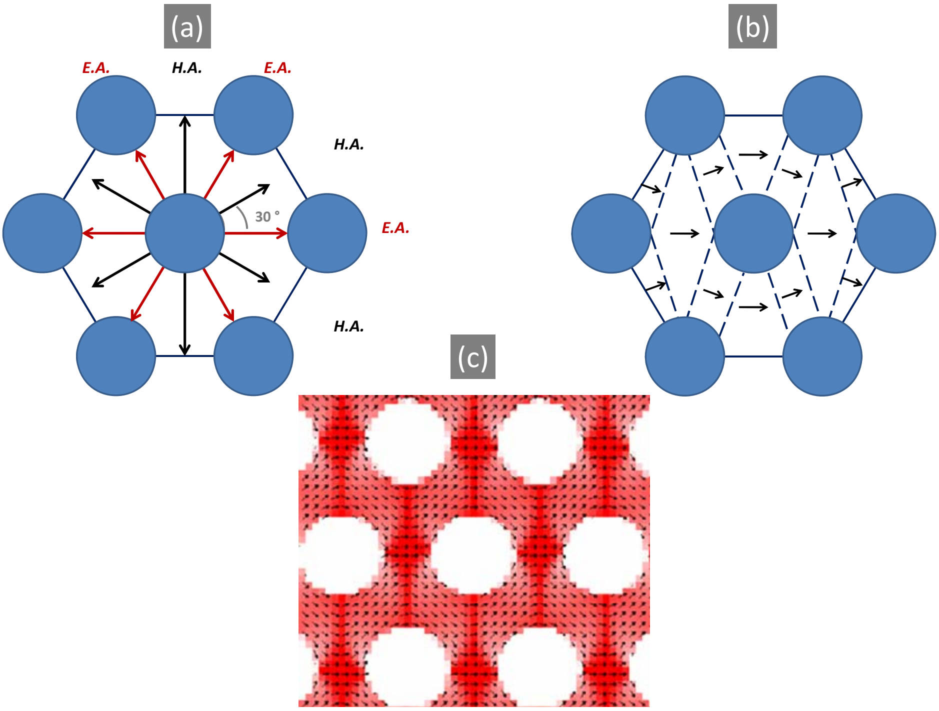

Figure # 1.6. (a) Hexagonal lattice, (b) it corresponding spin configuration and (c) simulation model from Ref. [37].

1.3.4.3. *Hexagonal lattice*

The hexagonal arrangement has a well-defined six-fold symmetry of the magnetic anisotropy [37,56] as in the last case, although the orientations of the easy and hard axes are reversed. Figure # 1.6 shows the hexagonal lattice (similar to the obtained using AAM templates) and the spin configuration, respectively [37].

The spin configuration in the remanence state follows the pattern of the lattice as a result of the local shape anisotropy induced by the holes; the spins are oriented around the holes with angles of ± 30° from the easy axis and the average magnetization lays parallel to the easy axis. This remanent configuration creates a strong demagnetizing field between the holes of the central row, probably due to the decreasing exchange energy of the wall [56]. Other works have shown that the remanent state creates domains with stripes that connect the holes in diagonal position, Figure # 1.6c [59,62].

1.4 COERCIVITY

What happens to the DW under the presence of a defect in a CTF? A periodic non-magnetic inclusion in a CTF reduces the local anisotropy energy, showing an interesting feature, the hardening effect on the magnetic properties when comparing to the corresponding CTF [55]. The presence of the pinning defects leads to an irregular DW motion consisting on a series of Barkhausen jumps as the wall skips from defect to defect [52]. If the defect width (L) is smaller than the DW width the coercivity is predicted by the micromagnetic calculations [63,64] to increase linearly with D. The DW is more strongly pinned if a larger number of defects fill the wall thickness.

Several works have demonstrated the relation between H_c and the geometric properties of the arrays. According to some works [59,63,65,66,67], H_c increases with 1/D, hence stronger magnetic fields are needed to overcome this pinning effect [68]. On the other hand, when D is kept constant, H_c is found to increase with d_P, due to the increasing of the local stray fields [59]. In general, the increases of the H_c with increasing d_P and D, is attributed to the pinning of DW due to the local dipolar effect [69].

$$H_c \, \alpha \, \frac{1}{D-d} \qquad \text{Eq. (1.7)}$$

According to the micromagnetic model, H_c saturates for larger defects. As expected, the coercivity decreases with the separation distance. The separation of the non-magnetic structures implies a decrease in the magnitude of the demagnetizing energy relative to the total energy.

The Inclusion Coercivity Theory [70] explain that if the defects are uniformly distributed on both sides of the DW, the total average force on the DW vanishes, thus only local fluctuations of the defects (dimensions of the nanoholes), are important contributions to act as pinning centers. The H_c will increases with d_P due to the larger stray fields.

Another study [71] explain that the magnetic reversal process depends on the defects present on the film, which serve both as nucleating centers, where reversed domains are formed, and as pinning centers, which block the motion of DW. The crystalline defects can be compare to the nanoholes in our study.

1.5 ANTIDOT ARRAYS OVER ANODIC ALUMINA MEMBRANES

Some studies are based on the antidot arrays over *anodic alumina membranes* (AAM) were a hexagonal patter is obtained; many different compositions were used in the mentioned works below, but only a few examples are referred in our study:

- IrMn/CoFe [72] where exchange bias was found to depends on the density of the defects and the separation between the holes.

- CoAlO antidot arrays [73] shows different magnetic and magneto-resistance behavior with porosity (surface ratio of holes to continuous film).

- Multilayer antidot arrays of Co/Cu/NiFe with different templates have been studied, as for example in block copolymer templates [74] where a two-step magnetization process was found.

- Py [75,76,77,78] obtaining the magnetic behavior with the dimensions of the antidots; besides dynamic measurements were made in these works. Due to the low magnetocrystalline constant of Py, the magnetic properties and the domain structures are determined by the geometrical properties of the arrays [17,79,80], although many studies have shown that the intrinsic anisotropy of the unpatterned film, or CTF, are still present into the arrays [18,51].

1.6 OBJECTIVES OF THIS WORK

This study is focus on the systematic study of the enhancement of the magnetic properties of magnetic thin films using a nano-patterned system: antidot arrays. The competition between the intrinsic and shape anisotropy together with the local effects originated by the antidots creates new scenery to engineer the magnetic properties of the thin films by tailoring the geometrical parameters.

In order to exploit the magnetic properties of the antidot arrays and applying them instead of the continuous thin film, the magnetic properties with different geometric properties must be deeply known. Particularly, the need to study these magnetic properties has led to use templates with the desired nano-dimensions and properties, but mainly with the possibility of relative easy manipulation. The presented AAMs possess exceptional features for the purposes of this work such as low cost, the reproducibility of the samples, the relative easy manipulation of the geometric properties and the desire nano-dimensions. Besides, these membranes have long-range porous area, in which the controlled pores diameter are of few tens of nanometers, and are hexagonally arranged within geometric domains of micrometric size. The total effective area is of order of cm^2.

The handling of the geometric properties of the AAMs is the keystone of this work, using chemical processes. The well-equipped laboratory at the Institute of Material Sciences of Madrid holds the necessary conditions for the manipulation of the membranes. The technique behind these systems is chemical in origin, which together with physical deposition method, i.e. sputtering, consist in a bottom-up method.

The structural and morphological characterizations of the arrays consist in the use of several techniques, which gives the geometric parameters that at the same time control the magnetic properties. The magnetic characterization was made using different systems and techniques, resulting in a complete overview of the magnetic behavior of the arrays.

1.7 THESIS OUTLINE

The principal results of the study of the antidot arrays are presented in the following Chapters.

In Chapter 1, an overview of the physical processes involving antidot arrays particularly magnetization reversal is addressed. The work is divided in the following sections: i) introduction; ii) an overview on the properties of the magnetic domain walls (DW) in continuous thin films (CTF), iii) the magnetic configuration in lithographed antidot arrays according to the lattice, iv) coercivity in the antidot arrays and v) a brief summary of the previous studies of antidot arrays over AAM.

In Chapter 2, the experimental techniques are described. We make an emphasis in the magnetic systems, in which different kind of measurements were employed. Each technique has a brief description of the system, and then a further explanation of the measurements is given.

In Chapter 3, the magnetic behavior according to the morphology and crystallographic structure (properties controlled through different sputtering parameters) were investigated in order to evaluate the quality of the Py films. This part of the work presents the fabrication and characterization of the anodic alumina membranes, of the continuous thin film of Py and Co. Finally the fabrication and characterization of the antidots arrays of Py over AAM are shown.

Chapter 4 is the main piece of this study, where the magnetic characterization of the Py antidot arrays, as a function of the geometric properties of the membranes, is deeply explained. The work presented in this chapter has the magnetic considerations on CTF and antidot arrays grown on top of AAM; the study was made using different geometric dimensions, namely pore diameter of the AAM (d_P), diameter of the antidot arrays (d), lattice parameter (D) and thicknesses (t_{Py}). The magnetic characterization was made using the Vibrating Sample Magnetometer, Magneto-Optic Kerr Effect magnetometry and Magnetic Force Microscopy, additionally was made a study of the magnetic domain structures by X-Ray Photoemission by Electron Microscopy.

In Chapter 5, antidot arrays with two different layers, made of different composition, are magnetically characterized. The chapter presents an introduction of the magnetic interactions expected to be present in the bi-magnetic soft/hard system, namely *exchange spring interaction*, which is typical in modern permanent magnets. Then an extensive study of the magnetic characterization of individual Co layer antidot arrays over AAM and the study of the soft/hard bilayer antidot system are presented.

2 CHAPTER 2

EXPERIMENTAL TECHNIQUES

Arrays of magnetic antidots were proposed as candidate material to be used in a large number of technological applications. The main advantage of these systems lays in the possibility of tuning the magnetic properties by careful control over the geometrical parameters (such as the film thickness, the pore diameter, separation and ordering). Various experimental techniques are available for the preparation of arrays of antidots, including different lithographic methods [29,30,26], the use of masks of self assembled spheres, and mechanical nano-indentation [81]. Each method presents a series of advantages and disadvantages with respect to production time, cost, ultimate size and shape of the holes, reproducibility, long range ordering and maximum size of the patterned area.

An alternative technique, proposed in this study, is the use of *anodic alumina membranes* (AAM) as nanostructured template to grow magnetic antidots. AAMs are obtained by a two step anodization process of an aluminum plate (disk) resulting in an arrays of self assembled pores perpendicular to the surface of the aluminum oxide film [38].The tunable hexagonal lattice and its long-range order, allied to the low cost and the small dimensions of the pores make AMMs a successful competitor to more expensive and time consuming lithography techniques.

In this study, antidots films were grown by a physical deposition technique: magnetron sputtering. The magnetic film sputtered over the membrane reproduces the pattern of the holes, and the magnetic properties are found to depend strongly on the geometric characteristics [45,82].

In this section, an overview of the experimental techniques concerning fabrication and characterization is presented. It is divided in four parts: i) fabrication techniques, ii) structural characterization, iii) topography analyses and iv) magnetic characterization. The work of this study, focus on improvements in the characteristics of the AAM templates aiming tailored magnetic properties. The experimental techniques are described making special emphasis in those involving our most active work.

2.1 FABRICATION TECHNIQUES

2.1.1 Anodic Alumina Membranes

A natural oxide layer of aluminum oxide (Al_2O_3), with a thickness of about 2 nm, grows when the metal is exposed to the atmosphere protecting the metal underneath. Further oxidation can be forced by means of electrochemical processes. Under particular conditions, such forced oxidation results in a nanoporous layer, known as anodic alumina membranes (AAM), amorphous in nature [83,84].

The use of the AAM became popular when Masuda and Fukuda [38] introduced a lithography-free method to attain AAMs and proposed these membranes as templates for functional nanostructures. Their exceptional characteristics, as the hexagonal self-assembling, high-ordered porous area, high reproducibility, and low cost production, have given this material the opportunity to be a great candidate for the production of nano-devices.

The electrochemical growth of AAMs is obtained using a two-step anodization process of the Al metal [38]. First, a deep cleaning and degrease of the Al disk was made with acetone and isopropanol in an ultrasound bath. Then, an electropolished process was made in order to decreases the roughness of the disk, with a solution of ethanol (C_2H_5OH) and perchloric acid ($HClO_4$), in a volume proportion of 75%:25% [85,86]. The solution must be at low temperature (between 0 and 3ºC) and vigorously shake (with a magnetic system) [87].

The anodization process is then carried out within an electrolytic bath with an specific voltage applied, depending on the desire *pore diameter* (d_P) and *interpore distance* (D) [88]. If the electrolyte cannot dissolve the alumina, the resulting oxide layer is continuous [89], otherwise a nanoporous oxide layer with a barrier layer at metal/oxide interface is obtained.

The resulting porous structure from anodization ordered in a hexagonal lattices [90], can be prepared with a wide range of geometrical parameters (d_P from 10 to 160 nm and D from 65 to 400 nm [91,92,93]. The geometrical properties depend strongly on the electrolyte, the temperature and the potential during the anodization process. A full description of the chemical and physical processes involved during the anodization, can be found in Refs. [55,87]. In this work the membranes were obtained by anodization in oxalic and sulfuric acids, yielding d_P = 35 and 25 nm, and D = 105 and 65 nm, respectively. In a 2-dimensional system, the hexagonal lattice offers the closest packing of uniform size cylindrical pore cells [94]. In AAMs it is possible to obtain hexagonal ordering, distributed over domains of around 1-3 µm size. Figure # 2.1 summarizes the anodization process.

Afterwards the AAMs were submitted to a wet-etching treatment in 5% of weight of phosphoric acid at 30 and 35 °C to widen the pores up to different final diameters.

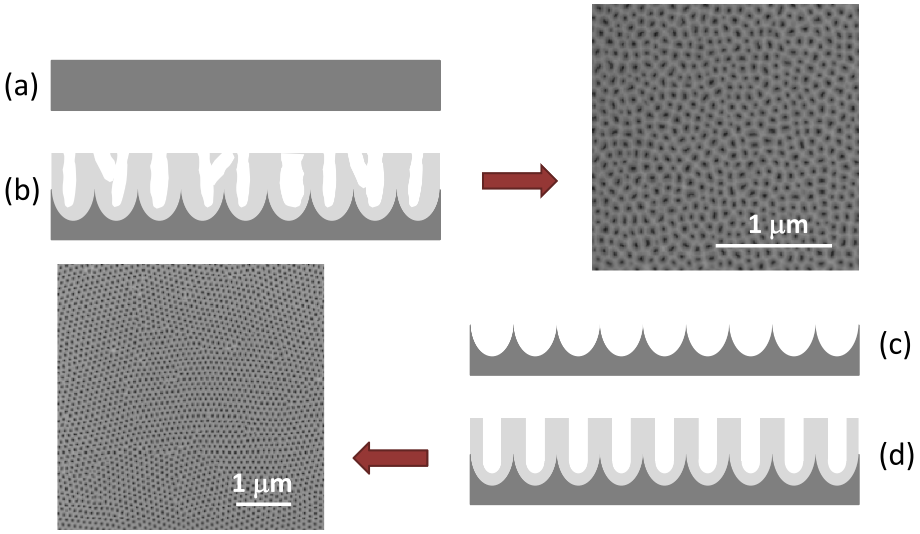

Figure # 2.1. Anodization process of an Al foil: (a) one starts from an electropolished Al surface; (b) cross-sectional scheme of a *AAM* after first anodization process with random nucleation of the pores in the top; (c) Al foil after removing the first anodized alumina revealing the engraved hole structure; (d) *AAM* after the second anodization process with an ordered pattern of nanoholes.

2.1.2 AAM surface Etching by Ion-Milling

The anodization process leads to *AAM* with a characteristic topography at its surface [95]. Such features are intrinsic to the method. Therefore, the membranes were polished by a low-angle ion-milling procedure to reduce the characteristic AAM surface roughness. Two different systems have been used for different families of samples.

The first system consisted of an 1160L 4-target Ion Beam Sputter Deposition system from Commonwealth Scientist Corporation at the INESC-MN facilities, as can be seen in Figure # 2.2. This system possesses two 3-cm diameter Kaufman dc ion sources, one for film deposition and the other for assisted deposition or ion-milling [21]. The low-incidence angle (10º) ion-milling was performed on a set of AAM substrates taking advantage of the average directionality of the beam and etching preferentially the surface without shortening the length of the nanopores [95].

The second system is a Reactive Ion Beam Etch System (*RIB*) - Etch 160 ECR, in the Microelectronic Institute of Madrid, Tres Cantos.

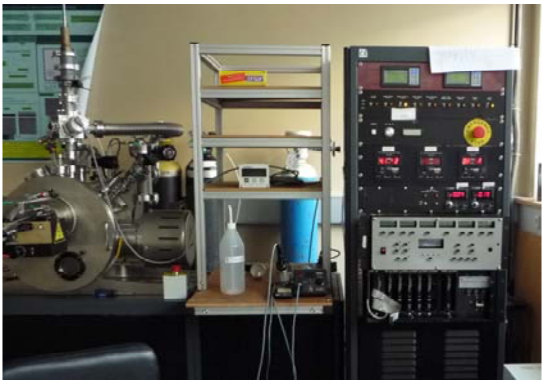

Figure # 2.2. Ion Beam Sputter Deposition system from Commonwealth Scientist Corporation at the INESC-MN facilities

2.1.3 Sputtering

The sputtering process is a physical vapor deposition method which is relevant for both research and technological applications of thin films. In the sputtering method, ionized gas, typically Argon, is accelerated towards a target (*cathode*), and hits the material to be deposited (*substrate*), as we can see in Figure # 2.3. By momentum transfer, the atoms are ejected and accelerated towards the substrate (*anode*). This method is a very efficient process, occurring under high vacuum conditions allowing the atoms to maintain a high mean free path.

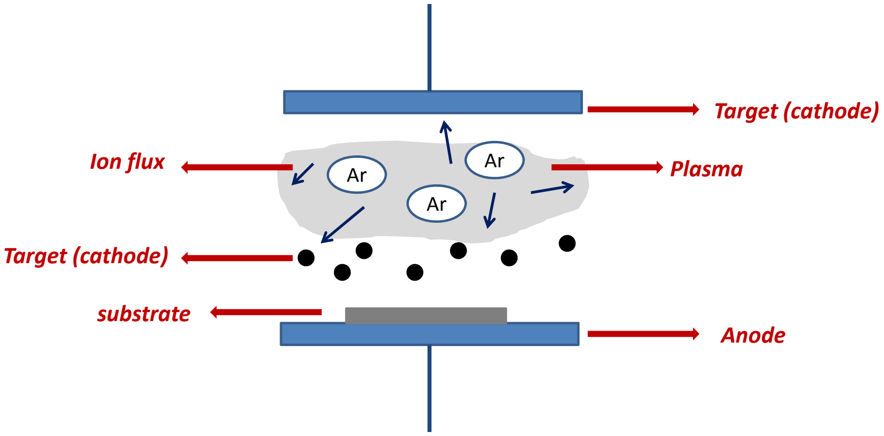

Figure # 2.3. Diagram of the sputtering process.

The application of magnetic field (magnetron sputtering) improves the ionization yield by decreasing the mean free path of the electrons, thus favoring the ionization of the gas. As a consequence, this system decreases the acceleration voltage, increasing the deposition rates for the sputtering process.

The main advantages of this method rely on the possibility of depositing a large number of elements or alloys, maintaining the initial stoichiometry of the target composition. In addition this method allows a high control over the deposition rates, and thus the thicknesses, which can vary from few angstroms to microns.

A home-made Magnetron Sputtering system was used, with typical argon pressure or *work pressure* (P_w) from $2.5 \cdot 10^{-3}$ to 10^{-4} mbar.

The sample holder is located at the end of a high vacuum magnetic manipulator, Figure # 2.4. Due to such arrangement, the sample holder is slightly magnetized and therefore a magnetic field of ~ 6 Oe is applied during film deposition. The effect of this field is negligible for hard-magnetic compositions (e.g. Co or NdFeB), but becomes significant if soft magnetic materials are deposited (e.g. NiFe, Fe).

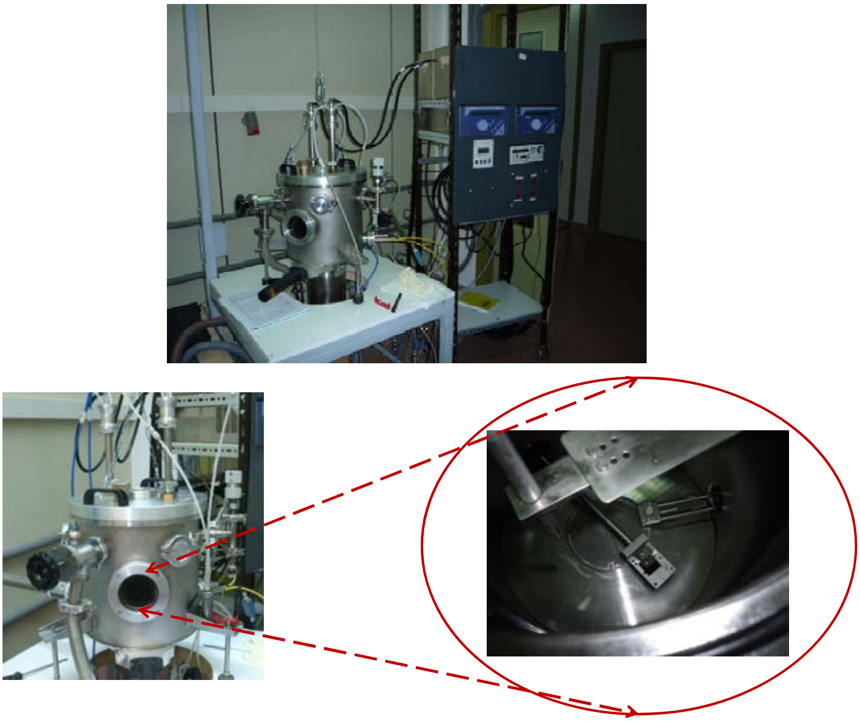

Figure # 2.4. Sputtering system with a zoom to the sample holder arm.

2.2 STRUCTURAL AND CHEMICAL CHARACTERIZATION

2.2.1 X-Ray Diffraction

The *x-ray diffraction* (*XRD*) is produced by the constructive interference of X-ray diffracted beam by planes parallel to the plane of diffraction. The XRD measures different structural properties, such as crystalline properties, the orientation, or the grain size [96].

From the Scherrer equation [97], Eq. (2.1) the average size of the out-of-plane crystals in a specific orientation {hkl} can be obtained from the diffraction peak broadening at half maximum intensity:

$$GS = \frac{K\lambda}{\omega \cos\theta}, \qquad \text{Eq. (2.1)}$$

where grain size or the average size of the crystals the out-of-plane grain size, K is the shape factor (typically 0.9 for round particles), λ is the incident X-ray wavelength, ω is width at half maximum in 2θ (in radians), θ is the Bragg angle.

The XRD measurements were performed at the SIDI, Universidad Autónoma de Madrid (UAM), with a X'Pert PRO X-ray diffractometer from PANalytical (Cu-K_α line with wavelength λ=1.54 nm) in the θ-2θ and grazing incidence geometries. Typical spectra parameters are a scan range from 10° to 90°, in 0.02° steps and an acquisition time of 300 ms per step.

2.2.2 X-Ray Reflectivity

The X-Ray Reflectivity (XRR) is a non-destructive technique used to measure the morphological properties of thin films, such as thickness, roughness or density [98,99].

The thicknesses were evaluated by the XRR measurements according to the Snell's Law, when an incident beam strikes the boundary between two different electronic densities (or refraction index, n) one part of the beam is transmitted and another reflected. For refraction indexes lower than the air ($n_{air} = 1$), a critic angle (θ_c) appears, in which when the incident angle (θ_i) is lower than θ_c, a total reflection is produced. In the Snell´s Law, the incident beam is at air (n_{air}) and the incident angle is the angle between the incident beam and the plane (boundary between the incident beam and the sample) [100].

For wavelengths of the order of the X-rays, almost all the compounds have refraction index lower than n_{air}, so the critic angle is between 0.1º and 0.6º [101,102].

When making the incident angle higher than the critical angle, the reflected beam from the interfaces (film and substrate) interferes, creating Kiessig fringes which periodicity is related to the thickness of the film. Figure # 2.5 shows an example of

Kiessig fringes. The relation between the Kiessig fringes and the thickness can be found elsewhere [103]. Further details about this technique are explained in Ref. 103.

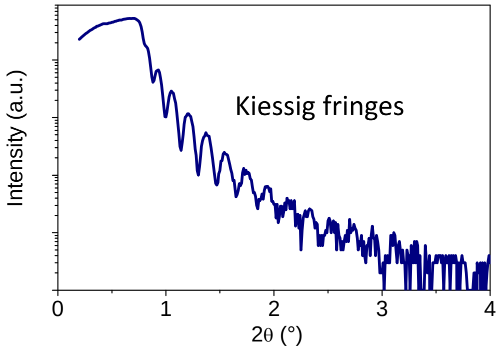

Figure # 2.5. Kiessig fringes of a 43 nm Py continuous thin film.

The XRR measurements were made in the θ-2θ Bragg-Brentano geometrical configuration, where the incident and the diffracted beam have the same angle relative to the sample surface. In this configuration a diffraction peak appears when the incident and the diffracted beam match a reciprocal lattice vector. The diffractometer used was a high resolution Bruker AXS D8 Discover at ICMM.

2.2.3 Energy Dispersive X-Ray Spectroscopy

Chemical information of particular samples was obtained by Energy Dispersive X-Ray Spectroscopy (EDS). Overall, the high energy of an incident beam ionizes the atoms, and when returning to the ground state, X-ray photons are emitted; the energy of these photons is characteristic for each element (X-ray fluorescence) [104].

The EDS detector was embedded in a Field Emission Scanning Electron Microscopy (FE-SEM), FEI Nova Nanosem 230 at ICMM, CSIC.

2.3 TOPOGRAPHY AND MORPHOLOGY

2.3.1 Atomic Force Microscopy

The *Atomic Force Microscopy* (*AFM*) is a high-resolution (fractions of a nanometer) scanning probe microscope. The AFM consists on a cantilever with a sharp tip (probe) at its end used to scan the sample surface. The interaction between the tip and the sample originates a deflection of the cantilever, measured through the deflection of an incident laser beam [105].

Two different modes can be used in the AFM system: contact mode, where the repulsion force between the tip and the sample is kept constant; and the dynamics mode, where the cantilever vibrates at resonance frequency and the amplitude is used as the feedback parameter. The tip can generate artifacts in the images, so a special care must be taken in the analysis of the results.

The system used is a Cervantes system from Nanotec Electrónica at ICMM.

From the AFM images, the average size of the in-plane crystals were measured by the calculus of the “auto-correlation” [106]. This operation evaluated the integral convolution of a multiplied image by itself, with a certain displacement in the axes X and Y. The auto-correlation image G is defined as:

$$G\ (k_1, k_2) = \sum f\ (x, y)\, f(x + k_1, y + k_2) \qquad \text{Eq. (2.2)}$$

where f(x,y) is the initial image, and k_1 and k_2 is the displacement in the axes X and Y respectively, with respect to the center of the image. The auto-correlation consists in a central peak which allows the calculation the average grain size from FWHM.

2.3.2 Scanning Electron Microscope

The *Scanning Electron Microscope* (*SEM*) uses the detection of the secondary electrons to produce the images. The generated secondary electrons depend on the energy of the incident beam, material and the surface of the sample. In the SEM images, the contrast is due to the morphology of the sample or due to a different compound in the sample [104]. The resolution goes from 3 to 20 nm.

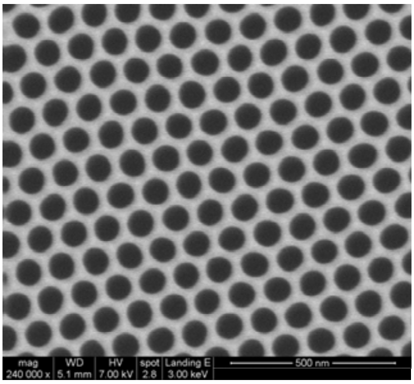

Figure # 2.6. SEM image of an AAM with d_P = 70 nm and D = 105 nm.

The morphology of the samples was addressed by the same system for the EDS measurements: FE-SEM, with a high resolution FEI Nova Nanosem 230, detector vCD, at ICMM. The parameters are: High voltage: 5 kV, landing energy: 3 keV. This equipment enables the observation of non-conductive samples with no need for metallization as it allows low-vacuum SEM images. Figure # 2.6 shows an example of an image obtained by SEM.

2.3.3 Ellipsometry

Ellipsometry spectroscopy is an optical technique based on the change of polarization of an incident light. This is a non-destructive technique and allows the determination of thickness and optical constants, such as *refraction index* (n), of thin films [107,108].

The optical constants define how light interacts with a material and allow one to calculate how deep electromagnetic radiation can penetrate into a material. The penetration depth is defined as the depth at which the intensity of the radiation inside the material falls to 1/e (about 37%) of its original value at (or more properly, just beneath) the surface.

The complex refractive index is a representation of the optical constants of a material; it is represented by Eq. (2.3). The real part or index of refraction, n, defines the phase velocity of light in the material and the imaginary part or extinction coefficient (κ), determines how fast the amplitude of the wave decreases. The extinction coefficient is directly related to the absorption of a material and is related to the absorption coefficient (χ), Eq. (2.4).

$$\hat{n} = n + i\kappa \qquad \text{Eq. (2.3)}$$

$$\chi = \frac{4\pi\kappa}{\lambda} \qquad \text{Eq. (2.4)}$$

$$\delta = \frac{1}{\chi} = \frac{\lambda}{4\pi\kappa} \qquad \text{Eq. (2.5)}$$

From the expression of the χ, the penetration depth (δ) can be calculated in Eq. (2.5). Where λ is the light wavelength, in this case its value is $\lambda = 632.8$ nm (red light of the MOKE system).

The surface magnetic characterization of the antidots is affected by this penetration depth, since the penetration is not the same in the CTF that in the case of the antidot arrays moreover depends on *d*. The magnitude of this penetration depth gives an approach to a more complete magnetic analysis when comparing the MOKE loops to the VSM measurements.

The equipment used in this work, is a dispersive ellipsometer SOPRA GES 5E, with a Xe lamp which allows adjusting different incidence angles over the sample. The spectral range goes from 190 to 2000 nm.

2.4 MAGNETIC CHARACTERIZATION

The magnetic characterization was made using different techniques. In this section the description of the equipments and techniques as well as the general analysis of the data is introduced.

.

2.4.1 Vibrating Sample Magnetometer

The Vibrating Sample Magnetometer (VSM) operates on Faraday's Law of Induction, detecting a voltage across the terminals of a coil when a magnetic field (flux) is varied within. In the VSM, the change in flux is achieved by a vibrating sample. This flux is proportional to the *magnetic moment* which is measured in *EMUs* and is displayed as a function of the *magnetic field* (H), the angle of the field, and the temperature of the sample.

The VSM system and it parts are presented in Figure # 2.7 and some of the parts are listed as follow:

1. Electrical device;
2. Vibrating system;
3. Sample;
4. Coils.

The sample is placed in the middle of a set of detection (pickup) coils in which a voltage is induced. An electromagnet surrounds the sample and pickup coils which are used for vary the field to which the sample is exposed, so the magnetization can be measured as a function of the applied field. The VSM's operating software can be set up to extract many different magnetic parameters in order to characterize a wide variety of magnetic samples of both high and low coercivity [109].

The magnetic characterization of the bulk system (magnetic thin film + substrate + defects and imperfection) was performed in an ADE system VSM, EV7 KLA-Tencor, using 6 different techniques:

1) *Hysteresis loops, (M-H)*;
2) *First magnetization curve or Virgin Curve Measurement* (*virgin*);
3) *Isothermal Remanence Measurement* (*IRM*);

4) *Reversible curve*;
5) *Switching Field Distribution* (*SFD);*
6) *First Order Reversal Curves* (*FORC*).

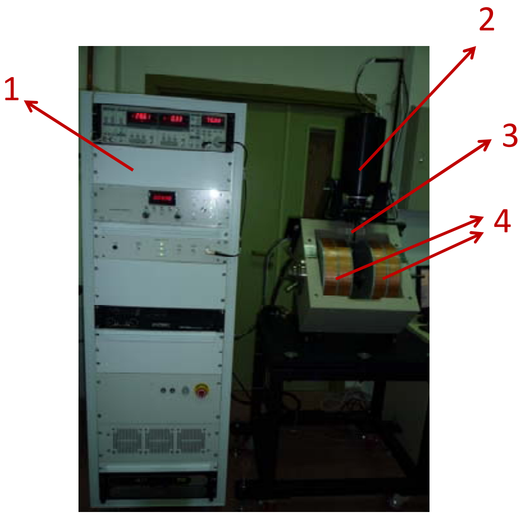

Figure # 2.7. VSM system with some of the parts.

- *Hysteresis loops, (M-H)*: measures the magnetization vs. applied magnetic field. The loops were obtained at room temperature under a maximum applied field of 1.8 T (for a gap between the electromagnets pieces of approximately 17 mm). Two different configurations were employed: *in-plane* (*IP*) in which the field is parallel to the plane of the sample, and *out-of-plane*, (*OOP*), where the field is perpendicular to the plane of the sample, Figure # 2.8.

In addition, measurements with different adjustable angles between 0 and 360º along the plane of the sample were taken.

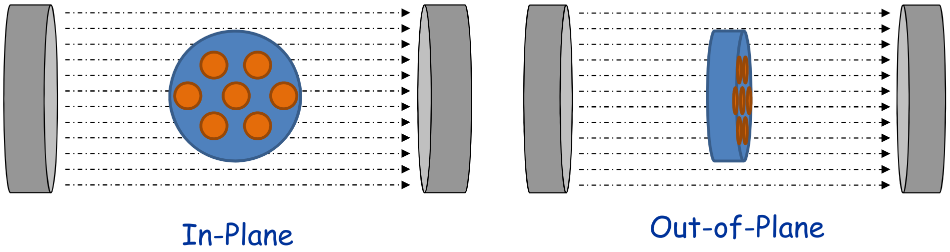

Figure # 2.8. IP and OOP configuration of the VSM

- *First magnetization curve or Virgin Curve Measurement* (*virgin*): measures the magnetic behavior of a demagnetized sample as a function of the applied field. The measurement is performed by measuring the magnetic moment as a function of a field that is slowly increased from 0 to a certain maximum field.

The measurement can be performed on an initially demagnetized sample or, alternatively, can be performed after demagnetizing a sample by ac demagnetization from a maximum applied field of 10 kOe.

- *Isothermal Remanence Measurement* (*IRM*): the IRM measures the remanent magnetization as a function of an increasing magnetizing field starting from a demagnetized state. After demagnetizing the sample, from a maximum applied field of 10 kOe, a small field is applied and subsequently removed after which the remanent moment is measured. This moment is plotted against the previously applied field. Next, a somewhat larger field is applied and subsequently removed, after which the next remanent magnetization is measured. The resulting curve looks comparable to the Virgin Curve.

The difference between the Virgin Curve and the IRM is generally attributed to the reversible changes in the magnetic material. The IRM curve gives information about the irreversible processes.

- *Reversible curve* (*rev*: from Virgin minus IRM), calculated by the subtraction of the IRM from the Virgin curve, which is linked to reversible mechanisms.

An example of these three curves is represented in Figure # 2.9. The normalization of the Virgin curve was made taken the saturation signal as 1, the IRM and the Reversal curves were normalized to this value (saturation of the Virgin curve), so the IRM and Reversible curves would be in proportion with the signal of the virgin curve, which comprises the total magnetization signal. From here the percentages of the IRM and the Reversible curves were calculated.

- *Switching Field Distribution* (*SFD*): Magnetization changes are caused by ‘switching’ of magnetic particles. The switching field determines how much magnetization is needed to switch a particle from negative to positive magnetization.

The SFD (derivative) can be taken from Virgin Curve, Hysteresis, IRM, and DCD. For best results, as it is suggested, the IRM curves were used, Figure # 2.10a.

The rate of change is determined by the number of particles switching:

$$SFD\ (H) = \frac{dM}{dH} \qquad \text{Eq. (2.6)}$$

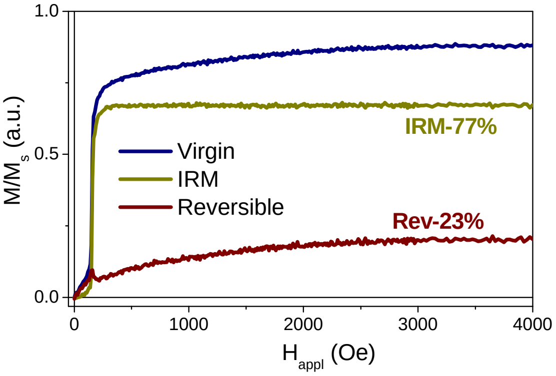

Figure # 2.9. Virgin, IRM and reversible curves of an antidot array of d = 43 nm and Py thickness of 43 nm.

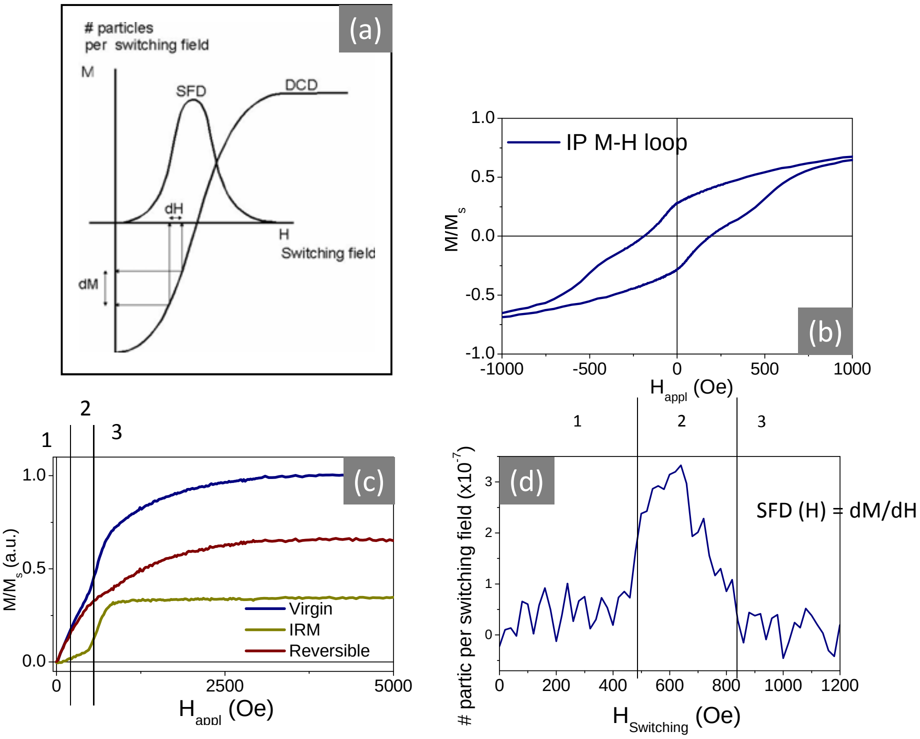

Figure # 2.10. (a) SFD curve, (b) M-H loop by VSM; (c) Virgin curve, IRM and Reversal curve; and (d) SFD of an arrays with d_P = 63 nm and thickness of 10 nm.

Joining all these curves, a lot of information can be obtained, as an example, the M-H loop, the reversal curves and the SFD of an arrays with d_P = 63 nm and Py thickness of 10 nm are represented in Figure # 2.10b-c-d, respectively.

Region #1: From 0 field to 460 Oe (line #1): the IRM has a raise.

Region #2: From 460 to 850 Oe: (line #3): the IRM suffers an abrupt increase.

Region #3: From 850 Oe to saturation: the IRM is already saturated.

In the SFD, the maximum value of "number of particles per switching field" is around 635 Oe (approximately the half of the field of Region #2), in other words, almost all the particles suffer the reversal magnetization at these field range, from 460 to 850 Oe.

As can be observed in the M-H loop, this arrays has a bi-phase behavior, in which may correspond to the two regions in the reversible curves. In some cases, when the loop has only single-phase magnetic behavior, the IRM has only one region, with a maximum saturation field (line #3 for example).

- *First Order Reversal Curves* (*FORC*): The FORC diagram was initially introduced by Mayergoyz [110] as a method to identify the Preisach distribution. Afterwards it was proposed by Pike and co-workers [111] as an experimental measurement for the characterization of the interaction between ferromagnetic particles. The FORC diagram does not require to be measured in a remanent state, and the sample does not need to be demagnetized [112].

While the *M-H* loops give information on the average behavior of the magnetic system, the FORC diagram includes not only interactions as a whole but is able to separate the mean field interaction effect (i.e. the interactions between the particles) [113,114,115], also gives information about the distribution of coercivities, being suitable to study the reversible and irreversible contributions present in the overall magnetization processes [114,115,116,117].

A point on the FORC diagram is obtained from the descending branch of the M-H loop by applying the following field sequence: (H_m, H_r, H), where H_m is the saturation field; H_r is the reversal field going from $-H_m$ to H_m; and H is the field at which the magnetic moment is measured, denoted as m_{FORC} (H, H_r). The FORC distribution is then given by the derivative in Eq. (2.7) [111].

$$\rho\ (H\ , H_r) = \frac{-1}{2}\frac{\partial^2 m_{FORC}}{\partial H \partial H_r} \qquad \text{Eq. (2.7)}$$

An example of a FORC diagram, which is the contour plot of this distribution is presented in Figure # 2.11, where exist a clear evidence of the presence of two magnetic phases, soft and hard magnetic. A more complex feature is also visible in between: an interference region, in which is given by the interaction coupling between the particles with low and high coercivity.

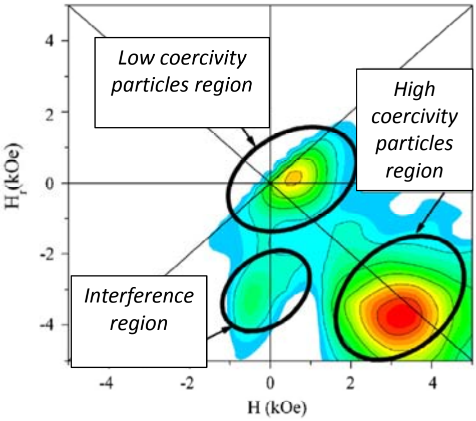

Figure # 2.11. The experimental FORC diagrams for samples with two different ratios between soft and hard magnetic components [113].

Despite the fact that the analysis of results is more intuitive for systems constituting single-domain magnetic entities, it can still be successfully applied to structures having a more complex magnetization reversal behavior.

After reversing the applied field direction, the change of magnetization M is only proportional to the fraction of pure irreversible processes (called hysteron: representation by a square hysteresis loop with coercivity H_c and a bias field H_u). [115]. The generalization of this concept leads to the FORC distribution function, which represents the statistical distribution of the mathematical hysteron.

In order to read the H_c and H_u mathematical hysteron parameters directly from the distribution, it is convenient to execute a change of coordinates, to define a coercive field axis (H_c) and an interaction field axis (H_u) [115]:

$$H_C = \frac{H - H_r}{2} \qquad \text{Eq. (2.8)}$$

$$H_u = -\frac{H + H_r}{2} \qquad \text{Eq. (2.9)}$$

The H_c axis represents the distribution of coercivities which is only related to the irreversible processes and is represented as a contour plot, ranging from red, for maximum values of ρ, to blue for minimum values of ρ, Figure # 2.12. The H_u axis corresponds to the interactions field, which can be interpreted as the antiparallel fields (opposite to the magnetization) originated in the present case mainly by the stray fields produced by the holes.

Even if the FORC distribution only represents direct information about magnetization irreversible processes, it is also influenced by the reversible ones in the presence of a non-static interaction field, such as a mean interaction field [115]. Consequently, the FORC diagram should be considered as a complete representation of the magnetization reversal behavior. For the irreversible contribution, it is needed to consider both the interaction field and switching field effects together [118].

The reversible information is represented with the gray-white line along the H_u axis, has (white: 100% reversible, black: 100%: irreversible).

The maximum position on the FORC distribution is labeled as $H_C^{FORC}$and it may not correspond directly to the coercivity measured by VSM. In addition, the parallel interaction field, H_{inter}, also affects the magnetization reversal process resulting in higher values on the H_c axis ($H_{inter} \alpha M_s$):

$$H_C^{FORC} = H_C + H_{inter} \;\; ; \;\; H_{inter} = kM \qquad \text{Eq. (2.10)}$$

In the present study, the reversible line was not used, since our systems posses always a mixture of reversible and irreversible process, and thus no clear additional information was obtained from the grey-strip., Instead the Reversible curve was obtained; and the contour plot was used only for interactions or coupling interpretations.

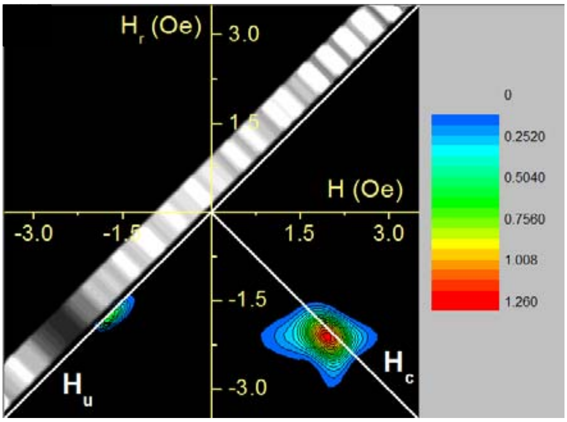

Figure # 2.12. FORC diagram of a CTF of Py with Py thickness of 18 nm.

2.4.2 Magneto-Optic by Kerr Effect

The *Magneto-Optical by Kerr Effect* (*MOKE*) effect occurs when light reflected from a magnetized surface changes in both polarization and reflectivity under an applied magnetic field. MOKE technique explores the interaction between the laser beam and the magnetic material, which gives origin to a rotation of the polarization axis. Since the magnitude of such rotation is proportional to the magnetization of the material we are able to perform (indirect) M-H measurements, by (direct) measurement of the angle between the polarization direction of the incident and leaving beam. MOKE analyses allows to us to obtain mostly the surface magnetic information since the penetration depth of the laser (λ = 632.8 nm) for Py is ~ 15 nm [119]. Therefore, the different magnetic reversal mechanism occurring either at the surface or within the bulk of the sample can be discriminated by comparing MOKE and VSM loops, making these complementary techniques in addressing the reversal mechanisms in samples where surface effects are crucial such as antidot arrays.

The Kerr intensity depends on the polarization of the light and the orientation of the magnetization vector of the sample. The light can be *p*-polarized (parallel to the incidence plane) or *s*-polarized (transversal to the incidence plane – always along the plane of the sample).

MOKE can be further categorized by the direction of the magnetization vector, the incidence plane and the reflecting plane, each category are presented in Figure # 2.13:

1. *Longitudinal MOKE;*
2. *Transversal MOKE;*
3. *Polar MOKE.*

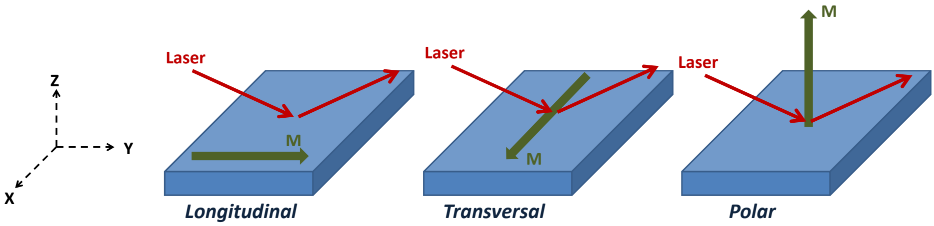

Figure # 2.13. MOKE geometries.

- In the *longitudinal effect,* the magnetization vector is parallel to both the reflection surface and the plane of incidence. The linearly polarized light incident on the surface becomes elliptically polarized after reflection; the change in polarization is directly proportional to the component of magnetization. Longitudinal geometry, within a first order approximation can provide information on the magnetization components M_y.

In this case, both s- and p-polarized light produce a small rotation on the polarization plane of the reflected light, which depends on the magnetization of the sample.

- In the *transverse* configuration, the magnetization is transversal to the plane of incidence and parallel to the surface. In this case, instead of measuring the polarity of the light after reflection, the reflectivity is measured. This change in reflectivity is proportional to the component of magnetization that is transversal to the plane of incidence and parallel to the surface, M_x.

In this case, if the light is p-polarized, the electric field is parallel to the incidence plane, so the magnetic field is transversal to the incidence plane (parallel to the magnetization vector of the sample), as can be seeing in Figure # 2.14. Thus the electric field of the light interacts with the orbital momentum of the electrons, having Kerr effect. The coupling L-S (angular momentum and spin momentum) is the responsible of the magnetic moment.

- When the magnetization vector is perpendicular to the reflection surface and parallel to the plane of incidence, the effect is called the *polar Kerr effect*. Polar geometry, within a first order approximation can provide information on the magnetization components M_Z. In this case, as in the longitudinal configuration, both s- and p-polarized light produce a small change on the polarization plane of the reflected light, which depends on the magnetization of the sample.

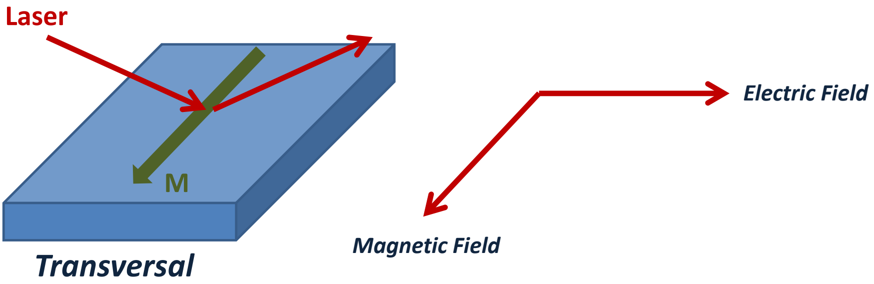

Figure # 2.14. Transversal configuration with p-polarized light.

Two different set-ups were used:

1. NanoMOKE^{TM}, from Durham Magneto Optics Ltd, was employed for *longitudinal magneto-optical Kerr* effect imaging and magnetometry measurements at the ICMM. The maximum field is approximately 500 Oe, with a red color laser (λ=632.8 nm). The frequency of the field goes up to 51 Hz.

2. A second MOKE set-up at the Nanomagnetic Laboratory (UAM) was used. This is a high resolution vectorial-Kerr setup (v-MOKE) [120] where the two *in-plane components* of the magnetization vector are acquired simultaneously during the reversal process. This setup has unique features that allow quantitative vector magnetometry to be performed.

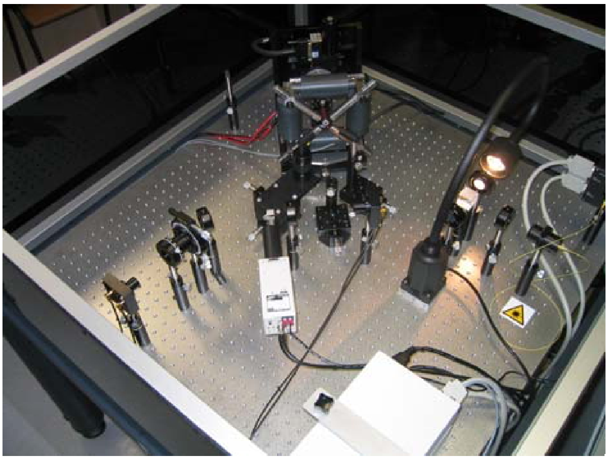

Figure # 2.15. NanoMOKE set-up and the optical parts.

In this setup, the combination of p-polarized incident light in longitudinal Kerr experiments and the simultaneous detection of the two orthogonal components of the reflected light, allow simultaneous determination of the parallel or longitudinal ($M_y = M_{para}$) and transversal ($M_x = M_{trans}$) magnetization components to the field direction. The rate of the applied magnetic field sweep rate is fixed to 10 Hz, and the signal is measured using a fast oscilloscope. Statistical noise is reduced by averaging several measurements taken under the same conditions. Vectorial-resolved hysteresis loops were recorded at room temperature as a function of IP angular rotation angle (α_H), keeping fixed the external magnetic field direction. The entire angular range was probed every 4.5º (from 0º to 360º), with 0.5º angular resolution. Further information about the set-up can be found in Ref. 121

The optical parts of the MOKE system are presented in the next figure and listed as follow:

1. Laser (HeNe);
2. Polarizer (out coming p-polarization);
3. Lens;
4. Sample;
5. Half lambda retarder;
6. Wollaston prism;
7. Photodiodes;
8. Magnetic Field.

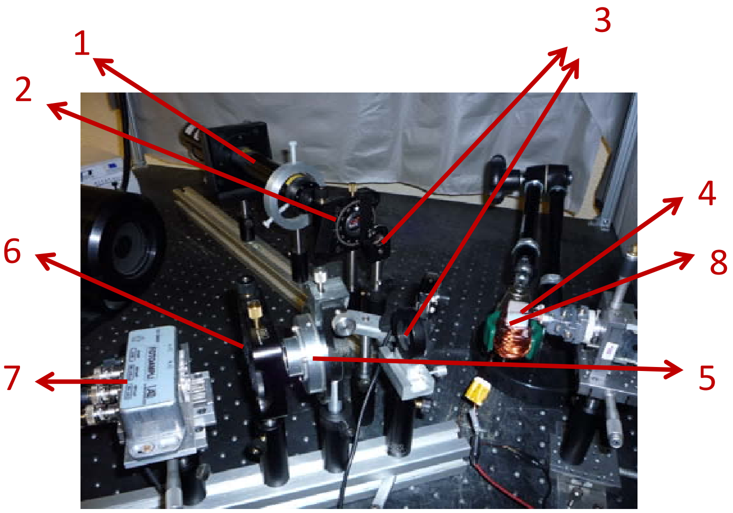

Figure # 2.16. MOKE set-up at the Nanomagnetic Laboratory (UAM) and the optical parts.

The sample is located in a sample holder with a eucentric goniometer and motor stage (for rotational purposes), and a xyz sample stage for positioning. The control unit is formed by a computer, function generator, current source and a digital oscilloscope. Further information regarding the system can be found in Ref. 121.

2.4.3 Magnetic Force Microscopy

The Magnetic Force Microscopy (MFM) is a Scanning Probe Microscope that maps the magnetic spatial distribution by the interaction between the tip and the sample. The MFM works in dynamical mode with a magnetic tip (a standard AMF tip is coated with a magnetic layer) [122]. The system is able to detect not only the atomic forces between the sample and the tip but the magnetic interaction [62,123].

The force between the sample and the tip is

$$\vec{F} = (m \cdot \nabla)\vec{H} \qquad \text{Eq. (2.11)}$$

Where m is the magnetic moment of the tip and H is the magnetic field applied to the sample.

The magnetic moment of the tip can affect the magnetic state of the sample, so the accurate kind of tip should be selected regarding the magnetic properties of the samples. The control detects the changes in the resonance frequency on the cantilever, which is induced by the magnetostatic interaction between the tip and the sample. Generally, the tip has an OOP component of the magnetic moment, so the MFM signal corresponds mainly to the out-of-plane magnetization of the sample.

The MFM signal is related to the orientation of the magnetization along the sample. As an example, Figure # 2.17 shows a sketch of a magnetic tip scanning a sample with magnetic domains with different magnetization orientations. The resulting image has: white color (repulsing interaction), the magnetic moments of the domains are in antiparallel direction relative to the tip; black (attractive interaction), when the magnetic moments are in the same direction; and grey when the magnetic moments are perpendicular to the moments of the tip (parallel to the plane of the sample).

A study of the magnetic domain structure of the antidot surface was performed by *Magnetic Force Microscopy* (*MFM*) from Nanotec Electrónica [105]. The probes are commercial Nanosensors PPP- LM-MFMR cantilevers with a force constant of 2.8 N/m and a resonance frequency of 75 kHz. Before the experiment, the probes are magnetized along their pyramid axis. As usual procedure in MFM, two images were recorded simultaneously, the topography, obtained at small tip–sample distance, and the frequency shift, which is obtained at a retrace distance of 30 nm.

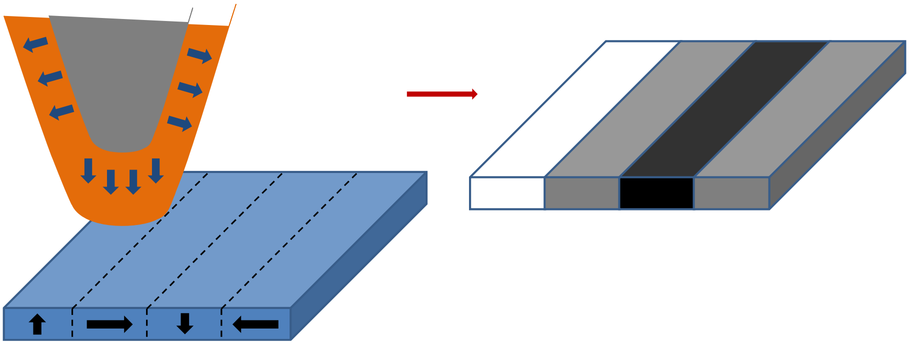

Figure # 2.17. MFM images after the tip has scan the magnetic moment of the sample

2.4.4 Photo-Emission Electron Microscopy (XPEEM)

The microscope technique is fundamentally based on the Photoelectric effect. When X-rays are absorbed by matter, electrons are excited from core levels into unoccupied states, leaving empty core states. Secondary electrons are generated by the decay of the core hole. Auger processes and inelastic electron scattering create a cascade of low-energy electrons of which some penetrate the sample surface, escape into vacuum and are collected by the PEEM optics. A wide spectrum of electrons is emitted with energies between the energy of the illumination and the work function of the sample. This wide electron distribution is the principal source of image aberration in the microscope since electron lenses are chromatic. PEEM is a surface sensitive technique since the emitted electron originates from a very shallow layer, although x-rays penetrate much deeper into the material. Most of the signal is generated in the top 2-5 nanometers [124].

Principles of X-ray magnetic circular dichroism spectroscopy, illustrated for the case of L edge absorption in a d band transition metal in Figure # 2.18. In a magnetic metal the d band is split into spin-up and spin-down states with different occupation. Absorption of right (left) circularly polarized light mainly excites spin-up (spin-down) photoelectrons. Since spin flips are forbidden in X-ray absorption, the measured resonance intensity directly reflects the number of empty d band states of a given spin. In XMCD spectroscopy it is equivalent whether the photon polarization is changed and the magnetization direction is kept fixed or whether the magnetization direction is changed and the photon helicity is fixed [135].

The nanospectroscopy end-station used in this experiment is located at the BESSY II synchrotron in Berlin, Germany. This technique combines a novel *spin-resolved photoelectron emission microscope* (*S-PEEM*) with a dedicated microfocus *plane grating monochromator* (PGM) beamline and full X-ray polarization control [125]. The *S-PEEM* allows probing the spin polarization at the Fermi level in single magnetic domains by spin-resolved microspectroscopy without averaging over multiple domains or defects [126].

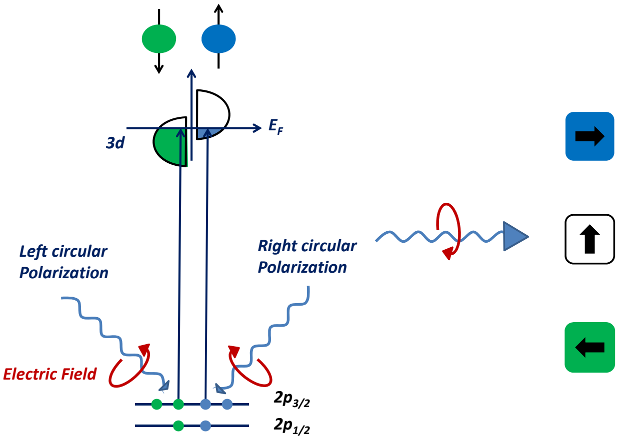

Figure # 2.18. Principles of X-ray magnetic circular dichroism spectroscopy [135].

The system is equipped with a commercial *PEEM* (Elmitec GmbH) with a 30 nm spatial resolution for synchrotron light excitation; the analysis of all three photoelectron spin components with sub-µm lateral resolution is given by two Mott polarimeters (Ferrovac GmbH). This facility offers the application of small magnetic fields during imaging.

In combination with synchrotron radiation, *PEEM* has proven to be an ideal tool for nondestructive investigations of systems consisting of a stack of layers, differing in their chemical composition and functionality [127,128]. By imaging via core-level excitation of photoelectrons or secondary electrons the technique combines spatial resolution in the range of 20 nm with chemical sensitivity, so that each constituent within the probing depth can be imaged separately. With additional lens aberration correction a lateral resolution of 1–3 nm is expected [129]. If the polarization of the X-ray beam is altered, the magnetic state of each element can be imaged via *XMCD* [130,131,132]. In combination with laser excitation also time resolved pump probe experiments are possible. Here we present an instrument which is in addition able to measure the spin-polarization of the emitted photoelectrons with spatial resolution. The angle between the incident X-ray beam and the sample surface is 16° (the resulting spin polarization is almost completely IP – cos 74°) [131].

The nanospectroscopy end-station used in this experiment is located at the BESSY II synchrotron in Berlin, Germany. This technique combines a novel *spin-resolved photoelectron emission microscope* (*S-PEEM*) with a dedicated microfocus *plane grating monochromator* (PGM) beamline and full X-ray polarization control [125]. The *S-PEEM* allows probing the spin polarization at the Fermi level in single magnetic domains by spin-resolved microspectroscopy without averaging over multiple domains or defects [133].

For the XPEEM experiment, an additional sputtering of Al was needed to create a conductive path, otherwise the sample would be charged by the X-Rays due to insulating AAM. The thickness of this sputtered Al is approximately of 100 nm. Figure # 2.19 shows the pattern of the Al over the sample.

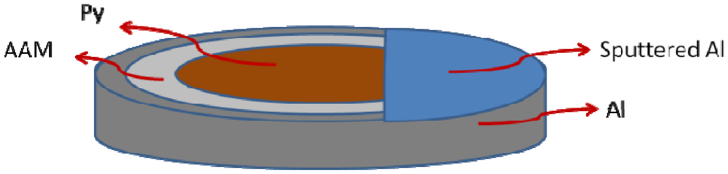

Figure # 2.19. AAM with sputtered Py and Al for contact purposes.

The magnetic imaging was a crucial point in many experiments, such as in the case of this work, where the aim was to observe the magnetic reversal process on the antidot arrays. For this purpose, the facility makes use of a microgap magnet (500 µm distance between the poles) at the rear of the sample. Figure # 2.20 shows the sample holder with the microgap magnet.

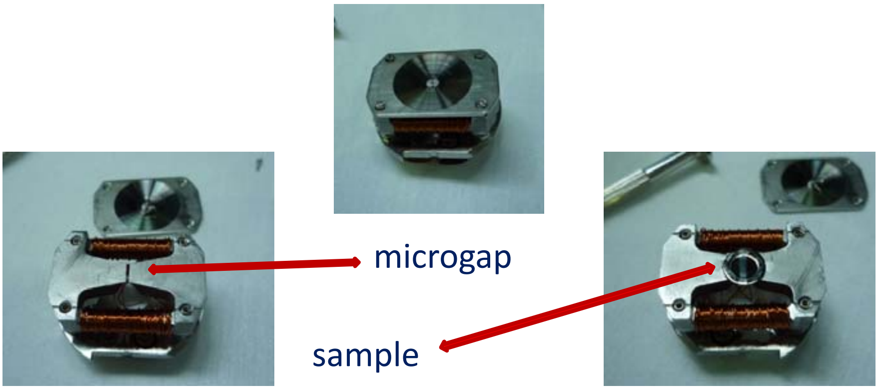

Figure # 2.20. Sample holder with a microgap magnet.

The geometry with the yoke behind the sample confines the magnetic field to a small area which is only about 500 µm wide. But this is still an order of magnitude larger than the typical field of view of the microscope. With this setup we could apply magnetic fields up to 330 Oe without significant distortion or reduction of the 30 nm lateral resolution of the S-PEEM. Deflections of the photoelectrons due to remaining magnetic stray fields, which still occurred, could be compensated by the electron optics of the S-PEEM [131].

Two sample holders were used, summarized in Table # 2.1. The first one allowing to measure under a magnetic field up to 120 Oe but capable of applying up to 360 Oe during very short periods of time (approximately 30-40 seconds), before bringing the sample back to its remanent state. This sample holder has a calibration constant of approximately 0.4 Oe/mA. The second sample holder allows one to measure under a magnetic field up to 135 Oe, and to apply for a short period of time (approximately 30-40 seconds), fields up to 405 Oe. In both cases, the field is applied along the plane of the samples, and its maximum strength corresponds to the ideal case in which the sample is in the center of the sample holder. All the images were taken in a field of view of 5 µm.

Table # 2.1. Sample holders (SH) used in the XPEEM experiment.

	Calibration Constant (Oe/mA)	**Maximum Field At remanence (Oe)**	**Maximum Applied Field (Oe)**
SH I	0.45	405	135
SH II	0.4	360	120

The field of view (the effective measured surface) corresponds to an area of 5 µm of diameter, as shown in Figure # 2.21.

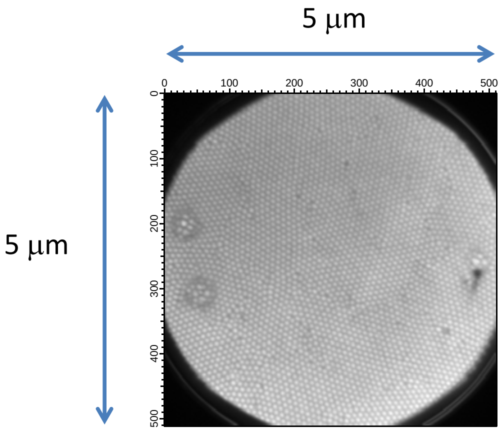

Figure # 2.21. Field of view of 5 μm of the XPEEM system.

The microscope images are obtained from emitted electrons or photoelectrons caused by the incident X-ray photons, but only if the energy of the photons is larger than the work function of the sample [134,135]. Elemental contrast is achieved by tuning the incident x-ray wavelength through absorption edges of elements. X-ray absorption and the resulting photoelectrons emission intensity is strongly enhanced at absorption edges. Areas on the surface containing the corresponding element emit more photoelectrons and thus appear bright in the PEEM image at a given absorption edge x-ray energy. The fine structure in the energy dependence of the x-ray absorption can be characteristic of the chemical bonding state of surface atoms. The differences in these images can be used to detect local bonding characteristics at the surface. Each element is described by two main structures namely the L_3 (lower energy) and L_2 absorption edges. As an example, the X ray Absorption Spectroscopy (XAS) for the ferromagnetic elements Co, Ni and Fe is presented in Figure # 2.22 and compared with a respective oxide form. If the sample has been oxidized, its energy scan will coincides with the oxide spectra of the metals in the figure.

To obtain magnetic imaging, two XPEEM intensity images are taken, left and right circularly polarized X-rays, from which their difference in intensity divided by their sum results in the XMCD contrast. The intensity in the XMCD image is proportional to the projection of the magnetization to the incident X-Rays wave vector, labeled as magnetization sensitivity direction (MSD). To identify its local orientation, magnetization with parallel or antiparallel direction to the polarization appears in the figures below as red or blue in the XMCD image (color on line), while magnetization perpendicular to MSD appears as white. The normalization of each image with different polarization was made dividing by an image of the same area in a saturating magnetic field. An example of a XPEEM image and the MSD scale are presented in Figure # 2.23.

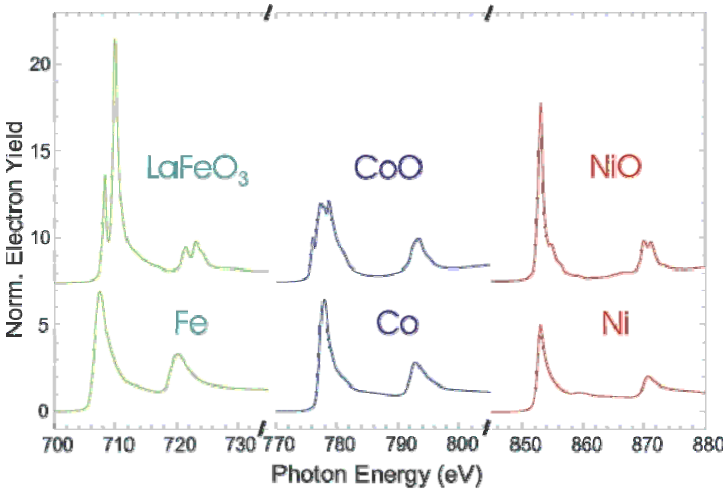

Figure # 2.22. L-edge X-Ray absorption spectra of Fe, Co and Ni, in the form of the elemental metals and as oxides [136].

XMCD and PEEM can be used to simultaneously measure (without alteration of the material) the absolute magnetic moments with elemental and chemical specificity, submonolayer surface sensitivity, and the ability to probe several nanometers of material.

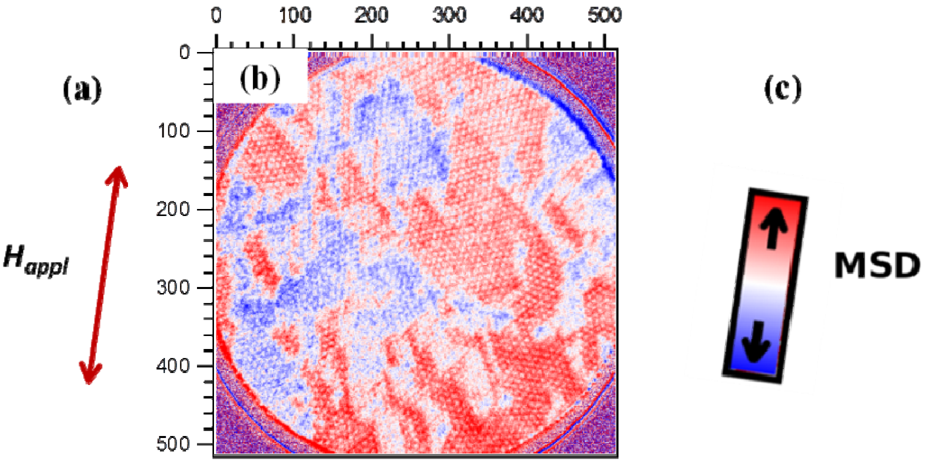

Figure # 2.23. (a) Direction of the field, (b) XMCD image of sample A, and (c) color contrast for the magnetization sensitivity direction, MSD

2.5 SUMMARY

A brief description of the systems used in this work was given. A variety of experimental techniques were used in order to find the optimal geometric and morphological properties of the AAM, and for the best magnetic characterization of the antidot arrays. An emphasis on the magnetic techniques was made.

3. CHAPTER 3

ANTIDOT ARRAYS GROWN ON ANODIC ALUMINA MEMBRANES

In this chapter the preparation and characterization of the *continuous thin film* (*CTF*), antidot arrays of *Permalloy* (*Py*) and *Cobalt* (*Co*) over *Anodic Alumina Membranes* (*AAM*) is presented. Many works show that the growth-induced or intrinsic anisotropies present in the unpatterned CTF are still present in the patterned arrays [18,29,57], so the intrinsic properties of the Py are studied. In order to unveil the role played exclusively by the geometry of the *AAM*, a soft magnetic material such as *Permalloy* (*Py:* $Ni_{80}Fe_{20}$) was used in this study. In Py, the excellent soft magnetic behavior is a consequence of a negligible magnetocrystalline anisotropy (K_1 = 0.03x10^5 erg/cm^3) [137], and in the particular proportion of 80:20 an absent magnetoelastic anisotropy. For this reason, Py found its way in a wide number of technological applications, including motor cores and magnetic recording materials [37,57] as well as in applications where variable stresses in thin films would otherwise cause a ruinously large variation in the magnetic properties. In addition, some antidot arrays of Co were prepared in order to study different magnetic effects in multilayer arrays.

The magnetic behavior according to the morphology and crystallographic structure (properties controlled through different sputtering parameters) were investigated in order to evaluate the quality of the Py films.

The work is divided in the following sections: i) AAM templates: fabrication and characterization; ii) Continuous thin film: preparation and characterization - Py and Co; iii) antidots arrays of Py over AAM: preparation and characterization.

3.1 ANODIC ALUMINA MEMBRANES

3.1.1 Fabrication

3.1.1.1 Anodization

A standard two step anodization process was used to obtain the *anodic alumina membranes* (AAM). Since the optimization of the anodization process is out of the scope of this thesis, further details regarding the pre-treatments requires, the anodization conditions, and their influence on the final properties of the AAM can be found in the following references [87].

In this study we focused on using a lower temperature for anodization in oxalic acid electrolyte (i.e. lower than the standard anodization temperature ~4-6 ºC), aiming a smaller *AAM pore diameter* (d_P), while retaining the same lattice parameter. Fabrication parameters for the AAM used in this study are detailed in Table # 3.1

When required, wet-etching treatment in 5% W phosphoric acid were made at 30 and 35 °C in order to enhance the d_P; in Table # 3.2 are summarized the final d_P in function of wet-etching treatment.

Furthermore, and in the particular case of our process, the Al disk used for the anodization showed a diameter of 8 mm, and the anodized area was 5 mm in diameter. For many measurements these dimensions are small enough to ensure the characterization of an uncut sample.

Table # 3.1. Conditions and parameters to obtain AAM.

Parameters	**Oxalic Acid**	**Sulfuric Acid**
Potential (V)	40	25
Concentration (M)	0.3	0.3
d_P (nm)	22	25
D	105	65
Temperature (°C)	0	0
1^{er} anodization time (hours)	24 to 48	16 to 24
2nd anodization time (hours)	3 to 10	3 to 6

Table # 3.2. Final d_P depending on the employed etching time; two distinct temperatures were considered.

Temperature (°)	**Initial d_P (nm)**	**Time (min)**	**Final d_P (nm)**
30	35	10	42
		15	48
		20	54
35	35	7	48
		3.5	40
		14	65
		21	75

3.1.1.2 Surface Etching by Ion-Milling

Two distinct systems were used to perform a reduction of the AAM surface characteristic topography and are described in Chapter 2. The experimental conditions for the first (IBD) and the second (RIB) systems are presented in Table # 3.3 and Table # 3.4, respectively.

Table # 3.3. Conditions for the IBD system Ion Milling polish of the AAM templates [55].

Conditions	Values
Argon flow (sccm)	6
V_B (V)	1000
I_B (mA)	29
V_{Ac} (V)	150
I_{Ac} (mA)	0.9
Angle	10º
I_D (A)	2.00
Rotation (rpm)	70
P_W (mTorr)	0.18 – 0.20

Table # 3.4. Conditions for the RIB system Ion Milling polish of the AAM templates.

Conditions	Values
Energy (eV)	500
Ionic density (σm/cm^2)	360-366
Argon flow (ml/min)	8.5
Argon Pressure (mbar)	$5.2 \cdot 10^{-8}$
\ttach angle with the plane of the sampl	15°
Time (min)	60-90

3.1.2 Geometrical Characterization

Microscopically, the geometric properties (d_P and *center-to-center nanoholes distance*, D) of the AAM which depend on the employed anodization condition were characterized by SEM measurements, Figure # 3.1. Using an image processor [138], the diameter of the nanopores and the distance between them were obtained by means of the average of the measurements of all the diameters and the distances, respectively.

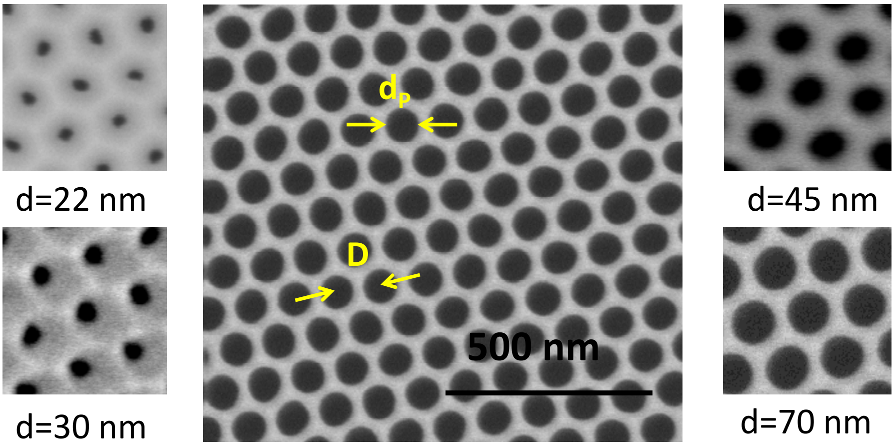

Figure # 3.1. (Center) SEM image of an antidot arrays with d_P = 70 nm and D = 105 nm; (left and right) hexagonal lattices with different d.

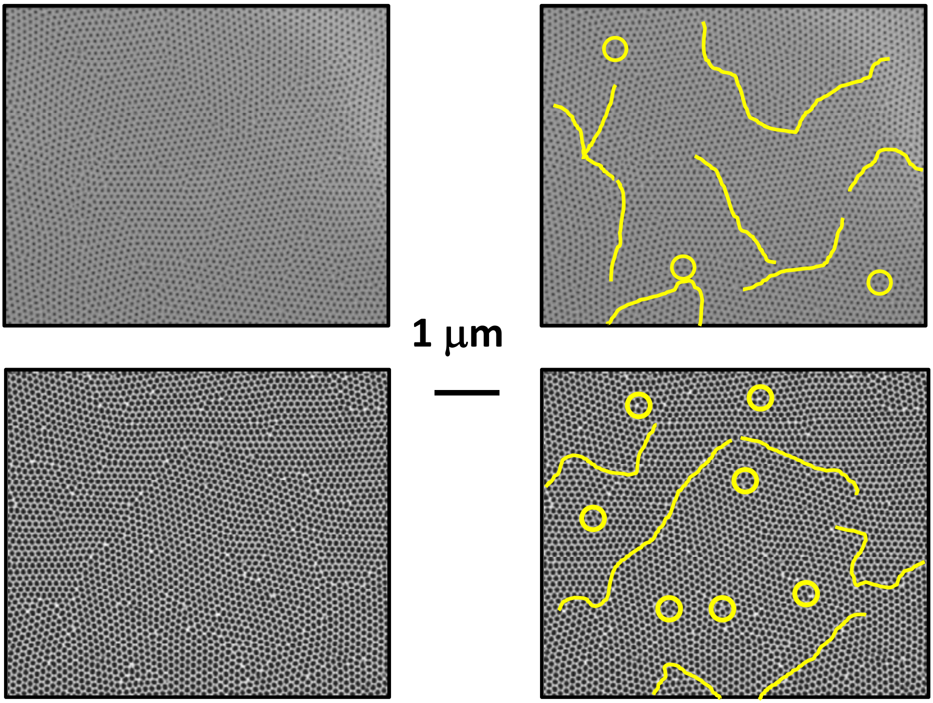

Figure # 3.2. SEM images of AAM templates with dislocations and defects; (a) d_P = 22 nm, (b) d_P = 75 nm.

Macroscopically, the AAM templates present a hexagonal order of circular holes, divided into geometric domains separated by dislocation-like boundaries. The templates have such long-range ordering restricted to domains of around 1-3 µm [42], each one with different lattice orientation. When comparing the lithographed antidot arrays with the ones obtained using AAM, the latter displays smaller holes sizes and lattice parameters. However, the main drawback relies on the presence of geometric domains, while lithographed arrays are monodomain. Figure # 3.2 shows SEM images of two examples of AAM with typical dislocations and defects.

3.1.3 Topographic Characterization - Roughness

The topography of the sputtered magnetic films over the AAM retains the templates characteristics, mimicking the roughness of its surface. The *Atomic Force Microscope* (AFM) study of the roughness of these templates, made before the etched surface, presents hill-like structures surrounding each pore. To better quantify the height of the hill-like structures, the roughness between the holes along the second-order distance was evaluated (see Figure # 3.3a). The drawing in Figure # 3.3b shows three different distances: the distance between adjacent holes (lattice parameter – D), the distance of second order between two holes (D’), and the edge-to-edge distance (D*).

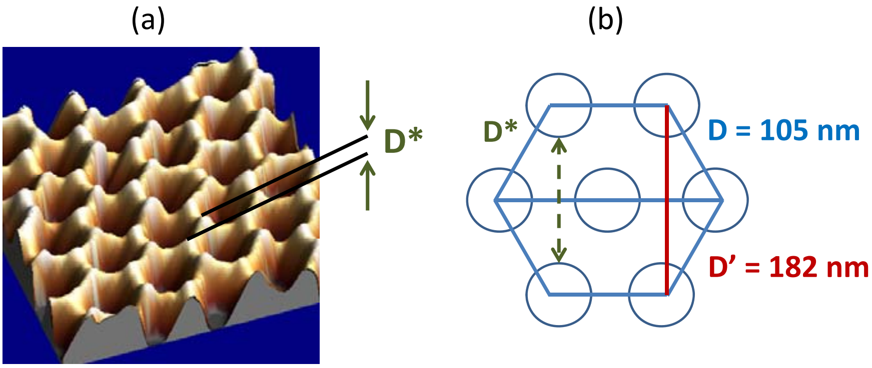

Figure # 3.3. (a) AFM image of an AAM with d_P = 60 nm and D = 105 nm; (b) drawing with three different distances of an AAM template.

The measurements were performed in AAM with different d_P, showing height hills (ΔZ) up to 40 nm. An example of an AFM profile is shown in Figure # 3.4; in this image the profile was made along D*, which gives height hills of approximately 18 nm.

From the profiles two different roughness categories can be distinguished:

1. related with the size of the pore diameter and

2. the hills that appear between pores.

Regarding the gentle hills, in the AAM without polished etched process, the hills are high enough to eliminate the property of the antidot arrays with continuous magnetic film (in this case the concept is different from the CTF; here the idea is an antidot array with the magnetic material in a continuous film – avoiding the creation of clusters of Py).

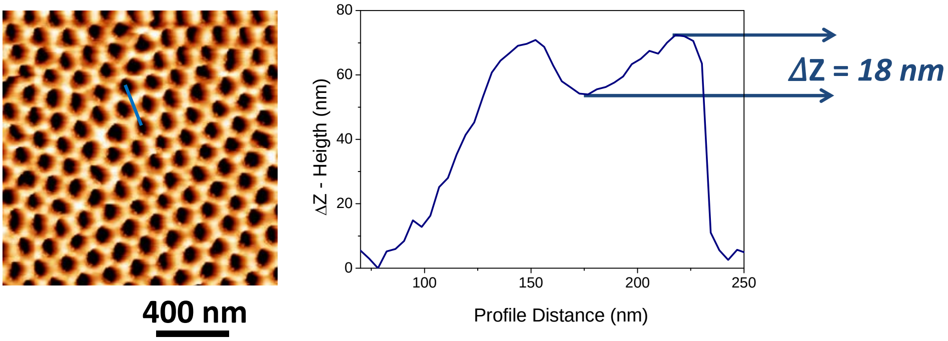

Figure # 3.4. AFM image of an AAM with d_P = 60 nm and D = 105 nm. The profile in the right corresponds to the line marked in the AFM image.

Although the templates were etched by low-angle ion-milling, some imperfections are still present, but the decrease in roughness is evident, as we can see in Figure # 3.5. From several images, the measured height of the hills, in the case of the membranes with 22 nm of diameter, goes from 0.9 to 4.8 nm [106], in the case of the membranes with d_P = 62 nm, the ΔZ goes from 2.1 to 16 nm. The following figure shows the profiles of the two different AAM after the ion-milling (d_P of 22 and 62 nm). The heights of the hills presented are 4.8 nm and 6.9 nm, respectively.

The hill height was evaluated measuring the profiles between the positions marked by the arrows (half of D*), Figure # 3.6. Thus the importance of these hills is negligible since this slight change in the height arises along more than 100 nm. More important is the main shape of the profile determined by the pore diameter of the membrane. The AFM profiles display a noticeable difference between both membranes. Albeit the interpore surface of the d_P = 22 nm membrane presents variations lower than 5 nm, the profile measured along the d_P = 62 nm membrane exhibits changes around 18 nm. In the latter case, the highest slopes of the profiles correspond to the regions close to the pore.

The vertical dashed lines in Figure # 3.6 correspond to the nominal inner walls of the pores for both AAM membranes. Indeed the measured slope is always lower than the real one due to the presence of - tip-sample convolution in the AFM image. This is particularly important in this kind of samples since due to its pyramidal shape the tip cannot go deep into the pore. The profile corresponding to d_P = 62 nm membrane shown in Figure # 3.6 is in agreement with this assertion since the surface should drop vertically after the limit of the pore wall.

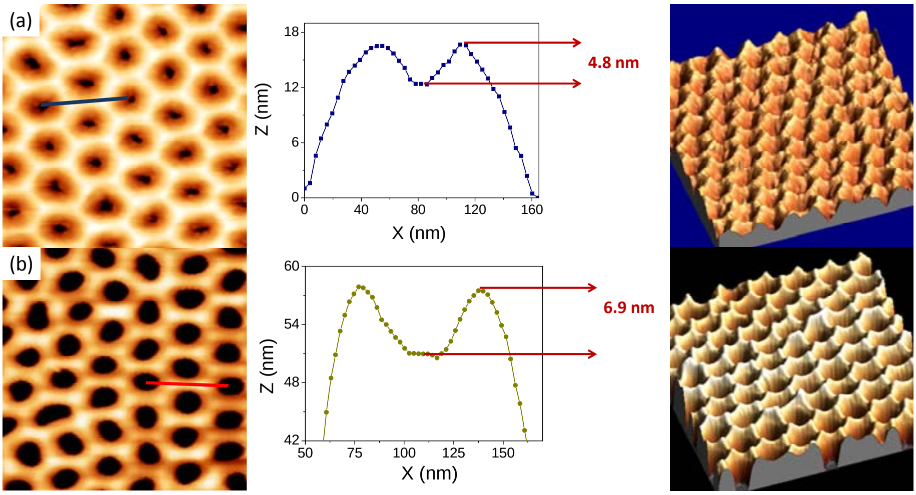

Figure # 3.5. AFM images with topography measurements of AAM with (a) d_P = 22 nm and (b) d_P = 62 nm.

As a result, taking into account the effective surface (between the nominal walls of the pores) the membranes after etched by ion-milling, show a low roughness. In the worse case, the height variation is less than 10 nm. Moreover, the thickness of the deposited Py layer decreases near the pore due to the step coverage of sputtering in a steep surface.

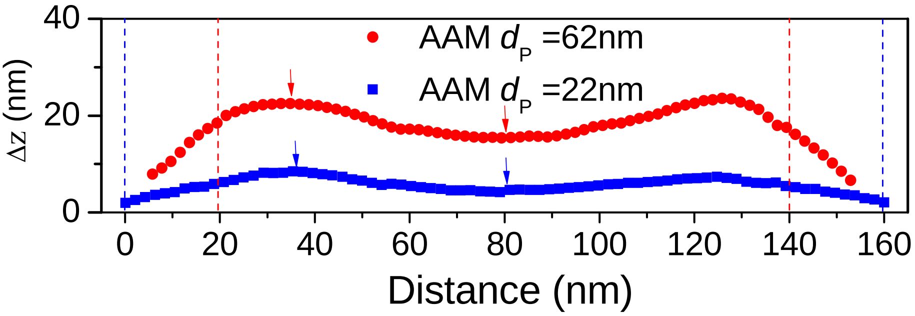

Figure # 3.6.Topography profiles of the two AAM membranes showed Figure # 3.5. Lines denote the nominal entering into the respective pores. The arrows indicate the position used to evaluate the height of the hills.

3.2 CONTINUOUS THIN FILM OF PERMALLOY

3.2.1 Preparation - Sputtering

The CTF prepared by sputtering, were grown with different conditions in order to study the morphological properties and choose the best parameters. The growth conditions are summarized in Table # 3.5. These conditions consist in the Ar or Work Pressure (P_w) and the *Radio Frequency* (RF) Power of the Sputtering system, which is constant in all the cases.

Table # 3.5. Sputtering conditions for Py composition.

Conditions	**Py**			
Power Pressure P_w (mbar)	$1.2 \cdot 10^{-3}$	$6 \cdot 10^{-3}$	$1 \cdot 10^{-2}$	$2.5 \cdot 10^{-2}$
RF Power (W)	60	60	60	60

During the following sections, the systematically characterization of the structure, chemical composition and crystallographic properties was performed with different techniques explained in Chapter 2. The *thickness of the Permalloy film* (t_{Py}) was furthermore measured with the aim to control the growth rate.

3.2.2 Structural and Chemical Characterization

The characterization of the Py was made in CTF over natural oxide Si (SiO). The in-plane (IP) crystal structure was obtained by *X-Ray Diffraction* (XRD), Figure # 3.7. These measurements were made in Py grown with different conditions, described in Table # 3.5. In all cases the mean peak was approximately at the same 2θ. This peak correspond to the grain direction along the [111] *fcc* crystalline phase of the $Ni_{81}Fe_{19}$, showing a polycrystalline behavior [139,140].

The *Energy Dispersive X-Ray Spectroscopy* (EDS) measurements indicate that the surface of the Py has oxidized, with a percentage of oxygen up to a 17%. The measurement was made at low energy to avoid deeper penetration of the X-Rays, preventing measuring the natural oxide of the substrate.

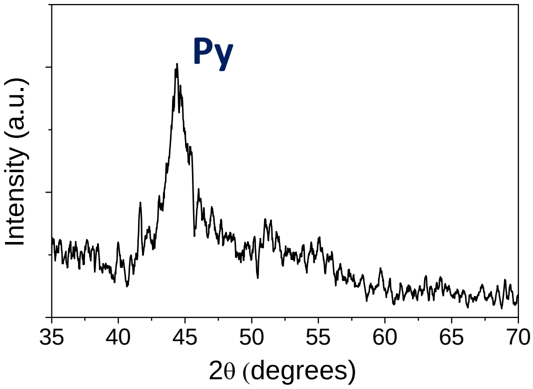

Figure # 3.7. XRD spectra of a CTF of 20 nm of thickness.

3.2.3 Thickness

The thicknesses, evaluated by *X-Ray Reflectometry* (XRR), were measured with different P_w and during different time. The rate and conditions of the Py sputtering are mentioned in Table # 3.6.

Table # 3.6. Py thicknesses in CTF with different sputtering time.

	Py	
P_W (mbar)	**time (sec)**	**t_{Py} (nm)**
$2.5 \cdot 10^{-2}$	180	22.4
	720	75.4
	927	100.8
	1140	119.3
$1.2 \cdot 10^{-3}$	59	5.6
	102	11.8
	205	18.6
	410	38.4
	480	43.1
	720	66.1
	1440	138

The thicknesses of the CTF were performed not only to control the growth rate, but in order to have an approximated value of the thickness in the antidot arrays. Due to the nanoholes pattern, the XRR technique does not have optimal results.

3.2.4 Grain Size

A study of the *in-plane* (IP-GS) and *out-of-plane grain size* (OOP-GS) of CTF with different P_w was made in order to estimate the best sputtering conditions. From a technological point of view, in order to achieve a high areal density in recording media, grains with diameters of about 3 nm are required [13]. It is important to make a complete characterization of the films; moreover it is crucial to find the best growth conditions for future applications.

All the films were deposited during 205 seconds, and the corresponding IP-GS and OOP-GS were measured by AFM and XRD, respectively. The values of OOP-GS with different P_w are presented in Table # 3.6, and the IP-GS and OOP-GS of the films with two different P_w are represented in Table # 3.7.

In the case of the films with different P_w, excepting P_1, the OOP-GS clearly decreases with increasing P_w. P_1 and P_4 have similar crystal sizes in the OOP component.

.

Table # 3.7.OOP-GS of Py in function of work pressure P_w.

Name	**P_W (mbar)**	**t_{Py} (nm)**	**OOP-GS (nm)**
P_1	$2.5 \cdot 10^{-2}$	24.6	3.1
P_2	$1.0 \cdot 10^{-2}$	24.7	6.5
P_3	$6.3 \cdot 10^{-3}$	25.2	5.9
P_4	$1.2 \cdot 10^{-3}$	20.0	3.6

The values of the OOP-GS in samples P_1 and P_4 are similar, so further characterization was made, the IP-GS. Table # 3.8 shows the resulting IP-GS of P_1 and P_4 with different thicknesses.

Table # 3.8. Distribution of GS of Py CTF with P_1 and P_4 with different thicknesses.

	P_W (mbar)	**t_{Py} (nm)**	**OOP-GS (nm)**	**IP-GS (nm)**
P_1	$2.5 \cdot 10^{-2}$	25	1	11
		75	1.1	13
		119	6.9	18
P_4	$1.2 \cdot 10^{-3}$	18	1.8	4.5
		35	7.2	3.2
		91	9.9	4.8

In the case of P_1, a cylindrical shape is deduced by the small grain size in the OOP component together with much bigger sizes along the plane of the film. In sample P_4, the deduced shape is ellipsoidal, with a more important growth along the OOP component; the IP size is almost constant, having almost no texture.

The latter characteristic is more desirable in the antidot arrays in order to avoid a fast closure of the nanoholes (along the plane of the films), so this growth condition ($P_w = 1.2 \cdot 10^{-3}$ mbar) is the optimal one.

As an example, Figure # 3.8 shows two AFM images with the surface roughness.

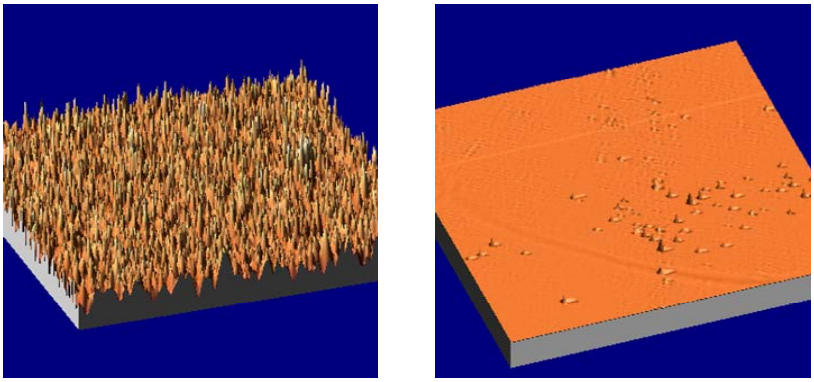

Figure # 3.8. AFM images of two CTF of Py with t_{Py} = 66 nm and P_w of (a) P_1 and (b) P_2.

3.3 ANTIDOT ARRAYS OF PY OVER ANODIC ALUMINA MEMBRANES

3.3.1 Preparation - Sputtering

The grain sizes and the roughness are important parameters for the selection of the optimal sputtering conditions for the preparation of the antidot arrays. The CTF showing the smallest GS and the lowest roughness are the ones grown with $P_w = 1{,}2 \cdot 10^{-3}$ mbar. The selected sputtering parameters for the preparation of the antidot arrays of Py are presented in Table # 3.9.

Table # 3.9. Sputtering conditions for the growth of Py antidot arrays.

Parameters	t_{Py} (nm)
P_w (W)	60
Pressure (mbar)	$1.2 \cdot 10^{-3}$
Rate (nm/sec)	0.09

The samples prepared for this work, are listed in the following table. And the following Sections consist in the characterization of the Py antidot arrays.

Table # 3.10. Samples of antidot films of Py

t_{Py} (nm)	Name	D (nm)
10	PyM59	105
	PyM68	105
	PyM69	105
	PyM63	105
	PyM32	105
	PyM33	105
18	Py2C	105
	Py3E	105
	Py4E	105
	Py5	105
	Py13A	65
	Py14A	65
	Py15A	65
20	PyM22	105
	PyM23	105
	PyM24	105
	PyM74	105
	PyM25	105
	PyM70	105
34	Py17A	105
	Py19A	105
	Py18A	105
	Py20A	105
	Py13B	65
	Py14B	65
	Py15B	65
43	PyM67	105
	PyM48	105
	PyM44	105
	PyM45	105
	PyM46	105
138	Py17B	105
	Py19B	105
	Py18B	105
	Py20B	105
	Py13D	65
	Py14D	65
	Py15D	65

3.3.2 Geometric and Topographic characterization - Roughness

The understanding of the morphological properties is crucial for the magnetic interpretation of the results. A special care must be taken when dealing with antidot arrays over AAM, because the growth process of the templates carries out inherent characteristics, namely roughness and defects.

The roughness of the AAM templates were measured before the growth of the Py, Section 3.1.3; but a deeper study was completed by the measurement of the roughness on antidot arrays. The selected arrays have d_P of 63 nm, because the templates show higher roughness (Section 3.1.3); and thicknesses of 5, 10, 20 and 34 nm. The profiles demonstrated that the height hills go from 0.8 to 4.1 nm in all the samples. The sputtered material on the top of the templates apparently softened the surface of the films, decreasing the roughness of the arrays.

Figure # 3.9, shows a selected sample with hills going from 1.2 to 4.1 nm of height, showing no significant change in the roughness.

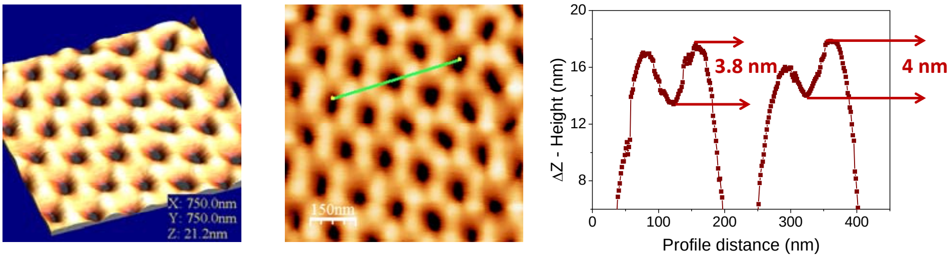

Figure # 3.9. AFM of an antidot array of $d_P = 63$ nm, $d = 61$ nm, $D = 105$ nm and $t_{Py} = 5$ nm.

3.3.3 Grain Size

The OOP-GSs of selected antidot arrays were measured by XRD. The obtained values are listed in Table # 3.11, while Figure # 3.10 shows a XRD graph of an antidot array. The OOP-GS show small differences between the different thicknesses, although there is a visible decrease in the arrays versus the CTF.

The IP-GS were not obtained because the pattern of the nanoholes produces discrepancies in the values of the grain diameters, when using the calculus of the "autocorrelation" [106]. Nevertheless, the small values of OOP-GS obtained in the antidot arrays are good enough for future technological applications.

Table # 3.11. OOP-GS of some antidot arrays of Py.

P_W (mbar)	t_{Py} (nm)	d_P (nm)	OOP-GS (nm)
$1.2 \cdot 10^{-3}$	18	54	1.5
	34	48	3.5
	138	35	5

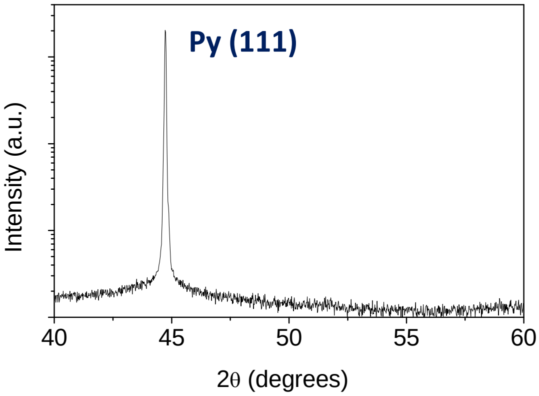

Figure # 3.10. XRD of an antidot arrays of Py with d_P = 48 nm, D = 105 nm and t_{Py} = 34 nm.

3.3.4 Morphological characterization

Another fundamental parameter involved in the magnetic properties of the antidot arrays, is the magnetic material co-deposited material around the entrance of the nanopores. Several studies [39,75,141] have shown that the sputter system deposits material inside the walls of the pores, which besides reduces the pore diameter. The thickness and depths of the films grown on the pore walls depend on both the film thickness and the pore diameter.

The step coverage of the sputtering was found to be of approximately 1 [55,141,142]; being 30 nm (the thickness inside the pore's walls) for the corresponding thickness of 30 nm (thickness of the antidot film). Figure # 3.11a shows a cross-section of a SEM image, demonstrating the tubular structure observed in the antidot arrays. Figure # 3.11b and c; show two outstretched drawing with the ratios between the diameters of the AAM and the arrays; and between the thickness and the material inside the wall of the pores, respectively.

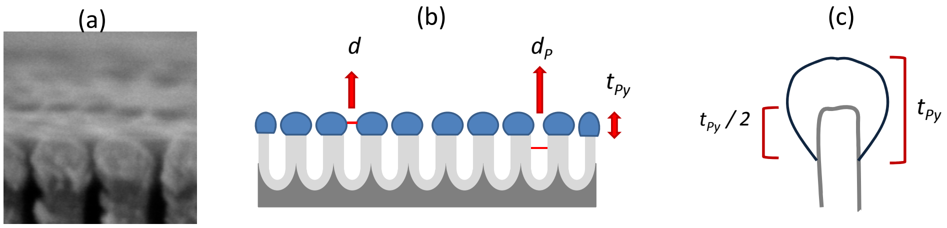

Figure # 3.11. SEM image of a cross-section of an antidot array of d_P = 42 nm, d = 26 nm and t_{Py} = 60 nm.

In Figure # 3.12, two SEM images are shown, where is possible to observe the sputtered material by the light and colors contrasts; the bright color (white) corresponds to the Py composition. Even when only a small amount of material is expected to reach the bottom of the pores [139], some of the SEM images show Py deposited in the periphery of the upper part of the walls, but not deeper inside them, neither at the bottom of the membrane. This is deduced by the absence of Py deeper inside of the pores' walls.

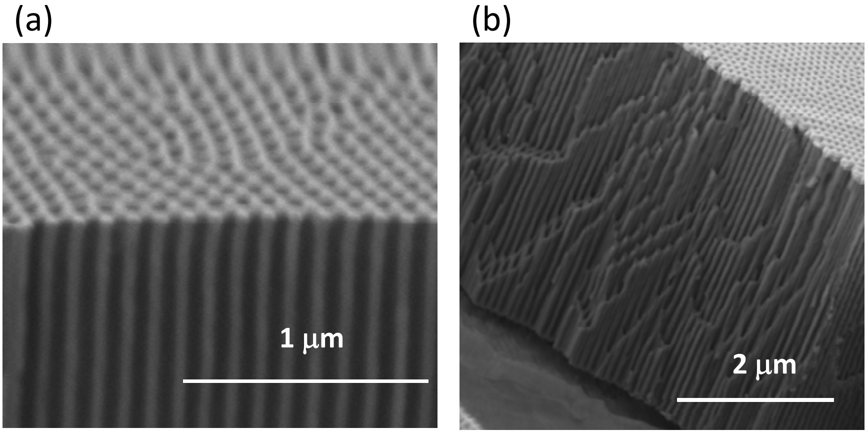

Figure # 3.12. SEM images of cross-section of an antidot arrays with d_P = 54 nm and (a) t_{Py} = 18 nm, and (b) t_{Py} = 138 nm.

As the film thickness increases, the nanoholes reduce their apparent diameter due to the co-deposition of material on the upper part of the pore wall [39,72,139]. Using top-view SEM image one can infer the *hole diameters of the antidot films* (d). Interestingly, an almost linear dependence between the d and the thickness of the deposited film has been found, decreasing d as the thickness increases (Figure # 3.13).

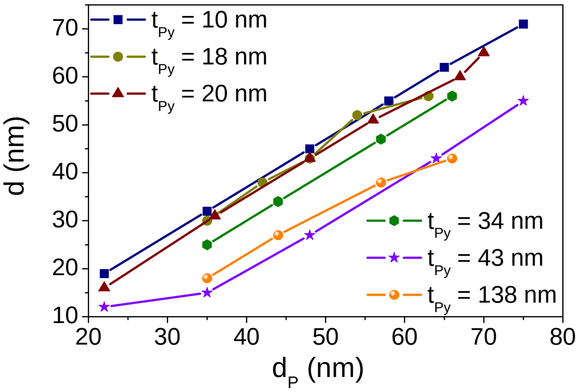

Figure # 3.13. Relation of the initial pore diameter (d) with the diameter of the holes of the arrays (d_P), with t_{Py}.

3.3.5 Penetration depth of the MOKE laser

The penetration depth of the light depends on the porosity of the films. The measured values of the optical constants of k and n, are presented in Table # 3.12 for λ = 632.8 nm (red light of the MOKE system). Figure # 3.14 shows a schematic drawing of the penetration depth of the laser.

Table # 3.12. Penetration depth of the red light of the MOKE laser over Py over Si and antidot arrays.

Name	t_{Py} (nm)	d_P (nm)	d (nm)	n	k	δ (nm)
CTF	20	-	-	2.12	3.43	14.7
Py17A	34	35	25	1.40	3.72	13.5
Py20A	34	66	56	2.11	2.28	22.1

The assumption of a linear behavior of δ with d, allows calculating the penetration depth of antidot arrays with different d. As for example, the corresponding δ in the sample with d of 54 nm would be approximately 19 nm. The calculated expression is:

$$\delta = 0.21 \cdot d + 10.2$$

Eq. (3.1)

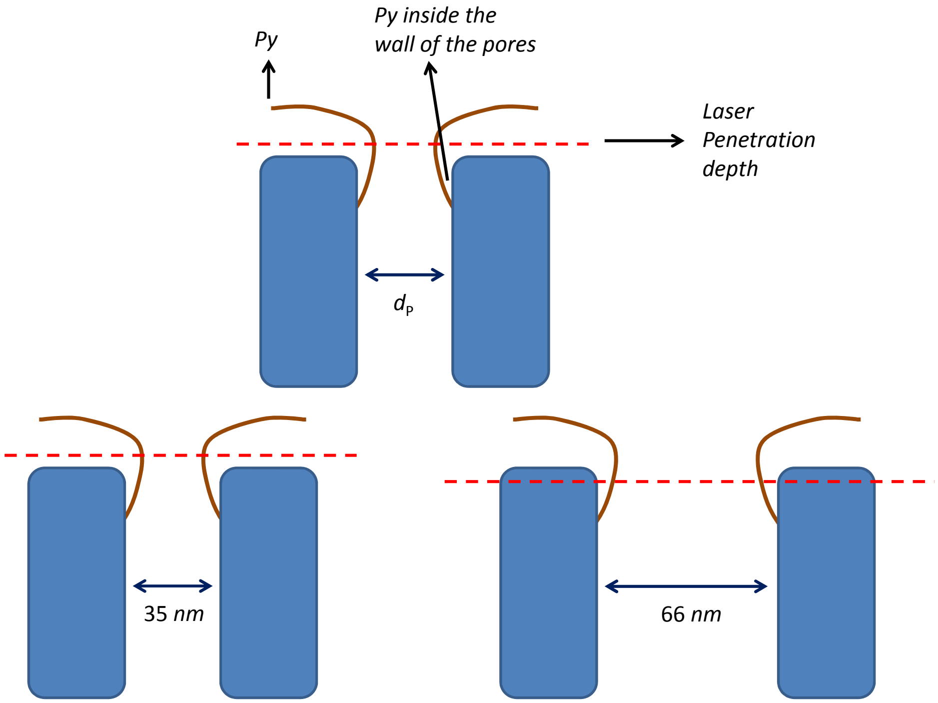

Figure # 3.14. Schematic drawing of the cross section of the antidot arrays with the corresponding penetration depth of the MOKE's laser.

3.4 CONTINUOUS THIN FILM OF COBALT

3.4.1 Preparation - Sputtering

A series of Co samples with different thicknesses were prepared with the sputtering system, some of the samples have an additional 2 nm of Al on the top of the films in order to avoid oxidation. Like the Py, the Co was grown over the natural oxide Si, SiO, without any heat treatment to manipulate the crystalline structure [135]. The sputtering conditions used for studied compounds are summarized in Table # 3.13.

Table # 3.13. Sputtering condition for Co composition.

Conditions	**Co**		
Power Pressure P_w (mbar)	$1.2 \cdot 10^{-3}$	$7{,}4 \cdot 10^{-3}$	$2.5 \cdot 10^{-2}$
RF Power (W)	60	60	60

3.4.2 Structural and Chemical Characterization

In the case of Co thin films, the XRD were made first by tetha-2tetha measurements, but the small thicknesses of the CTF cause a saturated signal, coming mainly from the Si substrate. Thus grazing incidence was made and thicker films were grown in order to see a better signal from the Co film. The background noise is very high, but still more counts from the Co film were obtained. These measurements were made with different conditions, and in all of them the mean peaks were approximately at the same 2θ.

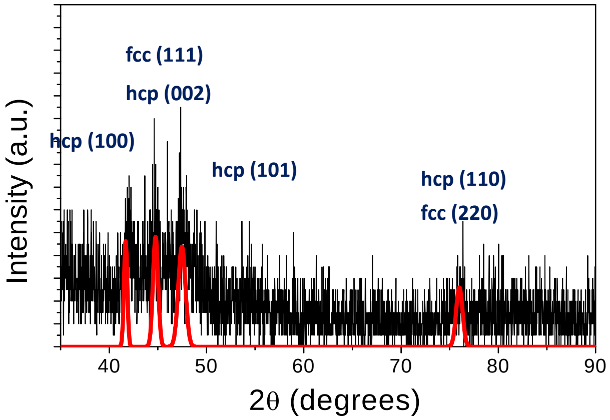

Figure # 3.15. XRD spectra of a CTF of 53 nm of thickness.

The XRD pattern of the CTF, exhibits three peaks around 44.7º, these peaks correspond to the *hcp* phase and the central peak to the *fcc* phase; so the overlapping of the central peaks may be interpreted as an overlapping of nano-crystalline peaks [135]. The *fcc* structure in bulk systems is stable only at temperatures above 425º [139] and has bigger grain sizes, thus the most appropriate interpretation could be a polycrystalline structure in the *hcp* phase.

3.4.3 Thickness

The thicknesses, evaluated by XRR, were measured with different P_w and during different time. The rate and conditions of the Py and Co are described in Table # 3.6.

Table # 3.14. Co thicknesses with different time.

	Co	
P_W (mbar)	*time (sec)*	*t_{Co} (nm)*
$2.5 \cdot 10^{-2}$	205	19.7
	410	39.8
	615	62.6
$1.2 \cdot 10^{-3}$	205	20.6
	410	34.5
	615	53

3.4.4 Grain Size

In the case of the Co thin films, the OOP-GS were calculated using the average of the width of the first three peaks, which are the strongest peaks, corresponding to the hcp (100), hcp (002) and hcp (200), Table # 3.15. According to Ref. 143, the grain sizes can grow along the plane up to 17 nm for $P_w = 2{,}5 \cdot 10^{-2}$ m bar, and up to 14 nm to $P_w = 1{,}2 \cdot 10^{-3}$ mbar. According to Ref.135, the maximum GS of the hcp phase is around 20 nm, but with annealing temperature up to 550 ºC.

Table # 3.15. Distribution of GS of some CTF of Co with different thickness and two different P_w.

	P_W (mbar)	**t_{Co} (nm)**	**OOP-GS (nm)**	**IP-GS (nm) by Ref. 143**
P_1	$2{,}5 \cdot 10^{-2}$	39.8	17	17
P_2	$1{,}2 \cdot 10^{-3}$	53	6.6	14

In the CTF, we can deduce a spherical and cylindrical shape for P_1 and P_4, respectively. As in the case of the Py CTF, a small grain size is desirable, so the optimal conditions for the growth of Co thin films are:

Table # 3.16. Sputtering conditions for the growth of Co antidot arrays.

Parameters	**t_{Co} (nm)**
P_w (W)	60
Pressure (mbar)	$1.2 \cdot 10^{-3}$
Rate (nm/sec)	0.1

3.5 ANTIDOT ARRAYS OF COBALT OVER ANODIC ALUMINA MEMBRANES

3.5.1 Structural and Chemical Characterization

The same procedure was performed over the antidot arrays of Co, showing a significant decrease of the peaks number 1 and 3, and an unexpected increases of the peak number 4 can be observed in Figure # 3.16. The crystals sizes in the OOP configurations are of approximately 18 nm in all the arrays.

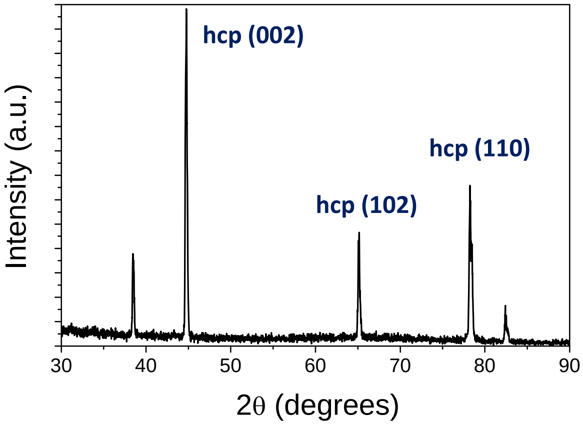

Figure # 3.16. XRD of an antidot arrays of Co with d_P = 35 nm, D = 105 nm and t_{Co} = 21 nm.

3.6 SUMMARY

We studied the growth conditions of the AAM, in order to find the optimal parameters to improve the geometrical and morphological properties of the membranes. The aim is to improve these features so we can avoid as much as possible any particular magnetic behavior due to the topography of the surface, or any other property.

Then, the geometrical and morphological characterization of the membranes and the antidot arrays was performed in this chapter.

4. CHAPTER 4

MAGNETIZATION - EXPERIMENTAL RESULTS

As discussed in Chapter 2, the magnetic characterizations performed using the VSM system provide information regarding the entire bulk nanohole array system. Therefore, the different contribution to the magnetic response arising from each geometric domain, their dependence on the coordinate sites, the influence of defects, or even the local effect of the holes on the alignment of the magnetization according to the local shape anisotropy axis, is averaged in a simple hysteresis curve. Additionally, more detailed in fraction can be gained by further insight into the local magnetic properties of the sample using Magneto Optical Kerr effect studies. Therefore, knowing the bulk behavior from VSM and the local behavior from MOKE hysteresis loops, we are able to infer the different magnetization reversal processes present at the surface and in the bottom of the antidot arrays thin films.

The work presented in this chapter is divided in the following sections: i) the magnetic considerations on continuous thin film and antidot arrays grown on top of AAM; ii) study of the magnetic properties of the antidot arrays with different geometric parameters, namely pore diameter of the AAM, diameter of the antidot, and lattice parameter; iii) study of the magnetization properties of the antidot arrays with different thicknesses; iv) study of the magnetic domain structures by X-Ray Photoemission by Electron Microscopy.

4.1 MAGNETISM ON Py CTF AND Py ANTIDOT ARRAYS OVER AAM

As explained in Chapter 1, the predominant contributions to the anisotropy in the continuous thin film (CTF) and the antidot arrays of Py come from:

1. The shape of the sample – macroscopic scale;
2. The induced field during films growth (≈ 6 Oe) – macroscopic scale;
3. The hexagonal ordering of the arrays and the dimensions of the nanoholes: pore diameter of the AAM (d_P), diameter of the antidot (d), and lattice parameter (D) – local scale (antidot arrays).

As explained in Chapter 1, the magnetic properties, such as DW width (δ_{DW}) and coercivity (H_c), of the arrays are conditioned by these anisotropies. Nevertheless another main factor that conditioned the magnetic response is the thickness (t_{Py}).

The understanding of the anisotropies is fundamental in this study, so each contribution was treated separately for the correct characterization of the CTF and the antidot arrays. Besides, a magnetic characterization of the CTF with thickness (different morphological properties) was performed.

As it is well known, Py is a very suitable material for this kind of studies due to its magnetization properties, shown in Table # 4.1 [52].

Table # 4.1. Magnetic properties of Py.

	A (erg/cm)	**M_s (emu/cm^3)**	**K (erg/cm^3)**	**l_{ex} (nm)**	**δ_{DW} (nm)**
fcc Py	$1.64 \cdot 10^{-6}$	880	$3 \cdot 10^3$	5.1	730

4.1.1 Continuous Thin Film

4.1.1.1 Demagnetizing factor – shape factor

The demagnetizing factor and the *demagnetizing field* (H_D) depend on the macroscopic shape and the density of the pores of the CTF, ultimately determining its magnetic behavior. The competition between the demagnetizing field and the growth-induced one, will lead to an effective anisotropy on the films.

To have a better understanding of the importance of this factor, thin films with both circular and rectangular shape were prepared by the sputtering system, over Si/SiO (natural oxide). In Figure # 4.1 two different shapes of CTF are represented. The expressions (in c.g.s.) used for the demagnetizing field and the shape factor were discussed in Chapter 1: Eq. (1.4) for the rectangular film, and Eq. (1.5) and Eq. (1.6) for circular shape (along *x* and out of plane, respectively). Then using the expressions of the demagnetizing field and the shape factor, the values of the CTF were calculated.

$$\text{Eq. (1.4):}\ H_D = -4\pi M_s \frac{t}{w}\ ;\ H_D = -4\pi M_s \frac{t}{h}$$

$$\text{Eq. (1.5):}\ N_x = \left(\frac{\pi}{4m}\right)\left(1 - \frac{4}{\pi m}\right)$$

$$\text{Eq. (1.6):}\ N_t = 1 - \frac{\pi}{2m} + \frac{2}{m^2}$$

The dimensions of circular and rectangular films are respectively: (a) diameter $x = 4$ mm and $m = 2{\cdot}10^5$ (m: ratio between the x and the thickness), (b) $w = 5$ mm and $h = 4$ mm; for both films the thickness is 20 nm.

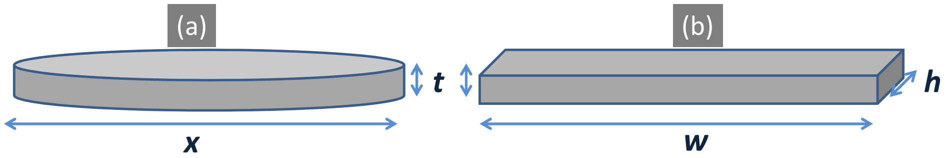

Figure # 4.1. CTF with (a) circular shape and (b) rectangular shape.

Table # 4.2. Demagnetizing factor and demagnetizing field of thin films with two different shapes.

	Applied magnetic field along:					
	x or *w*		*x* or *h*		*t*	
	N_D	H_D (Oe)	N_D	H_D (Oe)	N_D	H_D (Oe)
Oblate	$3.93 \cdot 10^{-6}$	0.055	$3.93 \cdot 10^{-6}$	0.055	≈ 4π	≈ 11 000
Rect.	$2.55 \cdot 10^{-6}$	0.044	$3.18 \cdot 10^{-6}$	0.055	≈ 4π	≈ 11 000

As can be seen in Table # 4.2, the demagnetizing field along the *out-of-plane* (OOP) axis (*t* side) in both shapes is very high, favoring the *in-plane* (IP) magnetization in both geometries. Besides, it is energetically favorable for the magnetization to lie along their longest direction since there are no surface poles to cause opposing fields.

In both cases, for the given orders of magnitude of the demagnetizing field along both sides *w* and *h*, the effective anisotropy is not influenced by the shape of the films, so any anisotropic behavior found on the CTF should be due to the magnetic field present during the sputtering process [144,145].

4.1.1.2 Induced Magnetic Field

A study of the magnetic properties at the surface of the CTF with different shapes, with different positions along the sample holder and different thicknesses (t_{Py} = 10, 20 and 40 nm), Figure # 4.2, was performed. The samples were prepared by the sputtering system, over Si/SiO (natural oxide). An angular dependence of H_c was performed in the NanoMOKE system. The 0 degrees, taken as the reference for the angular dependence, was the position parallel to the field direction of the arm of the sample holder.

The results of the angular dependences of the films with different thicknesses show a similar behavior: uniaxial anisotropy magnetization. As an example, Figure # 4.3 shows the angular dependence of three CTF (rectangular and diamond shapes) oriented in different direction with the sample holder. The samples present the maximum coercivity at approximately 0^{o}, thus as a conclusion, the two-fold behavior of the coercivity demonstrates that the induced field is more important than the shape anisotropy.

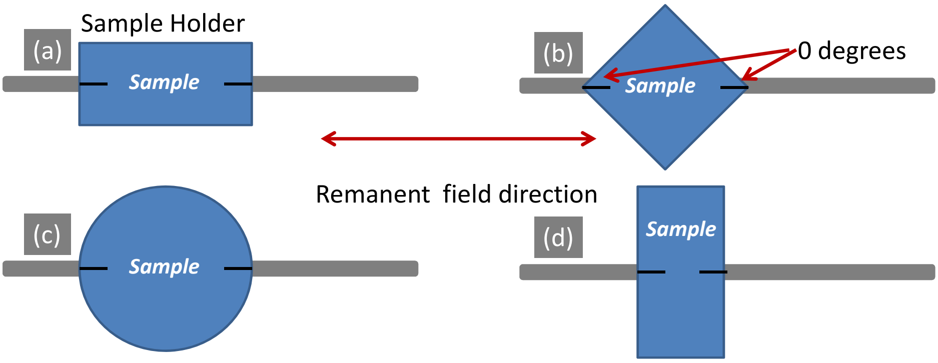

Figure # 4.2. CTF with different shapes and orientations relative to the sample holder of the sputtering system.

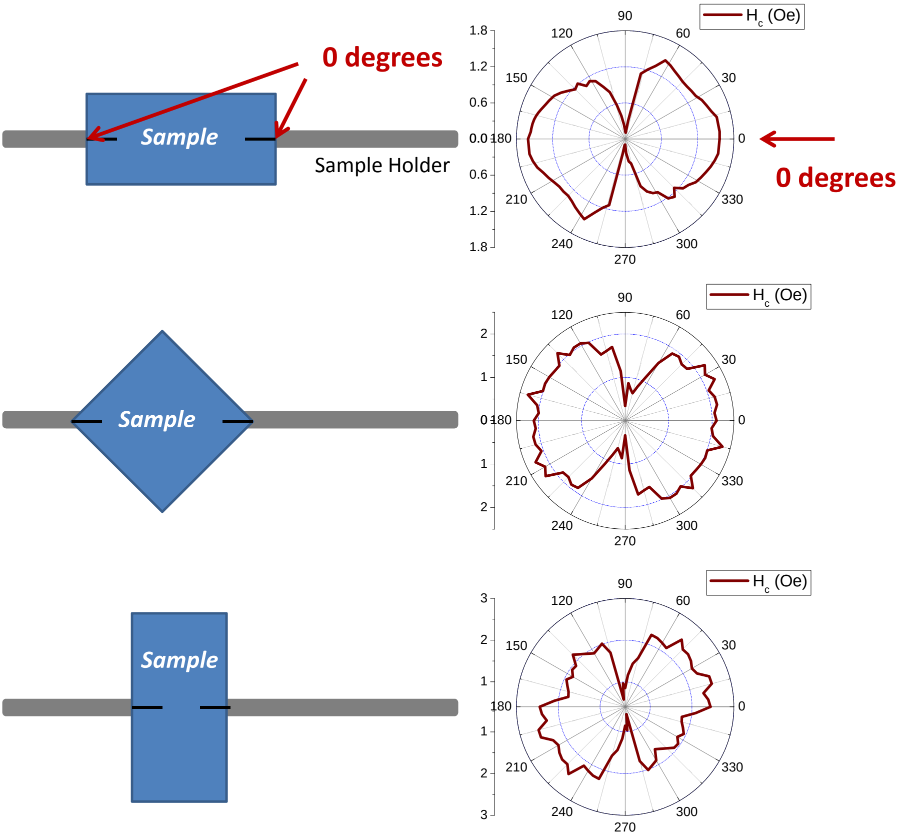

Figure # 4.3. Samples position relative to the sample holder and their corresponding angular dependence of H$_c$.

Some differences between the zero degrees and the maximum H_c are present in the measurements, and it is ascribed to some misalignments during placing the samples in the sputtering system.

A quick comparison between the IP demagnetizing field (Table # 4.2) and this induced field during deposition shows that the former is much smaller, and therefore the latter could be mainly responsible for the uniaxial anisotropy observed in the CTF.

4.1.1.3 Insights into the role of the Domain Wall

Using the expressions and the intrinsic constants described in Chapter 1, a bulk system of Py presents Bloch walls with the characteristic *DW width* (δ_{DW}) of approximately:

$$\delta_{Bl} = \pi\sqrt{\frac{A}{K}} = 730\,nm. \qquad \text{Eq. (4.1)}$$

However, the presence of the induced magnetic field during the sputtering, alter this δ_{DW}. From Eq. (4.2), the induced anisotropy constant due to the field with the intrinsic magnetic anisotropy constant (K_{ind}), can be obtained, thus the approximated δ_{DW} can be calculated.

$$H_k = \frac{2|K_1|}{M_S} \qquad \text{Eq. (4.2)}$$

$$H_{ind} = \frac{2K_{ind}}{M_S} \rightarrow K_{ind} = \frac{M_S\, H_{ind}}{2} \qquad \text{Eq. (4.3)}$$

$$\delta_{Bl} = \pi\sqrt{\frac{A}{K_u+K_{ind}}} \approx 530\,nm. \qquad \text{Eq. (4.4)}$$

In theory, the δ_{DW} of the Py CTF must be around 500 nm, but in Section 1.2 was explained that the walls widths depend strongly on the thickness of the films. In order to make a correct characterization of the Py CTF used in this work, M-H loops by VSM were obtained in films with different t_{Py}, and the experimental values of δ_{DW} were calculated using the effective anisotropy constant explained in Section 4.1.2.4. The experimental values of the DW have width around 20 nm, which are much smaller than the theoretical ones.

4.1.1.4 *Characterization of the magnetic properties with Grain Sizes*

A study of the anisotropy of CTF with different sputtering conditions (Table 3.8) was performed in order to observe the effect of the *grain size* (GS) over the magnetic properties. The magnetic behavior was measured by MOKE using an IP angular dependence. This IP angular dependence was obtained from 0° to 360°, every 15°, where the coercivity was measured in every angle, obtaining an angular distribution. As an example, Figure # 4.4 shows the M-H loops of two CTF prepared with different work pressure (P_w).

The *out-of-plane grain size* (*OOP-GS*) and the *in-plane grain size* (*IP-GS*) on CTF depends on the work pressure of the Argon (P_w) during the sputtering deposition. The measurements consist in the angular dependence of the H_c, changing the angle between the field and a random reference of the sample, always along the plane of the CTF. As a result, the sample shows a magnetic anisotropy, and a distribution of H_c.

The values of the distribution of H_c, depends on the used P_w. The lowest and the highest coercivity of the angular distribution are represented in Table # 4.3 (the GS were taken from Table # 3.8)

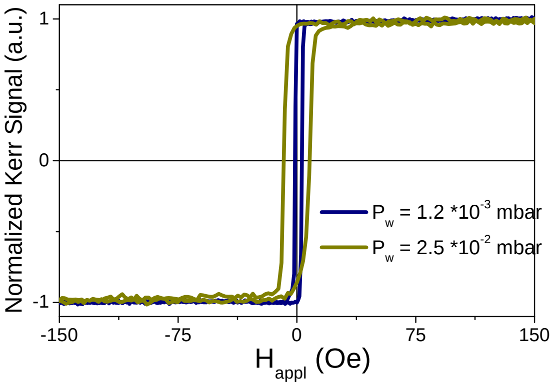

Figure # 4.4. IP MOKE loops of CTF with P_w of (blue) $1.2 \cdot 10^{-3}$ mbar and (green) $2.5 \cdot 10^{-2}$ mbar.

Table # 4.3. OOP-GS, t_{Py} and H_c distribution, in function to the work pressure P_w of CTF.

Name	P_W (mbar)	t_{Py} (nm)	OOP-GS (nm)	Max and Min H_c (Oe)
P_1	$2.5 \cdot 10^{-2}$	24.6	3.1	3.6-8.2
P_2	$1.0 \cdot 10^{-2}$	24.7	6.5	0.2-5.7
P_3	$6.3 \cdot 10^{-3}$	25.2	5.9	0.8-11.8
P_4	$1.2 \cdot 10^{-3}$	20.0	6.0	0.6-2.9

Although the GS and t_{Py} do not differ that much from each other, the distribution of coercivities does. The film P_3, presents the highest coercivity value with a broadest distribution. Sample P_1 and P_2 have also high values of coercivity, and the distribution is also broad, although in the case of P_1 the GS is the smallest. In the case of the P_4 film, the OOP-GS is relative big, but the distribution of H_c is much narrower. Figure # 4.5 shows the Kerr effect loop along the easy and hard axis of the film made with P_3 (largest H_c distribution).

According to Table # 3.9, the IP- and OOP-GS of the CTF shows a big difference between the P_1 and P_4 films, being much smaller in the latter case. The grain sizes of the films sputtered with the pressure conditions of P_4, which state a nano-crystalline material, denotes a negligible anisotropy.

Magnetically, P_4 shows the best conditions for deposition of the films over Si/SiO, hence the same conditions were used in the growth of the antidot arrays over AAM.

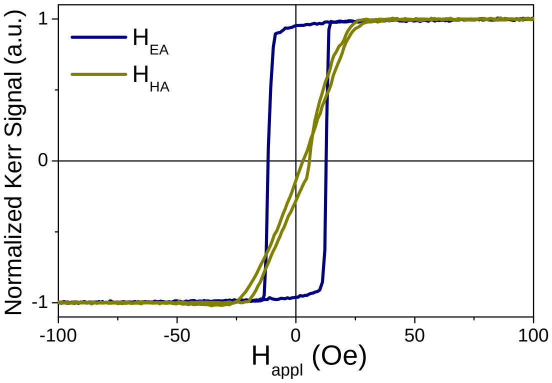

Figure # 4.5. IP MOKE loop for CTF made with P_3 along the (blue) easy axis and the (green) hard axis.

4.1.2 Antidots Arrays over AAM templates

4.1.2.1 Induced Magnetic Field

The applied field during the growth of the antidot arrays induces an uniaxial anisotropy in the CTF, but in the antidot arrays, the anisotropy has a competition between the induced one by the hexagonal lattice and the field during the growth. In Figure # 4.6, two angular dependence of H_c measured by VSM of two antidot arrays with different d_P are represented.

At the macroscopic scale, the applied field induces an uniaxial anisotropy in the arrays with the smaller d_P (= 22 nm). The change in the values of H_c does not exceed the 10 Oe, corresponding to the 50% of the maximum coercive field.

In the case of the antidot array with bigger d_P, the array does not show anisotropy induced by the applied field, presenting the expected isotropic behavior due to the geometric domains (treated in the next section). In this case, the change in magnitude between the higher and lower coercivity does not exceed 15 Oe, which is only approximately 5% of the maximum value; although the increases in H_c between d_P = 22 nm and 66 nm is huge. The applied field has not influence in the increases of H_c because the most important effect is due to the dimensions of the nanoholes. The physical explanation of the magnetic behavior with different dimensions of the nanoholes is explained in Sections 4.1.2.3 and 4.-1451752861.

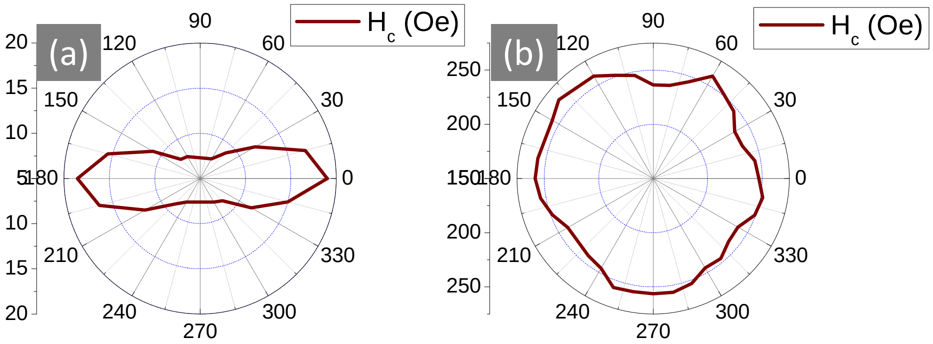

Figure # 4.6 Angular dependence of H_c of two antidot arrays with t_{Py} = 20 nm, D = 105 nm, and (a) d_P = 22 nm, (b) d_P = 66 nm.

4.1.2.2 Geometric Domains

The deposited magnetic film over the AAM replicates their underlying hexagonal pattern (Chapter 3), creating an antidot film with identical geometrical characteristics that the AAM. Nevertheless, this antidot film displays a magnetic response distinct from its CTF counterpart. The differences of the magnetic properties between continuous and antidot films can be explained by a change in the mechanism of the reversal magnetization.

Macroscopically, one geometric domain with hexagonal order has a defined orientation, but this orientation is different relative to each geometric domain; see Figure # 1.6 and Figure # 3.2. Magnetically each one has a different alignment of the local shape anisotropy (always IP of the sample), or the *magnetization easy axis* (*e.a.*), with respect to the applied magnetic field, having a well defined six-fold anisotropy (Section 1.3.4.3). This effect produced a multidomain behavior which averages the macroscopic anisotropy resulting in an isotropic-like magnetic behavior when measuring with the VSM system, as it was shown in other work [146].

Moreover, in addition to the nanoholes, dislocations like-boundaries and other imperfections (Figure # 3.2) may also act as domains nucleation sites or as pinning centers, anchoring the DW. However, these macroscopic defects have a weaker effect on the magnetic properties than the local presence of the nanoholes, as it will be demonstrated in the next section.

This particular feature of the antidots grown over AAM must be taken into account when interpreting the results, as for example of the MOKE measurements (where the surface magnetization plays a major role). In fact, regarding these particular measurements, three main points must be studied:

1. The spot diameter is not small enough to cover only one geometric domain, so multiple contributions to the magnetic signal must be taken into account. As an example, in Figure # 4.7, a laser spot with a diameter of approximately 3 μm is covering three different areas, where the measured surfaces include a different number of geometric domains. The black arrows indicate the e.a. direction of the lattice of the geometric domains. A hexagonal lattice is enlarged only for explanatory purposes. The applied magnetic field is aligned with the vertical axis.

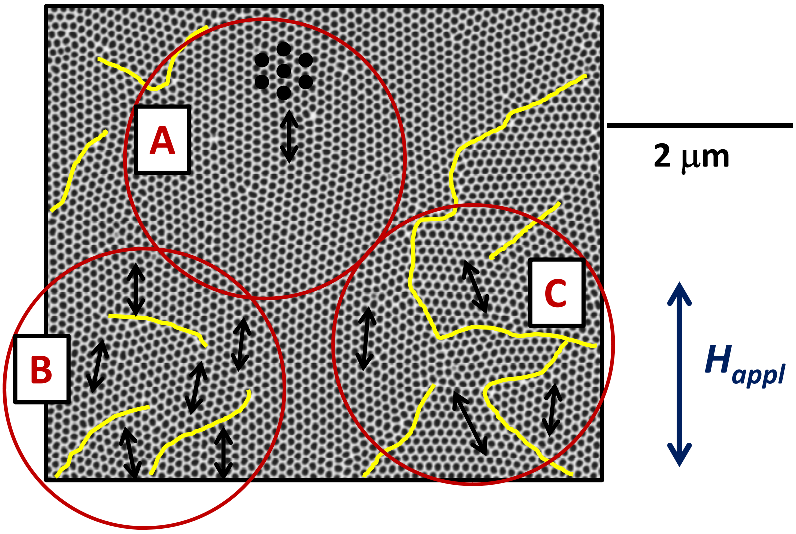

Figure # 4.7. Laser spot of 3 μm covering three different areas in an antidot array of d = 60 nm and D = 105 nm.

In the area A, the laser's spot covers almost a complete geometric domain. In here, the anisotropy should be similar to a six-fold behavior; on the contrary, the areas B and C have more than 3 geometric domains, therefore, the e.a. of each domain will contribute with a larger or smaller contribution to the measured anisotropy, displaying a different effective anisotropy from the expected six-fold.

As the laser spot increases, a larger number of geometric domains are covered, and therefore the averaged magnetic behavior will get closer to an isotropic-like behavior, where no effective anisotropy IP is observed, as in the case of the VSM loops.

2. The magnetic anisotropy of each domain is different depending on the exact position of the local e.a. of the hexagonal lattice relative to the direction of the field. When the measurements consists on the angular dependence of H_c by MOKE, and the laser spot is not focused on a fixed place over the sample, the magnetic contributions are originated from different geometric domains in every angle, so the measurements are not consistent with the anisotropy of a few (no more than 3 or 4 domains) geometric domains.

   In these particular measurements, the position of the laser relative to the geometric domains is crucial. As an example, the angular dependence of an antidot array with t_{Py} = 20 nm and d_P = 70 nm was measured. The position of the laser's spot along the surface of the array was intentionally changed in every angle, so the resulting dependence, shown in Figure # 4.8, consists in an average measurement of the H_c.

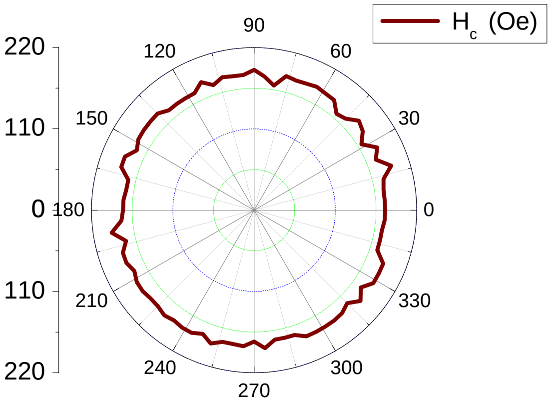

Figure # 4.8. H_c angular dependence of an antidot array with t_{Py} = 20 nm and d_P = 70 nm.

Therefore, the isotropic-like magnetic behavior is due to the magnetic signal from different domains in every angle. The magnetic anisotropy in arrays with the laser spot over the same position will be treated in the next section.

3. Different antidot arrays were measured by MOKE in different locations along the surface of every sample (always IP). The same last assumption was made; the magnetic signal depends on the geometric domains covered by the laser's spot, and depends on the local defects (such as dislocations or imperfections), which produce small local variations on the magnetic signal.

As an example, an array with t_{Py} = 20 nm, d = 44 nm and D = 105 nm is shown in Figure # 4.9. The MOKE loops show small local variations on the magnetic behavior and different local H_c, due to defects, dislocations, or by the alignment of the magnetization e.a. of each geometric domain. Imperfections and dislocations may affect the magnetic behavior of the measured area [147].

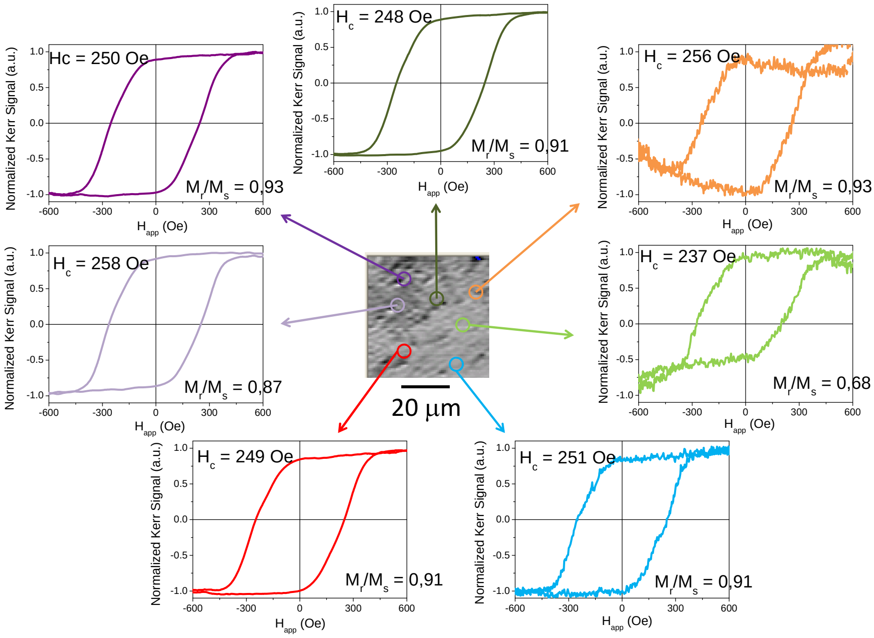

Figure # 4.9. MOKE loops in different places of an array with d_P = 35 nm and D = 105 nm.

4.1.2.3 *Hexagonal ordering of the arrays - geometry of nanoholes*

As mentioned in Chapter 1, the differences of the magnetic properties between continuous and antidot films can be explained by a change in the mechanism of the reversal magnetization, originated from localized stray field created by the nanoholes (see Figure # 4.10). Locally, the accumulated charges around the nanoholes produce stray fields inside the voids and dipolar interactions among the holes, each one with a different effect in the magnetic properties of the arrays. These magnetic considerations, which are listed below, depends on the dimension of the nanoholes:

1. *The stray fields* inside the voids [59,148,149,150] produce a local strong pinning of the DW. These fields are crucial in the DW pinning.
   In the Inclusion Theory [70] the study shows that an individual defect (or isolated defects, in which no interaction between them exists) produce a hardening effect due to the DW pinning, caused by the accumulated charges around the nanoholes, thus the coercivity increases.

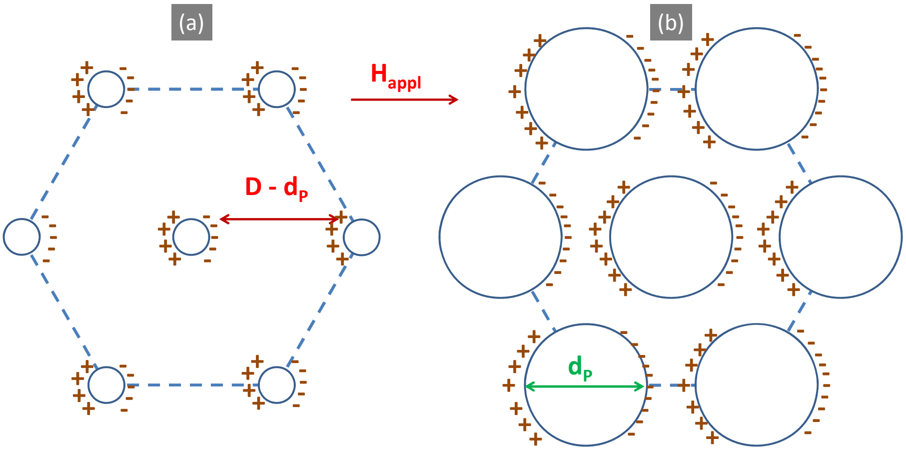

Figure # 4.10. Schematic drawing of two antidot arrays with accumulated charges around the nanoholes, (a) $d_P = 22$ nm, $D = 105$ nm; (b) $d_P = 75$ nm, $D = 105$ nm.

2. These accumulated charges around the nanoholes produce *dipolar fields* among the holes [29,75,78]. As d_P increases keeping D constant (or in a similar way increasing D keeping d_P constant), the distance between edge-to-edge of the holes decreases (less magnetic material among the holes): therefore, the spins are confined to smaller spaces and the accumulated charges are closer together, creating higher *dipolar interactions*. These dipolar interactions are the responsible of the reduced remanence [62,78,120,149,151]

As expected, the coercivity increases with the separation distance. The separation of the non-magnetic structures implies a decrease in the magnitude of the demagnetizing energy relative to the total energy. Figure # 4.10 represents the accumulated charges around the holes.

Using always the same hexagonal lattice, the geometric properties of the nanoholes were changed. Some relations between the different geometric parameters can be used, such as the relationship between d_P and D, named *Porosity* (*P*). P consists in the surface ratio of holes to continuous film. P depends on the diameter of the AAM template. In Table # 4.4, P values of the AAM obtained in this work are detailed.

$$P = \frac{\pi\, d^2}{2\sqrt{3}\, D^2} \rightarrow P\,(\%) = \frac{\pi\, d^2}{2\sqrt{3}\, D^2} \cdot 100 \qquad \text{Eq. (4.5)}$$

Table # 4.4. Porosity of AAM with different d_P.

d_P (nm)	D (nm)	P (%)
22	105	4
35	105	10.7
48	105	18.9
58	105	27.6
65	105	34.7
75	105	46.2
20	65	8.6
33	65	23.4
41	65	36.1

P increases as d increases; nevertheless, this parameter does not reflect the effect of increasing Py thickness of the antidot arrays. Accordingly, two alternative relationships were considered, the *antidot aspect ratio* (r), which also accounts for the non-perfect cylindrical shape of antidots: this ratio provides the relationship between the average d_P and d (see Chapter 3), with t_{Py}. r is higher for thinner films, and very small for thicker films. Furthermore, as second alternative ratio (r'), takes into account not only the effect of the average diameter of the pore and the antidot, but D as well; resulting in a ratio between the material among the nanoholes and the thickness.

$$r = \frac{d + d_P}{2\, t_{Py}} \quad \text{Eq. (4.6)}$$

$$r' = \frac{D - (\frac{d + d_P}{2})}{t_{Py}} \quad \text{Eq. (4.7)}$$

In Table # 4.5 are presented some of the antidot arrays used in this work with their corresponding ratios.

Table # 4.5. The aspect ratio of some of the antidots films with D = 105 and 65 nm and t_{Py} = 18 nm.

d_P (nm)	d (nm)	D (nm)	r	r'
35	30	105	1.8	4.0
42	38	105	2.2	3.6
48	43	105	2.5	3.3
56	52	105	2.9	2.9
63	56	105	3.3	2.5
20	15	65	0.9	2.6
33	29	65	1.7	1.9
41	36	65	2.1	1.5

In Table # 4.5, is possible to observe that as d_P and d increase, the ratio r increases, in a similar way that P, but the ratio r' decreases.

4.1.2.4 *Domain Walls and Experimental Effective anisotropy*

With the local anisotropy, an accurate calculation of the DW width can be made. However, a local model of the anisotropy is not possible to obtain, since it is not possible to calculate the local stray fields responsible for the anchoring of the DW. These contributions appear mostly along the sample's plane and are spatially variable according to the geometric parameters. Therefore a macroscopic model of the effective anisotropy was used to calculate the *effective anisotropy constant*, from the shape/magnetostatic/demagnetizing anisotropies due to the inclusion of nanoholes or voids into the CTF

In such way, it is possible to obtain an approximation of the anisotropy of the arrays using a simple and straightforward method, and thus easily infer on the magnetic properties of the material. Experimentally, the effective anisotropy constant is obtained from the IP and OOP loops, taking into account all the macroscopic effects, such as the defects and the dislocations [18,87]:

$$K_{eff} = K_{OOP} - K_{IP} = \int_{0\_OOP}^{M_S} \mu_0 H dM - \int_{0\_IP}^{M_S} \mu_0 H dM \qquad \text{Eq. (4.8)}$$

When the overall anisotropy of a film does not depend only on its intrinsic properties, but also depends on the geometrical properties of the nano-patterns, an estimation of the DW width can be done with experimental values of anisotropies obtained from M-H loops. In the approximation of a thin film to a single-domain particle (Stoner-Wolfharth model), the anisotropy field is defined as $H_a = H_{sat}$ (hard-axis) resulting in:

$$K_u = \frac{M_s H_a}{2} \qquad \text{Eq. (4.9)}$$

where H_a is the anisotropy field in Oe.

From the M-H loops is possible thus to obtain the effective magnetic anisotropy constant from the anisotropy field [18,68,87] as we can see in Figure # 4.11.

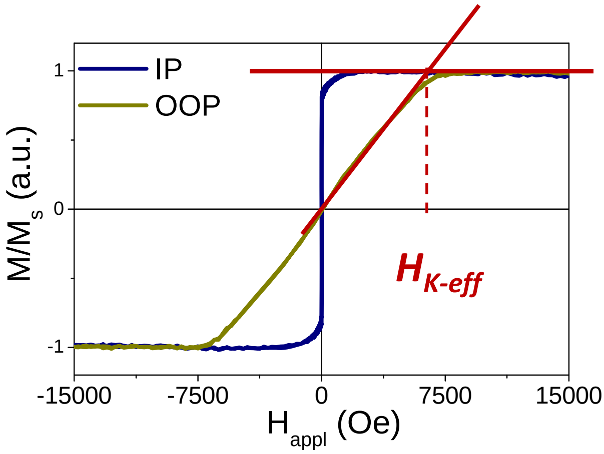

Figure # 4.11. IP and OOP M-H loop with the representation of the $H_{k\text{-eff}}$ of a CTF of thickness 34 nm.

Some information can be obtained from the macroscopic effective anisotropy constant are listed:

1. As the anisotropy constant of the arrays are closer to the ones of the CTF (in other words, increases) the magnetic behavior is more similar to the latter, being more important the IP magnetization (the anisotropy IP). This behavior should appear in the arrays with smaller d_P (the holes should contribute lesser to the film) and/or highest thickness.

2. As the constant decreases, the susceptibility of the OOP M-H loop increases, denoting an increasing contribution of the OOP component on the magnetization reversal.

3. As the constant increases, the magnitude of DW width decreases, allowing the nucleation of DW in between the holes (if applicable). This is expected in the arrays with bigger d_P, where the induced anisotropy is bigger; although in this case, the possibility of DW motion is smaller because the distance edge-to-edge between the nanoholes is too short.

An approximated calculation of the DW width can be obtained using this effective anisotropy constant; nevertheless, the DW width depends mostly on the intrinsic geometric properties. This approximation of the widths can only give a model of the DWs behavior, because in the case of the arrays, these walls are not the classical walls (non-classical long propagation as the DW in the CTF). Nevertheless, the walls propagation along the antidot arrays consist in several series of Barkhausen jumps or irreversible transitions as the wall skips from defect to defect [52]. So, from now on, the *non-standard* concept of DWs must to be present in all the analysis which includes DW motions.

The nucleation of DWs may occur at different sites of the arrays. Even if the ratio between D and d_P allows the creation and the displacement of DW, its motion will be short-ranged, because of the huge density of imperfections (defects and dislocations). So as mentioned before, the pinning effects lead to an irregular DW motion consisting on a series of Barkhausen jumps, and the spin configurations depend on the geometric properties of the lattice, creating different magnetic domain structures.

In summary, two possible cases of magnetic domain structures can be present in the antidot arrays:

1. The DW motion in arrays with smaller d_P can contain many holes, and in some cases many geometric domains, creating in this way *homogeneous magnetic structures.* Although the magnetic properties, as H_c and M_r, will change with the geometric properties.

2. As d_P increases, the magnetic material in between the holes decreases, as a result the wall will vanish rapidly or will not be created at all. At this point, where the pore interspaces (D-d) cannot contain the wall, the magnetization consists in a distribution of the spins among the holes (which at the same time depends on the geometric domains), consisting in a *non-homogeneous magnetic structures*.

4.1.2.5 *When there is no hexagonal ordering*

Finally, in an extreme case, an antidot array with no hexagonal ordering and no geometric domains, the array loses the local hexagonal anisotropy, even though the stray fields are still present. In this case, an averaged behavior due to the local anisotropy is expected.

For this section, an antidot array after the first anodization process (completely disordered) was made, where no hexagonal ordering was obtained. The dislocations are inexistent in this kind of arrays, and the sample can be compared to an amorphous packing of antidots with a broad distribution of d_P. A surface characterization was made (Kerr effect) in order to observed the anisotropy. In these measurements, the laser spot is always over the same area of the sample.

No isotropic behavior neither preferential axis magnetization was observed during MOKE characterization; instead, the magnetic behavior consists in a random magnetic signal at each angle, which depends on the asymmetric local stray fields. The DW anchoring in this case has a strong effect, which consist in random distribution giving as a result an asymmetric local variation signal. Figure # 4.12 shows the angular dependence of this array.

This result is important as it shows that the local hexagonal ordering provides an important anisotropic contribution to the magnetic properties of the arrays even though it has multiple contributions from the geometric domains when using the AAM templates.

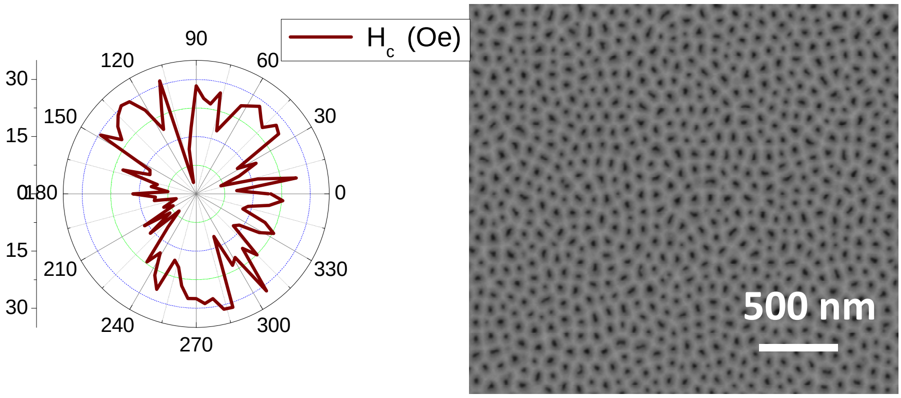

Figure # 4.12. H_c angular dependence and a SEM image of an antidot arrays with no hexagonal ordering, t_{Py} = 20 nm.

For the next sections, according to the magnetic properties of the CTF and the magnetic considerations on the arrays, several questions must be answered:
How the geometric properties of the arrays affect their magnetic characteristics;
If the distance edge-to-edge between the holes can comprise a DW;
The t_{Py} of the arrays influences the creation of the DW, as it does in the CTF.

4.2 MAGNETIC BEHAVIOR DEPENDENCE ON PORE DIAMETER AND LATTICE PARAMETER WITH CONSTANT THICKNESS OF 18 nm.

In this section, we present a study of the magnetization reversal process of the antidot arrays with different geometric properties [*pore diameter of the AAM* (*d_P*), *diameter of the antidot* (*d*), and *lattice parameter* (*D*)]. The analyzed samples are listed in Table # 4.6, with their corresponding *effective anisotropy constant* (*K_{eff}*).

Table # 4.6. Geometry characteristics of antidot films with t_{Py} = 18 nm and different d_P and D.

Name	**D (nm)**	**d_p (nm)**	**d (nm)**	**r**	**r'**	**K_{eff} (erg/cm^3)**
CTF	0	0	0	0	0	$3.9{\cdot}10^6$
Py13A	65	20	15	0.9	2.6	$4.4{\cdot}10^5$
Py14A	65	33	29	1.7	1.9	$9.7{\cdot}10^5$
Py15A	65	41	36	2.1	1.5	$8.8{\cdot}10^5$
Py2C	105	35	30	1.8	4	$4.8{\cdot}10^5$
Py4E	105	48	43	2.3	3.5	$3.9{\cdot}10^5$
Py5	105	56	51	2.9	2.8	$3.1{\cdot}10^5$
Py24A	105	66	61	3.5	2.3	$4.2{\cdot}10^5$

4.2.1 Surface Characterization

4.2.1.1 Magneto-Optics by Kerr Effect

The surface characterization provides important local information about the reversal mechanism in the upper part of the arrays. Taking into account the considerations about the MOKE system in Section 4.1.2.1, the measurements were carefully taken with the highest possible control of the laser position over the arrays. Both MOKE set-ups were used in this surface characterization, having each one different diameter of the laser's spot. In each measurement was clarified the corresponding size.

The macroscopic magnetic properties are directly related to the effective anisotropy and the magnetization reversal process can be determined by a simple inspection of the parallel and transversal loops [152,153]. A sharp transition in a loop denotes irreversible processes usually ascribed to DW displacement or irreversible rotations, and smooth transitions reversible processes typically magnetization rotation.

Figure # 4.13 shows a representative IP resolved hysteresis loop along the e.a. (α_H = 0°) and its transversal direction (α_H = 90°) for the 18 nm CTF.

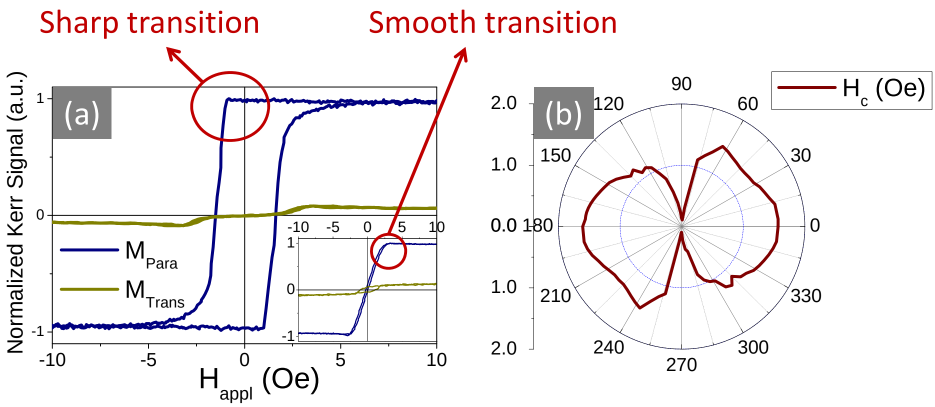

Figure # 4.13. (a) Kerr effect hysteresis loops along easy and hard (insets) axes and (b) Angular dependence of H_c of: a CTF (t_{Py} = 18 nm). M_{para} (blue) and M_{trans} (green) denote magnetization component parallel and transversal to the field direction.

The saturation signal of the parallel component is taken as 1; all other loops are normalized to this value. At $\alpha_H = 0^\circ$, a negligible M_{trans} and an irreversible transition in M_{para}, with a remanence close to 1 and a coercive field of about 1.5 Oe, were found, (Figure # 4.13a). The magnetization reversal close to the e.a. direction is dominated by irreversible transitions, DW motion, as is shown by the sharp transition in the M_{para} component. While close to $\alpha_H = 90^\circ$ (see inset of Figure # 4.13a), reversible transitions govern the magnetization reversal, demonstrated by the smooth transition around the h.a., with no hysteresis.

Figure # 4.13b shows the representative angular dependence of the CTF. These features reflect a two-fold symmetry of the magnetic anisotropy of the CTF [153]: a well-defined IP uniaxial magnetic anisotropy. This uniaxial behavior is consequence of the small magnetic field applied during deposition (≈ 6 Oe), since the 0° on the angular dependence of H_c, is parallel to the induced field produced by the arm of the sputtering system. The angular dependence of the remanence has the same biaxial behavior.

The evolution of M_{trans} can indicate the mechanisms of the magnetization reversal process. When the field is oriented parallel to the easy and hard-axes directions, the transversal component is zero during the reversal loop [154]. An example is shown in Figure # 4.14, where the loops of the e.a., -9° before and 9° after the e.a., are represented. When the field is along the e.a., the magnetization reversal takes place by nucleation and propagation of DW, or irreversible transitions, so $M_{trans} = 0$; the signal of M_{trans} changes direction before and after passing along the e.a.

On the other hand, when the field is swept parallel to an h.a. direction, the averaging of the signal over many hysteresis loops cancels the signal of M_{trans} [154,155].

When the field is applied at an angle slightly out of the easy and hard axes, the transversal component is not zero (Figure # 4.14: -9 and 9 degrees). When increasing the angle between applied field and e.a. or h.a. direction, the absolute values of M_{trans} increase; this indicates that the sample magnetization is not fully oriented parallel to the external field, but is aligned as close as possible to the nearest e.a., indicating sensitivity to the anisotropy.

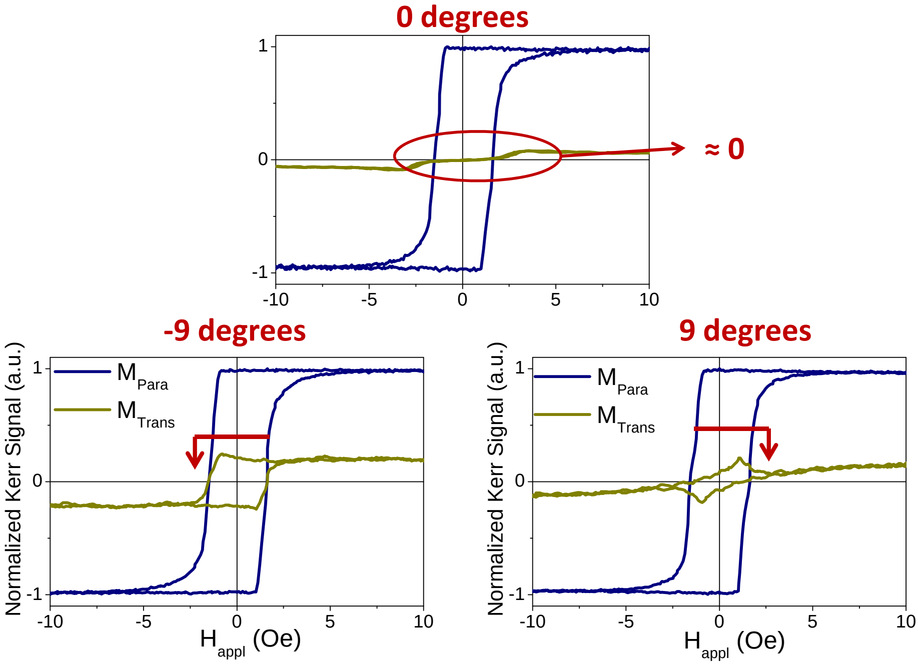

Figure # 4.14. Kerr magnetization curves of a CTF with t_{Py} = 18 nm, with the field applied at different angles from the e.a. The M_{para} and M_{trans} loops are shown with blue and red colors, respectively.

As an example of the antidot arrays, Figure # 4.15a and b, shows the Kerr effect M-H along easy and hard (inset) axes and the angular dependence of H_c, of an array with D = 65 nm and d_P = 20 nm, and D = 105 nm and d_P = 35 nm, respectively. For the antidot film, several distinct features are observed with respect to the CTF. First, very small differences are found when comparing the magnetization loops around e.a. and h.a. (inset), changing only in coercivity. Secondly, the coercive fields at the e.a. of these antidot films are almost one and two orders of magnitude larger than the CTF (respectively).

Figure # 4.15a an b shows irreversible transitions, but also noticeable is the nearly reversible contribution when reaching the magnetic switching. This suggests that a more complex magnetization reversal process is present where both DW motion and spin rotations, are involved when magnetizing the sample IP (the same behavior was found in the other arrays with different d_P). In the arrays, the nucleation of DWs may occur at different sites of the arrays, thus as mentioned in Section 4.1.2.4, and the pinning effect leads to an irregular DW motion consisting on a series of Barkhausen or irreversible jumps.

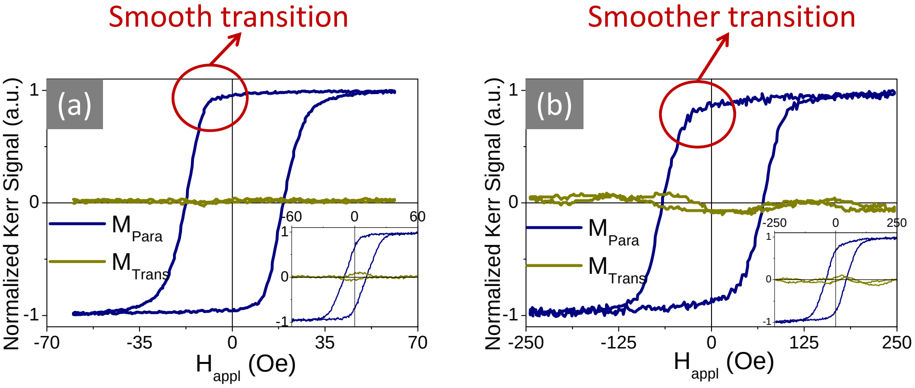

Figure # 4.15. Kerr effect hysteresis loops along easy and hard (insets) axes of the antidot arrays with (a) D = 65 nm and d_P = 20 nm, and (b) D = 105 nm and d_P = 35 nm. M_{para} (blue) and M_{trans} (green) denote magnetization component parallel and transversal to the field direction.

In Figure # 4.16a and b the angular dependence of H_c and magnetization remanence (longitudinal and transversal) of antidot arrays with D = 65 nm and d_P = 20 nm, are shown, respectively. In the H_c and the $M_{r\text{-trans}}$, a two-fold symmetry of the magnetic anisotropy was found, although a smaller second e.a. is found at 90º from the principal, resulting in a weak four-fold anisotropy.

Here, it is important to remark the laser spot's diameter (≈1 mm) and the geometric domains inside of it (Section 4.1.2.1). The MOKE averages around 500 domains, each one with different e.a. orientations; and as in the case of the VSM loops, the resulting behavior is isotropic. At this scale, the anisotropy has a competition between the induced magnetic field and the triaxial anisotropy due to the hexagonal lattice. In this case, as in the CTF, the 0º on the angular dependence of H_c, is parallel to the induced field produced by the arm of the sputtering system. This induced field only alters the H_c in each axis (which show no difference in the magnetization reversal mechanism at each axis), since all the loops have the same shape. The increases in H_c of the array when comparing to the CTF (12 times) is due to the nanoholes pattern, which anchor the DW.

Nevertheless, the important measurement to conclude about the anisotropy is the $M_{r\text{-long}}$, dependence, where an isotropic behavior is exhibited. Besides, the same isotropic behavior was found in the arrays with different d_P and D.

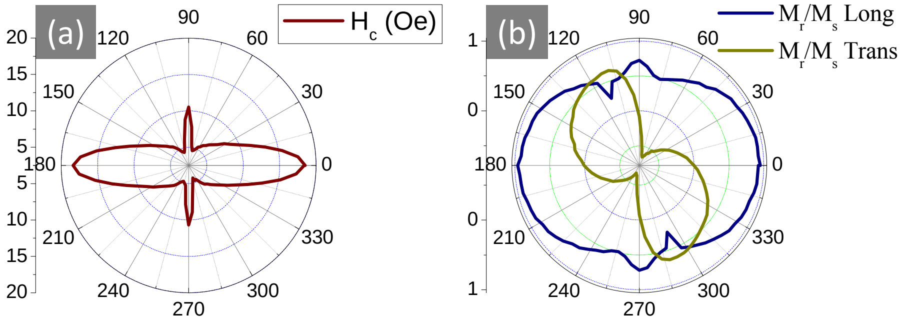

Figure # 4.16. (a) Angular dependence of H_c and (b) normalized magnetization remanence (longitudinal and transversal) of the array with D = 65 nm and d_P = 20 nm.

4.2.1.2 Magnetic Force Microscopy

The MFM signal corresponds mainly to the OOP component of the magnetic moment of the sample. Figure # 4.17 shows the MFM images (and the corresponding topography AFM images) at the remanence state for one selected antidot films with D = 105 nm and *d* = 61 nm. The MFM image reflects the correlation between hexagonal arrangement of antidots and surface magnetic distribution, where pairs of positive and negative magnetic charges accumulate around the nanoholes which owing to dipolar-like interaction align reproduce the hexagonal antidot ordering, as explained in Section 4.1.2.3.

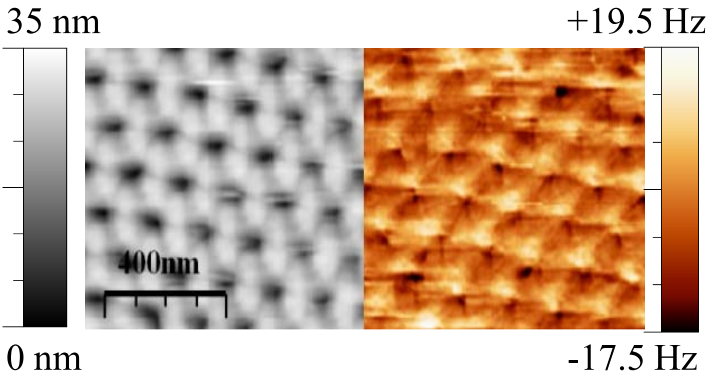

Figure # 4.17. AFM and MFM of a sample of D = 105 nm and d = 61 nm.

Along one of the axis of the hexagonal symmetry, accumulated charges around the nanoholes were found, while straight lines connecting adjacent nanoholes were observed along the other axes, exhibiting pseudo-domain walls following the hexagonal arrangement, similar to those reported for Ni antidot arrays in ref [62]. This magnetic structure will be discussed in detail in the following section.

The observed contrast reflects the presence of a noticeable OOP component of magnetization, which in principle can be ascribed to the higher OOP local shape anisotropy as a consequence of the shorter value of r’ ratio.

4.2.2 M-H Loops by Vibrating Sample Magnetometer

The M-H loops in the IP and OOP configuration obtained by VSM of a CTF of thickness of 18 nm are presented in Figure # 4.18a; while the virgin, the IRM and their respective percentage, in the IP configurations, are presented in Figure # 4.18b. The VMS loops show an isotropic behavior in the angular dependence.

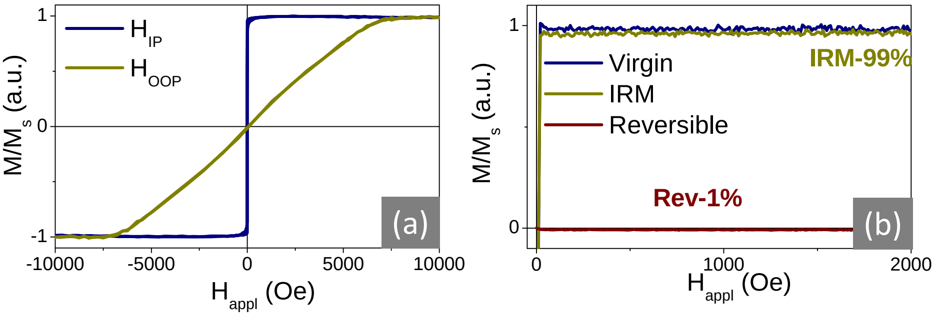

Figure # 4.18. (a) M-H loops in IP and OOP configuration; and (b) Reversal curves, for CTF with t_{Py} = 18 nm in IP configuration.

The M-H loop in the IP configuration shows the characteristic magnetic behavior of the Py CTF, with a square loop, with H_c of 1.6 Oe and a normalized *remanent magnetization* (M_r) of approximately 0.95. This behavior is ascribed to nucleation and propagation of DW, as in the MOKE loop. In the OOP configuration, the M-H loop shows the characteristic linear behavior with almost no M_r, ascribed to spin rotations.

The IRM curve describes the irreversible processes of the sample ascribed to the DW motion. In the CTF, this irreversible process corresponds to the 99% of the magnetization reversal process; meanwhile, the reversal curve denotes the reversibility, ascribed to reversible rotations, almost absent in the IP of the CTF. These curves are in accordance with the M-H loop.

In the case of the antidot arrays, Figure # 4.19, almost all the VSM M-H loops present a similar behavior as the MOKE M-H loops: a large irreversible jump, with nearly reversible contribution when reaching the switching field (smooth transitions), but a deeper analysis must be made in order to understand the magnetic behavior of the arrays.

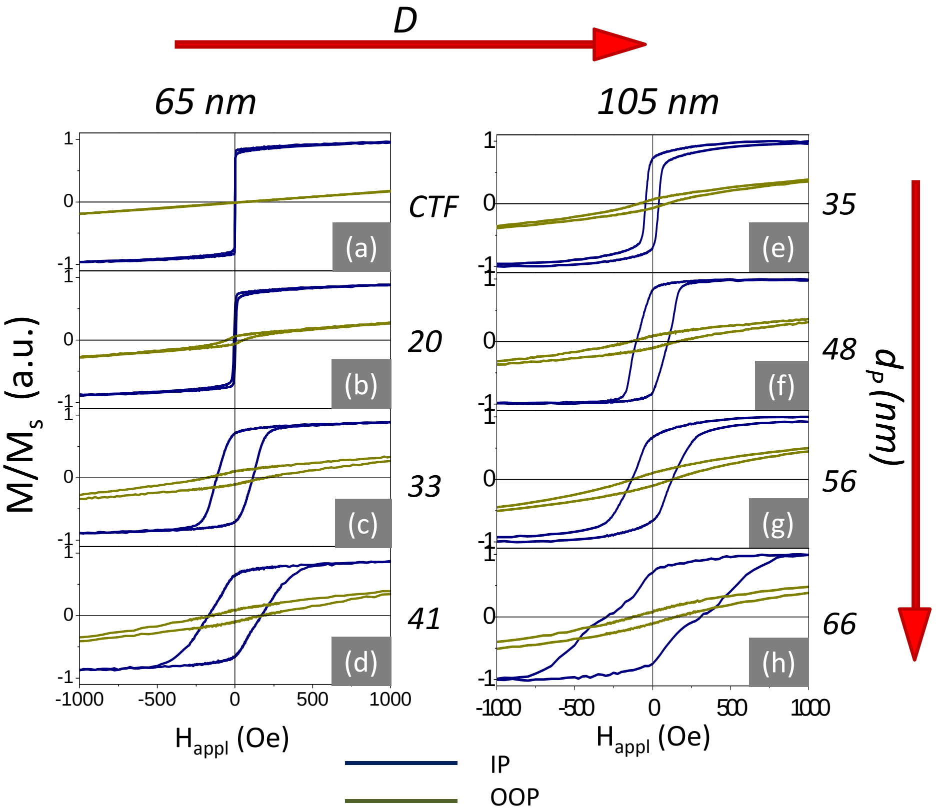

Figure # 4.19. M-H loops by VSM in IP and OOP configuration of: (a) CTF, (b) D = 65 nm, d_P = 20 nm, (c) D = 65 nm, d_P = 33 nm, (d) D = 65 nm, d_P = 41 nm, (e) D = 105 nm, d_P = 35 nm, (f) D = 105 nm, d_P = 48 nm, (g) D = 105 nm, d_P = 56 nm, (h) D = 105 nm, d_P = 66 nm.

The values of K_{eff} of the arrays in Table # 4.6 have an unexpected decrease with d_P, but not linearly, with respect to the CTF. The arrays with D = 65 nm, and r' = 1.9 and 1.5, have the highest values (although one order of magnitude lower than the CTF), denoting an important IP component. On the contrary, in the arrays with D = 105 nm, the lower effective anisotropy constants indicate an important OOP component. It is important to remember that this constant is a macroscopic model, where the local anisotropy was not calculated.

In all the arrays, theoretically the d_P are small enough to allow the motion of DW among the holes, nevertheless, analyzing the M-H loops in Figure # 4.19, is unlikely to have DW propagation in the arrays with bigger d_P (Figure # 4.19c-d-g-h).

In the cases of the arrays with smaller d_P in Figure # 4.19 b-e-f, the squareness of the IP M-H loops indicates nucleation of DW. In a previous study [55], the same behavior was found. In Figure # 4.20, the M-H loops of samples Py13A and Py2C are represented. Coming from positive saturation field (A in the figure), where the magnetization is parallel to the applied field, the sample has a reduction in M_r (B). When the field reverses, the abrupt jump is due to the DW motion in the continuous zones between the holes (C). Meanwhile the spins around the holes lie parallel to the holes boundaries. When the field increases, the spins rotate towards the direction of the applied field, with smoother behavior (D), until reaching saturation (E).

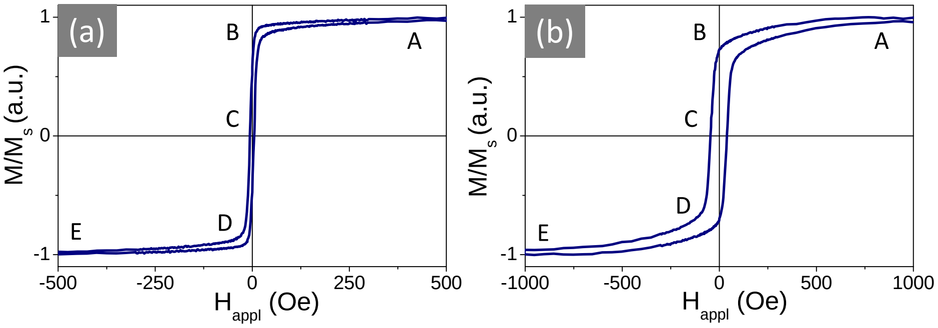

Figure # 4.20. IP M-H loops of sample (a) Py13A: D = 65 nm, d_P = 20 nm; and (b) Py2C: D = 105 nm, d_P = 35 nm.

In Section 4.1.2.4, was mentioned that different magnetic domain structures can be obtained with different d_P and D, and the magnetization reversal process depends on these structures. In the arrays with bigger d_P, the domains structures could reverse with a different mechanism. As in the last cases, in Figure # 4.21 are represented two samples with bigger d_P. Coming from positive saturation (A), the samples have a reduction in Mr (B) as well, but when the field reverses (C), the irreversible transition seems to be different to a DW motion.

Two possible options are considered in the point (C) in the continuous zones between the holes: the first one consists in irreversible rotations instead of DW motion. The second consideration consists in the DW nucleation at different sites of the sample with a series of Barkhausen jumps inside the geometric domains. Nevertheless a combination of both options may be considered. At the point (D), when the field increases, the spins have a smoother rotation towards the direction of the applied field, as in the last cases.

Some IP- and OOP M-H loops are represented in Figure # 4.22, in order to observe the effect of the OOP component: the OOP M-H loops behave like the IP M-H loop as d_P increases, demonstrating the important contribution of this component.

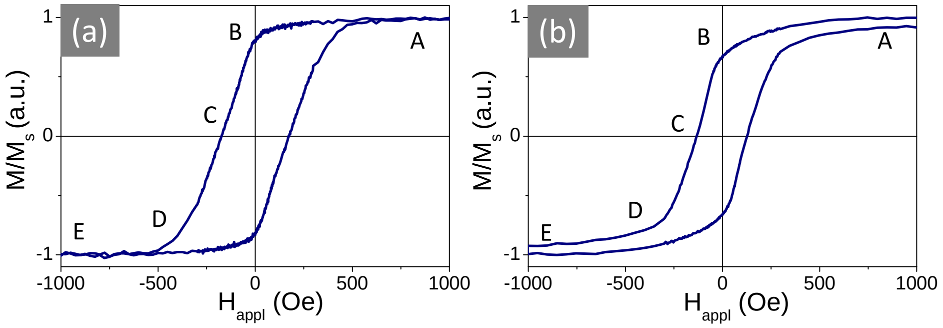

Figure # 4.21. IP M-H loops of sample (a) Py15A: D = 65 nm, d_P = 41 nm; and (b) Py5: D = 105 nm, d_P = 56 nm.

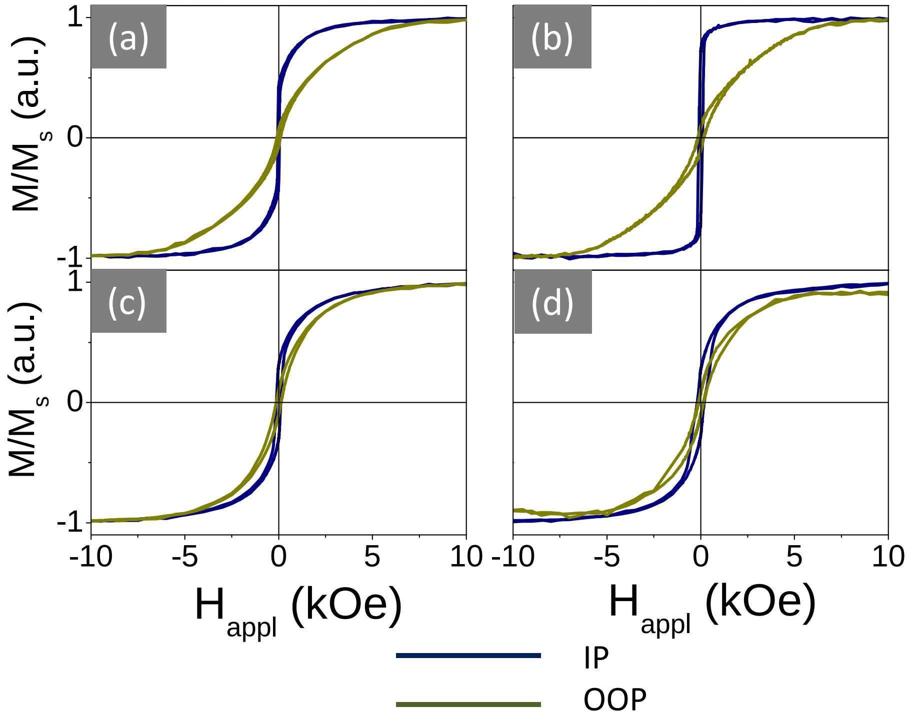

Figure # 4.22. M-H loops in IP and OOP configuration of the arrays with D = 105 nm: (a) d_P = 35 nm, (b) d_P = 48 nm, (c) d_P = 56 nm, (d) d_P = 66 nm.

From the M-H loops, the values of H_c and M_r were obtained, as shown in Figure # 4.23. In the case of the antidot arrays with D =105 nm, as d_P increases the IP-H_c also increases, consequence of the stronger pinning effect from the holes, while the OOP-H_c has an abrupt decreases in the two biggest d_P (not a linear behavior).

As d_P increases the IP susceptibility remarkably decrease (the IP M_r decreases (in good agreement with the results reported by Vovk [151] and Yu [78]), while the OOP susceptibility and M_r increases; thus an important OOP component is the responsible of different magnetic configurations. The M_r decreases because the spins around the holes lie parallel to the voids boundary in order to minimize the stray fields inside the nanoholes [55].

These results together with the macroscopic effective anisotropy constant, demonstrate an increase in the OOP component: the dipolar interaction between the nanoholes and the stray fields increase, compensating the magnetic domains structures with the OOP configuration of the spins. Additionally, the small roughness of the AAM contributes to lower the M_r when comparing to the corresponding CTF [55], because the magnetization of these hills get align in the OOP component, reducing the magnetostatic energy.

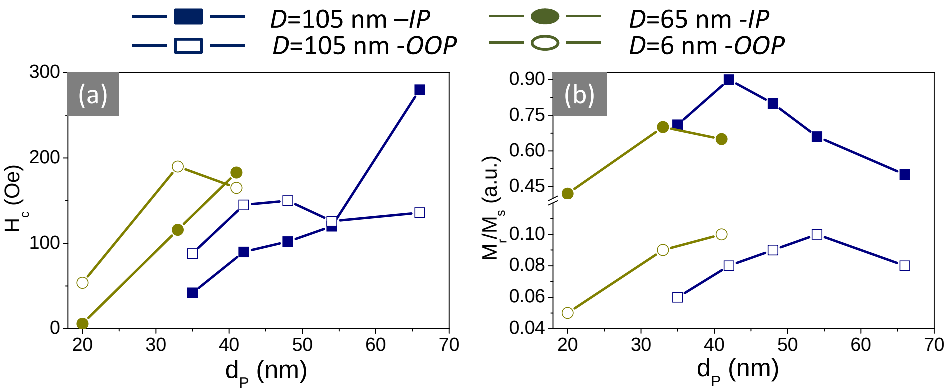

Figure # 4.23. (a) H_c, and (b) M_r/M_s vs. d_P.

In the case of samples with D = 65 nm, the IP-H_c and the OOP-H_c behave as in the arrays with D = 105 nm; increasing with d_P, except for the arrays with d_P = 41 nm. The IP and OOP-Mr behave very similarly to the arrays with D = 105 nm.

Making a comparison between the arrays with D = 65 and 105 nm and the same or similar d_P, is possible to observe higher coercivities in the former. This result is due to the dipolar interactions between the holes as a result of the smaller space (D = 105 nm: edge-to-edge from 70 to 40 nm; and D = 65 nm: edge-to-edge from 45 to 24 nm).

The relation between H_c with 1/D-d, r and r', Figure # 4.24, reflects the behavior of the coercivity with the geometric properties of the arrays, as explained in Section 1.4, H_c increases as the material among the nanoholes decreases (1/D-d), in other words, the inverse of the ratio r', which takes into account the thickness and the average of d and d_P, Figure # 4.24c (green line). The blue line in Figure # 4.24c shows the relation of H_c with the ratio r.

$$H_C\ \alpha\ \frac{1}{D-d_P};\ H_C\ \alpha\ r;\ H_C\ \alpha\ \frac{1}{r'} \qquad \text{Eq. (4.10)}$$

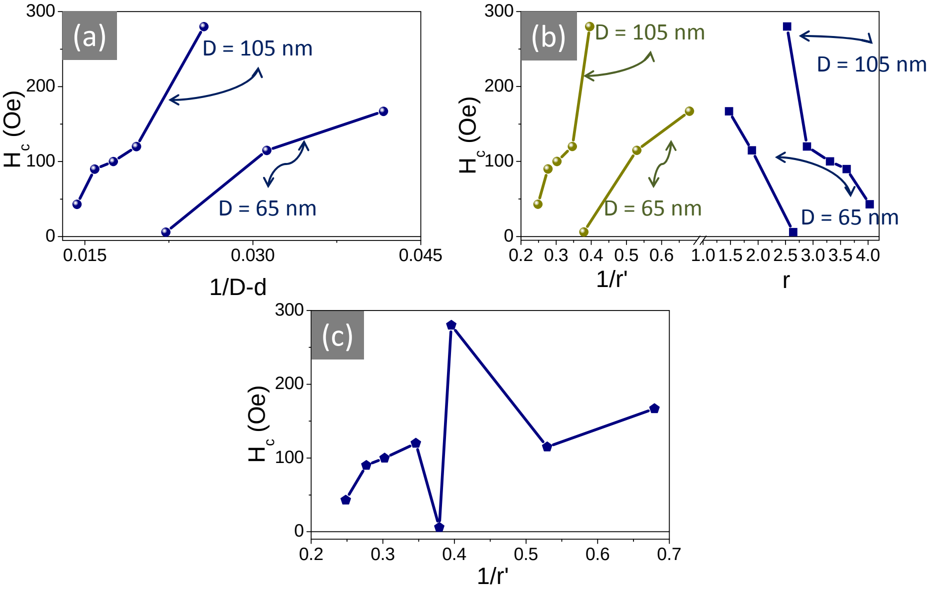

Figure # 4.24. H_c dependence vs. (a) 1/D-d, (b) 1/r' and (c) 1/r' and r.

In these relations of H_c, exist always a distinction between the arrays with different D, Figure # 4.24a and b; but if the relation is made only with the ratios r or r', the behavior is not completely linear, as is shown in Figure # 4.24c. Thus, a deeper comparison between several samples was made in order to understand the dependence of the stray fields and the dipolar interactions with d_P and D:

1. Samples with almost the same ratio r' (Py13A – Py24A), show that the difference between H_c is huge, even when the distances edge-to-edge between the nanoholes are similar (d_P = 20 and 66 nm respectively, and D = 65 and 105 nm, respectively). This effect can be explained by the accumulated charges around the nanoholes, which are the responsible of the dipolar interaction among the holes.
   These interactions depend on the density of the charges around the holes, being higher with increasing d_P (as can be seen in Figure # 4.10); in the former the density is lower due to the smaller d_P, decreasing the anchoring of DW, resulting in lower H_c [59,148,149].

2. The antidot arrays with similar ratio r, i.e. similar d_P and d (Py14A and Py2C; $r \approx 1.7$) – (Py15A and Py4E; $r \approx 2.2$), shows an enhancement of H_c when D is smaller. Here, in spite of similar d_P (density of accumulated charges around the holes), the dipolar interactions due to the proximity of the dipoles around the holes increases when D is smaller (Py14A and Py15A), raising the coercivity of these arrays [29,68,78,149]. As expected, the coercivity decreases with increasing D (and similar d_P). The separation of the non-magnetic structures implies a decrease in the magnitude of the demagnetizing energy relative to the total energy.

3. For arrays with $D^* \approx$ D-d (D^* = distance edge-to-edge; Py14A and Py5), the magnetic behavior is similar. The density of accumulated charges around the nanoholes and the distance between them, are of the same order of magnitude, therefore these antidot arrays have almost similar H_c.

4.2.3 First-order reversal curve analysis

From Figure # 4.25 to Figure # 4.28, show the FORC diagrams represented in color scale for the CTF and antidot samples with t_{Py} = 18 nm, respectively. Measurements were performed with the applied magnetic field along the IP easy direction and maximum amplitude of 300 Oe, reversal field steps of 6 Oe and saturation field of 15 kOe.

For the CTF, Figure # 4.25, a single main FORC distribution is observed ascribed to DW nucleation and propagation processes, with a narrow peak around the maximum value of H_C^{FORC}= 2 Oe. Interestingly, such a value is close to the H_c values obtained from VSM measurements indicating a negligible presence of interaction fields as expected for CTF.

Related to the antidot films of Py, the following information can be extracted:

1. Overall, values of H_C^{FORC} are bigger than H_c from the M-H loops. That behavior can be ascribed to an enhancement of local magnetic anisotropy, related to the high surface anisotropy, as a consequence of the stray fields originated by the antidots [118]. The material in between the pores produces dipolar interaction, increasing the coercivity in the FORC graphs. Comparing this effect on the arrays with the CTF, the latter has no surface anisotropy, negligible roughness, and so there in no contribution from the stray fields.

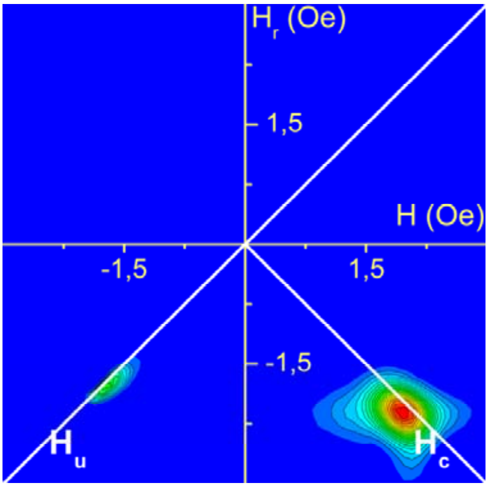

Figure # 4.25. FORC diagram of a CTF of Py.

Table # 4.7. Comparison between H_c from the M-H loops and the FORC diagrams.

Name	**d_p (nm)**	**d (nm)**	H_C^{MH} (Oe)	H_C^{FORC} (Oe)
Py2C	35	30	42	50
Py4E	48	38	102	150
Py5	56	51	120	200
Py24A	66	61	280	525
CTF	0	0	1.8	1.75
Py13A	20	15	6	13.03
Py15A	41	36	183	245

2. In comparison to the corresponding thin film, broader FORC distributions along H_c are visible for the antidot samples. Such behavior is indicative of a large switching field distribution due to the presence of *non-homogeneous magnetic structures*, as mentioned in Section 4.1.2.4. The presence of more than one peak in the H_c axis is a direct consequence of the large number of DW pinning sites due to locally distributed stray fields generated by the nanoholes.

3. Moreover, a contribution from magnetization rotation mechanisms can also be associated with the visible broadening along H_u. In Figure # 4.15 and Figure # 4.21, the smooth transitions due to the rotation mechanisms are observed. Therefore, the broadening along H_u with increasing nanohole size in these

samples, translates not only the effect of a strong pinning due to larger holes but also (to less extent) an enhancement in the rotation mechanisms.

4. Also with increasing d_P, a clear broadening of FORC distributions along the interactions axis, H_u, together with higher H_C^{FORC} values is observed. Such trend suggests a gradual enhancement of the antiparallel interactions with d_P, again ascribed to the stray fields produced by the nanoholes. This effect is particularly evident for the sample with d_P = 56 and 66 nm.

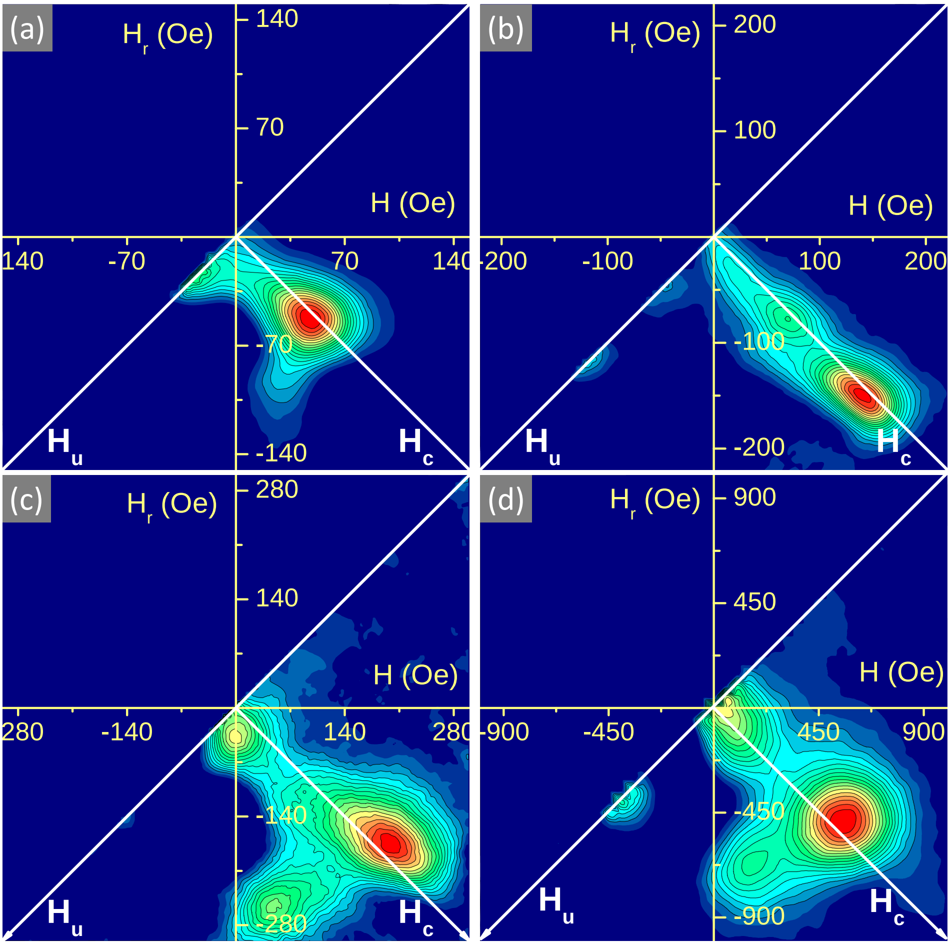

Figure # 4.26. FORC diagrams of antidot arrays with D = 105 nm and t_{Py} = 18 nm and d_P of (a) 35 nm, (b) 48 nm, (c) 56 nm, (d) 66 nm.

5. As a final remark about the antidot arrays with D = 105 nm, in the plot of d_P = 56 nm, Figure # 4.27, two peaks appear outside the H_c axis in the interference

region, Fig. 2.8. This effect is due to coupled interaction between the higher and the lower coercivities region. In this sample (see following section) a bi-phase behavior is appreciable in the MOKE loop, evidencing stronger interactions between the dipoles around the nanoholes. This bi-phase behavior is treated in Section 4.2.5.

The same peaks outside the H_c axis were obtained in the antidot array with d_P = 66 nm, although an extra peak was found along the H_u axis. Our deduction about the origin of this peak is the stronger dipolar interaction due to the increased proximity between the holes.

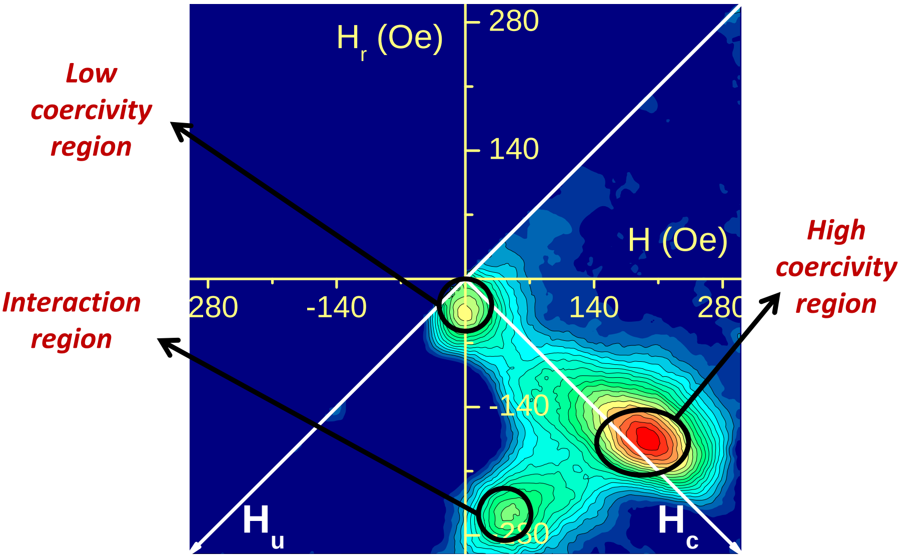

Figure # 4.27. FORC diagrams of antidot arrays Py5.

6. The antidot arrays with D = 65 nm, the H_c shows the same behavior as in the case of the arrays with D = 105 nm; nevertheless, the interactions seems to be smaller in the former. As explained in the last section, this behavior is due to the smaller d_P (smaller charge density around the nanoholes, as is shown in Figure # 4.10).

   Taking Py4E and Py15A as examples (d = 38 and 36 nm, respectively), the H_c and H_C^{FORC} are much higher in the latter, because in spite they have almost the same charges density around the nanoholes, the holes are nearest to each other. In samples with D = 65 nm, the FORC diagrams do not have (or have much lesser intensity) interference or interaction regions. This is due to the smaller d_P, thus lower density of accumulated charges around the nanoholes, produce lower interactions among them.

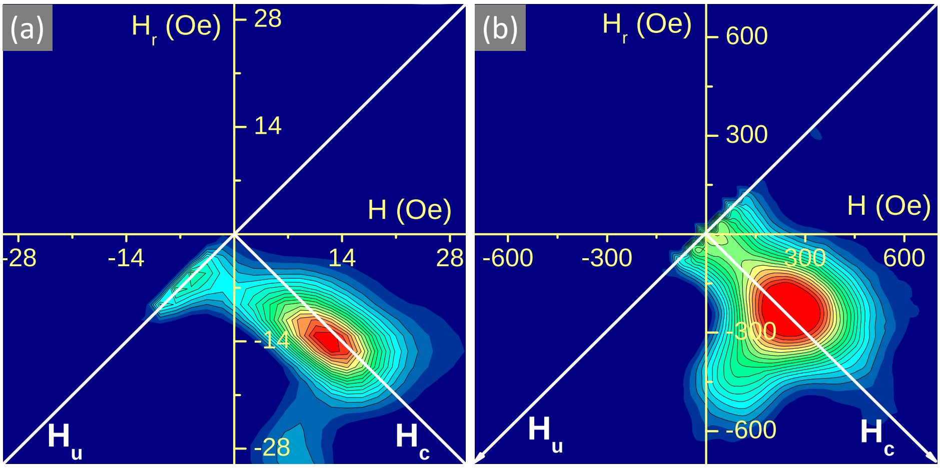

Figure # 4.28. FORC diagrams of antidot arrays with D = 65 nm and t_{Py} = 18 nm and d_P of (a) 20 nm and (b) 41 nm.

4.2.4 Surface Characterization vs. Bulk Behavior

A comparative analysis between IP-M-H loops by VSM and MOKE (NanoMOKE) was performed (for comparison purposes the normalization was made to the Kerr saturation signal). While from MOKE analyses one obtains mostly the surface magnetic information, from VSM measurement information regarding the average magnetization of the entire sample is obtained instead. Therefore, the different magnetic reversal mechanism occurring either at the surface or within the bulk of the sample can be discriminated by comparing MOKE and VSM loops. For Py arrays, the penetration depth (δ) of the laser goes from 13.5 to 22 nm with d_P from 35 to 56 nm, according to Table # 3.12.

Figure # 4.29 shows the loops for the antidot films with t_{Py} = 18 nm and different antidot geometric parameters and Figure # 4.30 displays the H_c from both systems.

Regarding the influence of the antidot diameter, in both VSM and MOKE loops the square shape vanish and the bi-phase behavior appears in the array with D = 105 nm and with d_P = 66 nm (VSM and MOKE), and d_P = 56 nm (MOKE).

In samples with D = 65 nm, the loops are very similar between them and only the coercivities have slightly different values. Furthermore, in the arrays with D = 105 nm, H_c takes clearly higher values for MOKE measurements, suggesting a slightly softer reversal mechanism at the bottom of the antidot films, with the reversal magnetization at lower fields.

However in the MOKE loops, in the case of d_P = 66 nm, the bi-phase magnetic effect has increased, and in the array with d_P = 56 nm, shows the same a bi-phase behavior (but to a lesser extent) and with different susceptibility.

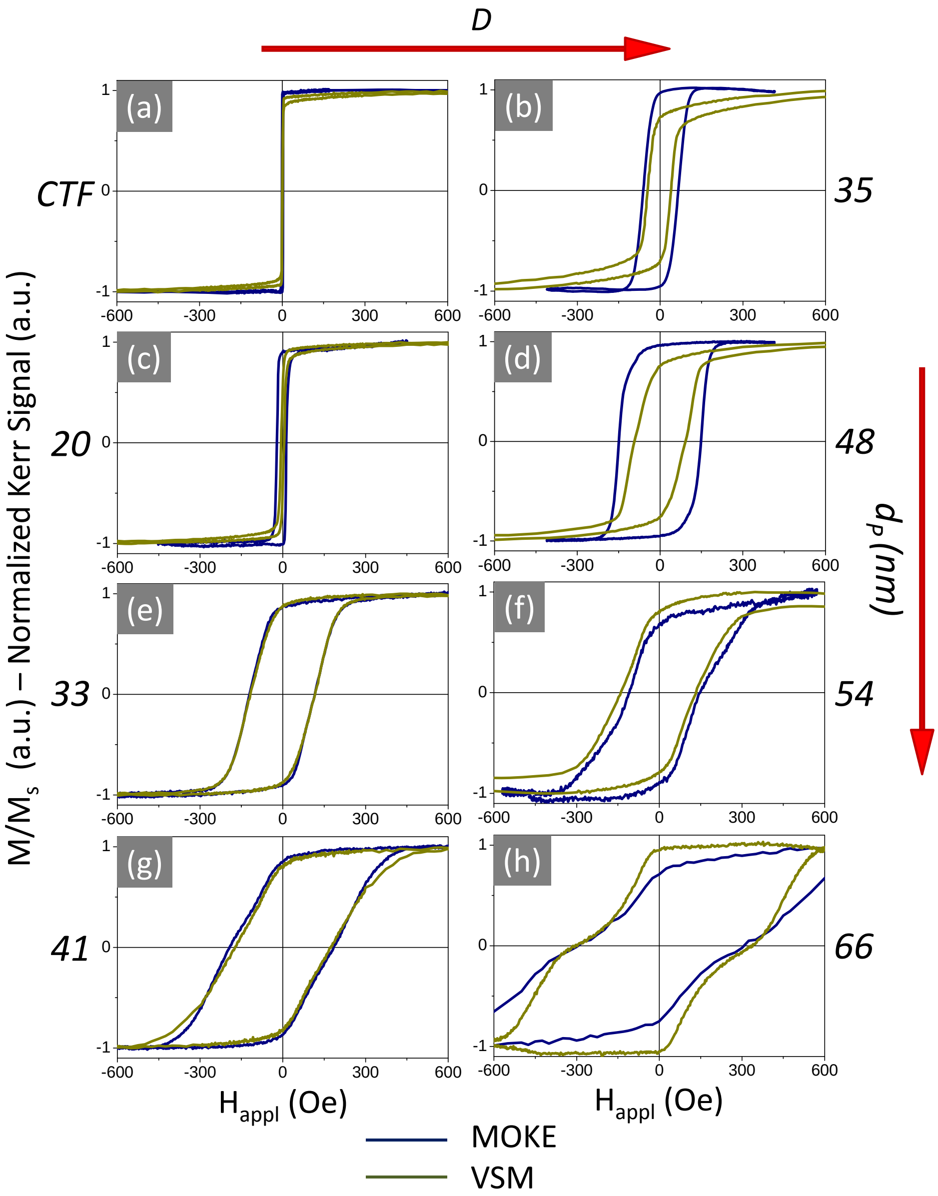

Figure # 4.29. Comparison between the MOKE and VSM M-H loops of the arrays with t_{Py} = 18 nm.

As it will be explained in the next section, the material inside the wall of the pores may contribute to this harder-magnetic phase, increasing its contribution for larger d_P. However, why is it more evident in the MOKE loops? probably due to the penetration depth of the laser together to the step coverage of the sputtering.

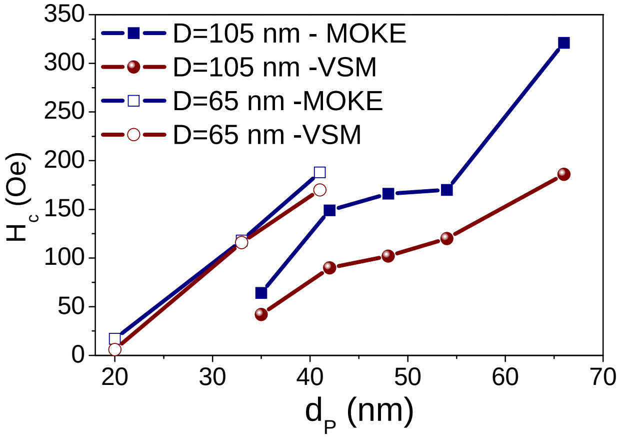

Figure # 4.30. Hc MOKE and VSM

4.2.5 Bi-phase magnetic behavior

An important remark must be made in the M-H loop with a bi-phase behavior, Figure # 4.19h. The possible reason of this two magnetic phases, could be that the hard magnetic-phase may correspond to the OOP component of the arrays (around the nanoholes), having the reversal magnetization at higher magnetic fields than the IP component. Some works [156] claim to have the same bi-phase behavior and an important OOP component in Co antidot arrays over AAM. The reasons of both behaviors are attributed to the fact that the material inside the walls of the pores can have a different magnetization orientation, OOP in this case, contributing to the harder magnetic phase, while the material in between the pores shows IP magnetization, corresponding to the softer magnetic phase, Figure # 4.31a. The IP- and OOP-M-H loops, Figure # 4.31b, demonstrate that the OOP component has almost the same magnetic behavior as the IP component, presenting almost the same M-H loop.

Although the material inside the walls of the pores is present in the entire array, this bi-phase behavior is only present in the biggest d_P with D = 105 nm, suggesting a more important contribution from the OOP component. This is mainly due to the step coverage of the sputtering method, see Section 3.3.4. The sputtering step coverage is 1, this means that for a t_{Py} = 18 nm a 18 nm coverage inside the pore wall is obtained, therefore as bigger the d_P, the ratio between the material among the holes and the one inside the membrane, is smaller; being the latter more important than in the arrays with smaller d_P.

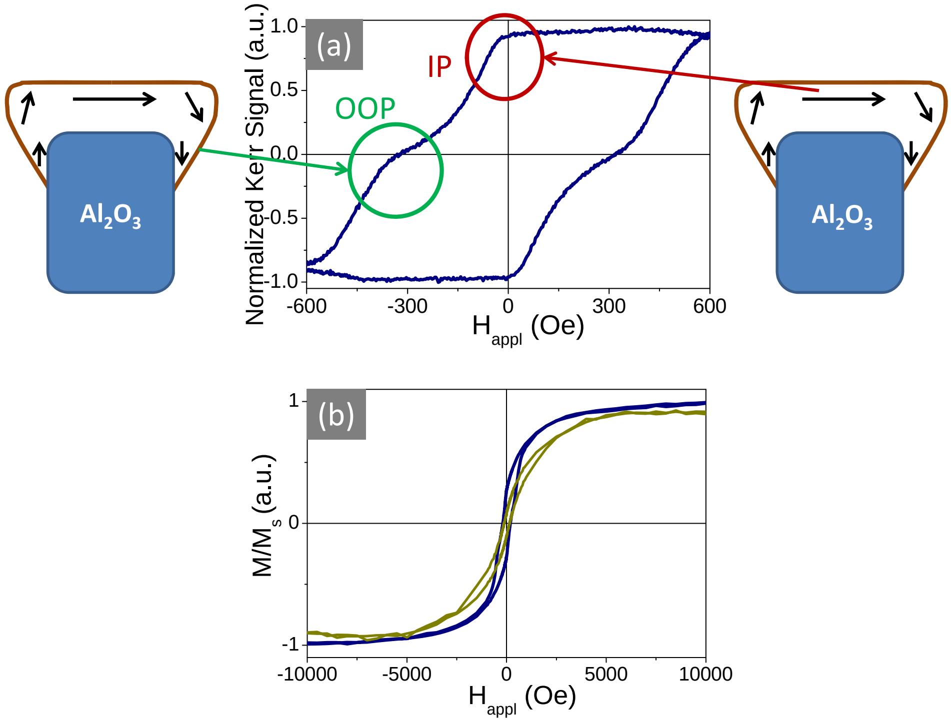

Figure # 4.31. (a) M-H loop indicating the possible signal form the Py over and inside the walls of the AAM’s pores, (b) IP and OOP M-H loop; of an arrays with d_P = 66 nm and D = 105 nm.

The material inside the wall of the pores enhances the OOP contribution [156], leading to a different magnetic configuration, as observed in the MFM. The magnetic structure of this sample shows a strong coupling between the dipoles around the nanoholes. When the edge-to-edge distance between pores becomes small enough, the magnetic poles around the edges of the pores strongly interact with those of neighboring pores, locking the magnetic configuration into a well defined and stable hexagonal sequence of pseudo-walls. This is particularly visible in the case of sample Py24A, presented in Figure # 4.32, where the thickness is almost the half of the distance edge-to-edge (≈ 40 nm).

This magnetic configuration is responsible for the unusual magnetic hysteresis reported in Figure # 4.29h. Near remanence, the magnetization presents a formation of a stable hexagonal structure of pseudo-domains around the pores. The sudden change of the magnetization at low field values (H ≈ 0) is because the sample comes out of saturation to a state where the magnetization is not stable. In this non-stable state, the pole density of the array is minimized.

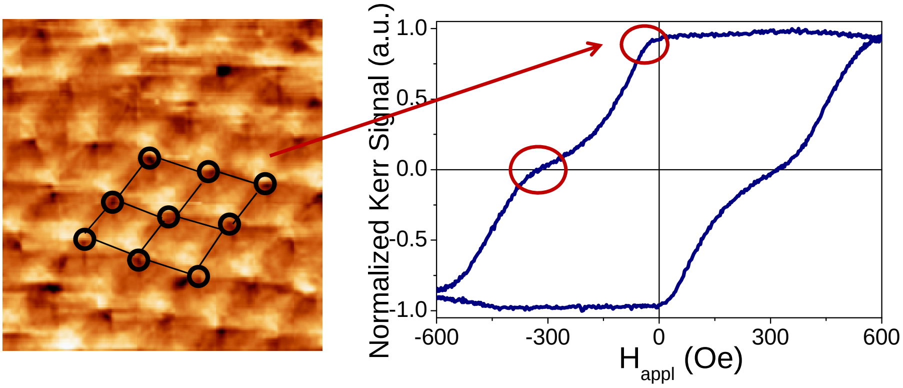

Figure # 4.32. Magnetic structures on MFM and the MOKE loop, of an array with d_P = 66 nm and D = 105 nm.

The second transition corresponds to the switching of the magnetization to a nearly uniform/stable pattern, but now with the opposite direction. The stability of this structure is responsible for the relatively high value of coercive field, of approximately 320 Oe, and the plateau region around it, which must change as the field increases, and find another stable structure with higher H_c. A similar bi-phase behavior appears in the simulation studied in Ref.157.

In summary, both the OOP component from the material inside the wall of the pores and the different local magnetic regions induced by the presence of antidots, create a magnetic structure with a dipolar configuration, and would be the responsible for the bi-phase behavior.

This magnetic configuration can be observed in other samples, having slightly smaller value of d_P as can be seen in Figure # 4.29g. In this case, the material inside the wall of the pores has a smaller contribution than in the arrays with bigger d_P. Assuming that the corresponding laser's penetration depth in the sample is 19 nm, Eq. (3.1), almost the same as the thickness, a small contribution from the material inside the pores was obtained, so a bi-phase behavior is noticeable in the MOKE loop. Notice that, MOKE is more sensitive to this component inside the wall of the pores due to surface sensitivity.

4.3 MAGNETIC BEHAVIOR DEPENDENCE ON THICKNESS

After studying the magnetic behavior of the antidot arrays with different geometrical properties, the study of the magnetic behavior with different t_{Py} and constant D (105 nm), was made. The analyzed samples are listed in Table # 4.8.

Table # 4.8. Geometry characteristics of antidot films with D = 105 and different t_{Py} and d_P nm.

t_{Py} (nm)	Name	D (nm)	d_p (nm)	d (nm)	r	r'
10	PyM59	105	22	20	2.1	8.4
	PyM68	105	35	32	3.4	7.2
	PyM69	105	48	45	4.7	5.9
	PyM63	105	56	55	5.6	4.9
	PyM32	105	65	62	6.4	4.2
	PyM33	105	75	71	7.4	3.2
18	Py2C	105	35	30	1.8	4.0
	Py4E	105	48	43	2.5	3.3
	Py5	105	56	52	3.0	2.8
	Py24A	105	66	61	3.5	2.3
20	PyM22	105	22	16	1.0	4.3
	PyM23	105	36	30	1.7	3.6
	PyM24	105	48	43	2.3	2.9
	PyM74	105	56	50	2.6	2.6
	PyM25	105	67	60	3.2	2.1
	PyM70	105	70	63	3.3	1.9
34	Py17A	105	35	25	0.9	2.2
	Py19A	105	44	34	1.1	1.9
	Py18A	105	56	47	1.5	1.6
	Py20A	105	66	56	1.8	1.3
43	PyM67	105	22	10	0.4	2.1
	PyM48	105	35	22	0.7	1.8
	PyM44	105	48	35	0.9	1.5
	PyM45	105	64	51	1.3	1.1
	PyM46	105	75	62	1.6	0.8
138	Py17B	105	35	10	0.2	0.6
	Py19B	105	44	12	0.2	0.6
	Py18B	105	57	23	0.3	0.5
	Py20B	105	66	30	0.3	0.4

4.3.1 Surface Characterization

4.3.1.1 MOKE

As in Section 4.2.1.1 samples with different thicknesses were characterized by MOKE. Only in this section are presented MOKE loops of some samples with D = 65 nm in order to make a proper comparison, but from the next section, all the analyzed samples have D = 105 nm. At first, the CTF with different t_{Py} exhibit an effective anisotropy behavior as the CTF with 18 nm of thickness, i.e. square shape in the longitudinal loop and linear magnetization behavior in the transversal loop. In this case, the 0º on the angular dependence of H_c, is parallel to the induced field produced by the arm of the sputtering system.

The only difference is the higher coercivity, showing H_c of approximately 2-3 Oe for samples with t_{Py} of 34 and 138 nm. As an example, Figure # 4.33 shows a representative IP resolved hysteresis loops along the e.a. (α_H = 0◦) and its h.a. (α_H = 90◦) for the 34 nm CTF.

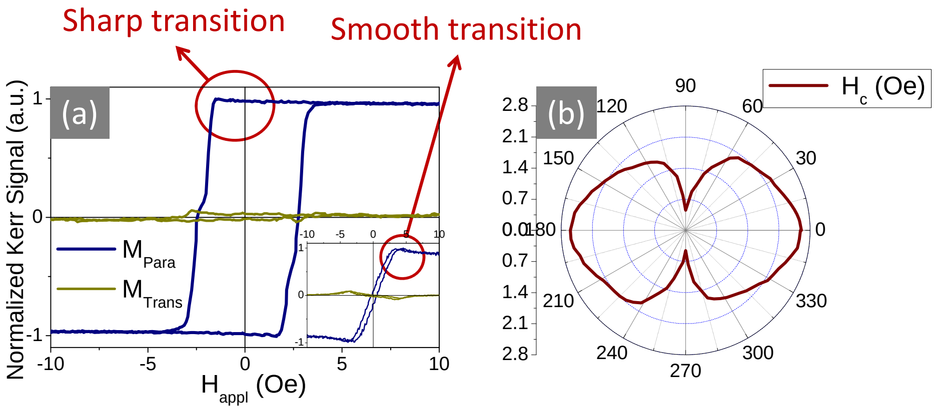

Figure # 4.33. (a) Kerr effect hysteresis loops along easy and hard (insets) axes and (b) Angular dependence of H_c of: a CTF (t_{Py} = 34 nm). M_{para} (blue) and M_{trans} (green) denote magnetization component parallel and transversal to the field direction.

For the antidot arrays, the magnetic behavior changes not only with the dimensions of the nanoholes, but with thickness of the film. In samples with t_{Py} = 34 nm, the same behavior as the arrays with t_{Py} = 18 nm was found, as represented in Figure # 4.34. The same smooth transition was found around the switching field, indicating rotations of the spins before the irreversible transition. The shape of the loops at the e.a. and h.a. are almost the same, with a slight change in H_c, thus, as in the case of the antidot arrays with

t_{Py} = 18 nm, the magnetization reversal mechanism are the same along both axes, only changes insignificantly the anchoring force.

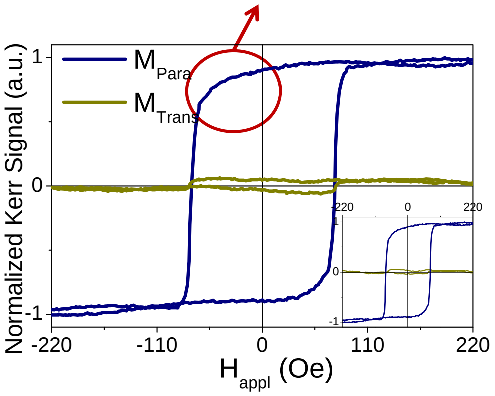
Smoother transition

Figure # 4.34. Kerr effect hysteresis loops along easy and hard (insets) axes of an antidot array with t_{Py} = 34 nm, D = 105 nm and d_P = 35 nm. M_{para} (blue) and M_{trans} (green) denote magnetization component parallel and transversal to the field direction.

But a different behavior was found in films with t_{Py} = 138 nm, where the irreversible process is visible thanks to the sharp transition around the switching field. In these films, Figure # 4.35, the reversal magnetization process seems to be led by DW motion. Even when the geometric properties of the arrays are different (d_P = 20 and D = 65 nm, d_P = 35 and D = 105 nm) the most important and predominant property is the thickness of the films. In this case, the antidot array behaves as a CTF, with the nanoholes almost closed. Nevertheless, one has to recall that underneath such almost continuous layer, the film still replicates the underlying pattern. This effect accounts rather well for the clear differences between H_c, as it is expected to increase with the size of the nanoholes.

The anisotropy found in the arrays measured with the 1 mm diameter of the laser's spot, Figure # 4.36, shows an isotropic behavior, which is supported by the same isotropic behavior of the remanence. These results were expected. From the deformed circular shape of the angular dependence (which coincides with the induced field of the sputtering system), is possible to deduce that a very small induced anisotropy is present due to the induced field during deposition. The change in H_c is lesser than 19%.

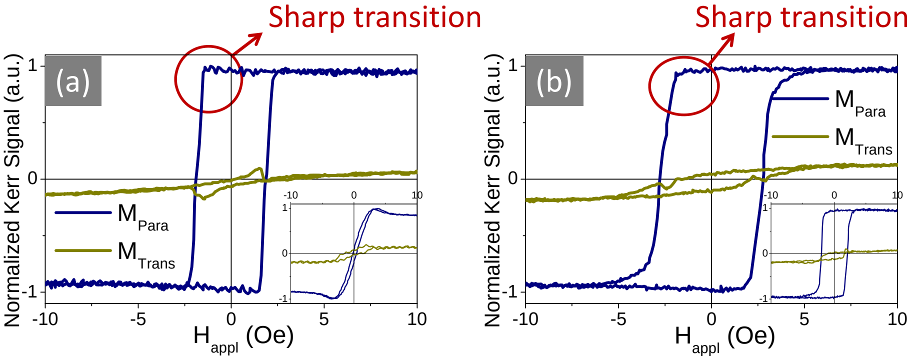

Figure # 4.35. (a) Kerr effect hysteresis loops along easy and hard (insets) axes of two antidot arrays with t_{Py} = 138 nm, and (a) d_P = 20 nm and D = 65 nm, (b) d_P = 35 nm and D = 105 nm. M_{para} (blue) and M_{trans} (green) denote magnetization component parallel and transversal to the field direction.

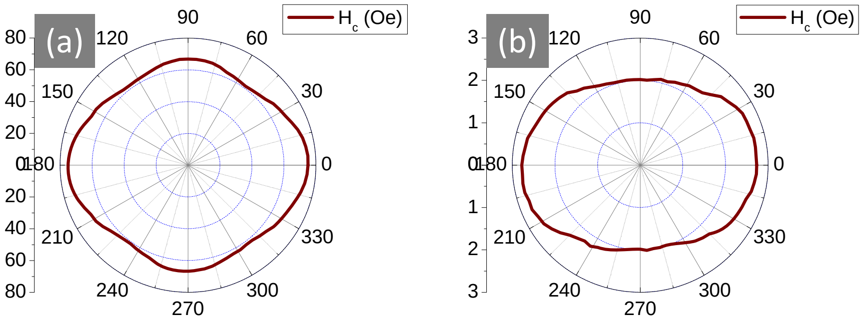

Figure # 4.36. Angular dependence of H_c of arrays with: (a) t_{Py} = 34 nm, d_P = 35 nm; (c) t_{Py} = 138 nm, d_P = 35 nm.

When comparing the angular measurement with the NanoMOKE system, where the diameter of the laser's spot lays around 3-4 µm, the expected result must depend on the number of the geometric domains measured. The contribution from different geometric domains can change according to the area covered by the laser's spot, as can be deduced by the different shapes and sizes of the folds in the angular dependence of H_c.

In the case that the laser covers only a few number of domains, the sample has a strong induced anisotropy due to the hexagonal lattice, which compete with the neighbors domains. The result of this competition will be the sum of the individual anisotropies, being enhanced in some cases, and in other cases some of the folds may be canceled.

As an example, Figure # 4.37 shows the H_c angular dependence of two arrays with $t_{Py} = 20$ nm. In the first case, this sum canceled one of the folds, resulting in a four-fold behavior. While in the second array, the laser covers almost one geometric domain, thus the anisotropy is similar to the six-fold behavior expected on a monodomain with hexagonal lattice. In these cases the change in H_c is higher than 45%.

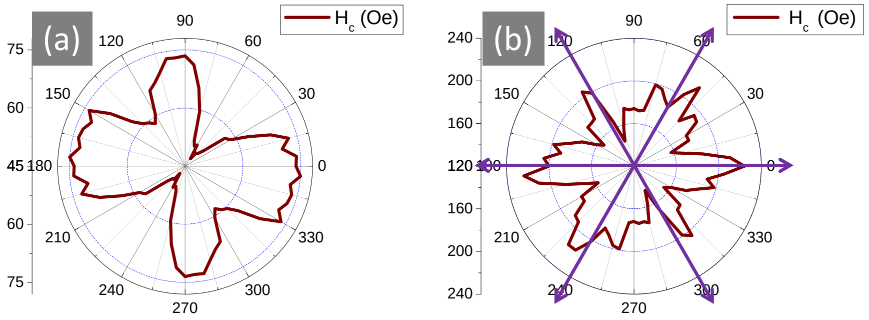

Figure # 4.37. Angular dependence of H_c of the arrays with $t_{Py} = 20$ nm, D = 105 nm and (a) $d_P = 35$ nm; (b) $d_P = 70$ nm. (Red line) experimental values; (purple lines) easy axes of the hexagonal lattice.

4.3.2 M-H Loops by Vibrating Sample Magnetometer

According to the results in the last section, two groups of arrays were determined according to t_{Py}. The M-H loops by VSM of each group with different d_P and thicknesses (D = 105 nm) are presented in Figure # 4.38 and Figure # 4.42. Each group corresponds to the following thicknesses:

1. $t_{Py} = 10$, 18 and 20 nm.
2. $t_{Py} = 34$ and 43
3. $t_{Py} = 138$ nm;

4.3.2.1 $t_{Py} = 34$, 43 and 138 nm

In order to observe in more detail the low-field region, magnetic saturation is not depicted in the figures.

The films with $t_{Py} = 138$ (Figure # 4.38e-l), in which the nanoholes are almost closed, approaches to the behavior of the CTF (higher M_r as can be seeing in Figure # 4.41c-d). As explained in the MOKE measurements, the magnetization reversal process takes place by DW motion in the plane of the film, in which Bloch-type walls are assumed, as can be observed from imaging by MOKE in Figure # 4.39. The image was taken in a demagnetized state, in a surface of 200 × 200 μm^2. The image shows the domain structure image for the antidot array with t_{Py} = 138 nm, in which topographic imperfections could act as nucleation sites for the creation of DW. The magnetic domains can be deduced by the color contrast. In these arrays a noticeable nearly reversible contribution when reaching the magnetic switching is observed. This behavior is the same found in Figure # 4.20, where a combination of DW motion and reversible rotations are present. Although the loops are very similar to the ones presented in the CTF (as the holes become closed), these arrays have coercivities defined by the geometry of the nanopores, increasing with d_P.

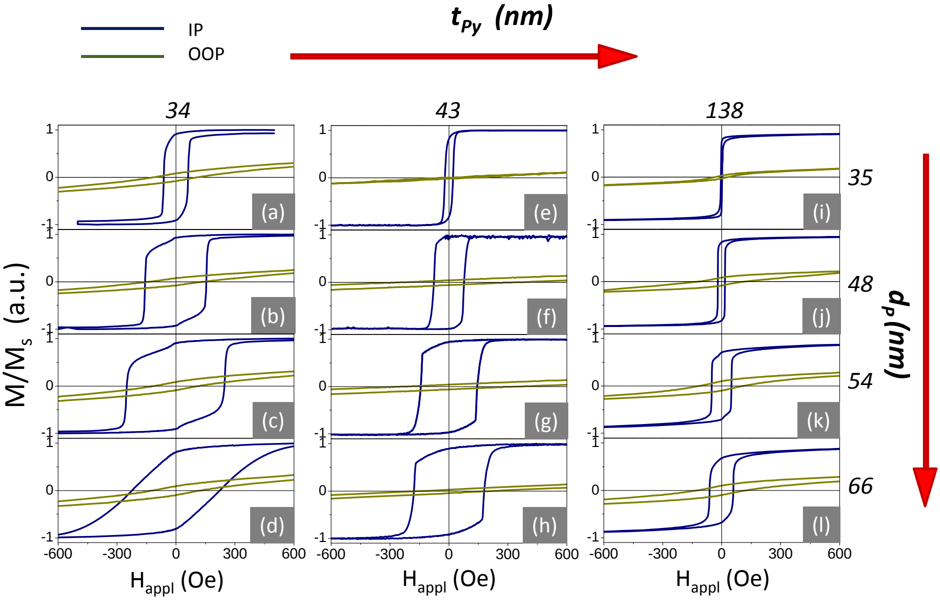

Figure # 4.38. VSM loops in IP and OOP configuration for arrays with different d_P and t_{Py} = 34, 43 and 138 nm.

For samples with t_{Py} = 34 and 43 nm, the aspect ratio, r, is close to 1, that is, the thickness of the films is similar to the average pore diameters, especially in the arrays with bigger d_P. In the arrays with bigger d_P, the dipolar interaction and the stray fields starts to be of the same order of magnitude. Therefore, the magnetization could lie OOP in order to reduce the energy, which is suggested in the film with r = 1.8 (d_P = 66 nm) in Figure # 4.38d. This magnetic behavior is similar to the one presented in Figure # 4.21, where the irreversible switching is carried out by irreversible rotations.

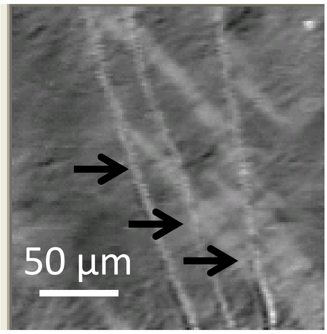

Figure # 4.39. Kerr effect image of antidot film with d_P = 54 nm and t_{Py} = 138 nm; the arrows indicate topographic imperfections, and the light-grey color correspond to the magnetic domains.

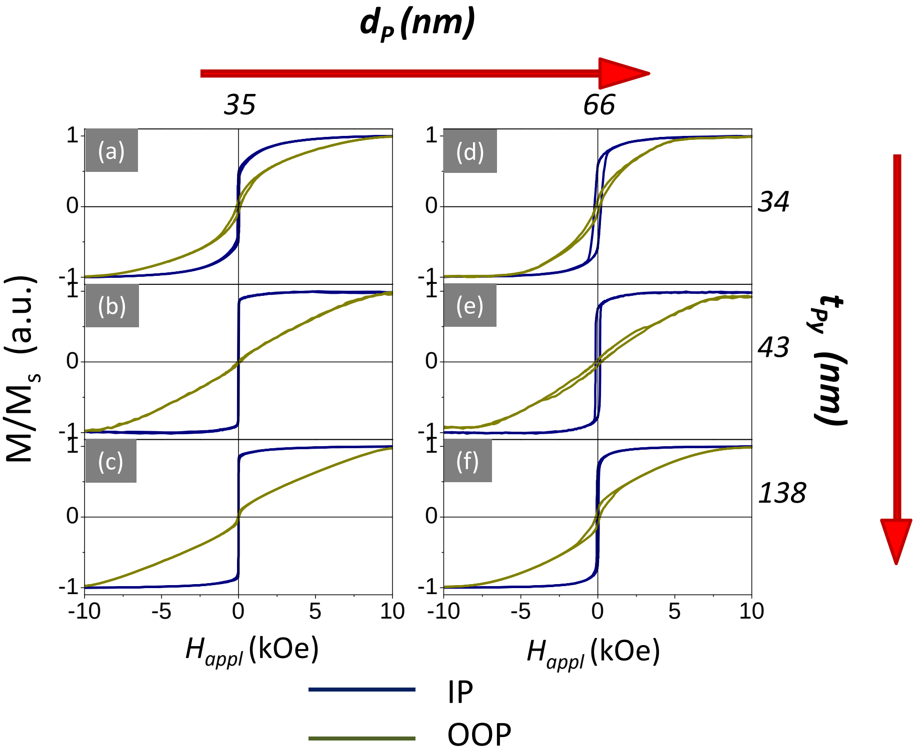

Figure # 4.40. M-H loops in IP and OOP configuration of the arrays with different d_P and t_{Py}.

The loops of the arrays with smallest d_P (Figure # 4.38a-e-f), present a square behavior, with the same magnetic response as the arrays with t_{Py} = 138 nm. In here the combination of DW motion and reversible rotations are the responsible of the magnetization reversal process, as explained in Figure # 4.20.

A different effect is present as a reversible contribution near the switching field (Figure # 4.38b-c-g-h). This effect is caused by a different mechanism, and it is more evident in samples of Figure # 4.38b-c, where a particular behavior is visible: a small jump after remanence, which disappears with d_P of 66 nm (Figure # 4.38 d). This effect is treated in Section 4.3.5.

In Figure # 4.40, the IP and OOP loops at higher fields are represented. In the arrays with t_{Py} = 34 nm and smaller d_P, the OOP loops have a hysteretic behavior with relative high susceptibility. The OOP-H_c is comparable to the IP-H_c, Figure # 4.41a- b, denoting an important OOP component; supported by the increases in M_r, Figure # 4.41c- d.

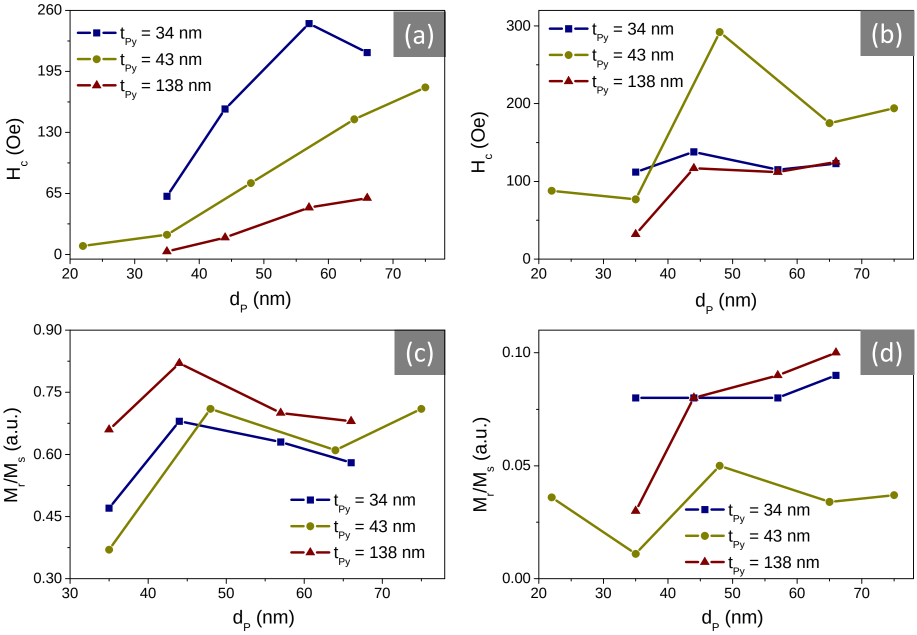

Figure # 4.41. H_c in (a) IP and (b) OOP configurations; normalized remanence in (c) IP and (d) OOP configurations, with t_{Py} = 34, 43 and 138 nm and different d_P.

In the case of the arrays with t_{Py} = 43 nm, the OOP M-H loops have a linear behavior, although with higher H_c, Figure # 4.41a- b. The only conclusion here is that these arrays have the magnetization along the IP of the sample but with an OOP component, much higher IP M_r.

The arrays with t_{Py} = 138 nm, the OOP M-H loops present on a large scale a h.a. magnetization with an almost linear behavior; although at lower fields, the loops have a hysteretic behavior with higher H_c, as can be seeing in Figure # 4.41a- b.

As explained in Section 1.4, the H_c increases with d_P due to the pinning effect (Inclusion theory), but in this work is possible to deduce that the H_c decreases with t_{Py}, approaching to the CTF behavior. The increases in IP M_r with t_{Py}, support the last statement (although suffer a reduction when comparing to the CTF). The increases of OOP H_c and OOP M_r in comparison to the CTF, denotes the presence of an important OOP component in the arrays.

4.3.2.2 t_{Py} = 10, 18 and 20 nm

For these samples, in turn, as the thickness decreases a significant reduction of the susceptibility, as well as of the IP remanence, were observed. In samples with t_{Py} = 18 and 20 nm, a more complex magnetization reversal process is present, where both, DW motion and spin rotations, are involved when magnetizing the sample in the IP configuration. As d_P increases, the magnetic behavior is similar as in the arrays in Figure # 4.21, where irreversible rotations in a *non-homogeneous magnetization distribution* take place, originated by the stronger local dipolar interactions around the nanoholes.

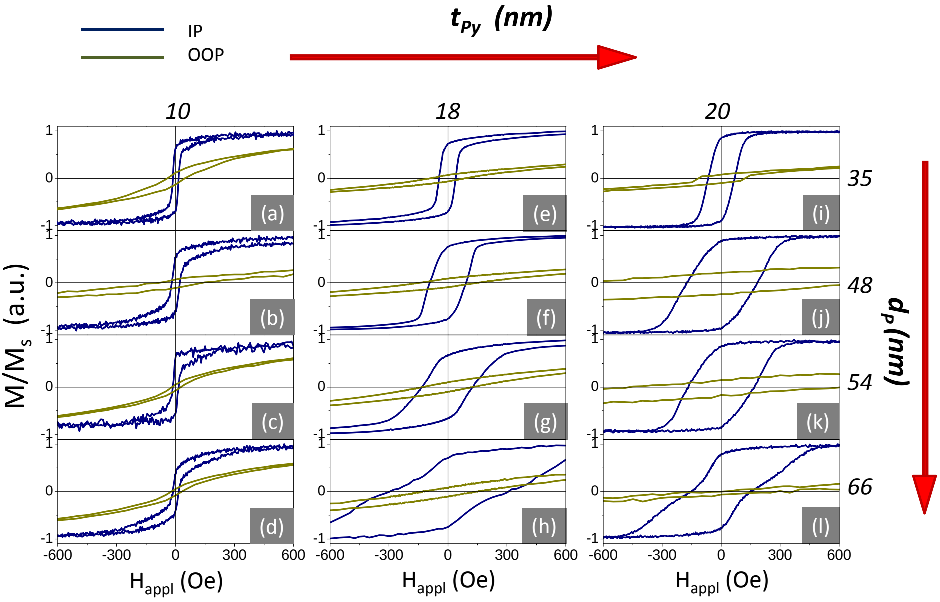

Figure # 4.42. VSM loops in IP and OOP configuration for arrays with different d_P and t_{Py}.

In samples with t_{Py} = 10 nm, the films are more inhomogeneous due to the topography of the AAM, which produce an irregular growth of the magnetic film, presenting lower values of H_c. The loops of the arrays with d_P = 35, 48, 56 nm (Figure # 4.42a-b-c) have the same behavior as the samples in Figure # 4.20, DW motions during the magnetization reversal, with reversible rotation when reaching saturation. In the array with d_P = 66 nm, the reversal process presents rotations when the field reverses, instead of DW motion, and reversible rotations when reaching saturation. This sample presents a deductible *non-homogeneous magnetic structure*, due to the lack of squareness in the loop and lower M_r, but this sample is deeply studied in Section 4.4.

Sample with t_{Py} = 18 nm and 20 nm behaves in a similar way, although with higher values of H_c in the latter (Figure # 4.44a). With bigger d_P, as in the case of t_{Py} = 18nm studied in Section 4.2.4, the magnetic behavior becomes a bi-phase magnetic behavior, Figure # 4.42l, caused by the same dipolar effect.

The OOP M-H loops show that for the arrays with smaller d_P and t_{Py} (Figure # 4.43a-b-d-e) the OOP component is extremely important, having almost the same magnetization reversal as the IP component. However, the array with d_P = 66 and t_{Py} = 20 nm, Figure # 4.43f, has a linear OOP M-H loop.

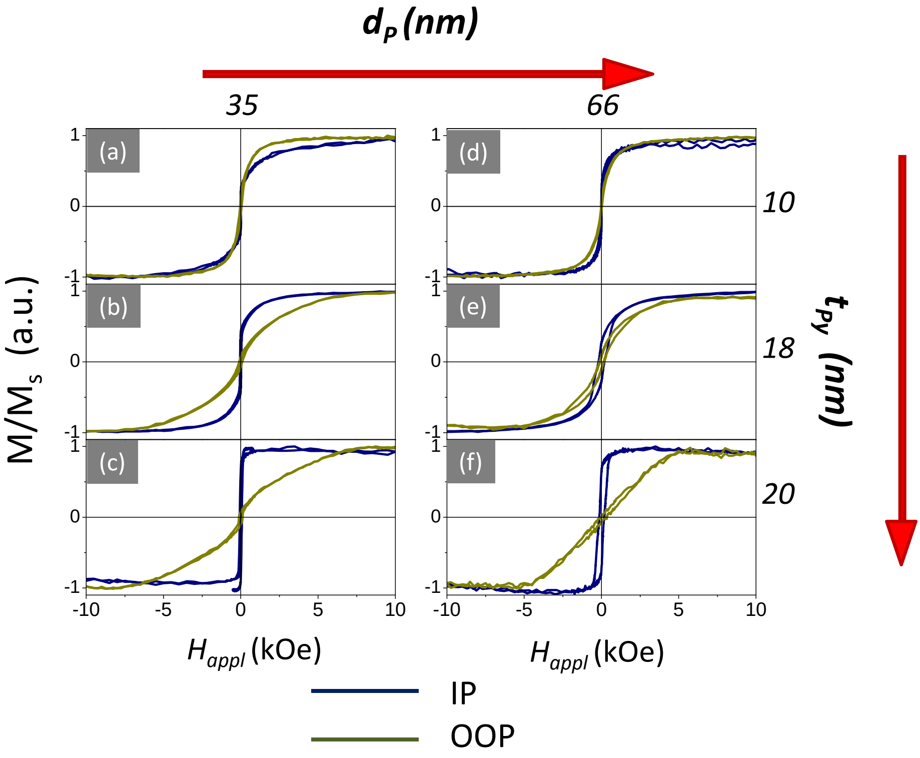

Figure # 4.43. M-H loops in IP and OOP configuration of the arrays different d_P and t_{Py}.

In Figure # 4.44 it is possible to observe that the IP- and OOP H_c increases with d_P. The OOP component is affected when the applied field has the OOP configuration, demonstrating that the spin configurations have an important OOP component. This is supported by the OOP M_r values, which are much higher when comparing to the CTF.

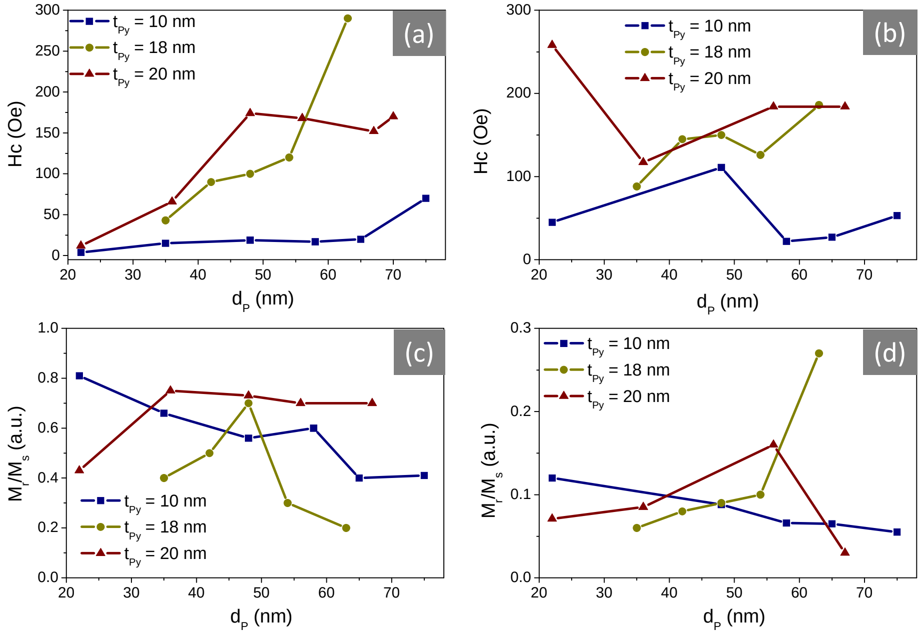

Figure # 4.44. H_c in (a) IP and (b) OOP configurations; normalized remanence in (c) IP and (d) OOP configurations, with t_{Py} = 10, 18 and 20 nm and different d_P.

4.3.3 Reversal Curves

As explained in Chapter 2, the reversal curves discriminates the irreversible and reversible process in the magnetization reversal. From these curves, some important information about their mechanism can be obtained.

According to the grouped samples, the reversal curves and Switching Field Distribution (SFD) of the arrays presented in this study are the ones with t_{Py} = 10, 20 and 43 nm, corresponding to the first and second groups. The reversal curves of the arrays with t_{Py} of 138 nm, present similar behavior as the CTF.

4.3.3.1 t_{Py} =10 nm

An example of the reversal curves, Figure # 4.45, shows the reversal curves of an array with t_{Py} = 10 nm and d_P = 66 nm. In accordance with the M-H loop by VSM, Figure # 4.42d, the reversible processes seems to be predominant in the magnetization reversal process, ascribed to reversible rotations, as explained before.

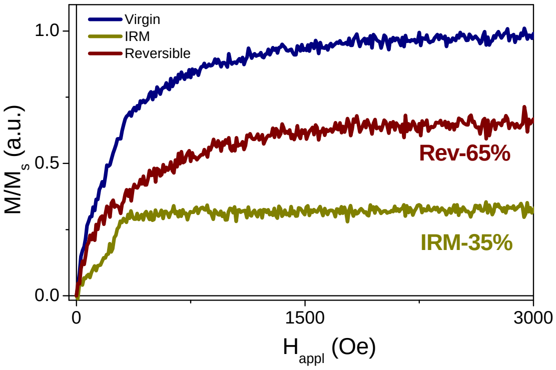

Figure # 4.45. IP-Virgin, IP-IRM and IP-Rev curves of the antidot array with t_{Py} = 10 nm and d_P = 66 nm.

In the case of smaller d_P, the irreversible processes are more predominant, as shown in the loops in Figure # 4.42a-b-c, where the reversible process is carried out by DW motion when the field reverses. The IP-Virgin curves, Figure # 4.46a, are in accordance with the M-H loops. The curves present an irreversible transition at lower fields; as d_P increases, these fields increase, and the susceptibility decreases. The decreases in the susceptibility in the Virgin curves are due to the OOP component present in the arrays, which increases with d_P.

In the case of the bigger d_P, the IP-virgin shows a slightly bi-phase behavior, as in the M-H loop in Figure # 4.42d.

The percentage of IP-IRM noticeably decreases with increasing d_P, Figure # 4.46b. This is a consequence of decreasing the magnetic material in between the nanoholes, where a stronger pinning is produced; thus the magnetization reversal occurs by reversible rotations around the holes. The abrupt raise in the IP-IRM percentage in d_P = 75 nm denotes a strongest pinning effect.

The values of SFD denote the “number of particles per switching field”; in this kind of samples the number of particles can be compared to the “volume of the magnetic material”, since is a nano-patterned thin film system instead of nanoparticles. This value denotes how much material reverse with the field. In Figure # 4.46c the SFD curve indicates that with increasing d_P, a higher field is needed to switch the magnetization of the arrays. This is totally in accordance with the anchoring of the spins due to the dipolar effect around the nanoholes.

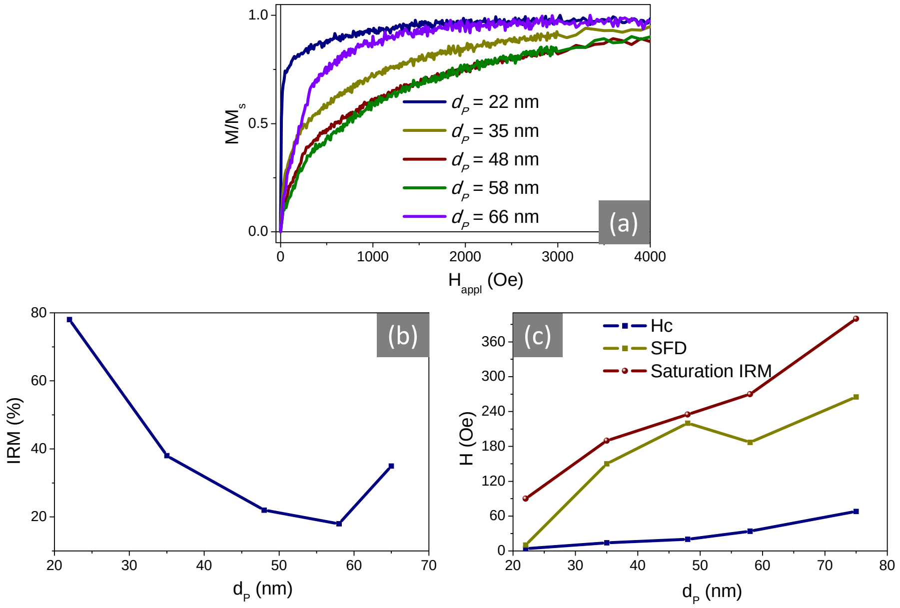

Figure # 4.46. (a) IP-Virgin curves; (b) IP-IRM % and (c) H_c, SFD and saturation field of the IRM curve, of the antidot arrays with t_{Py} = 10 nm.

The saturation field of the IRM curve indicates the field at which the IRM curve saturates. The increases of this field with d_P indicates the increase in the pinning effect due to the nanoholes. These values are not consistent with the values of H_c, which are much lower and almost constant with d_P. This inconsistency could be explained by the material inside the wall of the pores, which have an OOP component creating higher dipolar interactions, which anchor the spins around the nanoholes.

In the case of d_P = 66 and 75 nm, Figure # 4.45, the saturation IRM increases markedly, which is in accordance with the higher IRM percentage and the stronger pinning effect. In the OOP-IRM, the percentages of irreversibilities are around 10% in all the arrays, indicating that the rotations are the preferred mechanism for magnetization reversal. As an example in Figure # 4.47, is represented the OOP reversible curves of an antidot array with d_P = 22 nm. Nevertheless, these curves are not in accordance with the OOP M-H loops, Figure # 4.43, where the magnetization has the same behavior as the IP loops.

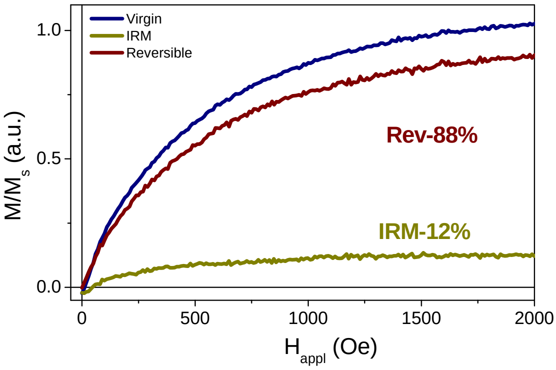

Figure # 4.47. OOP -Virgin, OOP-IRM and OOP-Rev curves of the antidot array with t_{Py} = 10 nm and d_P = 22 nm.

4.3.3.2 t_{Py} =20 nm

An example of the reversal curves of the arrays with t_{Py} = 20 nm, Figure # 4.48, shows how the reversible processes changes with d_P and t_{Py}. First, as d_P increases the irreversible processes increase, and with it the saturation field. In the smallest d_P, the IRM curve has an irreversible jump at lower field, then rotations take place until the magnetization lie parallel to the applied field. These curves support the magnetic behavior of the M-H loop in Figure # 4.42.

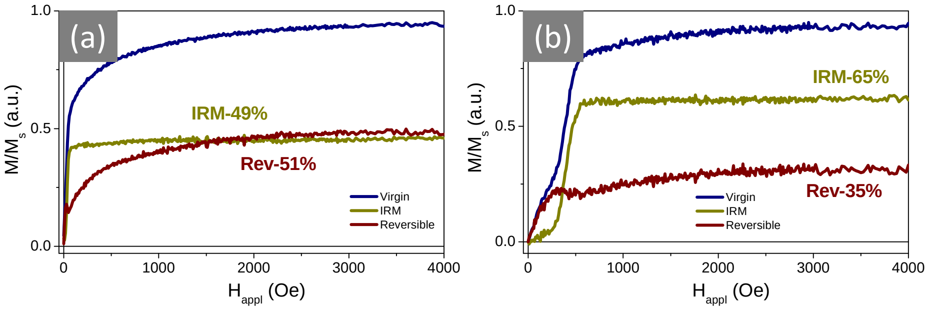

Figure # 4.48. IP-Virgin, IP-IRM and IP-Rev curves of the antidot array with t_{Py} = 20 nm and (a) d_P = 22 nm, (b) d_P = 66 nm.

In general, the Virgin curves, Figure # 4.49a, suffer several changes in comparison to the t_{Py} = 10 nm. As d_P increases, these curves saturate at higher fields and with an apparent bi-phase behavior, which are consistent with the loops presented in Figure # 4.42.

The IP-IRM percentages, Figure # 4.49b, increases and then decreases with d_P, with a maximum peak at d_P = 48 nm. From this d_P, the reversible processes are leading by irreversible rotations instead of DW motion, due to the stronger pinning effect and smallest distance between the nanoholes, as explained in 4.3.2.2.

In the case of these arrays, the SFD and the saturation field of the IP-IRM, increase d_P, Figure # 4.49c. The material inside the wall of the pores (with an OOP component), see Section 4.2.5, which creates a second-magnetic phase, produce a stronger dipolar effect, increasing the field needed to reversed the magnetic material of the arrays. The increases of the values of the saturation field of the IRM curves, is coming from the irreversible rotations. The smaller distance between the nanoholes cannot hold a DW. This statement is supported by the constant H_c for d_P larger than 48 nm.

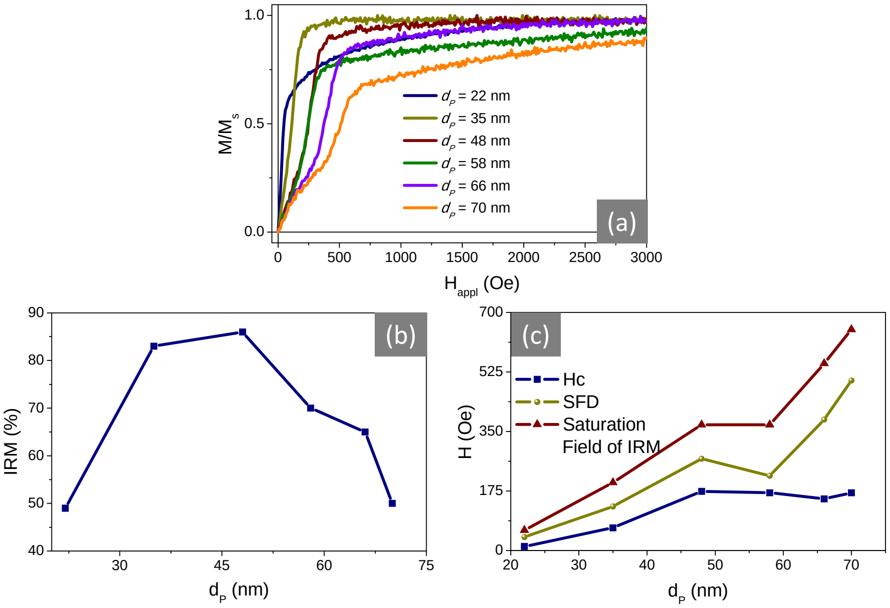

Figure # 4.49. (a) IP-Virgin curves; (b) IP-IRM % and (c) Hc, SFD and saturation field of the IRM curve, of the antidot arrays with t_{Py} = 20 nm.

In the case of the OOP reversible curves, a higher percentage concerning the reversible part is visible, which demonstrates that the reversible rotations are the main magnetization switching mechanisms. The highest OOP-IRM percentage is present in the array with d_P = 35 nm, Figure # 4.50; from this d_P, all the OOP-IRM curves have smaller percentages.

A strange behavior happens in the OOP-IRM curve when d_P is the smallest: a vertical jump is present in the OOP-Virgin and OOP-IRM curves at non-zero field. Then the reversible curve gets higher. This vertical line denotes an irreversible jump which could correspond to the material inside the wall of the pores with a strong OOP component, Section 4.2.5.

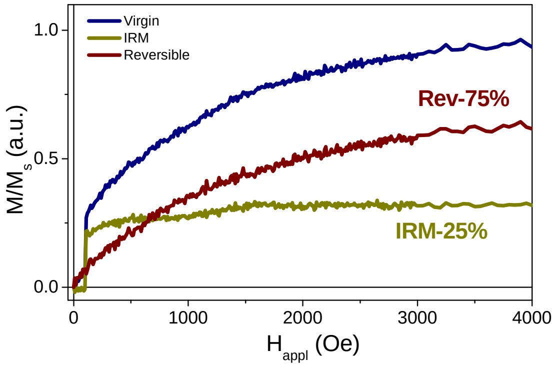

Figure # 4.50. OOP -Virgin, OOP-IRM and OOP-Rev curves of the antidot array with t_{Py} = 20 nm and d_P = 35 nm.

4.3.3.3 t_{Py} =43 nm

This t_{Py} belongs to the second group, in which the magnetization reversal shows a more square behavior, Figure # 4.38e-h, so the magnetization reversal process is evidently leading by DW motion in the arrays with smaller d_P, and irreversible jumps in bigger d_P. This behavior is observed in the reversible curves in Figure # 4.51, where the IRMs curves are predominant in bigger d_P. This is consistent with the fact that the spins rotate to get aligned with the applied field, until reaching the saturation, as can be seeing in the Virgin curve in Figure # 4.52a.

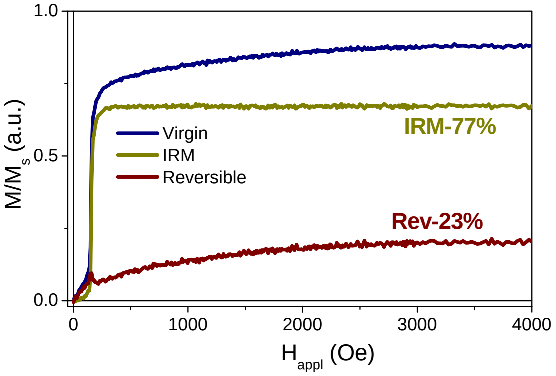

Figure # 4.51. IP-Virgin, IP-IRM and IP-Rev curves of the antidot array with t_{Py} = 43 nm and d_P = 66 nm.

The smallest d_P show higher IRM percentages, Figure # 4.52b, due to the DW motion. The Virgin curves in Figure # 4.52a are a clear evidence of the irreversibility of the arrays, where an initial irreversible jump reverses the overall magnetization. As in the last case (t_{Py} = 20 nm), the H_c, SFD and saturation field of the IRM curves, increase with d_P.

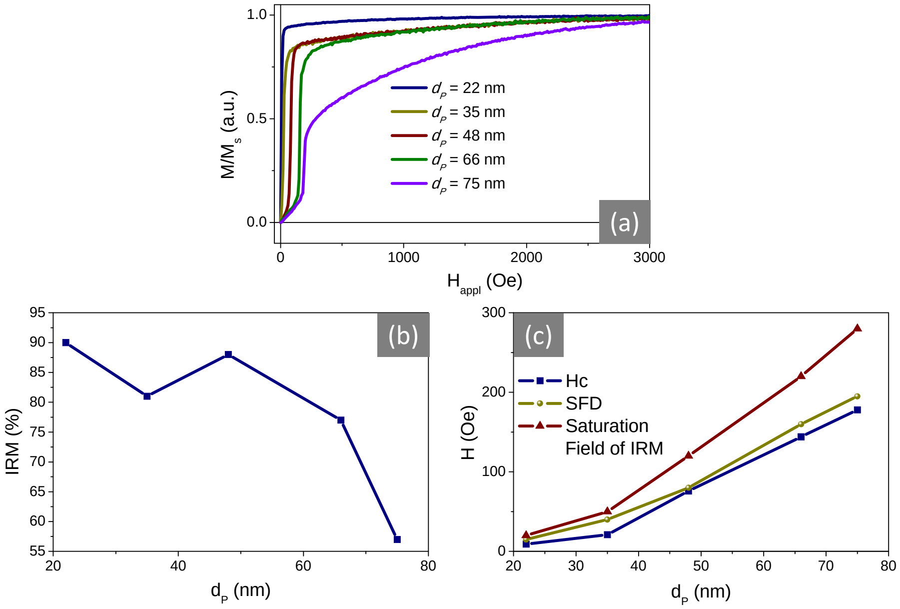

Figure # 4.52. (a) IP-Virgin curves; (b) IP-IRM % and (c) H_c, SFD and saturation field of the IRM curve, of the antidot arrays with t_{Py} = 34 nm.

The OOP reversal curves of the arrays with d_P = 22 nm shows that the OOP component inverts the magnetization by reversible rotations, although an irreversible process is present due to the OOP component present in the arrays.

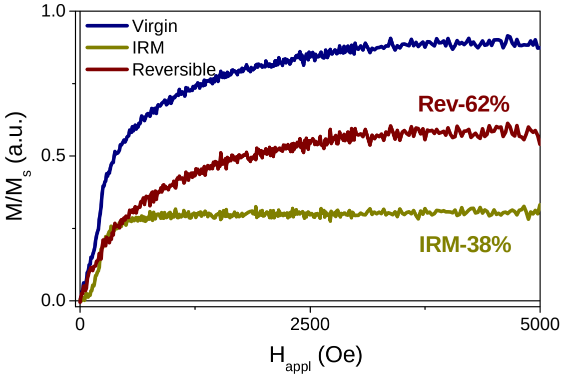

Figure # 4.53. OOP -Virgin, OOP-IRM and OOP-Rev curves of the antidot array with t_{Py} = 34 nm and d_P = 22 nm.

4.3.4 Surface Characterization vs. Bulk Behavior

As in Section 4.2.4, a comparison between the VSM and MOKE loops was made. The selected loops are presented in Figure # 4.54 as a function of d_P and t_{Py}.

MOKE and VSM M-H loops are very similar for samples with higher thicknesses, and only coercivity takes typically smaller values for VSM measurements suggesting a slightly harder reversal mechanism on top of films.

Notice that for the films with the smallest thickness (t_{Py} = 10, 18 and 20 nm) and bigger d_P, a different loop shape is observed with a strong bi-phase magnetic behavior.

In the special case of the arrays with t_{Py} = 10 nm, the magnetic configurations around the nanoholes could be similar to the ones presented in Section 4.2.4, where the amount of material in between the nanoholes decreases, and a strong IP magnetization produces the dipolar effect around the nanoholes creating this magnetic configuration, Figure # 4.32. As d_P increases, the MOKE loops show a more pronounce biphase behavior. As explained in Section 4.2.5, the material inside the wall of the pores could be the responsible of this harder-magnetic phase. Due to the bigger d_P and the lower thickness, the MOKE laser is able to measure the magnetic behavior of the material inside the pores, displaying this second magnetic phase. The same effect was observed in the antidot arrays with t_{Py} = 18 nm, where the MOKE's laser penetrates beyond the films.

In the arrays of t_{Py} = 34, 43 and 138 nm (except with d_P = 66 nm of the first thickness), there is a significant difference in the shape of VSM and MOKE loops after the remanence, near the switching field. VSM hysteresis loops show the contribution of a second softer magnetic phase, not observed by MOKE (even though the whole surface was checked), which suggests that the bulk and the surface have separate behaviors. This issue is treated in the next section.

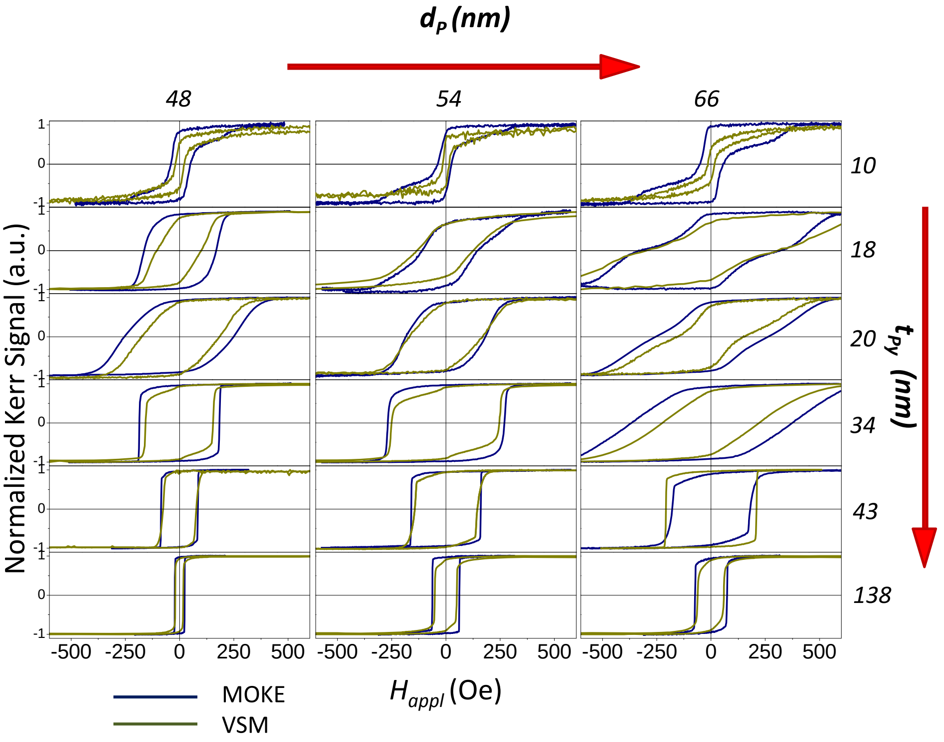

Figure # 4.54. VSM and MOKE loops of selected antidot arrays.

4.3.5 Remarks

In another study [67], a different magnetic behavior was found in arrays with different thicknesses, reflecting the progressive evolution of the arrays into a more homogeneous medium (decreasing d_P) with lesser Porosity. In a similar way, the arrays with higher thickness and reducing nanoholes, approach to a CTF magnetic behavior, adapting the medium to the DW propagation, as pointed out in Section 4.3.2, assumed Bloch-type walls.

The surface magnetization is an important feature of the arrays, which depends on the geometric properties of the nanoholes. The MOKE loops are expected to have similar behavior (at the surface of the arrays) if d is similar, no matter the thickness of the films and d_P (the diameter of the AAM). As explained in Section 3.X the laser's penetration depth depends on d, so a comparison between the M-H loops by MOKE between the arrays with the same d but different t_{Py} and d_P was made.

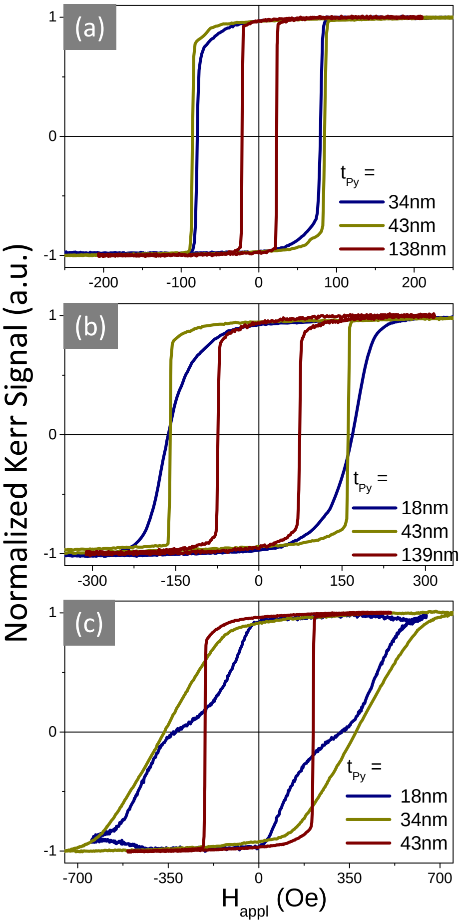

Figure # 4.55. MOKE loops of arrays with different d_P and t_{Py} but almost the same d, (a) d = 27 nm; (b) d = 43 nm; and (c) d = 56 nm.

The M-H loops by MOKE with the same d (± 1 nm) but different d_P and t_{Py}, are represented in Figure # 4.55. In the loops with d = 27 nm, Figure # 4.55a, the magnetic behavior presents an irreversible mechanism, with reversible rotations near the switching field in the three samples. The differences in H_c are minimal in the case of t_{Py} = 34 and 43 nm (very similar), and bigger in the case of t_{Py} of 138 nm, where the H_c is much smaller. No matter the thickness and the initial pore diameter (d_P), the overall magnetization are similar, although the H_c increases with t_{Py}.

In Figure # 4.55b, the loops are quite different. In these arrays the magnetization reversal mechanism changes, showing lower susceptibility in the thinnest film, but similar H_c with the array with t_{Py} = 43 nm. As presented before, the H_c in the array with t_{Py} = 138 nm, is lower.

Figure # 4.55c shows the arrays with d = 56 nm. Bigger differences are visible in these loops. The array with 18 nm of t_{Py}, is completely different, due to the fact that the MOKE measurements is more sensitive to the OOP contribution from the material inside the wall of the pores, as studied in Section 4.2.5, presenting a bi-phase behavior. Nevertheless, the magnetic behavior of the array with t_{Py} = 34 nm, has almost the same susceptibility and the H_c coincides with the hard-magnetic phase of the thinner array.

Even when the MOKE's laser measures almost the same depth (in the case of similar d), the effect of the material inside the pores' wall (at the bottom) plays an important role in the overall magnetic behavior. The differences between the arrays with the same d, are due to this assumption, creating interactions between the layers at the bottom and the surface of the films.

To probe this, a particular case was analyzed. The arrays with t_{Py} = 34 and 43 nm, where a second contribution near the switching field appears in the VSM loops. The penetration depth of the MOKE's laser of the array with d_P = 56 nm and t_{Py} = 34 nm (called A for this analysis), is approximately 19 nm. Thus the M-H loop by MOKE of this sample correspond to a layer with thickness of 19 nm from the surface (called layer B); while the M-H loop from the VSM correspond to the bulk system, see Figure # 4.56. The layer at the bottom (layer C), the remaining 15 nm, should have a similar M-H loop by MOKE as the sample with d_P = 56 nm and t_{Py} = 18 nm.

The division of the layer is represented in Figure # 4.56. We can assume that the overall layer of 35 nm behaves as the combination of 2 Py layers.

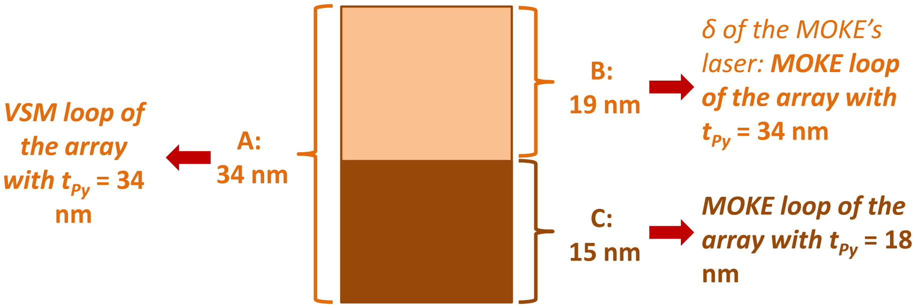

Figure # 4.56. Division of a mono-layer of Py with t_{Py} = 34 nm and d_P = 56 nm.

The magnetic behavior of each layer, B and C, are different as shown in Figure # 4.57a and b. If the layer behaves as a bilayer of Py, the sum in the correct proportion of the MOKE loops of B + C should be similar to the VSM loop of the layer A. The bottom, layer C, has the bigger holes and a larger influence from the material inside the pores, while the top, layer B, the holes are smaller, and the behavior is similar to a CTF.

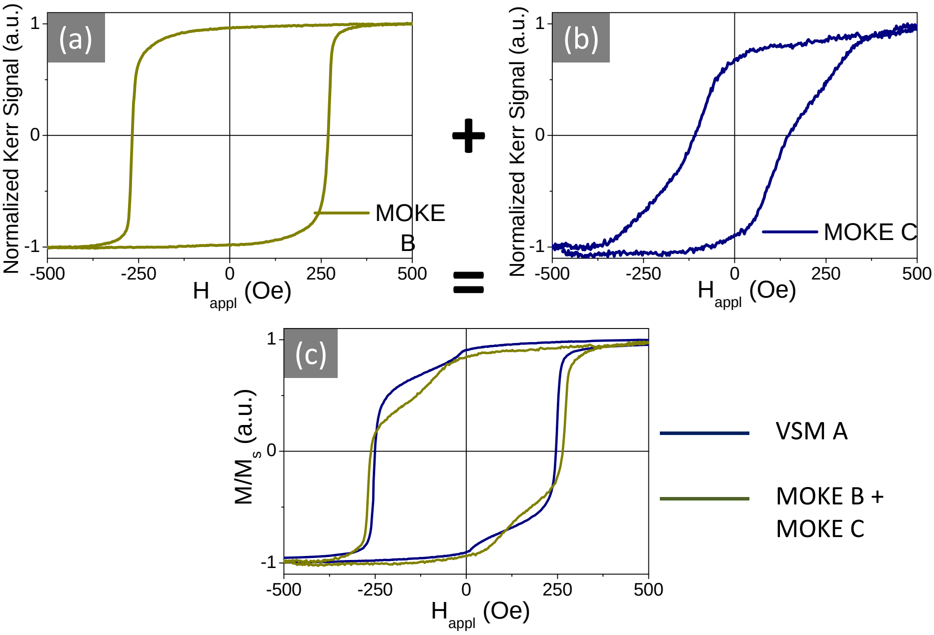

Figure # 4.57. M-H loops by MOKE of (a) layer A and (b) layer B. (c) Sum of MOKE loops = VSM loop

From Figure # 4.57c is possible to observe that the sum of the MOKE loops (t_{Py} 34 + t_{Py} 18) behaves in a very similar way as the VSM loop of the whole sample. The small jump near the switching field occurs at approximately the same field, and the coercivities are quite similar, 248 and 264 respectively. The small differences arise from the average character of the VSM measurements.

4.4 X-RAY PHOTOEMISSION ELECTRON MICROSCOPY

Selected antidot arrays samples show clearly interesting behaviors. Some of these samples were further measured in the XPEEM in order to observe the complex magnetic domain structures [158] and to deepen the knowledge of the magnetization reversal processes depending on the geometric parameters (keeping D constant). In addition, this technique enables the experimental determination of the magnetization reversal process with in-plane magnetic sensitivity, not only over a relative large area, but independently over different local geometric domains [146,159].

The magnetic results were compared with the magnetic behavior from VSM measurements and the surface magnetic characterization performed with MOKE. It should be noted that both, MOKE and XPEEM measurements, are comparable because both represent a measure of the surface magnetization with a penetration depth of around 15 nm and 10 nm, respectively, for CTF. Although both have a comparable field of view (the effective measured surface ≈ 5μm), the MOKE system measures the average magnetization of the total hexagonal arrangement inside an ordered geometric domains, recall Section 4.1.2.1, meanwhile the XPEEM has a spatial resolution of approximately 30 nm.

The study has been focused onto particular samples with specific magnetic behavior according to previous data obtained by MOKE. Two samples with different d_P and t_{Py}, were studied because of their particular geometry, dimensions and different aspect ratio, as indicated in Table # 4.9.

Table # 4.9. Antidot arrays with D = 105 nm for XPEEM experiment.

	d_P (nm)	**d (min)**	**t_{Py} (nm)**	**r**	**r’**
Sample A	65	62	10	6.5	4.2
Sample B	22	16	20	1.1	4.3

X ray Absorption Spectroscopy (XAS) for the ferromagnetic element of Ni, taken at the energy levels $L_{2,3}$ are presented in Figure # 4.58; making the comparison with the spectra in Figure # 2.22, where are shown the oxide form of Ni, shows that the samples present no detectable oxidation.

For all the measurement, the X-ray energy was tuned to the Ni L_3 edge, since Ni is the predominant element of Permalloy.

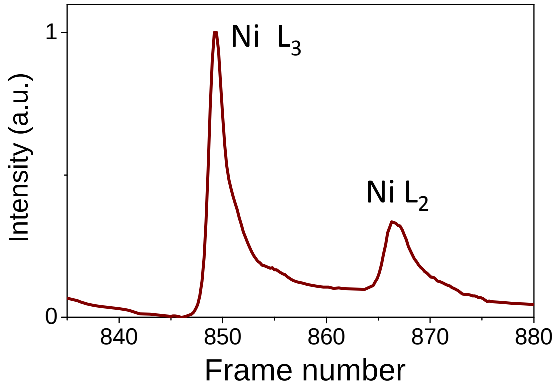

Figure # 4.58. XAS scan at the $L_{2,3}$ Edges of Ni.

4.4.1 Antidot Array with High Aspect Ratio

MOKE hysteresis loop of sample A (r = 6.5) is observed in Figure # 4.59a, with H_c = 53 Oe and saturation field of 380 Oe. As previously discussed (Section 4.3.4), two magnetic phases are deduced from the 2 large irreversible jumps, thus two regions can be identified: 1. higher susceptibility, from approximately 10 to 100 Oe; and 2. lower susceptibility, from 300 to 380 Oe; these regions can be ascribed to two well magnetic regions with different magnetic response. The irreversible jumps, which occurs approximately at ≈ 10 Oe (dash line #1) and 300 Oe (dash line #2), correspond to fractions of 2.5% and 85% regarding the total magnetization reversal for the soft and hard phases, respectively.

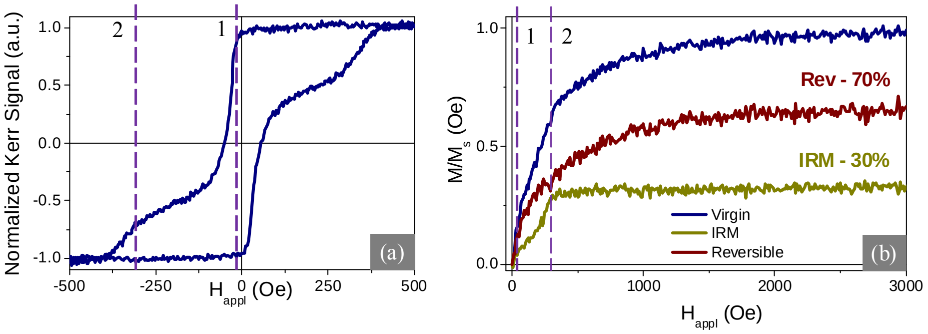

Figure # 4.59. (a) MOKE hysteresis loop and (b) VSM magnetization curves of sample A.

Figure # 4.59b shows the Virgin, IRM and Reversal curves with their respective percentage from the total magnetization signal of the Virgin curve. The reversible curve is predominant in the magnetization reversal process, indicative of rotations along the whole switching process. In the IRM curve is appreciable the two irreversible jumps observed in the Kerr loop (dash lines #1and #2). In between these two regions, is visible the change in susceptibility of the reversal process, which correspond to the two magnetic phases. From 0 to 300 Oe, the IRM curve correspond to the 50% of the whole process in which the domains reverse, but from 300 Oe the IRM curve saturates, and the domains are further aligned through rotation of the spins.

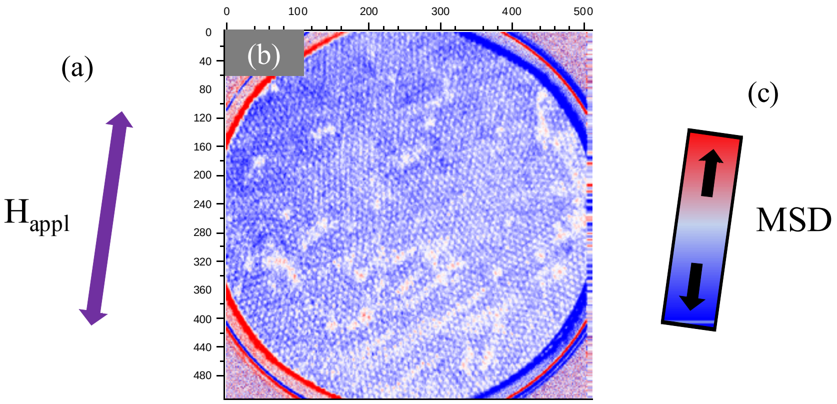

Figure # 4.60. (a) Direction of the applied field during the measurements and at remanent state; (b) XMCD image of sample A (at Ni energy); (c) the magnetization sensitivity direction (MSD).

This sample was placed in the Sample Holder I, Table # 2.1, and the experiment was divided in two parts:

1. Under applied magnetic field during the measurements: the sample was first nearly saturated at the maximum field, and finally increasing DC magnetic fields were applied where the images were taken. The fields go from 0 to +135 Oe.

2. *At remanence*: After saturating the sample (with the corresponding maximum applied field of -405 Oe, Table # 2.1), a small field is applied and subsequently removed after which the image is measured. Next, a larger field is applied and subsequently removed, after which the next image is measured. The magnetic field goes from -405 Oe (negative direction, represented by the blue color in the red-blue scale) to + 405 (positive direction, represented by the red color in the red-blue scale)

The direction of the applied field and the magnetization sensitivity direction (MSD: corresponding color scale with the direction of the magnetization) are shown in Figure # 4.60.

4.4.1.1 With applied magnetic field during the measurements

A quantitative analysis of each XMCD image can be performed to estimate the net magnetization under given applied field by ascribing locally the corresponding magnetic moment. Integrating this value over an area (the entire field of view of 5 µm) enables the evaluation of the corresponding hysteresis loops.

Figure # 4.61 shows the hysteresis loop of sample A obtained after quantitative analysis of individual XMCD images taken under increasing applied magnetic field (blue curve) and the symmetric curve (green curve) is the mirrored XPEEM curve for explanatory purposes. The images with the corresponding fields are presented in Table # 4.10.

Table # 4.10. Applied magnetic field with the corresponding images.

Image	**Magnetic Field (Oe)**
a	-135.0
b	+11.8
c	+20.0
d	+22.6
e	+26.7
f	+35.6
g	+53.8
h	+89.9
i	+135.6

From the first XMCD image in Figure # 4.61 which corresponds to -135 Oe (after saturation at -405 Oe) to the second one at almost zero magnetization, the net magnetization changes drastically (from blue to mix of blue, red and white) with an important irreversible jump (at around 20 Oe). The mix of colors denotes the existence of regions with negative, positive and perpendicular magnetization. At this point, the magnetization almost reaches H_c of the sample, showing the first step of the reversal process.

The following images correspond to increasing applied field: one observes a significant irreversible magnetization process at around 20 Oe and then magnetization grows with more reduced susceptibility up to the maximum field at +135 Oe. Note that the reversing magnetization at local regions mimics the geometric domains until magnetic saturation.

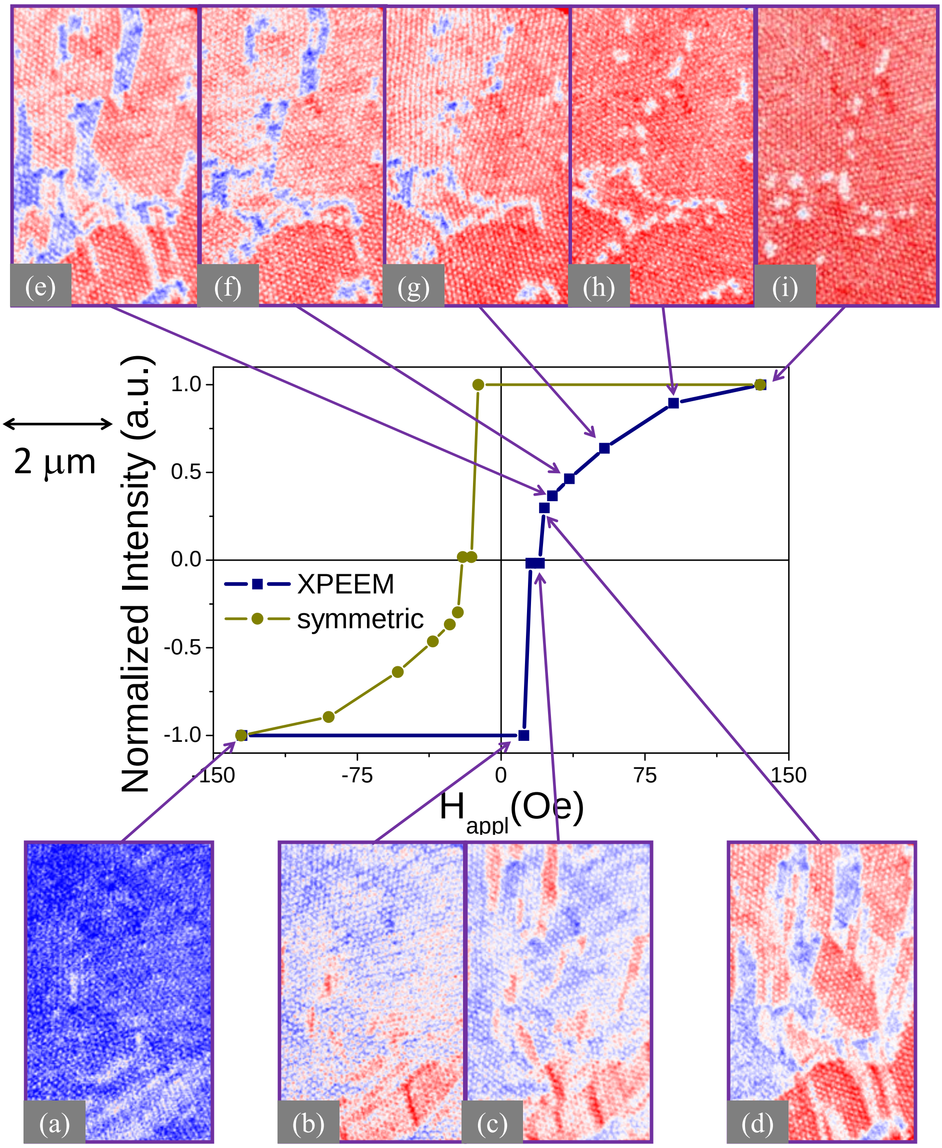

Figure # 4.61. Hysteresis loop of sample A as deduced from XMCD images after applying a negative field of -405 Oe and then shifting the applied field to different values (blue curve) and the mirrored XPEEM curve (green curve). The color scale with the magnetization direction is defined in Figure # 4.60.

The XMCD images corresponding to the hysteresis loop show the *non-homogeneous magnetic structures* created during the reversal magnetization process: first, at lower fields, nucleation of DWs at different sites of the samples is visible, mostly at some defects [35,160], as shown in Figure # 4.62 left, in which the image correspond to (c) in

Figure # 4.61. With fields high enough, short-range displacements of DWs occurs (with sizes of 1 μm or shorter), increasing the domains size aligned towards the positive direction inside a corresponding geometric domains, Figure # 4.62 right. The increase of domains parallel to the positive field through adjacent geometric domains requires higher fields to overcome the dislocations.

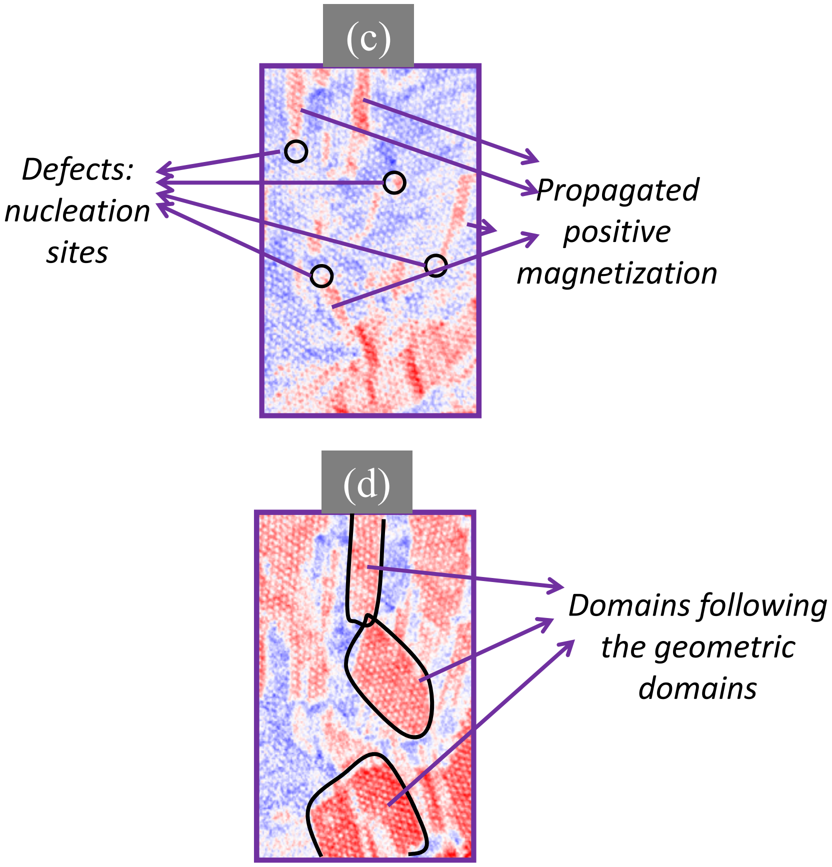

Figure # 4.62. Defects and propagated magnetic domains in the corresponding images "c" and "d" of Figure # 4.61.

A rough comparison between hysteresis loops obtained by XPEEM with the MOKE measurements in Figure # 4.63, indicates that the XPEEM maximum applied field only enables the study of the irreversible magnetization process of the softer phase, i.e. the magnetization after the first irreversible jump (from 0 to 135 Oe). From this saturated image, Figure # 4.63c, we can see that the non-inverted regions correspond to very small regions with white colors, possibly corresponding to the OOP component, being the hard-magnetic phase. In agreement with this statement, as explained in Figure # 4.31, the material inside the wall of the pores may be the source of this OOP component.

Nevertheless, the saturation of the sample in both systems (XPEEM and MOKE) was reached approximately at the same field, +405 Oe, as can be seen in Figure # 4.63a and d. The irreversible processes of the harder phase are attained by MOKE and high-field reversible processes are only achieved by VSM. The image corresponding to the H_c in the XPEEM loop is represented by Figure # 4.63d.

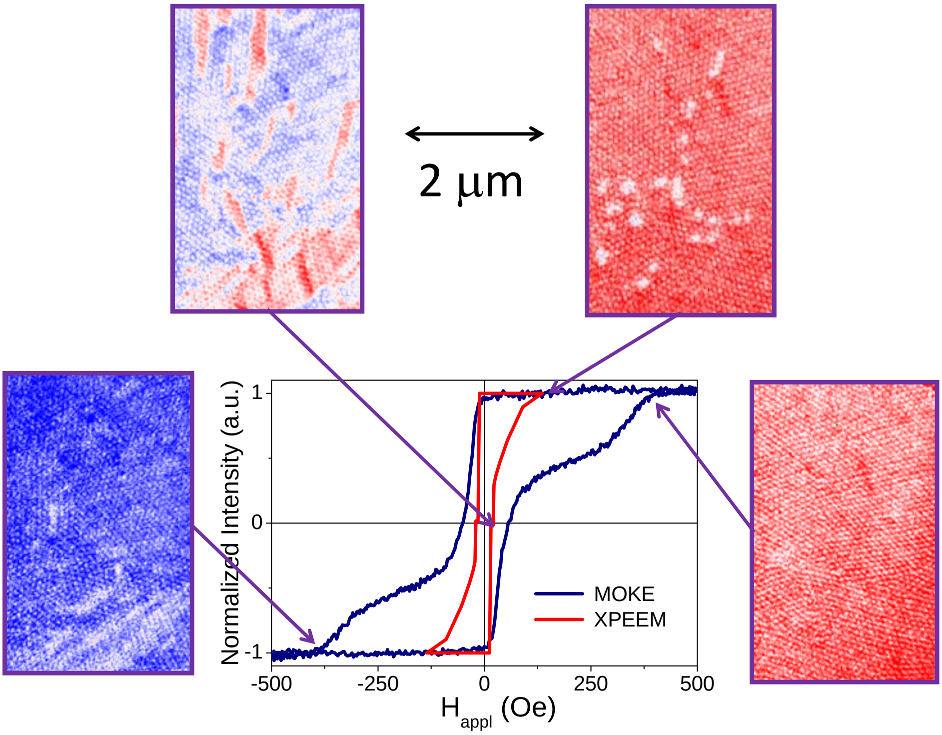

Figure # 4.63. XPEEM and MOKE loops with the corresponding XPEEM images.

In the XMCD images the reversal process seems to happen at lower fields than in the MOKE loop. As an example, the value of H_c is approximately 42% higher in the MOKE loop. Another difference can be found in the saturated XPEEM image in Figure # 4.59d, where more than 90% of its magnetic moments have been inverted; meanwhile in the MOKE loop the percentage of the reversed moments correspond to the 72% of the magnetic moments.

4.4.1.2 At remanent state

Figure # 4.64a shows a XPEEM image at the L_2 and L_3 Ni edge of the same area which depicts the topography with indication of geometry defects: dislocations like-boundaries and imperfections (yellow lines). The comparison between magnetic and topological images enables one to correlate the magnetic and geometrical domains. The XMCD image at remanence are shown in Figure # 4.64b-j, with their corresponding fields applied before remanence.

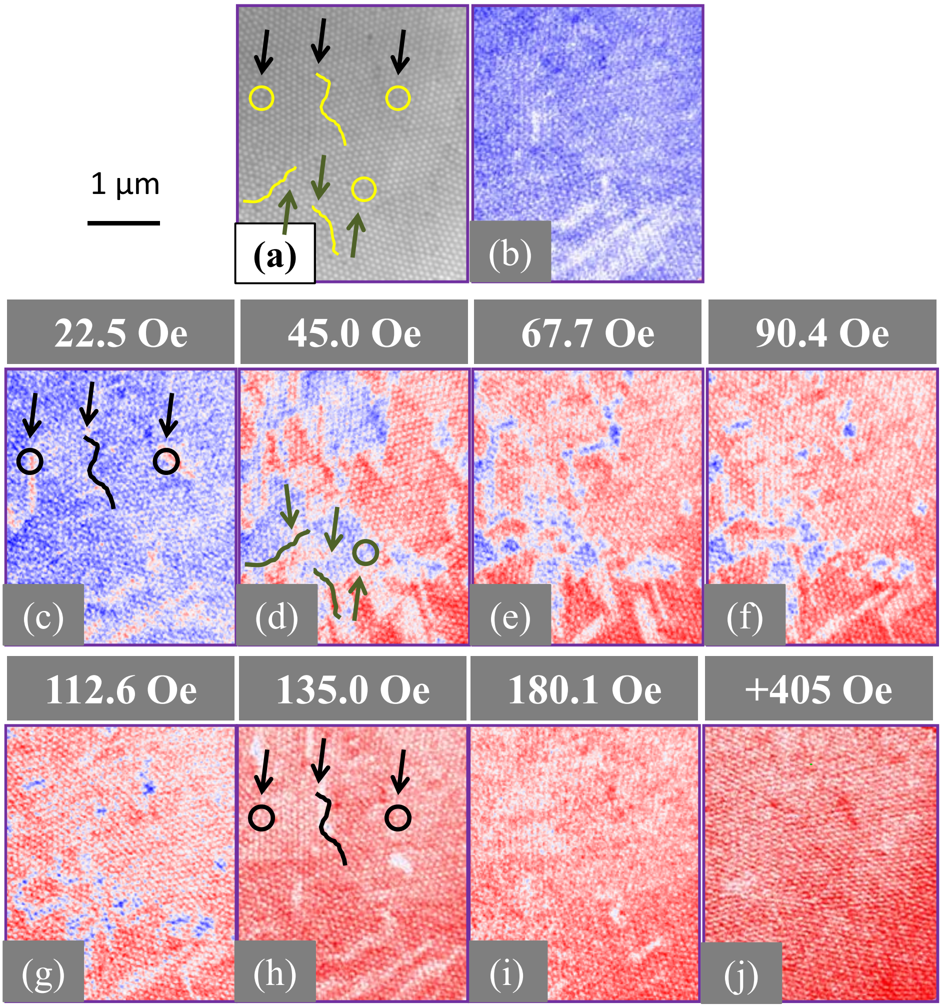

Figure # 4.64. XMCD images at remanent state with its corresponding fields; color scale with the magnetization direction in Figure # 4.60c.

After applying a saturating negative field (-405 Oe) the image is expected to be fully blue, Figure # 4.64b. From this point the applied field was set to different positive values (then zero) at which the XMCD images were taken, Figure # 4.64b-j.

Topological imperfections (marked in black, green and yellow in Figure # 4.64a) can be identified along the XMCD images, clearly affecting the magnetization. From the comparison between Figure # 4.64b and c, the marked defects in black, can be understood as nucleation sites or pinning centers for the propagation of DW (as in the measurements in Section 4.4.1.1), from where the displacement of the DW (colored in red) reverses the magnetization inside the corresponding geometric domains increasing the region with positive magnetization, Figure # 4.64d.

The dislocations act as pinning centers anchoring the DWs corresponding to magnetic domains parallel to the blue magnetization direction, slowing down the switching process. Along these dislocations, the magnetization exhibits a significant perpendicular component to the X-Rays, as indicated by their "white" color in Figure # 4.64d-g.

Important information can be gained by the comparison between the remanence state (zero applied magnetic fields) and the magnetic state under an applied magnetic field. Three different fields were used: 22.5; 45 and 90 Oe; the XMCD images are shown in Figure # 4.66 and the corresponding different values along the M-H loop are represented in Figure # 4.65.

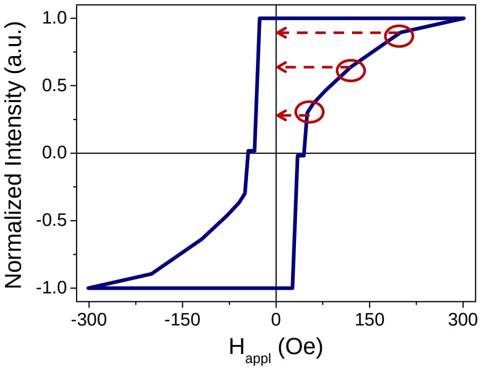

Figure # 4.65. Magnetic fields used at remanence (arrows) and under the applied magnetic field.

Figure # 4.66a shows a XPEEM image at the L_3 Ni edge of the same area which depicts the topography with indication of geometry defects: dislocations (green and purple lines) and punctual imperfections (black circles). Figure # 4.66 shows the XMCD images corresponding to the magnetic domain structure under selected values of applied field (bottom row) and at remanence (upper row). Note that the differences in the positive magnetization between the images at remanence (Figure # 4.66b to d) and the images with applied magnetic field (Figure # 4.66e to g) enable one to identify the degree of irreversibility.

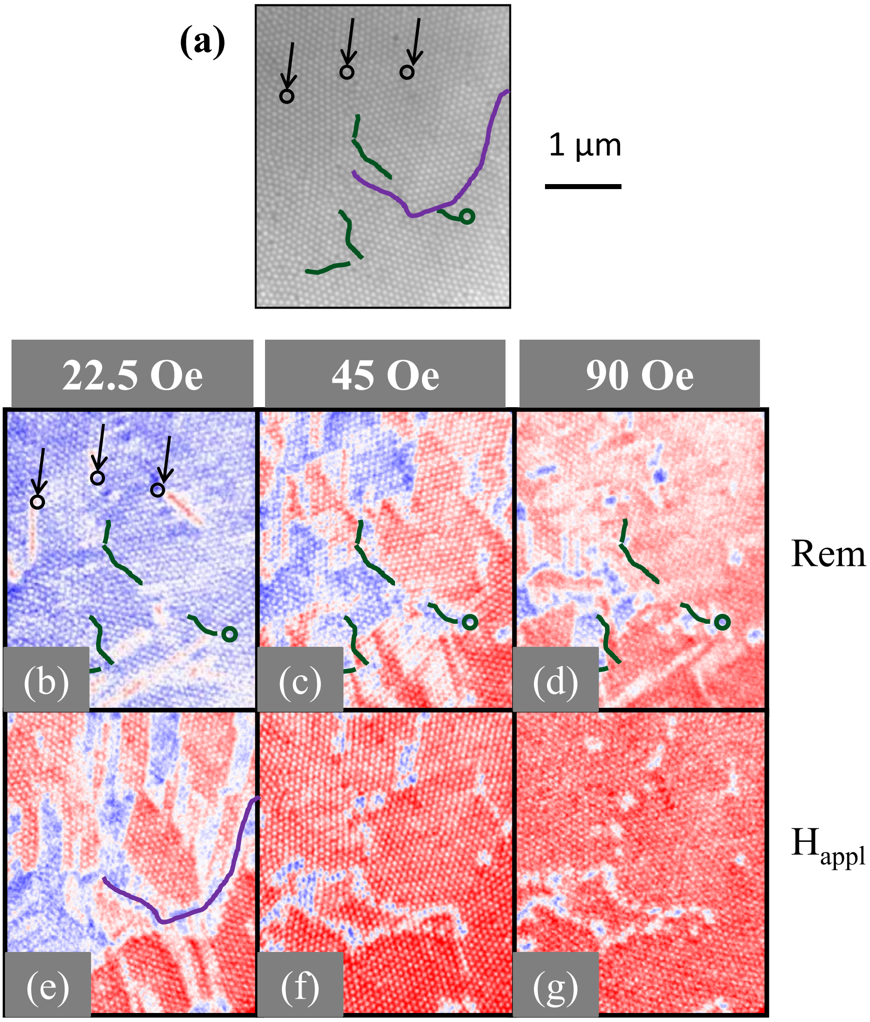

Figure # 4.66. For Sample A: (a) XPEEM image denoting the geometrical domains of the samples together with some dislocations and punctual defects; XCMD images of the magnetic domain structure at (b) to (d) remanence (Rem) and (e) to (g) at magnetized states (H_{appl}).

After saturating the sample at a negative field, an applied magnetic field is set to a positive value of 22.5 Oe at which the XMCD image (Figure # 4.66e) is taken. This image indicates that magnetization in a significant fractional volume of the sample has reversed its orientation (as deduced from the major red areas), and enable a direct a correspondence with the topological domains. As an example, the purple line marks the position of one dislocation which acts as pinning site hindering the reversal. Thus, as the applied field is removed (remanence: Figure # 4.66b), the magnetization is mostly “blue” denoting that a significant fractional region has changed the magnetization direction. Also, a given fractional volume has reversed the magnetization in an irreversible way, in comparison with the initial (totally blue) negatively saturated state. Here, three defects marked with black circles act as nucleation sites, encouraging an irreversible-like magnetization reversal process (some coincide with defects where DW nucleates in the images with applied magnetic field).

A similar comparison can be done for the case of increased applied field. Increasing the positive applied fields (Figure # 4.66c) results in larger regions with inverted “positive” (red color) magnetization orientation that partially suffer an irreversible reversal.

It is worthwhile to notice that for the higher field (90 Oe) the magnetization in Figure # 4.66d has not reached a full saturated state due to the presence of reversible rotations (returning to the initial state of magnetization), showing a significant difference with the magnetization state in Figure # 4.66g (almost saturated).

In turn, under higher fields, Figure # 4.66c-d, the regions inside geometrical domains seem to reverse the magnetization mostly by irreversible processes thanks to the anchoring effect from the dislocations. The “positive” magnetization inside the domains is favored, but their reversal process requires higher fields to overcome these pinning.

4.4.1.3 Geometrical and magnetic domains

One of the most important outcomes of XPEEM analysis in these system is to obtain information on the local magnetization process (over several numbers of geometrical domains). This study was made in order to determine if the magnetic behavior inside each geometric domain depends on the orientation of the underlying lattice.

The red arrows in Figure # 4.67 show the orientation of the applied field and the dashed lines indicate the orientation of the nearest local geometrical direction of the hexagonal symmetry, or *e.a.*, of the corresponding geometrical domain. Each domain has a different lattice orientation, resulting in a distinct local magnetic anisotropy. As a consequence, each geometric domain has different local coercivity, H_c, obtained from the local hysteresis loop, Figure # 4.68.

The highest H_c corresponds to an alignment of the magnetic field with the *e.a.* (Chapter 1); meanwhile the lowest H_c would correspond to an effective in-plane h.a. at an angle of 23º, which almost coincide with the h.a. direction at 30º of the hexagonal lattice explained in Chapter 1. Table # 4.11 shows the coercivity of each geometrical domain and Figure # 4.68 represents how the hardness depends directly on the lattice orientation.

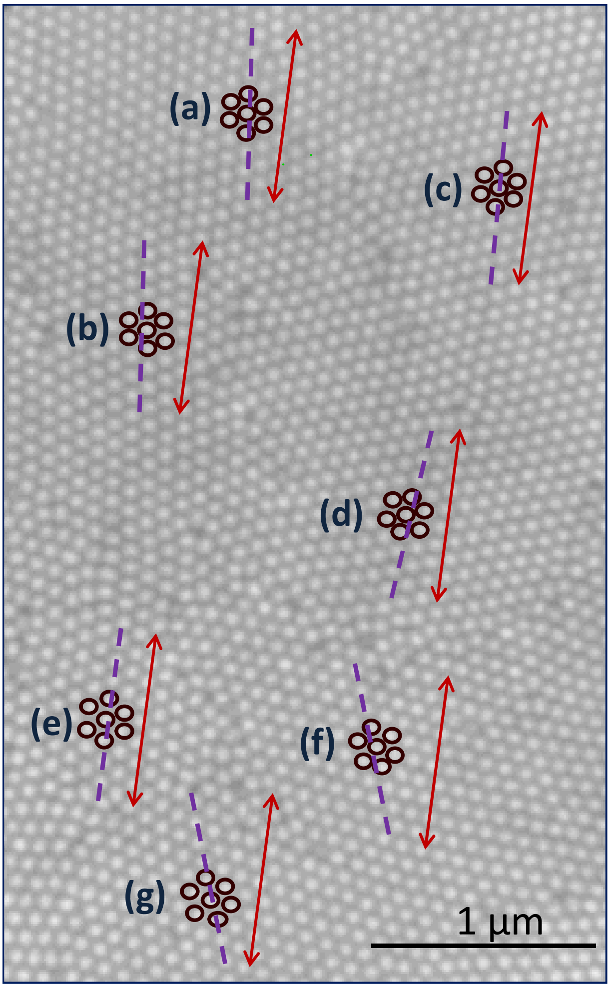

Figure # 4.67. XPEEM image containing several topological domains (the red arrows mark the orientation of the applied magnetic field and the discontinuous lines show a particular the orientation defining the hexagonal order of the lattice).

In the ideal case where all the geometric domains have the same orientation, the H_c of the system would be 24.8 Oe, but in the real case, the geometric domains have different lattice orientation, thus the H_c is an averaged from all the domains. A good way to demonstrate this fact, is calculating the coercivity of the hysteresis loop in Figure # 4.61, which is approximately H_c = 18.2 Oe, and calculating the averaged value from Table # 4.11, which corresponds to H_c = 17.2 Oe. The great concordance between these two values demonstrates that the loop actually represents the average magnetic behavior.

This result is extremely important because could explain the differences between the values of H_c in the VSM and in the MOKE systems. As mentioned in Sections 4.2.4 and 4.3.4, one explanation could be the different magnetic phases at the bottom and at the surface of the films, but another plausible reason could be that in the MOKE system the measured number of geometric domains is much lesser than the measured domains in the VSM system. The average of the magnetic behavior of lesser number of geometric domains, results in higher H_c, since the differences in orientations are lesser.

Table # 4.11. Coercivity of each geometrical domain marked in Figure # 4.67.

Geometric Domain	**Angle of deviation of the e.a. with the field (°)**	**H_c (Oe)**
e	0	24.8
c	4	20.7
a	7	16.2
b	7	16.2
d	7	16.2
g	19	13.5
f	23	12.6

$$H_{average} = \frac{H_e + H_c + H_a + H_b + H_d + H_g + H_f}{N}$$

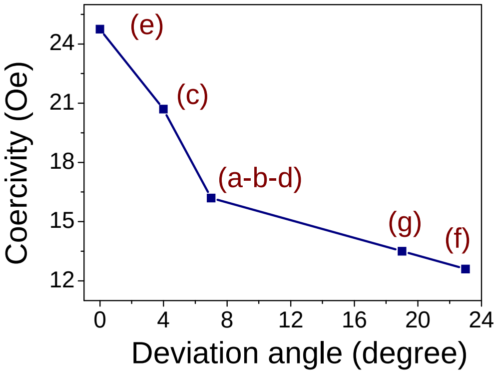

Figure # 4.68. Coercivity, Hc, as a function of the angle between such orientation and the field (each value is marked with the corresponding domains on Figure # 4.67).

Effectively, the magnetic behavior inside each geometric domain depends on the orientation of the e.a. relative to the applied field, demonstrating that the deduced *non-homogeneous magnetic structures* are formed as a consequence of the different local magnetic anisotropy of the geometric domains. And the second phase could be due to the OOP component, in addition to further domain alignment (rotation) with increasing magnetic field. The competition between the IP stray fields and the upper-bottom surfaces interaction, define the IP or OOP components of the magnetization. In Figure # 4.69 the IP and OOP loops are represented.

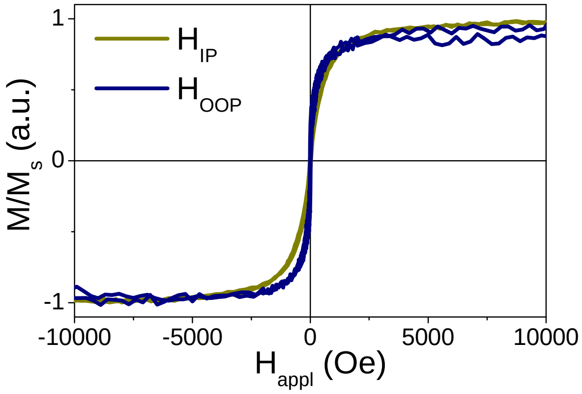

Figure # 4.69. In-plane (IP) and Out-of-Plane (OOP) loops by VSM of Sample A

There is a clear softer behavior in the OOP M-H loop, which can be correlated with the above mentioned second harder phase. Making use of the loops and the calculated effective anisotropy, we deduce an effective anisotropy of ≈ 10^4 erg/cm^3, one order of magnitude higher than the anisotropy constant of a CTF of Py [2]. Nevertheless, both M-H configurations show almost the same magnetic behavior, deducing that the higher IP dipolar inter-hole interactions is compensated with an important OOP component, which in turn may correspond to the rotation plane of the magnetization (analogous to the Bloch walls).

This technique clearly shows how the magnetic configuration follows the pattern of the template, demonstrating that the magnetic behavior is actually an average of the magnetic behavior coming from all the geometric domains. In the same way, the MOKE system measures the average magnetization from different geometric domains, Figure # 4.9.

4.4.2 ANTIDOT ARRAYS WITH LOW ASPECT RATIO

The hysteresis loop of sample B (r = 1.1) is shown in Figure # 4.70a. It is worthwhile to mention that the distance between antidots (edge-to-edge) is significantly larger for sample B (D-d ≈ 90 nm) than in sample A (D-d ≈ 43 nm), so DWs could have a longer-range displacement in the former.

The loop exhibits a single large Barkhausen jump denoting a single phase behavior, with coercivity of around 27 Oe, and a remanence near to 1, which roughly correspond to the magnetically soft phase in the loop of sample A. Figure # 4.70b shows the reversal curves with indication of the percentage of reversible and irreversible processes. The IRM curve has an important increase at low field up to about 60 Oe, where the curve saturates. Up to 60 Oe, the reversal mechanism consists in the nucleation and irreversible propagation of DW, but from 60 Oe the magnetization reaches its saturation by reversible rotations. As deduced from the high-field region, Figure # 4.70b, both, reversible and irreversible processes contribute, equally to the whole magnetization process.

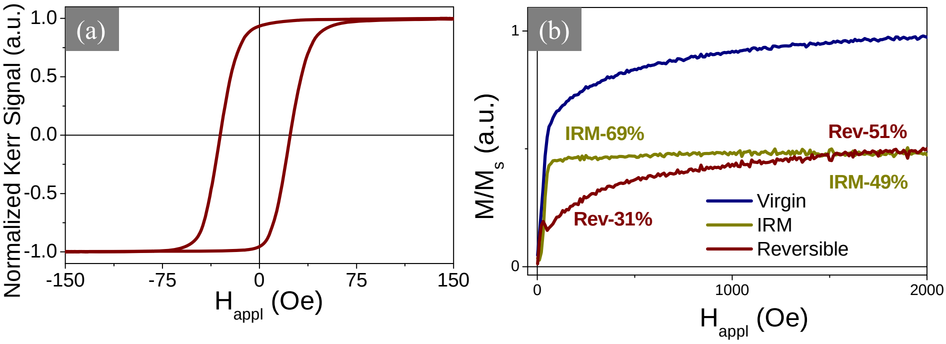

Figure # 4.70. (a) MOKE hysteresis loop of sample B and (b) VSM magnetization curves.

Figure # 4.71a shows an absorption XPEEM image with left circularly polarized X-rays, where local sites inside geometrical domains are marked with circles in order to follow the reversal magnetization process. Few dislocation-like defects are also marked with discontinuous yellow lines separating topological domains.

Figure # 4.71 shows the XMCD images, which correspond to the irreversible process: the sample was nearly saturated under the maximum field of +360 Oe and then each image was taken at remanent state after increasing the field in the opposite direction step by step, until nearly saturating at -360 Oe. Note that, unlike for sample A, for sample B the maximum applied field was strong enough to overcome the irreversible regions deducing the rotations as the final step of the reversible processes.

From the images in Figure # 4.71, the local evolution of irreversibilities can be followed (with initial saturation along the positive direction, marked as red). It is possible to observe that there are two main processes: i) up to image f (H_{appl} = -22 Oe, a value close to coercivity as deduced from MOKE loop), the predominant color is red denoting that up to that field processes are mostly reversible; even more, topological regions with different contrast are clearly observed already in image d which indicate that DW can be locally pinned at the border between geometrical domains (dislocation); ii) from images above h (H_{appl} = 57 Oe), dominant color is already blue indicating that most irreversible processes have already happened.

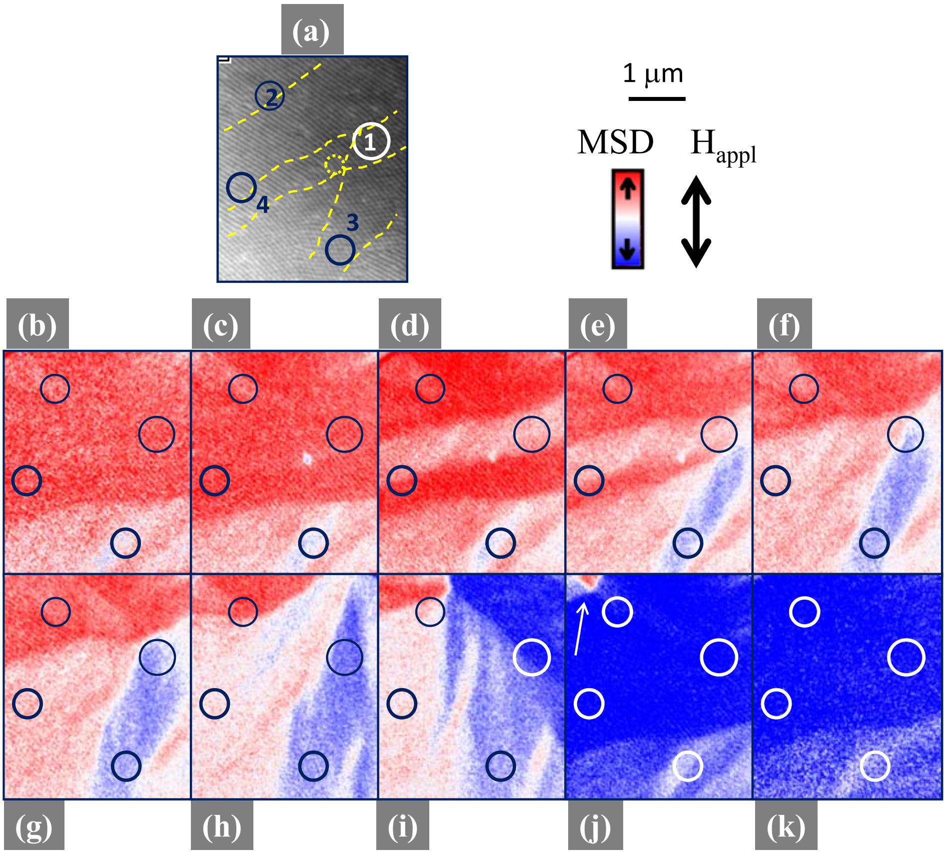

Figure # 4.71. (a) Image of sample B with left circularly polarized X-rays. XMCD images taken at remanence after nearly saturating under +360 Oe and then applying magnetic field H_{appl} = (b) 0 Oe, (c) -2.04 Oe, (d) -10.04 Oe, (e) -13.76 Oe, (f) -22.16 Oe, (g) -27.04 Oe.

With smaller d_P, as the coercivity was reached, the interactions cause the geometric domains undergo cooperative switching, i.e. they switch in clusters rather than individually.

Figure # 4.72a and b show the hysteresis loops obtained in local regions 3 and 4 marked in Figure # 4.71a through XMCD images. Note that region 3 is completely inside a topological ordered domain while region 4 contains a dislocation-like defect border between two geometric domains. A comparison between these loops indicates that region 3 is magnetically softer, with H_c = 10 Oe, while region 4 is significantly harder, with H_c = 55 Oe, and contains two steps in its magnetization process which can be actually ascribed to the region inside the domain (softer) and in the border between domains (harder). This two-phase magnetic behavior is averaged out when considering a sufficiently large area enclosing several domains and corresponding borders.

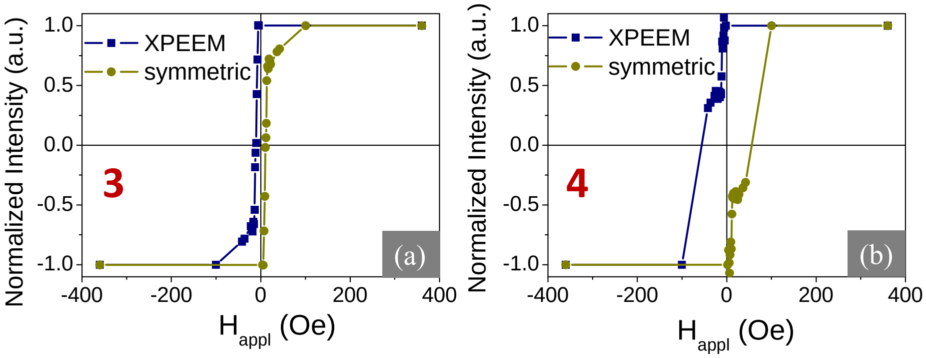

Figure # 4.72. Local hyster4esis loops inside topological domains 3 and 4 in Figure # 4.71a.

The most important difference between this sample and sample A is that the magnetic configuration in sample B contains a larger number of nanoholes but mainly due to the smaller d_P, being the magnetic domains much bigger and homogeneous than in sample A.

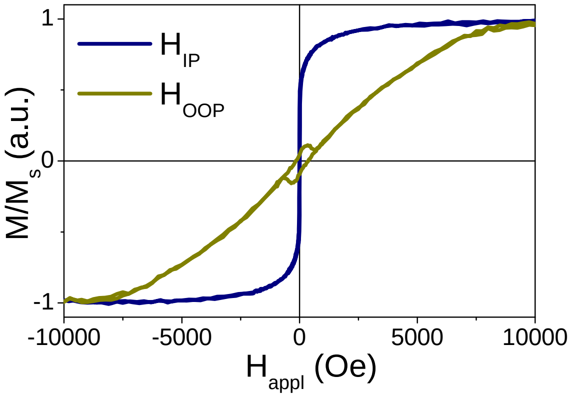

Figure # 4.73. In-plane (IP) and Out-of-Plane (OOP) loops by VSM.

For the analysis of the OOP component, Figure # 4.73 displays the IP and OOP M-H loops by VSM. The effective anisotropy is of the order of 10^6 erg/cm^3, one order of magnitude higher than sample A, despite the d_P of the nanoholes are much smaller. But the dipolar effect between the bottom and the surface is lower in thicker films, maintaining most of the magnetization along the plane of the film. The OOP loop, Figure # 4.73, corresponds to an almost linear behavior (a h.a. behavior), but the high coercivity (≈ 250 Oe), denotes an important OOP component, which could be due to the same rotation mechanism in sample A.

4.5 SUMMARY

The magnetic properties of the CTF and antidot arrays prepared with different sputtering conditions were measured; from this magnetic characterization. The experimental DW measured by the IP and OOP M-H loops is much smaller than the theoretical ones. The applied magnetic field during the sputtering is found to affect both the anisotropy of the film and the DW properties as well.

We found that the geometric domains, the boundaries-like dislocations, the dimensions of the nanoholes arranged in a hexagonal lattice, influenced the magnetic behavior of the antidot arrays. We found a relationship between coercivity, the dimension of the nanoholes and thickness. An important characterization by imaging the magnetic structures of the antidot arrays was made, founding a great relation between the dimensions of the nanoholes and the domains structure.

5. CHAPTER 5

ANTIDOT ARRAYS OF Co AND Co/Py OVER ANODIC ALUMINA TEMPLATES

5.1 INTRODUCTION

The objective of this chapter is to study the magnetic behavior of bilayer antidot thin films. In the previous chapter the magnetic behavior of Py antidot thin films with a relative magnetic soft character was studied. Now, we are considering Co antidot films which in principle are expected to exhibit a harder behavior, with high anisotropy and saturation magnetization. Finally, antidots of Co/Py bi-magnetic systems were sputtered over *anodic alumina membranes* (AAM), with the aim to investigate the influence of the presence of antidots in the magnetic behavior. We expect that the magnetic interaction of the interface of the two layers will be relevant to determine such behavior. As an advantage of these systems, additional thermal processes (increasing the nucleation field and improving the energy product, relative to their counterpart *continuous thin film*, CTF) are not necessary [161]. Co/Py bilayers have been extensively studied in the form of thin films, and here we are focusing on the antidot arrays.

Because of the presence of two magnetic phases with soft (Py) and harder (Co) magnetic character, a exchange spring magnet interaction is expected. In this regard, we will remind some general characteristics like in modern permanent magnets. The influence of the presence of antidots will then superpose to that exchange spring interaction.

The chapter is divided into three different sections: i) introduction of the magnetic interactions expected to be present in the bi-magnetic soft/hard system, namely *exchange spring interaction*, which is typical in modern permanent magnets; ii) magnetic characterization of individual Co layer antidot arrays over AAM; and iii) study of the hard/soft Co/Py bilayer antidot system.

5.2 EXCHANGE SPRING INTERACTIONS

The *Exchange Spring magnets*, or *spring magnets*, are typically nano-composite materials composed of hard and soft magnetic phases that interact by exchange coupling [162,163]. Based on micromagnetic simulations, these systems are expected to exhibit enhanced energy product compared to conventional single-phase materials. They combine high magnetization from the soft phase and a high anisotropy from the hard phase, attaining in this way a high energy product [164,165,166,167], which represents twice the maximum magnetostatic energy available from a magnet of optimal shape [168].

These nano-composites consist of randomly oriented hard grains, which are randomly dispersed, through the bulk processing methods used to fabricate them [169,170,171]. However, experimentally high energy product is difficult to achieve because several factors are difficult to control, such as grain size of both soft and hard crystallites, and the crystallographic alignment of the hard grains.

The theoretical limit for the maximum energy product of a given magnetic material is given by [164]:

$$(BH)_{max} = \frac{J_s^2}{4\mu_0} = \frac{(\mu_0 M_s)^2}{4\mu_0} = \frac{\mu_0 M_s^2}{4} \qquad \text{Eq. (5.1)}$$

The energy product denotes the performance of a permanent magnet. It is expressed in units of *gauss oersted* (GOe) for CGS units and the maximum energy product is given as $(BH)_{max}$. This product represents the area inside the second quadrant of the B-H loop that describes the available energy density of a material [172]. This value shows a yardstick for the maximum amount of magnetic flux taken out from the magnet per unit volume. When a magnetic circuit is designed to come to the maximum energy product point, the magnet volume is made the smallest possible.

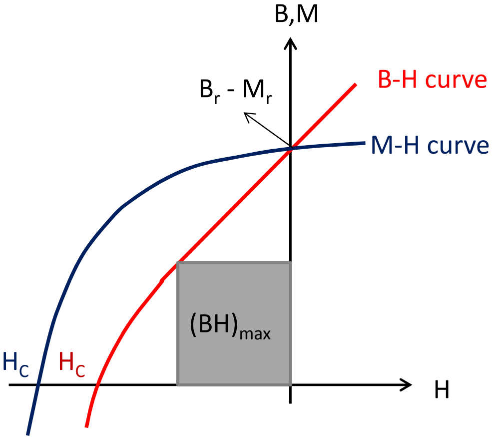

Figure # 5.1. (red) B-H Curve, (blue) M-H Curve, and $(BH)_{max}$. H_c: Coercivity of M and B curves, respectively.

A survey on the magnetic properties of some well known materials of both categories indicates that the quantity magnetization of saturation (M_s) is for most hard-magnetic materials considerably lower than for many common soft-materials. However, for materials with sufficiently high coercivity (H_c) values, as represented in Eq. (5.2**)**, the theoretical limit for the energy product is limited only by the M_s and is given by Eq. (5.3), [162,163,164,165]

$$H_c > 2\pi M_s \qquad \text{Eq. (5.2)}$$

$$(BH)_{max} \leq (2\pi M_{sat})^2 \qquad \text{Eq. (5.3)}$$

Therefore many studies have considered composite materials consisting of two suitably dispersed and mutually exchange-coupled phases, the first one hard-type, providing a nucleation field high enough for irreversible magnetization reversal, and the second one is a soft-type material with M_s as high as possible, in order to attain a high average magnetization saturation. Additionally, the soft-material may envelop the hard-phase regions in order to prevent their corrosion.

These types of composite systems were first observed by Coehoorn et al. [5] in a melt-spun $Nd_{4.5}Fe_{77}B_{18.5}$ sample that, when annealed, consisted of a mixture of $Nd_2Fe_{14}B$, Fe_3B and Fe phases. These samples exhibited desirable hard-magnet properties even though they consisted of 85% soft phases (Fe_3B and Fe) and only 15% hard phase ($Nd_2Fe_{14}B$) [168]. Skomski and Coey explored the theory of exchange coupled films and predicted that a giant energy product of 120 MGOe (about three times that of commercially available permanent magnets at the time) might be attainable by exploiting the exchange-spring mechanism in oriented nanostructured magnets [165,166].

Skomski predicted a giant energy product of 137 MGOe in suitable nanostructured exchange spring magnets with an oriented hard phase [173]. In comparison, the theoretical limit of the energy product for Nd–Fe–B is 64 MGOe, and that limit is rapidly being approached in commercial products. The best of the hard-materials contains about 25 wt% or more of a rare earth metal, which adds to their price and raises serious problems with respect to chemical stability.

Interleaving hard and soft magnetic thin film layers seems to be very suitable system because the coupled magnetic multilayer retains the essential aspects of spring magnets but without the structural complexities of random nano-composites.

Several theoretical approaches [167,173,174,175,176,177,178,179,180,181] confirm that the most important parameter in characterizing the switching behavior is the dimension of the soft phase. For a thin soft-phase layer over a hard-phase layer, there is a critical thickness below which the soft phase is rigidly magnetically coupled to the hard phase, and the magnetization of the two phases reverses at the same nucleation field resulting in a rectangular hysteresis loop. For thicker soft layers, the reversed domain nucleates at significantly lower fields and the switching is characterized by inhomogeneous reversal [168]. Although the value of the nucleation field (H_N) depends on the material parameters of both the hard and soft layers, the critical soft-layer thickness is found to be roughly twice the width of a domain wall (DW) in the hard magnetic phase [164,166,175], which is given by:

$$\delta_h = \pi \sqrt{\frac{A_h}{K_h}} \qquad \text{Eq. (5.4)}$$

where A_h and K_h are the exchange and anisotropy constants of the hard phase, respectively. Thus, this exchange length determines many of the physical properties of these systems irrespective of the sample geometry.

Soft-layer thickness values smaller than δ_h

For layer thickness values less than the critical value δ_h, the two phases are magnetically rigidly coupled and the composite system is characterized by the averaged magnetic properties of the two layers. The magnetization is expected to switch at a nucleation field [173] given by

$$H_N = \frac{2(t_h K_h + t_s K_s\ )}{t_h M_h + t_s M_s} \qquad \text{Eq. (5.5)}$$

with anisotropy (K_s and K_h), magnetization (M_s and M_h), and layer thickness values (t_s and t_h) of the soft (sub-index s) and hard layers (sub-index h), respectively.

Soft-layer thickness values larger than δ_h

For thicker soft layers, the coercivity of the soft layers drops quickly well below that of the hard layer, which results in the final degradation of the hard-magnet properties of composite systems.

Several studies [174,182] determined that the soft layer remains parallel to the hard layer for fields less than the *exchange field* (H_{ex}), Eq. (5.6). Once the magnetic field exceeds H_{ex} magnetic reversal proceeds via magnetization rotations in the soft layer.

$$H_{ex} = \frac{\pi^2 A_s}{2M_s t_s^2} \qquad \text{Eq. (5.6)}$$

5.3 MAGNETIC BEHAVIOR DEPENDENCE WITH *d_P* AND D

In this section, a study of the magnetization reversal process of the Co antidot arrays with different geometric properties, as *AAM's pore diame*ter (d_P), *diameter of the antidot* (d), and *lattice parameter* (D) was performed. The magnetic constants of bulk Co are presented in Table # 5.1, and the geometry characteristics of the studied samples are collected in Table # 5.2.

.

Table # 5.1. Magnetic properties of the Co [2,52]

	Anis.	**A (erg/cm)**	**M_s (emu/cm^3)**	**K (erg/cm^3)**	**l_{ex} (nm)**	**δ_{DW} (nm)**
hcp Co	Strong	$2.81\cdot 10^{-6}$	1422	$4.12 \cdot 10^{6}$	8.3	26
fcc Co	Weak	$3.00\cdot 10^{-6}$	1445	$-1.2 \cdot 10^{6}$	15.8	50

Table # 5.2. Geometry characteristics of the Co antidot films.

Name	**D (nm)**	**t_{Co} (nm)**	**t_{Al} (nm)**	**d_p (nm)**	**d (nm)**
Co105/35	105	20	2	35	25
Co105/48	105	20	2	48	38
Co105/61	105	20	2	61	51
Co105/75	105	20	2	75	65
Co65/25	65	20	2	25	15
Co65/35	65	20	2	35	25
Co65/45	65	20	2	45	35

5.3.1 Angular dependence of Coercivity and Remanence of Co Continuous Thin Film

A first magnetic characterization was made by VSM continuous thin film (CTF); it includes the angular dependence of coercivity (H_c) and remanence (M_r) along the plane of the sample.

The angular dependence of H_c and M_r; together with the *in-plane hysteresis loop* (IP M-H) along the easy (e.a.) and hard axis (h.a.) of a CTF of Co with t_{Co} = 20 nm, are presented in Figure # 5.2. Note that the angular anisotropy, here and in the cases showed below, is enhanced by the scaling (actually, H_c grows just from around 30 to 35 Oe).The IP M-H loop along the e.a. presents a high squareness, which is ascribed to a magnetization reversal by domain wall (DW), with H_c = 35 Oe and M_r/M_s = 0.85. The loop along the h.a. denotes a more complex magnetization process with seemingly reversible and irreversible rotations. From the data, a uniaxial magnetic anisotropy is deduced.

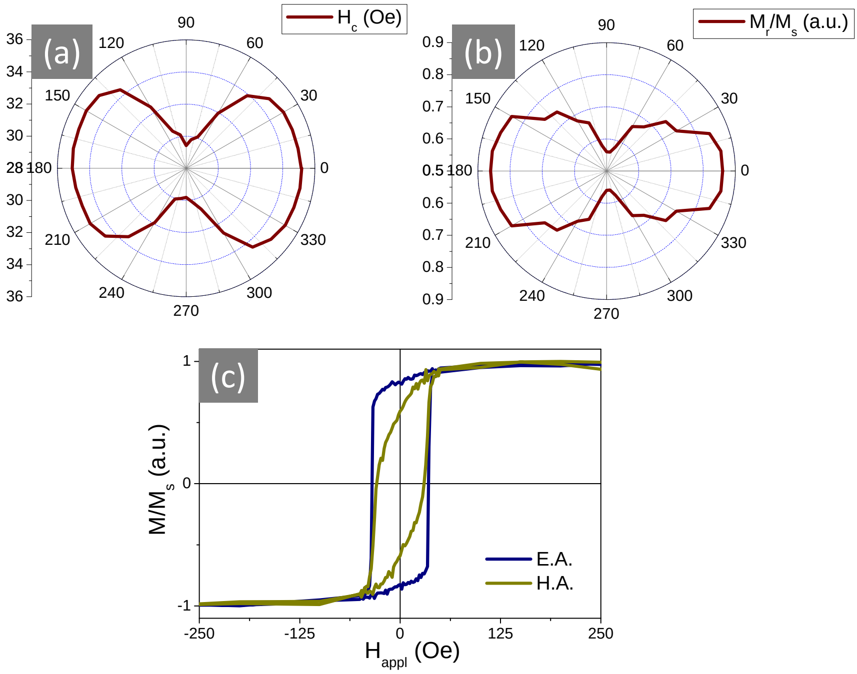

Figure # 5.2. Angular dependence of (a) H_c and (b) normalized M_r; and (c) M-H loops along the e.a. and h.a. of a CTF of Co with t_{Co} = 20 nm.

The reported anisotropy in Co in *hcp* phase is uniaxial when the magnetization lays in the out of the plane (OOP) axis [52], but if the magnetization lies in the basal plane (IP), the anisotropy has a three axial behavior [52]. Other works have reported that Co thin films in *hcp* phase have an IP uniaxial anisotropy [172,183]. Nevertheless, Kumar and Gupta [172] claimed that the observed anisotropy in the *hcp* phase has not a magnetocrystalline origin, but instead it is related to the sputtering preparation system. Fermento et al, grown Co over Ta buffer layer obtaining a strong anisotropy in the plane of the Co layer [185].

In our work neither temperature treatment nor buffer layers were employed. As explained in Chapter 3, Co films present a polycrystalline structure in the *hcp* phase. The obtained effective anisotropy in the Co films might have an induced contribution from the applied field during sputtering, in addition or rather than magnetocrystalline origin. Our result agrees with those presented in Ref. [184], where an applied field of 20 Oe during the deposition produces an uniaxial anisotropy.

5.3.2 General analysis of Co antidot arrays M-H hysteresis loops by VSM

The IP and OOP hysteresis loops of the Co antidot arrays are presented in Figure # 5.3a, for arrays with increasing d_P and fixed values of D (105 and 65 nm) and t_{Co} = 21 nm. The evolution of H_c and M_r with d_P is given in Figure # 5.3b and c, respectively. The IP loops of the antidot arrays were measured for the applied field along the easy axis magnetization orientation (derived from the angular dependence of H_c and M_r of the results treated later).

The general magnetic effect produced by the nanoholes of the Co antidot arrays is not very different to that of the Py arrays (M-H loops in Figure # 4.19). The main difference lies in the much larger H_c, Figure # 4.23 and Figure # 5.3b. In comparison with the CTF (in Figure # 5.2), H_c increases 8.8, 10, 16 and 27 times, in the arrays with D = 105 nm and d = 25, 38, 51, 65 nm, respectively.

Recalling the reasons of using Co, we have the relatively high anisotropy and saturation magnetization, and the relative hard magnetic behavior. One special feature of using nano-patterned arrays is the enhancement of their magnetic properties with regards to those of the CTF, such as H_c (as was studied in Chapter 4). The application of these arrays for technological purposes could be possible thanks to these characteristics.

In previous works [172,185], the coercivity of a Co layer has been reported not to exceed values of 25 Oe, unless the layers are deposited under temperature annealing. Taking H_c = 25 Oe as a reference value of the CTF, and H_c = 35 Oe as the experimental value from this work, Figure # 5.2, the values of H_c of the arrays were evaluated. Table # 5.3 collects the H_c values of Co antidot arrays. The increase with regards to CTF coercivity is also given. All the values were taken from the e.a. of the IP M-H loops.

According to these values, it is evident that the use of the antidot arrays enhances the coercivity. The array with the largest diameter has the highest H_c, nevertheless if we compare the arrays with the same d_P but different D, H_c is much higher in the arrays with D = 65 nm. As in the case of the Py arrays (Section 4.2.2), the dipolar interactions are stronger due to the smaller distance between nanoholes.

From the IP and OOP loops by VSM, a calculation of the DW width (δ_{DW}) was made (as explained in Section 4.2.X, we consider a macroscopic model). The values of δ_{DW} are listed in Table # 5.4. In comparison to the Py arrays, the Co has smaller DW width due to the stronger magnetocrystalline constant [52], thus the presence of DW is expected. In the arrays with d = 25 nm and D = 105 nm, the reversal magnetization process in the IP configuration is carried out by DW motion, deduced from a typical high squareness of the loop and the high M_r. When d_P increases, the susceptibility and M_r decrease. A different behavior is suggested in the array with d = 38 nm and D = 105 nm, where the smallest value of M_r was obtained. In these arrays, the mechanism of the magnetization reversal is completely different, which is ascribed to spin rotations.

The magnetic behavior in the arrays with d = 51 and 65 nm, and D = 105 nm, is similar as the Py arrays with d_P = 54 and 66 nm, and D = 105 nm, where the loops are tilt and a quasi-bi-phase behavior appears. This behavior seems to be originated by the geometry of the AAM, and by an important OOP component.

These loops show that even though the Co has different magnetic constants and higher coercivity, the geometry properties of the AAM define both the anisotropies and the reversal magnetization process. A good probe of this statement is coming from the OOP loops, in which much lower H_c were obtained, although they are not totally linear; indicating an important OOP component due to the presence of the nanoholes.

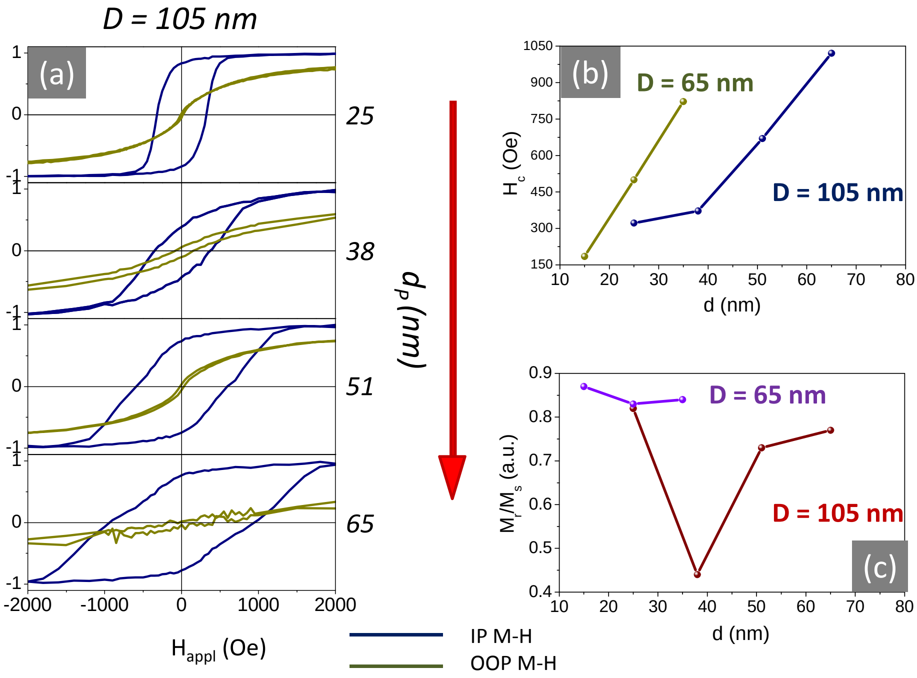

Figure # 5.3. (a) IP and OOP M-H loops of Co antidot arrays, t_{Co} = 20 nm; (b) H_c with d; (c) M_r with d.

Table # 5.3. H_c of the Co arrays.

Layers	H_c (Oe) of Arrays	Growth percentage
Co105/35	327	862%
Co105/48	372	994%
Co105/61	670	1635%
Co105/75	1021	2800%
Co65/25	185	428%
Co65/35	500	1330%
Co65/45	822	2248%

Table # 5.4. DW width of the Co arrays with D = 105 nm.

Name	d_p (nm)	d (nm)	δ_{DW} (nm)
Co105/35	35	28	93
Co105/48	48	39	
Co105/61	61	51	83
Co105/75	75	65	28

5.3.3 Angular dependence of Coercivity and Remanence of Co Antidot Arrays

As discussed in Section 4.1.2.2 for Py antidot arrays, the presence of the antidots gives rise to a complex multidomain magnetic distribution. That results in the averaging of the macroscopic anisotropy resulting in an isotropic-like magnetic behavior.

In the case of the Co antidot arrays of our study, a modest bi-axial anisotropy in the IP configuration was found, as can be seen in Figure # 5.4. This behavior may be produced by the effect of the competition between the induced magnetic anisotropy due to the applied field during the sputtering and the local magnetization energy around the nanoholes.

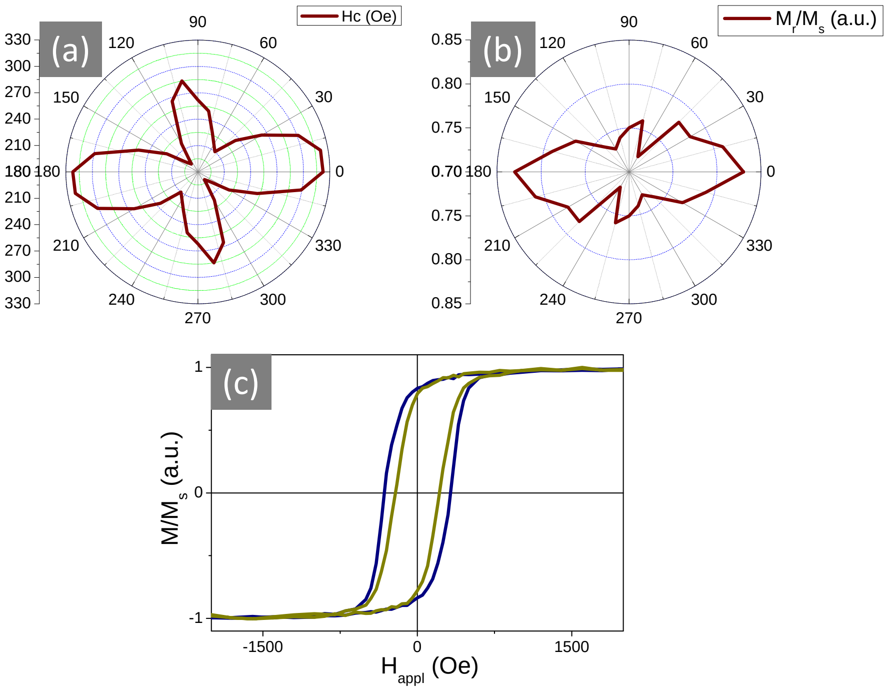

Figure # 5.4. Angular dependence of (a) H_c and (b) normalized M_r; and (c) M-H loops along the e.a. and h.a. of the Co105/35 array.

The shape of the M-H loops along the e.a. and h.a. are very similar, suggesting that the magnetic reversal mechanism is the same in both axes (see Figure # 5.4c). This reversal mechanism consists in motion of DWs that are pinned at the nanoholes. In addition, rotation of spins around the nanoholes should also contribute to the whole process, as explained in Section 4.2.2for the case of Py arrays.

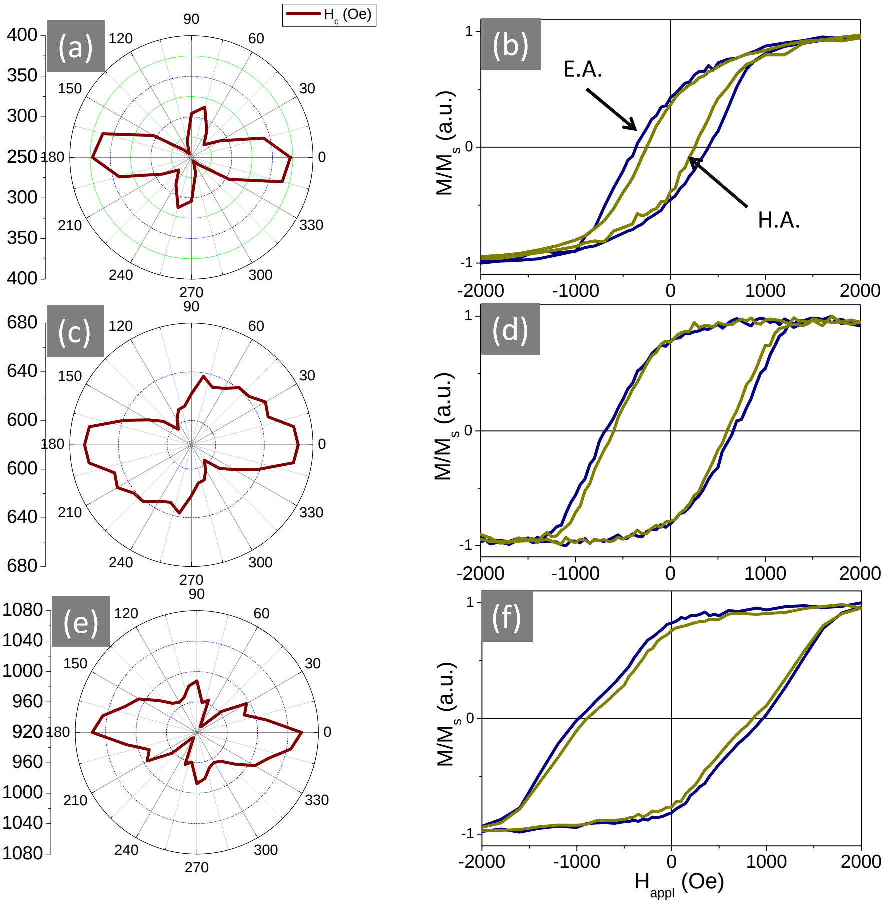

Figure # 5.5. Angular dependence of H_c and M-H loops along the e.a. and h.a. of (a) Co105/48 array, (c) Co105/61 array and (d) Co105/75 array.

Figure # 5.5 shows the evolution of results with increasing d_P and constant D (105 nm). The angular dependence of H_c of the arrays with increasing d_P show also a small anisotropy (see Figure # 5.5a-c-e), and again, the M-H loops along the e.a. and the h.a are very similar (Figure # 5.5b-d-f). It is important to note the increase of coercivity and remanence with d. It shows a stronger pinning effect of the nanoholes together with a larger contribution of rotational processes.

The results for Co antidot arrays with D = 65 nm are represented in Figure # 5.6. As in the previous case, a small mostly uniaxial anisotropy is observed. Also, an increase of the magnetic hardening is observed with increases of d.

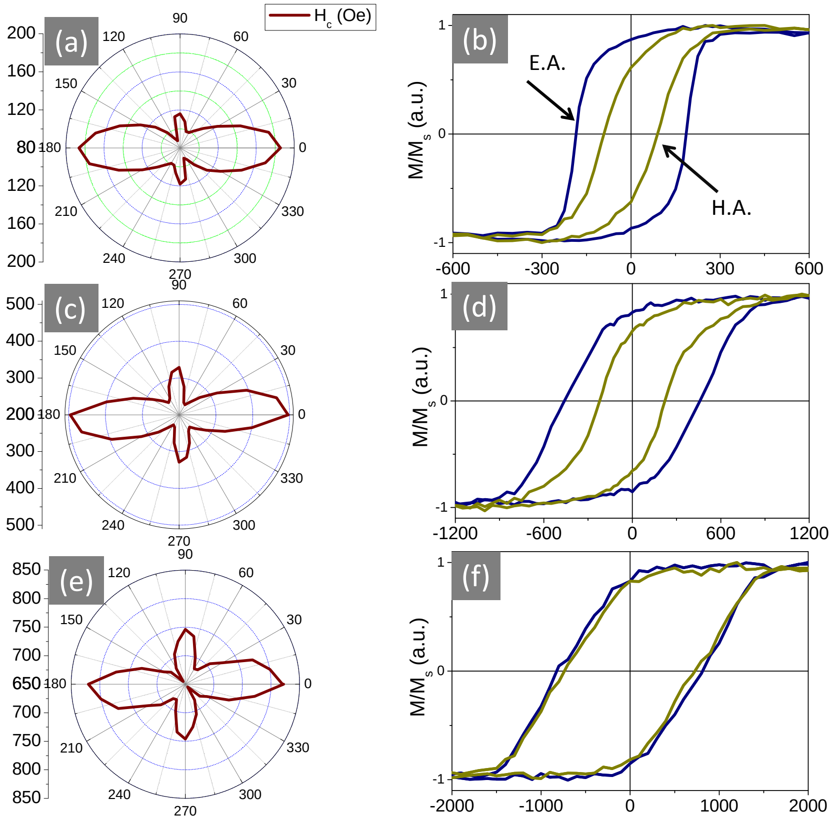

Figure # 5.6. Angular dependence of H_c (left) and M-H loops along the e.a. and h.a. (right) of (a) Co65/25 array, (c) Co65/35 array, and (d) Co65/45 array.

In many works [186,187], it was confirmed that the magnetization behavior is determined by the geometry characteristics of the antidot arrays, namely the d_P and D. That determines the value of H_c as a balance between shape and intrinsic anisotropy terms. The DW anchoring is due to the pinning of the DW at the nanohole edges in the vicinity, where the demagnetizing field is significant. This effect was discussed in Chapter 4.

5.3.4 First-order reversal curve analysis

Figure # 5.7 shows the FORC diagrams represented in color scale for Co antidot samples with t_{Co} = 21 nm and different d_P. Summarized results are collected in Table # 5.5. Measurements were performed with the applied magnetic field along the IP easy direction and maximum amplitude of 2000 Oe, reversal field steps of 40 Oe and saturation field of 15 kOe.

Table # 5.5. H_c of M-H loops and FORCs

Name	**D (nm)**	**d_P (nm)**	**d (nm)**	H_C^{MH} (Oe)	H_C^{FORC} (Oe)
Co29B	105	35	28	327	360
Co30B	105	48	39	372	663
Co31B	105	61	51	590	880
Co32B	105	75	65	986	1318

Relative to the antidot films of Co, the following information can be extracted:

1. The values of H_C^{FORC} are bigger than H_c from the M-H loops. That behavior can be ascribed to an enhancement of local magnetic anisotropy, as a consequence of the stray fields originated by the antidots. Besides, the material inside the wall of the pores produces dipolar interaction parallel to the magnetization, and affects the reversal process. From the comparison between the FORC diagrams of Py and Co arrays, it was deduced that the differences are mainly due to the geometry of the arrays rather than to a compositional effect.

2. Broader FORC distributions along H_c are visible. Such a behavior is indicative of a large switching field distribution, as a consequence of the large number of DW pinning sites due to locally distributed stray fields, and the different magnetic configurations inside different geometric domains.

3. The broadening of FORC distributions along the interactions axis, H_u, with increasing d_P (in this case bigger and more inhomogeneous than the Py arrays) suggests a gradual enhancement of the antiparallel interactions with d_P, again ascribed to the stray fields inside the voids, which affect more in the Co arrays. This effect is particularly evident in the origin of the FORC distributions, where a bias is present along the H_u axis.

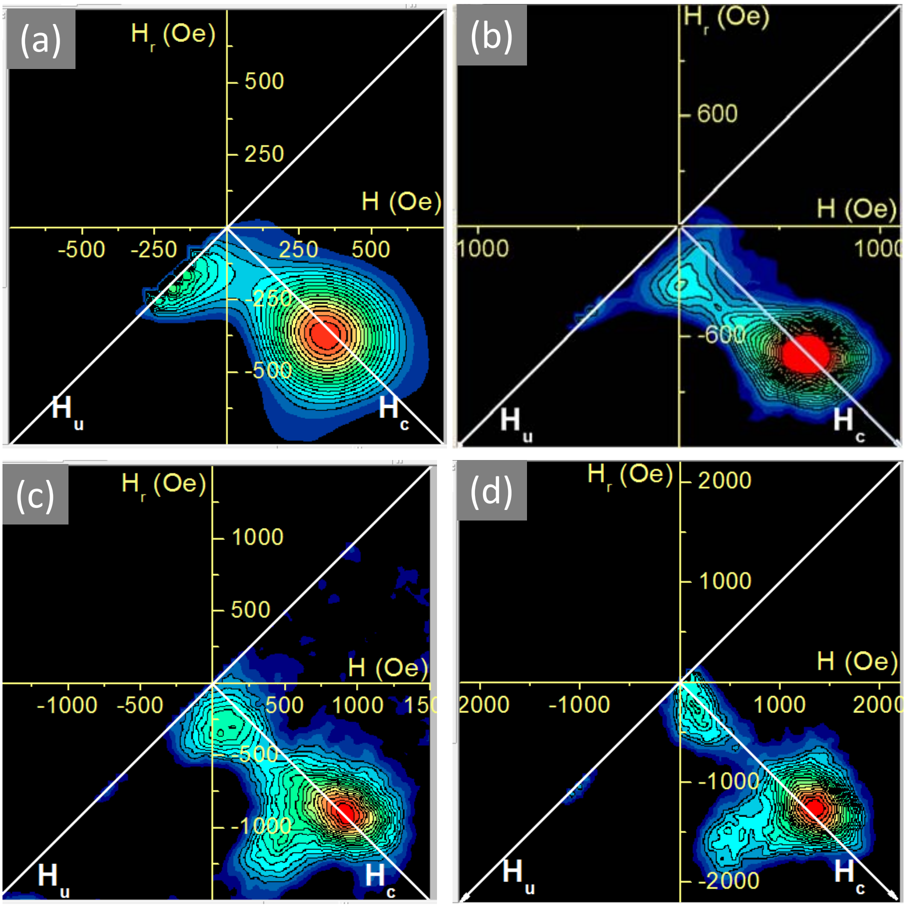

Figure # 5.7. FORC diagrams of the Co arrays with D = 105 nm.

4. The interactions region grows with d_P, as in the case of the Py arrays. But in this case, in the plot of d_P = 75 nm, Figure # 5.8, two peaks appear almost completely outside the H_c axis in the interference region. Even though these peaks do not have high signal (red color) as the principal one (high coercivity region), their presence is due to coupled interaction between the higher and the lower coercivities region which are almost detached (the low coercivity region is almost separate from the high H_c region).

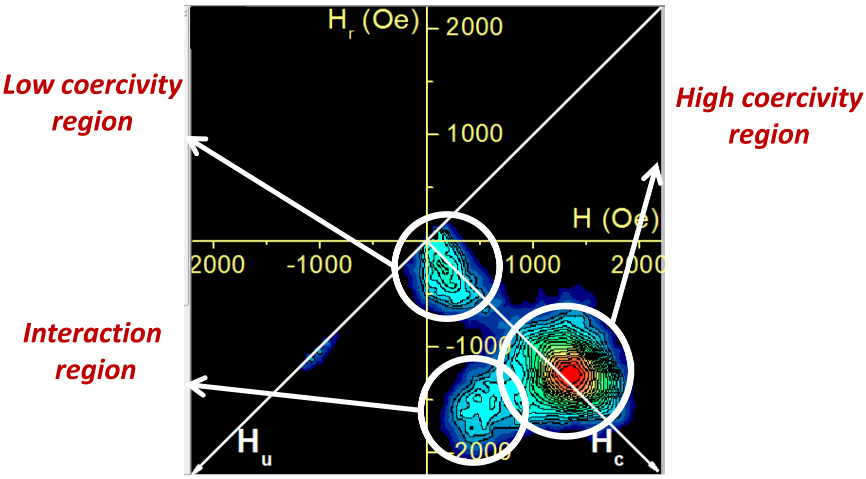

Figure # 5.8. FORC diagram of Co105/75.

5.4 MAGNETIC BEHAVIOR OF ANTIDOT ARRAYS OF Co/Py BILAYERS

The magnetic properties of bilayer antidot arrays were studied by VSM and MOKE. The geometric characteristics of studied samples are presented in Table # 5.6. The magnetization reversal behavior of the soft layer was examined using a series of Co/Py bilayer structures with different Py layer thickness. The thickness of Co was kept constant at 28 nm. The δ_{DW} of the antidot array of Co(28) was estimated to be 20 nm.

Table # 5.6. Characteristics of the arrays of Co and Co/Py.

Name		D (nm)	d_p (nm)	d (nm)	t_{Co} (nm)	t_{Py} (nm)
CoPyM55 →	Co(28)	105	35	25	28	0
CoPyM49 →	Co(28)/Py(10)	105	35	22	28	10
CoPyM58 →	Co(28) /Py(20)	105	35	19	28	20
CoPyM57 →	Co(28) /Py(43)	105	35	15	28	43

5.4.1 M-H Loops by Vibrating Sample Magnetometer

5.4.1.1 General Analysis by VSM

The IP M-H loops measured by VSM of the CTF and the corresponding antidot array are represented in Figure # 5.9. All the loops represented in this figure were measured along the e.a. (referred to Figure # 5.10 and Figure # 5.11). From the loops, we can deduce the following information:

- Figure # 5.9a, Co(28): the antidot array hardens the material with respect to its corresponding CTF.

- Figure # 5.9b, Co(28)/Py(10): the nano-patterning hardens the bilayer system and both layers are completely coupled. The reversal process of the Py layer is dominated by the interaction with the Co layer [184]. The presence of the Py antidot array increases the H_c with regards to that of the array of the Co layer, as can be deduced from the comparison between the curves in Figure # 5.9a and b.

- Figure # 5.9c, Co(28)/Py(20): the presence of the nano-pattern, produces a hardening in the bilayer system with regards to the corresponding CTF; it is interesting to note that particularly in the Co hard phase. The layers in this case are almost decoupled, as deduced form the two large irreversible processes ascribed to the soft, Py, and hard, Co, antidot layers. The presence of Py antidot layer produces a decrease in the H_c in comparison to individual layers.

- Figure # 5.9d, Co(28)/Py(43): the two phases are again decoupled. Note also the larger fractional volume of the Py layer deduced from the jump amplitude of the softer layer. In this case the nano-pattern softens the bilayer system. The layer of Py dominates the bilayer system, as can be deduce from the comparison between the Co(28) and Co(28)/Py(43) (blue curves of Figure # 5.9a and d).

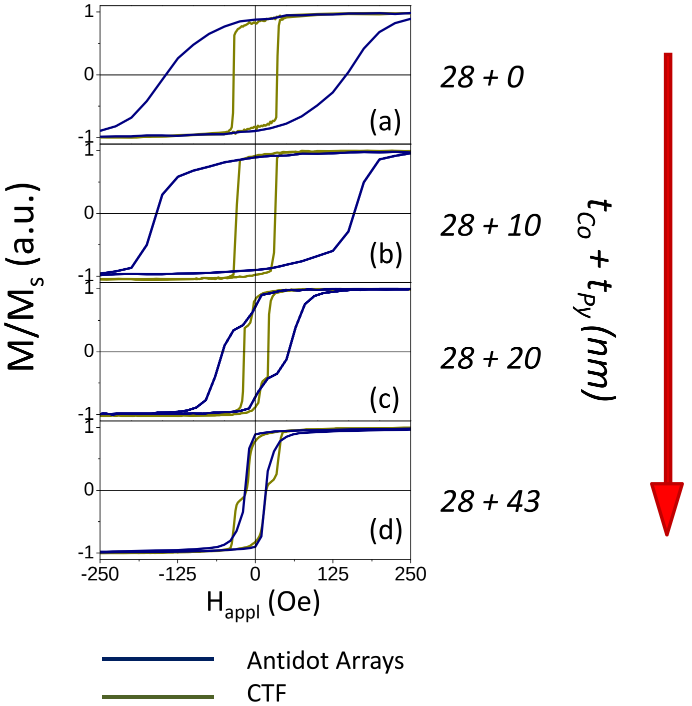

Figure # 5.9. IP M-H loops by VSM of the antidot arrays and their counterparts CTF, along the e.a.

The values of the H_c of the CTF and the antidot arrays are presented in the following table in order to observe how H_c decreases with t_{Py}. Note that the H_c of the bilayer systems do not represent that of the individual layers.

Table # 5.7. H_c of the Co/Py CTF and arrays.

Layers	H_c (Oe) of *CTF*	H_c (Oe) of Arrays	Growth percentage
Co(28)	35	146	320%
Co(28)/Py(10)	30	160	433%
Co(28) /Py(20)	19	26	36%
Co(28) /Py(43)	16	16	0%

The H_c of Co(28)/Py(10) has an increase of 9.6% with respect to the Co(28) arrays by the only presence of the Py layer. Meanwhile bigger increases in the H_c of the arrays in comparison with their counterpart CTF were obtained.

5.4.1.2 Angular Dependence of Coercivity

The IP angular dependence of H_c, of Co and Co/Py antidot arrays was performed in order to analyze the magnetic effect that the presence of the Py layer produces on the magnetic behavior of the Co layer.

The angular dependence of H_c and M_r of the CTF was analyzed in the previous section and represented in Figure # 5.2. The behavior of the CTF with t_{Co} = 20 and 28 nm are nearly the same.

The angular dependence of H_c and the loops along the e.a. and h.a. of the Co(28) array are represented in Figure # 5.10. From these results we can deduce that there is a small anisotropy in the plane of the sample (i.e. an apparent biaxial anisotropy of coercivity results only in a maximum variation from 110 to 145 Oe).

As in the case of the Co arrays in Section 5.3.1, the angular dependence of H_c obtained is similar, presenting a reduced four-fold behavior with values between 110 and 135 Oe. M_r is nearly constant, as can be deduced from the IP M-H loops at three different angles (along the e.a., h.a. and at 90º), presented in Figure # 5.10b.

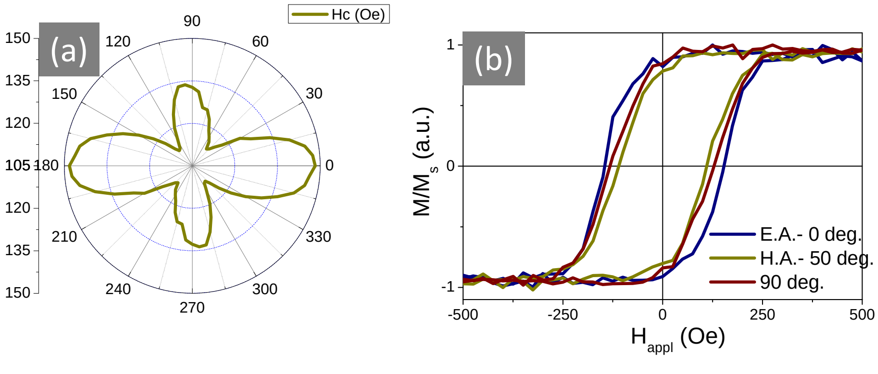

Figure # 5.10. (a) Angular dependence of H_c and (b) IP M-H loops along the e.a., h.a. and 90º of the Co(28) array.

The angular dependences of H_c and M_r of the CTF of Co(28)/Py(10), Figure # 5.11a, exhibit the similar two-fold behavior as the CTF of Co(28). Nevertheless, the most relevant aspect is the magnetic softening introduced by the presence of the upper Py antidot layer. Now, H_c take values between roughly 15 and 35 Oe.

The evolution of M_r can be seeing in Figure # 5.11b, in which the IP M-H loops from the e.a. to the h.a. are represented in the same graph. In this sample, the layer of Py is coupled to the harder layer of Co [186,187].

In the case of the Co(28)/Py(10) antidot array, a much higher values of coercivity are obtained (H_c of around 155 Oe) in comparison with the counterpart CTF. In addition, the angular dependences of both H_c and M_r, show almost no anisotropy. This result can be seeing in Figure # 5.11c and d. This result is rather in agreement with the expected anisotropy in the antidot arrays using the AAM as a template [146].

As explained in Section 5.2, when the softer layer is smaller than the DW width of the harder layer (20 nm in the Co layer), the layers are magnetically rigidly coupled and the composite system is characterized by the averaged magnetic properties of the two layers. In this case, the Py magnetic behavior is dominated by the underlying Co phase which forces the Py to switch together with the Co phase. In summary, we have only one magnetization process.

In the case of the CTF of Co(28)/Py(20), the sample becomes again very soft, with H_c between 5 and 25 Oe, and an apparent anisotropy is also observed, see Figure # 5.11e. In the loops along the e.a. and h.a in Figure # 5.11f, it is possible to observe the presence of a bi-phase magnetic behavior. It indicates that there is certain coupling between the layers, but not as much as in the case of the CTF of Co(28)/Py(10). Each transition (reversal at given fields) is associated to each magnetic phase: Py and Co.

In the angular dependence of H_c (and M_r-not shown) of the Co(28)/Py(20) antidot array, Figure # 5.11g, an uniaxial behavior was found.

The effect of the Py nano-patterning is enhancing the layers of the counterpart CTF, as in the case of the antidot array of Co(28)/Py(10), but in this case the hardening is smaller. The magnetic contribution from both phases becomes relevant and can be observed in a two step magnetization process in the M-H loop along the e.a. in Figure # 5.11h. The low field reversal can be attributed to the switching of the Py while the high-field transition represents the change in magnetization of the Co layer.

Along the h.a. of the Co layer, the magnetization switches completely by reversible rotations, and the bi-phase behavior disappears. At this position, both layer switch at the same field, almost with a linear behavior, with lower remanence.

In the Co(28)/Py(43) CTF, the anisotropy almost disappears, as can be deduced from the angular dependence of H_c (the most significant growth of the H_c goes approximately from 16 to 18 Oe) in Figure # 5.11i. The M-H loops along two orthogonal angles, present a reduced bi-phase behavior, as can be seeing in Figure # 5.11j. In this sample, both layers are almost completely coupled with the switching determined by the soft layer.

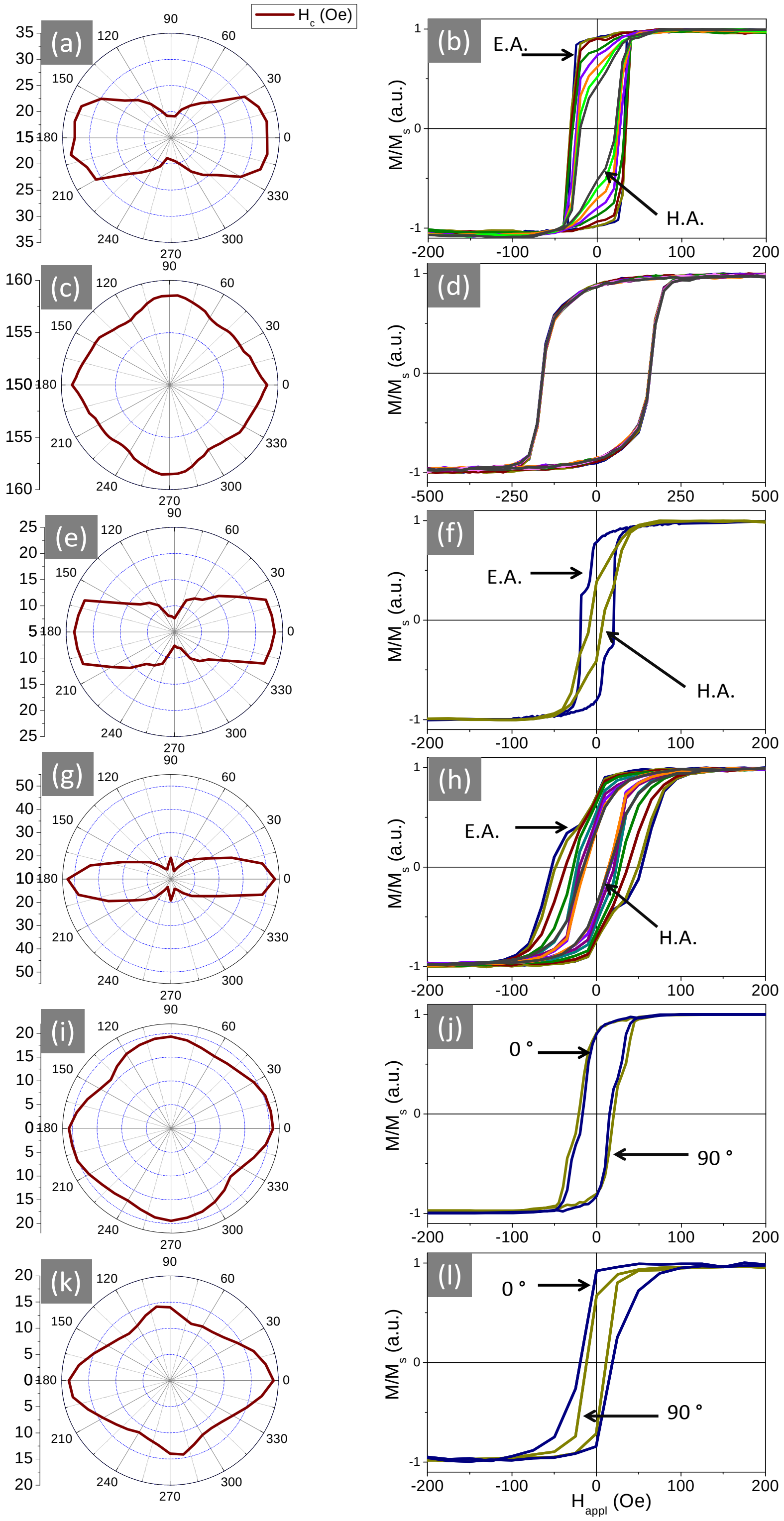
Hc (Oe)
(a)
(b)
E.A.
H.A.
M/Ms (a.u.)
(c)
(d)
(e)
(f)
E.A.
H.A.
(g)
(h)
E.A.
H.A.
(i)
(j)
0 °
90 °
(k)
(l)
0 °
90 °
-200
-100
0
100
200
-500
-250
250
500
Happl (Oe)

Figure # 5.11. (a) Angular dependence of H_c and (b) IP M-H loops from the e.a. at 0º to the h.a. at 90º of the Co(28)/Py(10) CTF. (c) Angular dependence of H_c and (d) IP M-H loops from 0º to 90º of Co(28)/Py(10) antidot array. (e) Angular dependence of H_c and (f) IP M-H loops of the e.a. and the h.a. of the Co(28)/Py(20) CTF. (g) Angular dependence of H_c and (h) IP M-H loops from 0º to 90º of Co(28)/Py(20) array. (i) Angular dependence of H_c and (j) IP M-H loops at 0º and 90º of the Co(28)/Py(43) CTF. (k) Angular dependence of H_c and (l) IP M-H loops at 0º and 90º of the Co(28)/Py(43) array.

In the antidot arrays with Co(28)/Py(43), the magnetic behavior (much lower H_c and shape) of the bilayer system is completely dominate by the layer of Py, see Figure # 5.11l. In this sample, the nano-patterning has almost no effect on the total magnetization process. Recalling Section 5.2, for thicker soft layers than the DW width of the harder layer, the coercivity of the soft layers drops quickly the H_c of the composite, degrading the hard-magnet properties of the system. This arises because magnetization of the soft layer reverses at fields well below that of the hard layer. The H_c of the Co/Py bilayer system is, in fact, very close to that of the Py antidot film, Figure # 4.23.

The angular dependence of H_c of this antidot array was found to be very similar to its corresponding CTF, Figure # 5.11k, although an uniaxial anisotropy is still noticeable. In this sample, as in the case of the Co(28), the shape of the loops along the 0º and 90º, are almost the same, but with a very small difference in H_c and M_r.

5.4.2 M-H Loops and Reversal Curves by MOKE

The surface characterization by MOKE was performed in order to evaluate the magnetic behavior mainly in the Py layer. Figure # 5.12 shows the loops of the single layer of Co(28) and Py(X) arrays, together with the Co(28)/Py(X), (X = 10, 20 and 43 nm). The M-H loops were taken in the IP configuration along the e.a. of each system. The magnetic behaviors of the Co(28)/Py(X) arrays observed in the MOKE measurements are in good agreement with the magnetization measurements performed by VSM.

In Figure # 5.12a the Py(10) array, shows a very soft magnetic behavior. The Co(28)/Py(10) shows a coupled bilayer, because the loop of the Py monolayer becomes a single large irreversible jump, defined by the Co layer. In this sample, the thickness of the Py layer is lower than the δ_{DW} of the Co layer, Section 5.2. The H_c of the bilayer system is almost the same as the Co(28) array, although the loop presents a higher squareness.

Figure # 5.12c, shows that the coercivity of the Co(28)/Py(43) array is almost the same as the H_c of the Py antidot film, the bilayer system is determined by the Py layer.

The bilayer system is coupled again; the loop consists in one single large irreversible jump. In this case, the Py layer is thicker than the DW width of the Co film, so the soft phase (Py layer) nucleates at significantly lower fields, and determined the coercivity of the bilayer system, as explained in Section 5.2.

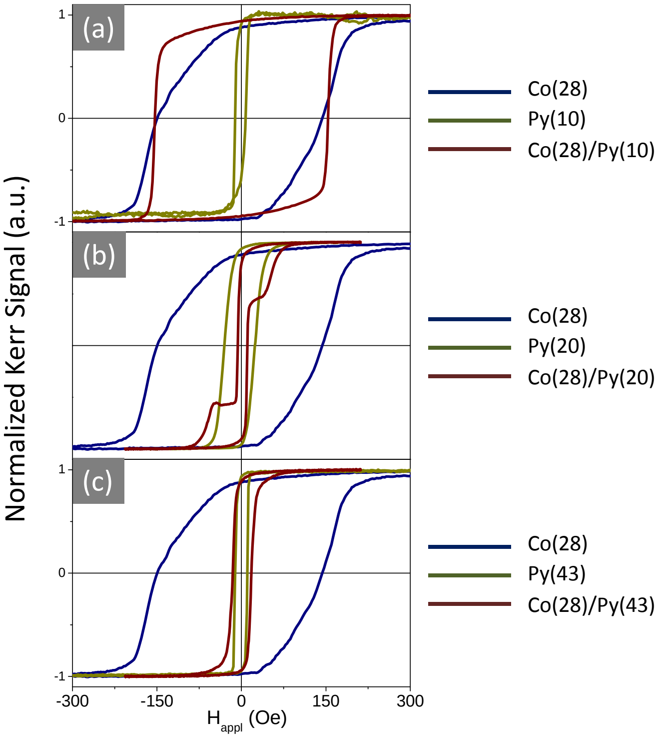

Figure # 5.12. M-H loops by Kerr effect of the Co, Py and Co/Py arrays.

In the case of the array with a Py layer of 20 nm of thickness, the two step magnetization process is more evident. The switching of the Py layer occurs at lower field, while the high-field transition represents the change in magnetization of the Co layer. Nevertheless, the magnetization switching of the Co layer occurs at much lower field.

In this array, the thickness of Py layer has almost the same value as the DW width of the Co layer. As mentioned in Section 5.2, the soft layer remains parallel to the hard layer for fields less than the exchange field, once the magnetic field exceeds this exchange field, the magnetic reversal proceeds via a rotation of the magnetization in the soft layer. This occurs because the soft layer is strongly pinned at the interface while the magnetization at the center or at the surface of the soft layer is freer to follow the orientation of the external field.

This effect is shown schematically in Figure # 5.13, where a hard/soft magnetic bi-layer is presented. The coupled spins in the soft layer exhibit continuous rotation as in a Bloch wall, with increasing angle of rotation with increasing distance from the interface of the hard layer. Such magnets exhibit reversible demagnetization curves since the soft layers rotate reversible back into alignment with the hard phase if the reverse field is removed. This reversing process is often referred to as an exchange-spring process by analogy with the elastic motion of a mechanical spring.

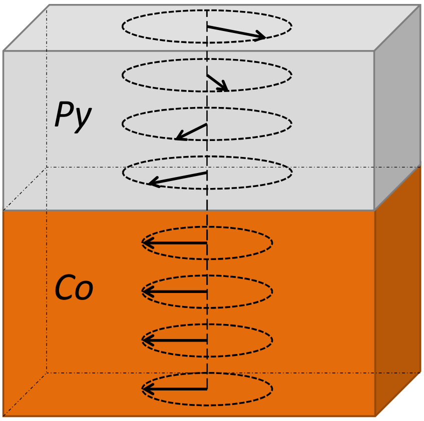

Figure # 5.13. Illustration of a magnetic exchange-spring state in the Co/Py bi-layer system [168].

In order to investigate the presence of a coupling between the two phases, and thanks to the two step nature of this particular sample, a low field study of the Py remagnetization process has been performed by MOKE, leaving the underlying Co layer magnetically unchanged, Figure # 5.14. The M-H loop by Kerr effect is represented in Figure # 5.14a, where the bi-phase behavior is more evident, and the irreversible field (H_{irr}) correspond to the second irreversible transition. This H_{irr} is referring to the field needed to switch the magnetization of the Co layer; once this field is overcome the magnetization of the Co layer switches the direction.

The bilayer system was pre-magnetized at positive high field (≈ 200 Oe) so to overcome the H_{irr} of the Co layer. Then the field was swept at different fields, where only the Py layer magnetizes, as shown in Figure # 5.14b-d. The coupling with the Co is reflected by the bias field experience by the Py.

As mentioned before, the exchange-bias occurs because the soft layer is strongly pinned at the interface, while the magnetization at the surface of the Py layer is freer to follow the orientation of the external field. As the field increases (not exceeding the H_{irr}), the bias increases, because the Co layer keeps the magnetization direction, while the magnetization of the Py layer gets more aligned to the applied field. The bias disappears when the field is near to H_{irr}. At higher fields than H_{irr}, the composite system behaves as two different entities, with the two step magnetization process. In summary, the magnetic behavior is dominated by the bias field due to the remanence of the hard layer.

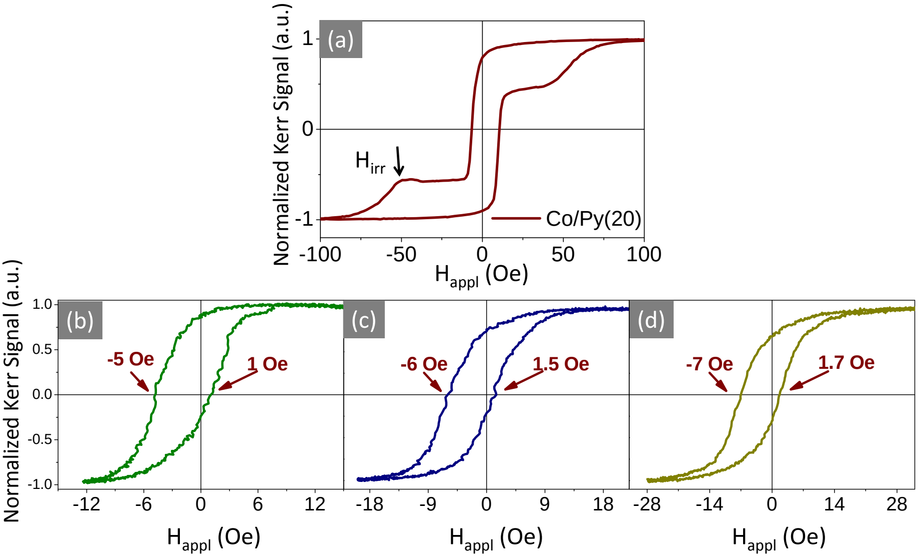

Figure # 5.14. (a) M-H loops by Kerr effect with marked H_{irr}; (b-d) Bias field of the Co(28)/Py(20) array at different maximum applied field.

5.4.3 Evaluating the Increases of the $(BM)_{max}$ Product

5.4.3.1 Theoretical Values

For the $(BH)_{max}$, taking Eq. (5.1) and the values of Table # 5.1, the theoretical value for the Co(28) CTF is:

$$(BH)_{max} = \frac{J_s^2}{4\mu_0} = \frac{\mu_0 M_s^2}{4} = 0.2\ MGOe \qquad \text{Eq. (5.7)}$$

5.4.3.2 Experimental values

For the experimental calculation of the $(BH)_{max}$, the M-H loops must to be plotted in B-H form. The maximum energy density of a permanent magnet is determined by the point on the second quadrant branch of the B-H loop, which gives the largest area for an enclosed rectangle [52].

From the following expressions, the M axis of the experimental M-H loop must be changed by B [188].

$$\vec{B} = \mu_0 (H + M) = H + \mu_0 \vec{M} = H + 4\pi\vec{M}\ (c.g.s) \qquad \text{Eq. (5.8)}$$

The unit of M is emu/cm^3, but the magnetic moment given by the VSM is emu; thus an approximation of the volume is needed. First, the shape of the antidot film is approximately cylinder, with a thickness of 28 nm (2.8·10^{-6} cm) [in the case of Co(28)] and a radius of 2 mm (0.2 cm). As the material corresponding to the voids is sputtered inside the wall of the pores, it is possible to deduce that there is no material looses. With this value of volume, the magnitude of m [emu] was changed to M [emu/cm^3] and the axis of M was change to B with the expression in Eq. (5.8**)**.

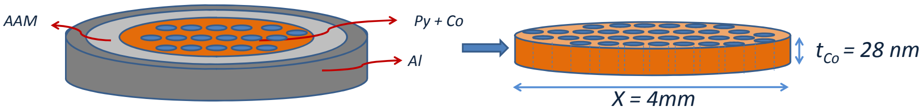

Figure # 5.15. Approximated volume of the film with the antidot arrays.

$$V = \pi r^2 \cdot t_{Co} = 3.52 \cdot 10^{-7}\ cm^3 \qquad \text{Eq. (5.9)}$$

The B-H loop of the Co(28) CTF and antidot array are represented in Figure # 5.16a and b, where the rectangle with the maximum value of BH is represented with a grey rectangle. The corresponding value of the Co(28) CTF is 0.14 MGOe and the product of the corresponding array is 0.25 MGOe. The latter is more consistent with the theoretical value in Eq. (**5.7)**, but still is extremely low for its application as “spring magnets”. Although an increases of 78% of the product of $(BH)_{max}$ of the antidot in comparison with the CTF, shows the hardness enhancement of the magnetic properties when using antidot arrays.

$$CTF: (BH)_{max} = 0.14\ MGOe \qquad \text{Eq. (5.10)}$$

$$Antidot\ array: (BH)_{max} = 0.25\ MGOe \qquad \text{Eq. (5.11)}$$

In the case of the arrays of Co(28)/Py(10), the volume corresponds to:

$$V = \pi r^2 \cdot t_{Co+Py} = 4.78 \cdot 10^{-7}\ cm^3 \qquad \text{Eq. (5.12)}$$

And from the B-H loops of the antidot arrays together with the corresponding CTF are represented in Figure # 5.16c and d. In the case of the CTF, the product increases with respect to the Co(28) CTF, and has a value of 0.15 MGOe. In the antidot array a visible increases in the value of B and a slight higher value of H_c, results in an increases of the $(BH)_{max}$ of 0.37 MGOe. The increase of the product with respect to the Co(28) array is 44% and with respect to the CTF is 140%.

$$(BH)_{max} = 0.37\ MGOe \qquad \text{Eq. (5.13)}$$

Table # 5.8. Values of the product $(BH)_{max}$ of the CTF and the antidot arrays.

Layers	***(BH)**$_{max}$*	
	CTF (MGOe)	**Arrays (MGOe)**
Co(28)	0.14	0.25
Co(28)/Py(10)	0.15	0.37

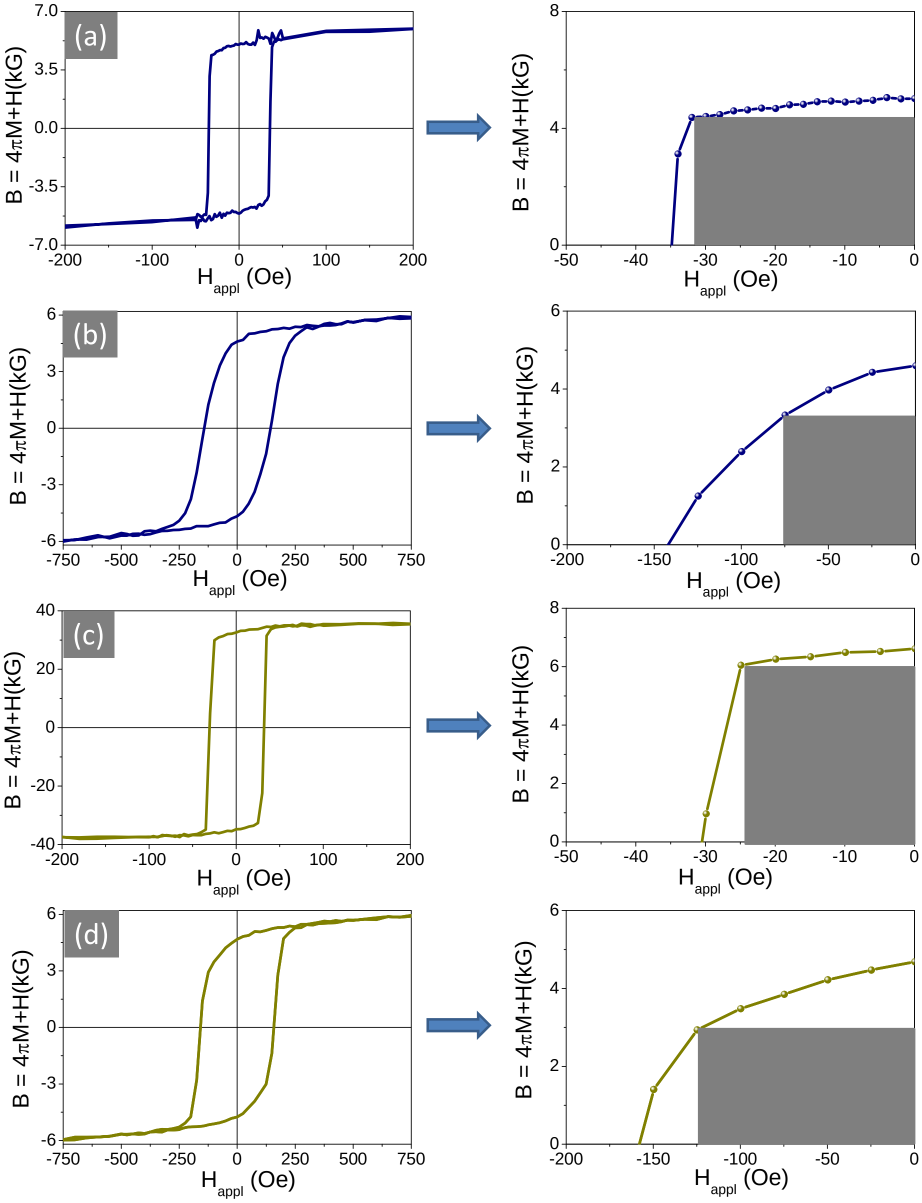

Figure # 5.16. B-H loop (left) and $(BH)_{max}$ product (right) in the second quadrant of (a) Co(28) CTF; (b) Co(28) antidot array; (c) Co(28)/Py(10) CTF; (d) Co(28)/Py(10) antidot array;

5.5 SUMMARY

The magnetic characterization of the Co antidot array was performed, determining the same enhancement of the magnetic properties, as in the case of the Py antidot arrays. The magnetic behavior of the Co/Py bilayer system was determined, finding the relation between the thickness of the Py layer and the coupling between both layers.

6. CHAPTER 6

6.1 CONCLUSIONS

We present a summary of the most important conclusions of the studies carried out in this work.

A systematic study on the preparation and morphology properties of anodic alumina membranes and antidot thin films was presented in Chapter 3. The more interesting conclusions in this regard are:

a) Concerning the preparation of the porous alumina templates, a smaller pore diameter in the anodic alumina membrane (AAM) is obtained when lower temperatures were applied during the anodization process. This feature gives us a broader range of diameter of the nanoholes.

b) In order to achieve the optimum flatness of the final antidot surface, an etching by ion-milling was performed to the AAM surface to reduce its intrinsic roughness.

c) Controlled production of AAM allowed us to obtained antidot thin films of Permalloy (Py) and Cobalt (Co) with tailored antidot diameter from 10 to 70 nm, and thickness up to 138 nm.

d) The sputtering conditions need to be carefully selected to produce thin films with small grain size of the Py and Co, in order to achieve the optimal topographic and morphological characteristics of the antidot arrays.

e) A partial closure of the antidot diameter occurs during the sputtering growth of the metallic film over the membrane. A relationship between the final antidot diameter and thickness was determined.

f) An estimation of the penetration depth of the MOKE's laser on the Py antidot arrays was determined using the ellipsometry system, going from 13 to 22 nm in the arrays with 25 and 56 mm of diameter, respectively. Thanks to these results a more precise analysis of the hysteresis loop by Kerr effect was made.

An analysis of the magnetic properties of the Py antidot arrays was presented in Chapter 4. The parallel magnetic characterization of the continuous thin films (CTF) and the antidot arrays grown under different sputtering conditions allows us to find the most important parameters influencing the magnetic behavior. The magnetic characterization of the antidot arrays with different dimensions gave us a deeper understanding of the magnetization process of the samples. The most important conclusions of this chapter are:

a) The antidot arrays over the AAM reproduce the hexagonal lattice of the templates. The inclusion of the pattern of nanoholes to the CTF produces a significant magnetic hardening with an increase of coercivity up to 200 times.

b) The geometric domains and the boundaries-like dislocations play an important role in the magnetic behavior of the arrays, contributing to the creation of peculiar magnetic domain structures.

c) The dimensions of the nanoholes determine the magnetic behavior of the antidot arrays and produce different magnetic domain structures. The interactions among the accumulated charges around the nanoholes are the main responsible of the magnetic alteration on the arrays in comparison to their counterpart CTF, creating important out-of-plane component.

d) Distributed charges around the nanoholes induce local magnetic fields that modify the local distribution of magnetic moments in their neighborhood.

e) For small-diameter antidots, they give rise to moderate magnetic hardening.

f) For high-diameter antidots, a reorientation of magnetic moments towards out-of-plane directions originated a significant in-plane magnetic hardening.

g) With regards to the influence of the thickness, CTF with tiny thickness contains Néel walls which disappear with the presence of the antidot arrays due to the magnetic energy stored in the surface of the pores. Moreover, antidot arrays with large thickness keep the magnetization process by motion of Bloch walls, as in the CTF, although the coercive field drastically increases.

Several techniques were employed in this characterization deepening in the magnetic properties of the antidot arrays. Such as, surface characterization by Kerr effect or FORC diagrams by VSM. The most important conclusions about these techniques are:

h) The MOKE system allows us to discriminate the behavior at the surface from the bulk system, showing hysteresis loops that are different from the ones taken by

VSM. As the thickness of the arrays decreases, more differences between the loops by both techniques were obtained.

i) The Kerr effect allows us to determine the direct influence of the material inside the wall of the pores. When the thickness is thin enough and the antidot diameter is large we observe a kind of bi-phase behavior.

j) The diameter of the laser must be taken into account during the characterization by MOKE due to the geometric feature of the antidot arrays over AAM. If the spot has a diameter big enough to cover several geometric domains, the analysis of the results should consider the behavior of many domains with different orientation of the easy axis.

k) The FORC measurements support and complement the analysis performed with the hysteresis loops. These diagrams give complementary information regarding the irreversible processes involved in the magnetization reversal. This technique allows us discriminating the overall magnetic behavior from the interaction processes.

A special characterization by imaging was performed by XPEEM. The magnetization process, as followed by the XPEEM images under increasing in-plane applied field, is clearly determined by the topological ordering of the antidot arrays. Owing to the lack of other anisotropy terms, we conclude that two geometrical facts determine the magnetization process in Py antidot arrays hexagonally ordered at the microscopic scale:

a) For films with D = 105 nm and larger antidot diameter, the partial balance between stray fields generated by charges at the lateral surface of antidots and at the upper-bottom surface promotes a modest in-plane effective magnetic anisotropy. Besides, that the geometric parameters cause that the topography dominates the magnetic structure creating *non-homogeneous magnetic structures*.

b) We found pinning mechanism at the border of geometric domains; a softer magnetization process takes place inside geometric domains, while harder process are originated at the borders of such geometric domains.

c) The magnetic behavior inside each geometric domain depends on the orientation of the e.a. relative to the applied field, demonstrating that the *non-homogeneous magnetic structures* are formed as a consequence of the different local magnetic anisotropy of the geometric domains. These domains behave as grains or crystals with individual e.a. orientation relative to the applied field, and the average of all the domains is the overall magnetic property of the system. The coercivity of the system is lower than the presented in each individual geometric domain.

d) We should finally emphasize that the high-spatial resolution and sensitivity of XPEEM technique under applied magnetic field, enables the magnetic characterization at a very local scale (down to 20 nm) including magnetic domain structure imaging and quantitative hysteresis loops analysis. Nevertheless, complementary MOKE and VSM magnetic measurements are necessary to reach a full understanding of the magnetization process.

An analysis of the magnetic properties of the Co and Co/Py antidot arrays was presented in Chapter 5. The Co/Py magnetic characterization was performed with different Py thickness, showing different coupling effects. The most important conclusions of this chapter are:

Regarding the Co antidot arrays:

a) Co antidot arrays exhibit magnetic hardening with regards to the Co CTF. That is similar to what was deduced for Py antidot arrays.

b) The hardening depends on the dimensions of the antidots: increasing the antidot diameter results in the increase of in-plane coercivity as a result of the more complex magnetization distribution and enhanced pinning at the antidots.

About the effect of the presence of an addition softer Py layer over the Co antidot films:

c) The effect of Py on the magnetic behavior of the bi-layer film depends on the relative thickness of Py and Co.

d) For Py thickness smaller than the exchange length or domain wall width of the Co layer, the Py is fully coupled to the Co film. Besides that, the exchange coupling induces a magnetic hardening in comparison with the single Co antidot layer.

e) For intermediate thickness of Py, both layers contribute with differentiated process, as deduced from the presence of two larger irreversibilities.

f) For very large Py layer thickness, the system is coupled and the coercivity is determined mostly by that of the Py.

6.2 CONCLUSIONES

Presentamos un resumen de las conclusiones más importantes de los estudios realizados en este trabajo.

En el Capítulo 3, se presentó un estudio sistemático sobre la preparación y las propiedades morfológicas de las Membranas Porosas de Alúmina Anódica (MPAA) y las láminas de antidots. Con respecto a esto, las conclusiones más interesantes son:

a) Concerniente a la preparación de las plantillas de alúmina porosa, un diámetro más pequeño se obtuvo cuando aplicamos una temperatura más baja de 0º durante el proceso de anodización. Esta propiedad nos da un rango más amplio de diámetros de los nano-agujeros.

b) Con el fin de lograr una superficie de antidots más plana, se ha realizado un pulido por ataque iónico sobre la superficie de las MPAA, con el propósito de reducir su rugosidad intrínseca.

c) Una producción controlada de las MPAA nos ha permitido obtener láminas delegadas de antidots de Permalloy (Py) y Cobalto (Co) con diámetros desde los 10 hasta los 70 nm, y con grosores de hasta 138 nm.

d) Las condiciones de sputtering (o pulverización catódica) se han seleccionado de manera cuidadosa, para producir láminas delgadas con tamaño de grano suficientemente pequeños, tanto de Py como de Co; esto con el fin de lograr arreglos de antidots con características topográficas y morfológicas óptimas

e) Un cierre parcial en el diámetro de los antidot se produce durante el crecimiento de las láminas metálicas sobre la membrana. Se determinó la relación entre el poro final del antidot y el grosor.

f) En los arreglos de antidots de Py, se estimó la profundidad de penetración del láser del MOKE usando el sistema de elipsometría, cuyos valores van desde los 13 hasta los 22 nm en los arreglos con 25 y 56 nm de diámetro final de antidots, respectivamente. Gracias a estos resultados, hemos podido realizar un análisis más preciso de los ciclos de histéresis tomados por el MOKE.

En el Capítulo 4, se presentó un análisis de las propiedades magnéticas de los arreglos de antidot de Py. La caracterización paralela de las láminas continuas delgadas y los arreglos de antidot crecidas por sputtering con diferentes condiciones, nos permite encontrar los parámetro más importantes que influencia el comportamiento magnético. La caracterización magnética de los arreglos de antidot con diferentes dimensiones nos dió un entendimiento más profundo sobre el proceso de imanación de las muestras. Las conclusiones más importantes de este capítulo son:

a) Los arreglos de antidot sobre MPAA reproduce la red hexagonal de las membranas. La incorporación del patrón de nano-agujeros en las láminas delgadas producen un endurecimiento magnética significante, con un incremento de coercitividad de hasta 200 veces.

b) Los dominios geométricos y las dislocaciones que actúan como fronteras, juegan un papel importante en el comportamiento magnético de los arreglos, contribuyendo a la creación de estructuras de dominios magnéticos peculiares.

c) Las dimensiones de los nano-agujeros determinan el comportamiento magnético de los arreglos de antidot y producen dominios magnéticos diferentes. Las interacciones entre las cargas acumuladas alrededor de los agujeros, son los principales responsables de la alteración magnética en los arreglos en comparación con sus contrapartes láminas delegadas, creando un componente importante fuera del plano.

d) Las cargas alrededor de los nano-agujeros inducen campos magnéticos que modifican la distribución local de los momentos magnéticos en sus vecindades.

e) Para diámetros pequeños de antidots, dan lugar a moderado endurecimiento magnético.

f) Para un diámetro mayor de antidots, una reorientación de los momentos magnéticos hacia direcciones fuera del plano, se originó una significativa en el plano magnético endurecimiento.

g) Con respecto a la influencia del grosor, las láminas delgadas con grosores pequeños, contienen paredes de Néel las cuales desaparecen por la presencia de la red de agujeros debido a la energía almacenada en la superficie de los poros. Por otra parte, los arreglos de antidot con grosores mayores mantienen el proceso de imanación por movimiento de paredes de Bloch, al igual que en las láminas continuas, aunque el campo coercitivo aumenta drásticamente.

Varias técnicas se emplearon en la caracterización profundizando en las propiedades magnéticas de los arreglos de antidots. Así como una caracterización superficial por el efecto Kerr, o con diagramas de FORC por VSM. Las conclusiones más importantes acerca de estas técnicas son:

h) El sistema MOKE permite la discriminación del comportamiento de la superficie del sistema completo, mostrando ciclos de histéresis diferentes a los tomados en el VSM. A como el grosor de los arreglos disminuyen, mayores son las diferencias encontradas entre los ciclos tomadas por cada técnica.

i) El efecto Kerr permite determinar directamente la influencia del material dentro de las paredes de los poros. Cuando los arreglos tienen grosores suficientemente delgados y diámetros de los agujeros grandes, hemos observado un tipo de comportamiento bifásico.

j) El diámetro del laser debe tomarse en cuenta durante la caracterización del MOKE, debido a las propiedades geométricas de los arreglos de antidot sobre MPAA. Si el spot tiene un diámetro suficientemente grande como para cubrir varios dominios geométricos, el análisis de los resultados debe considerar el comportamiento de muchos dominios con ejes fáciles con diferentes orientaciones.

k) Las medidas de FOCR respaldan y complementan el análisis hecho con los ciclos de histéresis. Estos diagramas dan información complementaria con respecto a los procesos irreversibles involucrados en la inversión de imanación. Esta técnica permite la discriminación del comportamiento general de los procesos de interacciones.

Una caracterización especial por toma de imágenes fue realizada por XPEEM. El proceso de imanación, seguida de imágenes por XPEEM con aumento de campo aplicado a lo largo del plano, está claramente determinado por el ordenamiento topológico de las matrices de antidot. Debido a la falta de otros términos de anisotropía, llegamos a la conclusión de que el proceso de imanación en las matrices de antidot hexagonal ordenados de Py, está determinado por dos factores geométricos a escala microscópica:

e) Para matrices con D = 105 nm y diámetros mayores de antidot, el balance parcial entre los stray fields generados por las cargas a los laterales de la superficie de los agujeros, y entre las superficies superior-inferior, promueven una modesta anisotropía efectiva en el plano de la muestra. Además, los parámetros geométricos causan que la topografía sea dominante en la creación de dominios magnéticos, creando *estructuras magnéticas no-homogéneas*.

f) Hemos encontrado mecanismos de anclaje en los bordes de los dominios geométricos; un proceso de imanación más blando tiene lugar dentro de los dominios geométricos, mientras procesos más duros se originan en los bordes de dichos dominios.

g) El comportamiento magnético dentro de cada dominio geométrico depende de la orientación del eje fácil con respecto al campo aplicado, demostrando que las *estructuras magnéticas no-homogéneas* se forman a consecuencia de las diferentes anisotropías magnéticas locales de los dominios geométricos. Estos dominios se comportan como granos o cristales con orientación individual del eje fácil con respecto al campo aplicado, y el promedio de todos los dominios corresponde al comportamiento magnético total del sistema. La coercitividad de todo el sistema es mucho más baja que la que posee cada dominio geométrico.

h) Finalmente debemos hacer énfasis en que la alta resolución espacial y la alta sensibilidad de la técnica de XPEEM bajo campo aplicado, permite la caracterización magnética a una escala local (de hasta 20 nm) incluyendo la toma de imágenes de los dominios magnéticos y el análisis cuantitativo de los ciclos de histéresis. No obstante, medidas complementarios por MOKE y VSM son necesarias por lograr un entendimiento completo de los procesos de imanación.

El análisis de las propiedades magnéticas de matrices de antidot de Co y Co/Py fue presentada en el Capitulo 5. La caracterización magnética de Co/Py fue realizada con diferentes grosores de Py, demostrado diferentes efectos de acoplamiento. Las conclusiones más importantes de este capítulo son:

Con respecto a las matrices de antidot de Co:

g) Las matrices de antidot de Co exhiben un endurecimiento con respecto a las láminas continuas de Co. Este comportamiento es similar a la deducida en las matrices de Py.

h) El endurecimiento depende de la geometría de los antidots: mayor diámetro resulta en el incremento de la coercitividad en el plano como resultado de una distribución más compleja de imanación y el mayor anclaje en los antidots.

A cerca de los efectos presentes por la adición de la lámina blanda de Py en las láminas de antidots de Co:

i) El efecto de Py en las propiedades magnéticas en las láminas bi-capa depende de el grosor relativo de Py y Co.

j) Para grosores de Py menores a la longitud de canje o a la anchura de las paredes de dominios de la lámina de Co, el Py es completamente acoplado al Co. Además, el acoplamiento de canje induce a un endurecimiento magnético en comparación a la lámina de matrices de antidot de Co.

k) Para grosor intermedio de Py, ambas capas contribuyen con procesos diferentes, como se ha podido deducir por la presencia de dos grandes irreversibilidades.

l) Para grosor mayor de la capa de Py, el sistema está acoplado y la coercitividad está determinado principalmente por el Py.

6.3 PUBLICATIONS

Several contributions were made during these four years of work. The publications directly from this study are:

1. "X-*Ray Photoemission Electron Microscopy Studies of Magnetization in Py Antidot Array Thin Films*", K. J. Merazzo, C. Castán-Guerrero, J. Herrero-Albillos, F. Kronast, F. Bartolomé J. Bartolomé, J. Sesé, R. P. del Real, L.M. García, M. Vázquez, *Phys. Rev. B,* vol.85, no. 18, pp.184427, 2012.

2. "*Geometry-dependent magnetization reversal mechanism in ordered Py antidot arrays*", K. J. Merazzo, D. C. Leitao, E. Jiménez, J. P. Araujo, J. Camarero, R. P. del Real, A. Asenjo and M. Vázquez, *J. Phys. D: Appl. Phys.*, vol.44, no.50, pp. 505001, 2011.

3. "*Dependence of magnetization process on thickness of Permalloy antidot arrays*", K. J. Merazzo, R. P. del Real, A. Asenjo, and M. Vázquez, *J. Appl. Phys.*, vol.109, no.7, pp.07B906, 2011

Several collaborations and studies during these four years which are not related directly to this work were performed:

4. "*Anisotropic magnetoresistance in vanishing-magnetostriction amorphous microwires with different geometries*", K. J. Merazzo, G. A. Badini Confalonieri, M. Vázquez, and F. Batallán Casas, *IEEE Trans.Magn,* vol. 46, no. 2, pp. 361, 2010

5. "*Fabrication and magnetic characterization of cobalt antidot arrays: effect of the surrounding continuous film*", C. Castán, J. Sesé, J. Bartolomé, F. Bartolomé, J. Herrero-Albillos, F. Kronast, P. Strichovanec, K. J. Merazzo, M. Vázquez, P. Vavassori and L.M. García, *J. Nanosci. Nanotechnol*. Accepted

6. "*Micromagnetism of dense Permalloy antidot lattices from anodic alumina templates*", P. Gawronski, K. J. Merazzo, O. Chubykalo-Fesenko, R.P. del Real and M. Vázquez, *EPL*.in progress.

7. "*Anisotropic magnetoresistance in biphase microwires*". G. Infante, K. J. Merazzo, G. A. Badini-Confalonieri, F. Batallán, and M. Vázquez, *J. Appl. Phys*., vol. **105**, no. 7, pp. 07A320, 2009.

8. "*Frequency dependence of switching field in the soft nucleus of FeSiB-CoNi microwires*". G. Infante, J. Torrejón, K. J. Merazzo, G. A. Badini-Confalonieri, M. Vázquez, *Phys. Status Solidi A*, vol. 206, no. 4, pp. 622, 2009.

9. “*Circular Magnetoelastic Anisotropy Induced in the Nucleus of a FeSiB-CoNi Soft-Hard Bi-Phase Microwire*”. J. Torrejón, G. Infante, K. J. Merazzo, and G. A. Badini-Confalonieri, *IEEE Trans.Magn,* vol. 44, no. 11, pp.3942, 2008

Additionally, some contributions are in progress:

10. “*Antidot arrays of Co and Co/Py over anodic alumina templates*”, K.J. Merazzo, G. A. Badini Confalonieri, R. P. del Real and M. Vázquez, in progress.

11. “*Magnetic Characterization of Co antidot arrays*”, K.J. Merazzo, G. A. Badini Confalonieri, R. P. del Real and M. Vázquez, in progress.

REFERENCES

---

[1] R. P. Feynmann, “There is plenty of room at the bottom”, *Eng. Sci*., vol. 23, pp. 22, 1960.

[2] C. A. F. Vaz, J. A. C. Bland and G. Lauhoff, “Magnetism in ultrathin film structures”, *Rep. Prog. Phys.,* vol.71, no.5, pp.056501, 2008.

[3] M. N. Baibich, J. M. Broto, A. Fert, F. Nguyen Van Dau, F. Petroff, P. Etienne, G. Creuzet, A. Friederich and J. Chazelas, “Giant Magnetoresistance of (001)Fe/(001)Cr Magnetic Superlattices ” *Phys. Rev. Lett*., vol.61, no.21, pp.2472, 1988.

[4] G. Binasch, P. Grünberg, F. Saurenbach and W. Zinn, “Enhanced magnetoresistance in layered magnetic structures with antiferromagnetic interlayer exchange”, *Phys. Rev.* B, vol.39, no7, pp.4828, 1989.

[5] W. J. Gallagher and S. S. P. Parkin, “Development of the magnetic tunnel junction MRAM at IBM: From first junctions to a 16-Mb MRAM demonstrator chip”, *IBM J. Res. Dev*., vol.50, no.1, pp.5, 2006.

[6] G. A. Prinz, “Spin-Polarized Transport”,*Phys. Today*, vol.48, no.4, pp.58, 1995.

[7] G. A. Prinz, “Magnetoelectronics”, *Science*, vol.282, no.5394, pp. 1660, 1998.

[8] S. A. Wolf, D. D. Awschalom, R. A. Buhrman, J. M. Daughton, S. von Molnar, M. L. Roukes, A. Y. Chtchelkanova and D. M. Treger, “Spintronics: A Spin-Based Electronics Vision for the Future”, *Science*, vol.294, no.5546, pp.1488, 2001.

[9] I. Zutic, J. Fabian and S. Das Sarma, “Spintronics: Fundamentals and applications”, *Rev. Mod. Phys*., vol.76, no.2, pp. 323, 2004.

[10] M. Bowen, M. Bowen, V. Cros, F. Petroff, A. Fert, C. Martínez Boubeta, J. L. Costa-Krämer, J. V. Anguita, A. Cebollada, F. Briones, J. M. de Teresa, L. Morellón, M. R. Ibarra, F. Güell, F. Peiró, and A. Cornet, “Large magnetoresistance in Fe/MgO/FeCo(001) epitaxial tunnel junctions on GaAs(001)”, *Appl. Phys. Lett*., vol.79, no.11, pp.1655, 2001.

[11] S. S. P. Parkin, C. Kaiser, A. Panchula, P. M. Rice, B. Hughes, M. Samant and S. H. Yang, “Giant tunnelling magnetoresistance at room temperature with MgO (100) tunnel barriers ” *Nat. Mater*., vol.3, pp.862, 2004.

[12] S. Yuasa, T. Nagahama, A. Fukushima, Y. Suzuki and K. Ando, “Giant room-temperature magnetoresistance in single-crystal Fe/MgO/Fe magnetic tunnel junctions”, *Nat. Mater*., vol.3, pp.868, 2004.

[13] D. Suess, T. Schrefl, R. Dittrich, M. Kirschner, F. Dorfbauer, G. Hrkac, and J. Fidler, “Exchange spring recording media for areal densities up to 10 Tbit/in2”, *J. Magn. Magn. Mater.*, vol.290-291, pp.551, 2005.

[14] D. Suess, T. Schrefl, S. Fähler, M. Kirschner, G. Hrkac, F. Dorfbauer, and J. Fidler, “Exchange spring media for perpendicular recording”, *Appl. Phys. Lett.*, vol. 87, no.1, pp. 012504, 2005.

[15] Y. Tserkovnyak, A. Brataas, G. E. W. Bauer and B. I. Halperin, “Nonlocal magnetization dynamics in ferromagnetic heterostructures ”, *Rev. Mod. Phys.*, vol.77, no.4, pp.1375, 2005.

[16] A. O. Adeyeye, S. Goolaup, N. Singh, W. Jun, C. C. Wang, S. Jain and D. Tripathy, “Reversal Mechanisms in Ferromagnetic Nanostructures”, *IEEE Trans. Magn.*, vol.44, no.7, pp.1935, 2008.

[17] C. C. Wang, A. O. Adeyeye and N. Singh, “Magnetic and transport properties of multilayer nanoscale antidot arrays”, *Appl. Phys. Lett.*, vol.88, no.22, pp. 222506, 2006.

[18] R. P. Cowburn, A. O. Adeyeye and J. A. Bland, “Magnetic domain formation in lithographically defined antidot Permalloy arrays”, *Appl. Phys. Lett.*, vol.70, no.17, pp.2309, 1997.

[19] M. B. A. Jalil, “Bit isolation in periodic antidot arrays using transverse applied fields
”, *J. Appl. Phys.*, vol.93, no.10, pp.7053, 2003.

[20] J. G. Zhu, and Y. Tang, “Micromagnetics of Percolated Perpendicular Media”, *IEEE Trans. Magn.*, vol.43, no.2, pp.687, 2007.

[21] G. Gubbiotti, S. Tacchi, M. Madami, G. Carlotti, A. O. Adeyeye, and M. Kostylev, “Brillouin light scattering studies of planar metallic magnonic crystals”, *J. Phys. D: Appl. Phys*, vol.43, no.26, 264003, 2010.

[22] M. I. Montero, Kai Liu, O. M. Stoll, A. Hoffmann, J. J. Åkerman, J. I. Martín, J. L. Vicent, S. M. Baker, T. P. Russell, C. Leighton, J. Nogués and Ivan K Schuller, “Nanostructures and the proximity effect”, *J. Phys. D: Appl. Phys.,* vol.35, no.19, pp. 2398, 2002.

[23] J. M. Gonzalez, O. A. Chubykalo-Fesenko, F. Garcia-Sanchez, J. M. T. Bruna, J. Bartolome, and L. M. G. Vinuesa, “Reversible magnetization variations in large field ranges associated to periodic arrays of antidots”, *IEEE Transactions on Magnetics,* vol.41, no. 10., pp.3106, 2005.

[24] V. V. Kruglyak, S. O. Demokritov, and D. Grundler, “Magnonics”, *J. Phys. D: Appl. Phys.*, vol.43, no.26, pp.264001, 2010.

[25] S. Neusser and D. Grundler, “Magnonics: Spin Waves on the Nanoscale”, *Adv. Mater.*, vol.21, no.28, pp.2927, 2009.

[26] L. J. Heyderman, F. Nolting and C. Quitmann, “X-ray photoemission electron microscopy investigation of magnetic thin film antidot arrays”, *Appl. Phys.Lett.*,vol.83, no.9, pp.1797, 2003.

[27] R.P. Cowburn, A.O. Adeyeye, J.A.C. Bland, “Magnetic switching and uniaxial anisotropy in lithographically defined anti-dot Permalloy arrays”, *Journal of Magnetism and Magnetic Materials* vol.173, no.1, pp.193, 1997.

[28] L. Torres, L. Lopez-Diaz, O. Alejos, J. Iñiguez, “Micromagnetic study of lithographically defined non-magnetic periodic nanostructures in magnetic thin films”, *Physica B*, vol 275, no. 1–3, pp.59, 2000.

[29] A. O. Adeyeye, J. A. C. Bland and C. Daboo, “Magnetic Properties of Arrays of holes in Ni80Fe20 film”, *Appl. Phys. Lett.*, vol. 70, no. 23, pp. 3164, 1997.

[30] I. Guedes, M. Grimsditch, V. Metlushko, P. Vavassori, R. Camley, B. Ilic, P. Neuzil and R. Kumar, “Magnetization reversal in an Fe film with an array of elliptical holes on a square lattice”, *Phys. Rev.* B 67, no.2, pp.024428, 2003.

[31] C. Castán, J. Sesé, J. Bartolomé, F. Bartolomé, J. Herrero-Albillos, F. Kronast, P. Strichovanec, K. J. Merazzo, M. Vázquez, P. Vavassori and L.M. García, “Fabrication and magnetic characterization of cobalt antidot arrays: effect of the surrounding continuous film”, *J. Nanosci. Nanotechnol.* Accepted

[32] A. Krasyuk, S.A. Nepijko, A. Oelsner, C.M. Schneider, H.J. Elmers, and G.Schonhense, “Magnetic stray fields of patterned permalloy structures investigated by photoemission electron microscopy”, *Appl. Phys. A*, vol.88, no.4, pp. 793, 2007.

[33] W. Y. Lee, H. T. Leung, W. Zhang, Y. B. Xu, A. Hirohata, C. C. Yao, B-Ch. Choi, D. G. Hasko and J. A. C. Bland, “Magnetization reversal and magnetic anisotropy in Co network nanostructures”, *IEEE Trans.Magn,* vol. 35, no.5, pp.3475, 1999.

[34] A. Yu Toporov, R. M. Langford and A. K. Petford-Long, “Lorentz transmission electron microscopy of focused ion beam patterned magnetic antidot arrays”, *Appl. Phys. Lett.*, vol.77, no.19, pp.3063, 2000.

[35] I. Ruiz-Feal, L. Lopez-Diaz, A. Hirohata, J. Rothman, C.M. Guertler, J.A.C. Bland, L.M. Garcia, J.M. Torres, J. Bartolome, F. Bartolome, M. Natali, D. Decanini, and Y. Chen, “Geometric coercivity scaling in magnetic thin film antidot arrays”, *J. Magn. Magn. Mater.*, vol.242–245, no.1, pp. 597, 2002.

[36] P. Vavassori, V. Metlushko, R. M. Osgood, III,, M. Grimsditch, U. Welp, G. Crabtree, Wenjun Fan, S. R. J. Brueck, B. Ilic and P. J. Hesketh “Magnetic information in the light diffracted by a negative dot array of Fe”, *Phys. Rev. B*, vol.59, no.9, pp.6337, 1999.

[37] C. C. Wang, A. O. Adeyeye, and N. Singh, “Magnetic antidot nanostructures: effect of lattice geometry”, *Nanotechnology,* vol. 17, no.6, pp. 1629, 2006.

[38] H. Masuda and K. Fukuda, “Ordered Metal Nanohole Arrays Made by a Two-Step Replication of Honeycomb Structures of Anodic Alumina”, *Science*, vol. 268, no. 5216, pp.1466, 1995.

[39] Z. L. Xiao, C. Y. Han, U. Welp, H. H. Wang, V. K. Vlasko-Vlasov, W. K. Kwok, D. J. Miller, J. M. Hiller, R. E. Cook, G. A. Willing, and G. W. Crabtree, “Nickel antidot arrays on anodic alumina substrates”, *Appl. Phys. Lett.*, vol.81, no.15, pp.2869, 2002.

[40] G. A. Badini Confalonieri, K. R. Pirota, M. Vazquez, N. M. Nemes, M. Garcia-Hernandez, M. Knobel, and F. Batallan, “Magnetic and transport properties in ordered arrays of permalloy antidots and thin films”, *J. Appl. Phys.*, vol.107, no.8, pp.83918, 2010.

[41] M. Vazquez, K. R. Pirota, D. Navas, A. Asenjo, M. Hernández-Vélez, P. Prieto, and J. M. Sanz, “Ordered magnetic nanohole and antidot arrays prepared through replication from anodic alumina templates”, *J. Magn. Magn. Mater.*, vol. 320, no.14, pp.1978, 2008.

[42] K. R. Pirota, P. Prieto, A. M. J. Neto, J. M. Sanz, M. Knobel, and M. Vázquez, “Coercive field behavior of permalloy antidot arrays based on self-assembled template fabrication”, *J. Magn. Magn. Mater.*, vol.320, no.14, pp.e235, 2008.

[43] V. M. Prida, K. R. Pirota, D. Navas, A. Asenjo, M. Hernández-Vález and M. Vázquez, “Self-Organized Magnetic Nanowire Arrays Based on Alumina and Titania Templates”, *J. Nanosci. Nanotechnol.*, vol.7, pp.272–85, 2007

[44] L. W. McKeehan and P. P. Cioffi, “Magnetostriction in Permalloy”, *Phys. Rev.*, vol.28, no.1, pp.146, 1926.

[45] K. J. Merazzo, D. C. Leitao, E. Jiménez, J. P. Araujo, J. Camarero, R. P. del Real, A. Asenjo and M. Vázquez, “Geometry-dependent magnetization reversal mechanism in ordered Py antidot arrays”, *J. Phys. D: Appl. Phys.*, vol.44, no.50, pp. 505001, 2011.

[46] K.H.J Buschow and F.R. de Boer, “Physics of magnetism and magnetic materials”, Springer Ed. ISBN-13: 978-0306474217, 2003

[47] M. Redjdal, “Transitional domain wall structure in Permalloy magnetic films with decreasing thickness”, *IEEE Trans.Magn,* vol. 36, no. 5, pp.3071, 2000.

[48] M. Redjdal, J. Giusti, M. F. Ruane, and F. B. Humphrey, “Thickness dependent wall mobility in thin Permalloy films”, *J. Appl. Phys.*, vol.91, no. 10, pp.7547, 2002.

[49] L. W. McKeehan and P. P. Cioffi, “Magnetostriction in Permalloy”, *Phys. Rev.*, vol.28, no.1, pp. 146, 1926.

[50] T. Trunk, M. Redjdal, A. Kakay, M. F. Ruane and F. B. Humphrey, “Domain wall structure in Permalloy films with decreasing thickness at the Bloch to Néel transition”, *J. Appl. Phys*, vol.89, no.11, 2001.

[51] P. Vavassori, G. Gubbiotti, G. Zangari, C.T. Yu, H. Yin, H. Jiang, G.J. Mankey, “Magnetization reversal in micro-size negative dot arrays in permalloy film”, *J. Magn. Magn. Mater*., vol. 242–245, no. 1, pp. 585, 2002.

[52] R.C O'Handley, “Modern magnetic materials: principles and applications”, SN-9780471155669, Wiley-interscience publication, New York, United States of America, 2000.

[53] E.F. Kneller, “The Exchange-spring magnet: a new material principle for permanent magnets”, *IEEE Trans.Magn,* vol. 27, no.4, pp.3588, 1991.

[54] J. A. Osborn, “Demagnetizing Factors of the General Ellipsoid”, *Phys. Rev*., vol. 67, no.11-12, pp.351, 1945.

[55] Diana Cristina Pinto Leitão, “Micro and Nano Patterned Magnetic Structures”, Ph.D. study, Department of Physics and Astronomy Faculty of Sciences of the University of Porto, Portugal, 2010.

[56] F. García-Sánchez, E. Paz, F. Pigazo, O. Chubykalo-Fesenko, F. J. Palomares, J. M. González, F. Cebollada, J. Bartolomé and L. M. García, “Coercivity mechanisms in lithographed antidot arrays”, *EuroPhysic. Lett.* , vol.84, no. 6, pp. 67002, 2008.

[57] I. Guedes, M. Grimsditch, V. Metlushko, P. Vavassori, R. Camley, B. Ilic, P. Neuzil, and R. Kumar, “Domain formation in arrays of square holes in an Fe film”, *Phys. Rev. B*, vol. 66, no. 1, pp. 014434, 2002.

[58] I. Guedes, N. J. Zaluzec, M. Grimsditch, V. Metlushko, P. Vavassori, B. Ilic, P. Neuzil, and R. Kumar, “Magnetization of negative magnetic arrays: Elliptical holes on a square lattice”, *Phys. Rev. B*, vol. 62, no.11, pp. 719, 2000.

[59] P. Vavassori, G. Gubbiotti, G. Zangari, C. T. Yu, H. Yin, H. Jiang, and G. J. Mankey, “Lattice symmetry and magnetization reversal in micron-size antidot arrays in Permalloy film”, *J. Appl. Phys*., vol.91, no.10, pp. 7992, 2002.

[60] N. G. Deshpande, M. S. Seo, X. R. Jin, S. J. Lee, Y. P. Lee, J. Y. Rhee, and K. W. Kim, “Tailoring of magnetic properties of patterned cobalt antidots by simple manipulation of lattice symmetry”, *Appl. Phys. Lett*., vol. 96, no. 12, pp. 122503–3, 2010.

[61] C. T. Yu, H. Jiang, L. Shen, P. J. Flanders, and G. J. Mankey, “The magnetic anisotropy and domain structure of permalloy antidot arrays”, *J. Appl. Phys*., vol.87, no.9, pp.6322, 2000.

[62] M. Jaafar, D. Navas, A. Asenjo, M. Vázquez, M. Hernández-Vélez, and J. M. García-Martín, “Magnetic domain structure of nanoholes arrays in Ni films”, *J. Appl. Phys*., vol.101, no.9, pp.09F513, 2007.

[63] D. I. Paul, “General theory of the coercive force due to domain wall pinning”, *J. Appl. Phys*., vol.53, no.3, pp. 1649, 1982.

[64] R. Friedberg and D. I. Paul, “New Theory of Coercive Force of Ferromagnetic Materials”, Phys. Rev. Lett., vol.34, no.19, pp. 1234, 1975. Erratum: vol.34, no.19, pp. 1415, 1975.

[65] X. Chen and P. Gaunt, “Domain wall pinning by magnetic inhomogeneities in Sm(CoNi)2.5”, *J. Appl. Phys*., vol 67, no.9, pp.4592, 1990.

[66] J. A. Jatau and E. Della Torre, “One-dimensional energy barrier model for coercivity”, *J. Appl. Phys*., vol 73, no.10, pp.6829, 1993.

[67] J. A. Jatau, M. Pardavi-Horvath, and E. Della Torre, “Enhanced coercivity due to a local anisotropy increase”, *J. Appl. Phys*., vol 75, no. 10, pp. 6160, 1994.

[68] D. Navas, M. Hernández-Vélez, M. Vázquez, W. Lee, and K. Nielsch, “Ordered Ni nanohole arrays with engineered geometrical aspects and magnetic anisotropy”, *Appl. Phys. Lett*., vol. 90, no.19, pp.192501, 2007.

[69] J. M. D. Coey, “Hard Magnetic Materials: A Perspective”, *IEEE Transactions on Magnetics*, vol. 47, no. 12, pp. 4671, 2011.

[70] H. R. Hilzinger and H. Kronmuller, “Statistical theory of the pinning of bloch walls by randomly distributed defects”, *J. Mag. Magn. Mat.,* vol. 2, no. 1-3, pp. 11, 1975.

[71] A. Aharoni, “Domain wall pinning at planar defects”, *J. Appl. Phys*., vol. 58, no. 7, pp.2677, 1985.

[72] M. T. Rahman, N. N. Shams, D. S. Wang and C. H. Lai, “Enhanced exchange bias in sub-50-nm IrMn/CoFe nanostructure”, *Appl.Phys. Lett*., vol.94, no.8, pp. 082503, 2009.

[73] Y. G. Ma, S. L. Limand, C. K. Ong, “Evolution of magnetic and transport properties in pore-modified CoAlO antidot arrays”, *J. Phys. D: Appl. Phys*., vol. 40, no. 4, pp. 935, 2007.

[74] V. P. Chuang, W. Jung,C. A. Ross,J. Y. Cheng, Oun-Ho Park and Ho-Cheol Kim, “Multilayer magnetic antidot arrays from block copolymer templates”, *J. Appl. Phys*., vol. 103, no. 7, pp.07430, 2008.

[75] P. Prieto, K. R. Pirota, M. Vazquez, and J. M. Sanz, “Fabrication and magnetic characterization of permalloy antidot arrays”, *Phys. Stat. Sol. (a),* vol.205, no. 2, pp.363, 2008.

[76] C. Gao, K. Chen, L. Lü, J. Zhao, P. Chen, “Out-of-plane coercive field of Ni80Fe20 antidot arrays”, *J. Mag. Magn. Mat.,* vol. 322, no.21, pp.3278, 2010.

[77] E. Vassallo Brigneti, C.A. Ramos, E. Bermúdez Ureña, K. Pirota, M. Vázquez, P. Prieto, J.M. Sanz, “Ferromagnetic resonance and magnetization in permalloy films with nanostructured antidot arrays of variable size”, *J. Mag. Magn. Mat.,* vol. 320, no.14, pp. e257, 2008.

[78] M.Yu, L. Malkinski, L. Spinu, W. Zhou, and S. Whittenburg, “Size dependence of static and dynamic magnetic properties in nanoscale square Permalloy antidot arrays”, *J. Appl. Phys*., vol. 101, no.9, pp.09F501, 2007.

[79] F. J. Castaño, K. Nielsch, C. A. Ross, J. W. A. Robinson, and R. Krishnan, “Anisotropy and magnetotransport in ordered magnetic antidot arrays”, *Appl. Phys. Lett*., vol 85, no.14, pp.2872, 2004.

[80] A. A. Zhukov, A. V. Goncharov, P. A. J. de Groot, P. N. Bartlett, and M. A. Ghanem, “Magnetic antidot arrays from self-assembly template methods”, *J. Appl. Phys*., vol.93, no. 10, pp.7322, 2003.

[81] M. Jaafar, D. Navas, M. Hernandez-Velez, J.L. Baldonedo, M. Vázquez, and A. Asenjo, “Nanoporous alumina membrane prepared by nano-indentation and anodic oxidation”, *Surface Science*, vol. 603, no.20, pp.3155, 2009.

[82] K. J. Merazzo, R. P. del Real, A. Asenjo, and M. Vázquez, “Dependence of magnetization process on thickness of Permalloy antidot arrays”, *J. Appl. Phys*., vol.109, no.7, pp.07B906, 2011.

[83] A. P. Li, F. Müller, A. Birner, K. Nielsch, and U. Gösele, “Hexagonal pore arrays with a 50–420 nm interpore distance formed by self-organization in anodic alumina”, *J. Appl. Phys*., vol.84, no.11, pp.6023, 1998.

[84] O. Jessensky, F. Müller, and U. Gösele, “Self-organized formation of hexagonal pore arrays in anodic alumina”, *Appl. Phys. Lett*., vol.72, no.11, pp.1173, 1998.

[85] H. Masuda, F. Hasegwa and S. Ono, “Self-Ordering of Cell Arrangement of Anodic Porous Alumina Formed in Sulfuric Acid Solution”, *J. Electrochem. Soc*., vol. 144, no.5, pp. L127, 1997.

[86] A.P. Li, F. Müller, A. Birner, K. Nielsch and U. Gösele, “Polycrystalline nanopore arrays with hexagonal ordering on aluminum”, *J. Vac. Sci. Technol. A*, vol.17, no.4., pp.1428, 1999.

[87] David Navas Otero, “Fabricación y Caracterización de Arreglos de Nanohilos Magnéticos en Películas Nanoporosas de Alúmina Anódica”, Ph.D. thesis, Universidad Autónoma de Madrid and Consejo Superior de Investigaciones Científicas; Madrid, Spain, 2007.

[88] R. Lizarbe, "Teoría y práctica de la lucha contra la corrosión", ed. CSIC, Madrid, Cap. XVI Y XVII (1984).

[89] G. Hass, "On the Preparation of Hard Oxide Films with Precisely Controlled Thickness on Evaporated Aluminum Mirrors", *J. Opt. Soc. Amer.*, vol. 39, no.7, pp. 532, 1949.

[90] F. Keller, M. S. Hunter, and D. L. Robinson, "Structural Features of Oxide Coatings on Aluminum", *J. Electrochem. Soc.*, vol.100, no. 9, pp. 411, 1953.

[91] S. Z. Chu, K. Wada, S. Inoue, M. Isogai, Y. Katsuta, and A. Yasumori, "Large-scale fabrication of ordered nanoporous alumina films with arbitrary pore intervals by critical potential anodization", *J. Electrochem. Soc.*, vol.153, no.9, pp.B384, 2006.

[92] W. Lee, R. Ji, U. Gosele, and K. Nielsch, "Fast fabrication of long-range ordered porous alumina membranes by hard anodization", *Nat. Mater.*, vol.5, no.9, pp. 41, 2006.

[93] F. Zhang, L. Xiaohua, P. Caofeng, and Z. Jing, "Nano-porous anodic aluminium oxide membranes with 6 - 19 nm pore diameters formed by a low-potential anodizing process", *Nanotech.*, vol.18, no.34, pp. 345302, 2007.

[94] H. Masuda, H. Asoh, M. Watanabe, K. Nishio, M. Nakao, and T. Tamamura, "Square and triangular nanohole array architectures in anodic alumina", *Adv. Mater.,* vol.13, no.3, pp. 189, 2001.

[95] R. Fermento, D. C. Leitao, J. M. Teixeira, A. M. Pereira, F. Carpinteiro, J. Ventura, J. P. Araujo and J. B. Sousa, "Structural, magnetic and transport properties of ion beam deposited Co thin films", *J. Non-Cryst. Solids*, vol. 354, no.47-51, pp.5279, 2008

[96] J.I. Langford and A.J.C. Wilson, "Scherrer after sixty years: A survey and some new results in the determination of crystallite size", *J. Appl. Cryst.*, vol.11, no. 2, pp.102, 1978.

[97] E. Hecht, "Óptica", Addisson Wesley Iberoamericana, Madrid, 2000.

[98] A. Espinosa de los Monteros Royo, "Ferromagnetismo en láminas y heteroestructuras basadas en óxido de estaño", PhD Thesis, Universidad Autónoma de Madrid and Consejo Superior de Investigaciones Científicas; Madrid, Spain 2009.

[99] B. Lengeler, "X-Ray Absorption and Reflection in the Hard Range X-Ray Range", Ed. M. Campagna and K. Rosei, North Holland, Amsterdam, 1990.

[100] A. van der Lee, "Grazing incidence specular reflectivity: theory, experiment, and applications", *Solid State Sci.*, vol. 2, no.2, pp. 257, 2000.

[101] E. Céspedes, “Ferromagnetism in wide band gap materials: Mn-ZnO and Mn-Si3N4 thin films”, PhD thesis, Universidad Autónoma de Madrid and Consejo Superior de Investigaciones Científicas; Madrid 2009.

[102] C. Prieto and A. de Andrés, Técnicas de Difracción de Rayos X en “Láminas Delgadas y Recubrimientos: Preparación, propiedades y aplicaciones.”, Ed. J.M. Albella, CSIC, Madrid 2003.

[103] Eduardo Salas Colera, “Estudio Por Espectroscopia Brillouin de las Ondas Acústicas de Superficie en Láminas Delgadas Depositadas por Sputtering: Influencia de la Nanoestructura”, Ph.D. thesis, Universidad Autónoma de Madrid and Consejo Superior de Investigaciones Científicas; Madrid, Spain, 2011.

[104] J.A. Martín Gago, “Microscopía para el estudio de materiales y láminas delgadas en Láminas Delgadas y Recubrimientos: Preparación, propiedades y apliciones.”, Ed. J.M. Albella, CSIC, Madrid 2003.

[105] M. Jaafar, J. Gomez-Herrero, A. Gil, P. Ares, M. Vazquez and A. Asenjo, “Variable-field magnetic force microscopy”, *Ultramicroscopy*, vol.109, no.6, pp.693, 2009.

[106] I. Horcas, R. Fernandez, J.M. Gomez-Rodriguez, J. Colchero, J. Gomez-Herrero and A. M. Baro, “WSXM: A software for scanning probe microscopy and a tool for nanotechnology”, *Rev. Sci. Instrum.*, vol.78, no.1, pp. 013705, 2007.

[107] R.Azzam and N.Bashara, “Ellipsometry and polarized light”; Oxford, 1977.

[108] H. G. Tompkins and W. A. McGahan, “Spectroscopic Ellipsometry and Reflectometry”, John Wiley & Sons, 1999.

[109] D. Speliotis, “Getting the Most From Your Vibrating Sample Magnetometer”, ADE Technologies, Inc., Newton, MA, USA

[110] I.D. Mayergoyz, “Mathematical Models of Hysteresis, Springer”, New York, 1990.

[111] C.R. Pike, A.P. Roberts, K.L. Verosub, “Characterizing interactions in fine magnetic particle systems using first order reversal curves”, *J. Appl. Phys.*, vol.85, no.9, pp. 6660, 1999.

[112] P.E. Kelly, K. O’Grady and P.I. Mayo, “Switching mechanisms in cobalt phosphorus thin films”, *IEEE Trans. Magn.*, vol.25, pp.3880, 1989.

[113] H. Chiriac, N. Lupu, L. Stoleriu, P.Postolache, and A. Stancu, “Experimental and micromagnetic first-order reversal curves analysis in NdFeB-based bulk exchange spring type permanent magnets”, *J. Magn. Magn. Mater.*, vol. 316, no. 2, pp. 177, 2007.

[114] F. Béron, D. Ménard and A. Yelon, “First-order reversal curve diagrams of magnetic entities with mean interaction field: A physical analysis perspective”, *J. Appl. Phys.*, vol. 103, 07D908, no.7, 2008

[115] F. Béron, L.P. Carignan, D. Ménard and A. Yelon, “Extracting Individual Properties from Global Behaviour: First-order Reversal Curve Method Applied to Magnetic Nanowire Arrays” from “Electrodeposited Nanowires and their Applications”, Nicoleta Lupu (Ed.), pp. 228, (Vienna: IN-TECH), ISBN: 978-953-7619-88-6, 2010.

[116] S. Middelhoek, “Domain Walls in Thin NiFe Films”, *J. Appl. Phys.*, vol. 34, no.4, pp. 10541, 1963.

[117] A. Ghahremaninezhad and A. Dolati, *J. Alloy Comp.*, vol.480, pp.275, 2009

[118] F. Béron, K. R. Pirota, V. Vega, V. M. Prida, A. Fernández, B. Hernando and M. Knobel, “An effective method to probe local magnetostatic properties in a nanometric FePd antidot array”, *New J. Phys.*, vol.13, pp. 013035, 2011.

[119] J. C. A. Huang, F. C. Tang, W. W. Fang, R. L. Liu, Y. M. Hu, C. K. Lo, Y. Liou, Y. D. Yao, W. T. Yang, C. P. Chang, and S. Y. Liao, “Studies of the magnetic anisotropies of Co(1100)/Cr(211) and Co(1120)/Cr(100) multilayers”, *J. Appl. Phys.*, vol.79, no.8, pp. 4790, 1996.

[120] J. Camarero, J. Sort, A. Hoffmann, J. M. García-Martín, B. Dieny, R. Miranda, J. Nogues, “Origin of the Asymmetric Magnetization Reversal Behavior in Exchange-Biased Systems: Competing Anisotropies”, *Phys. Rev. Lett.*, vol.95, no.5, pp.057204, 2005

[121] Erika Jiménez Romero, “Experimental study of angular-dependent magnetic properties of nanostructures: Influence of Magnetic Anisotropy”, Ph.D. thesis, Universidad Autónoma de Madrid, Dpto. de Física de la Materia Condensada; Madrid, Spain, 2011.

[122] M. Jaafar, A. Asenjo, M. Vazquez, “Calibration of coercive and stray fields of commercial magnetic force microscope probes”, *IEEE Trans. on Nanotechnology*, vol. 7, no.3, pp.245, 2008.

[123] D. Navas, M. Hernandez-Velez, A. Asenjo, M. Jaafar, J.L. Baldonedo, M. Vazquez, “Preparation and magnetic characterization of Ni membranes with controlled highly ordered nanohole arrays”, *IEEE Trans.Magn,* vol. 42, no.10, pp.3057, 2006.

[124] Tutorial PEEM technique,
http://xraysweb.lbl.gov/peem2/webpage/Project/TutorialPEEM.shtml

[125] F. Kronast, J.Schlichting, F. Radu, S. Mishra, T Noll, and H. A. Dürr, “Spin resolved photoemission microscopy and magnetic imaging in applied magnetic fields”, *Surf. Interface Anal.*, vol.42, no.10-11, pp.1532, 2010.

[126] A. Gloskovskii, J. Barth, B. Balke, G. H. Fecher, C. Felser, F. Kronast, R. Ovsyannikov, H. A. Dürr, W. Eberhard, G. Schönhense, "A spatially resolved investigation of the local, micro-magnetic domain structure of single and polycrystalline Co2FeSi", *J. Phys. D:Appl. Phys.*, vol. 40, no.6, pp.1570, 2007.

[127] E. Bauer, "Photoelectron spectromicroscopy: present and future", *J. Electron Spectrosc. Relat. Phenom.*, vol. 114, pp.975, 2001.

[128] C. M. Schneider, G. Schönhense, "Investigating surface magnetism by means of photoexcitation electron emission microscopy", *Rep. Prog. Phys.*, vol. 65, no. 12, pp. 1785, 2002.

[129] R. Fink, M. R. Weiss, E. Umbach, D.Preikszas, H.Rose, R.Spehr, P. Hartel, W. Engel, R. Degenhardt, R. Wichtendahl, H. Kuhlenbeck, W. Erlebach, K. Ihmann, R. Schlógl, H. J. Freund, A. M. Bradshaw, G. Lilienkamp, Th. Schmidt, E. Bauer, G. Benner, "SMART: a planned ultrahigh-resolution spectromicroscope for BESSY II", *J. Electron Spectrosc. Relat. Phenom.*, vol. 84, no. 1–3, pp.231, 1997.

[130] F. Nolting, A. Scholl, J. Stöhr, J. Fompeyrine, H. Siegwart, J.-P. Locquet, S. Anders, J. Lüning, E. E. Fullerton, M. F. Toney,M. R. Scheinfein, H. A. Padmore, "Direct observation of the alignment of ferromagnetic spins by antiferromagnetic spins", *Nature*, vol.405, pp.767, 2000.

[131] H. Ohldag, A. Scholl, F. Nolting, S. Anders, F. U. Hillebrecht, J. Stöhr, "Spin Reorientation at the Antiferromagnetic NiO(001) Surface in Response to an Adjacent Ferromagnet", *Phys. Rev. Lett.*, vol. 86, no.13, pp.2878, 2001.

[132] S. B Choe, Y. Acremann, A. Scholl, A. Bauer, A. Doran, J. Stöhr, H. Padmore, "Vortex core-driven magnetization dynamics", *Science*, vol. 304, pp. 420, 2004.

[133] A. Gloskovskii, J. Barth, B. Balke, G. H. Fecher, C. Felser, F. Kronast, R. Ovsyannikov, H. A. Dürr, W. Eberhard, G. Schönhense, "A spatially resolved investigation of the local, micro-magnetic domain structure of single and polycrystalline Co2FeSi", *J. Phys. D: Appl. Phys.*, vol. 40, no.6, pp. 1570, 2007.

[134] S. Anders, H. A. Padmore, R. M. Duarte, T. Renner, T. Stammler, A. Scholl, M. R. Scheinfein, J. Stöhr, L. Séve, and B. Sinkovic, "Photoemission electron microscope for the study of magnetic material", *Rev. Sci. Instrum.*, vol. **70**, no. 10, pp. 3973, 1999.

[135] J. Stöhr, H. A. Padmore, S. Anders, T. Stammler and M. R. Scheinfein, "Principles of x-ray magnetic dichroism spectromicroscopy", *Surf. Revi. and Lett.*, Vol. 5, no. 6, pp. 1297, 1998.

[136] Web site: http://www-ssrl.slac.stanford.edu/stohr/xmcd.htm

[137] L. W. McKeehan and P. P. Cioffi, "Magnetostriction in Permalloy", *Phys. Rev.*, vol.28, no.1, pp. 146, 1926.

[138] Web site: http://rsbweb.nih.gov/ij/docs/index.html

[139] R. Fermento, D.C. Leitao, J.M. Teixeira, A.M. Pereira, F. Carpinteiro, J. Ventura, J.P. Araujo and J.B. Sousa, “Structural, magnetic and transport properties of ion beam deposited Co thin films”, *Non-Crystalline Solids 9*, vol. 354, no.47–51, pp. 5279, 2008.

[140] J. C. A. Huang, Y. M. Hu, and C. C. Yu, “Magnetic and structural characterization of HCP permalloy films grown by molecular beam epitaxy”, *J. Appl. Phys*., vol.83, no.11, pp.7046, 1998.

[141] D. Navas, F. Ilievski, and C. A. Ross, “CoCrPt antidot arrays with perpendicular magnetic anisotropy made on anodic alumina templates”, *J. Appl. Phys*., vol. 105, no. 11, pp. 113921–6, 2009.

[142] Y. Lei and W. K. Chim, “Shape and Size Control of Regularly Arrayed Nanodots Fabricated Using Ultrathin Alumina Masks”, *Chem. Mater*., vol. 17, no. 3, pp. 580, 2005

[143] Miriam Jaafar Ruiz – Castellanos, “PROCESOS DE IMANACIÓN EN LA NANOESCALA MEDIANTE MICROSCOPÍA DE FUERZAS MAGNÉTICAS”, Ph.D. thesis, Universidad Autónoma de Madrid and Consejo Superior de Investigaciones Científicas; Madrid, Spain, 2009.

[144] D. E. Heim, “Design and Operation of Spin Valve Sensors”, *IEEE Trans.Magn,* vol. 30, no. 2, pp.316, 1994.

[145] P. P. Freitas, R. Ferreira, S. Cardoso and F. Cardoso, “Magnetoresistive sensors”, J. Phys.: Condens. Matter., vol.19, no.16, pp.165221,2007.

[146] T. Bobek, N. Mikuszeit, J. Camarero, S. Kyrsta, L. Yang, M. Á. Niño, C. Hofer, L. Gridneva, D. Arvanitis, R. Miranda, J. J. de Miguel, C. Teichert and H. Kurz, “Self-Organized Hexagonal Patterns of Independent Magnetic Nanodots”, *Adv. Mater*., vol.19, pp. 4375, 2007.

[147] K. J. Merazzo, C. Castán-Guerrero, J. Herrero-Albillos, F. Kronast, F. Bartolomé J. Bartolomé, J. Sesé, R. P. del Real, L.M. García, M. Vázquez, “X-Ray Photoemission Electron Microscopy Studies of Magnetization in Py Antidot Array Thin Films”, *Phys. Rev. B,* vol.85, no. 18, pp.184427, 2012.

[148] J. Lohau, S. Kirsch, A. Carl, and E. F. Wassermann, “Quantitative determination of the magnetization and stray field of a single domain Co/Pt dot with magnetic force microscopy”, *Appl. Phys. Lett*., vol.76, no.21, pp.3094, 2000.

[149] A. Krasyuk, S.A. Nepijko, A. Oelsner, C.M. Schneider, H.J. Elmers and G. Schönhense, “Magnetic stray fields of patterned permalloy structures investigated by photoemission electron microscopy”, *Appl. Phys. A*, vol 88, no. 4, pp. 793, 2007.

[150] J. M. D. Coey, “Hard Magnetic Materials: A Perspective”, IEEE Transactions on Magnetics, vol. 47, No. 12, 2011

[151] A. Vovk, L. Malkinski, V. Golub, S. Whittenburg, C. O’Connor, J.-S. Jung, and S.-H. Min, “Preparation, structural characterization, and dynamic properties investigation of permalloy antidot arrays”, *J. Appl. Phys*., vol. **97**, no.10, pp. 10J506, 2005.

[152] D. Ecija, E. Jimenez, N. Mikuszeit, N. Sacristán, J. Camarero, J. M. Gallego, J. Vogel and R. Miranda, “Symmetry breaking effects in epitaxial magnetic thin films: Nonsymmetric reversal and butterfly remanence behavior”, *Phys. Rev. B*, vol.77, no.2, pp. 024426, 2008.

[153] P. Perna, C. Rodrigo, E. Jiménez, F. J. Teran, N. Mikuszeit, L. Méchin, J. Camarero, and R. Miranda, “Tailoring magnetic anisotropy in epitaxial half metallic La0.7Sr0.3MnO3 thin films”, *J. Appl. Phys*., vol. 110, no.1, pp. 013919, 2011.

[154] D. Ecija, E. Jimenez, J. Camarero, J.M. Gallego, J. Vogel, N. Mikuszeit, N. Sacristán, and R. Miranda, “Magnetisation reversal of epitaxial films of ϒ’-Fe4N on Cu(100)”, *J. Magn. Magn. Mater*., vol. 316, no.2, pp. 321, 2007.

[155] J. Camarero, J. Sort, A. Hoffmann, J.M. García-Martín, B. Dieny, R. Miranda, J. Nogués, “Origin of the Asymmetric Magnetization Reversal Behavior in Exchange-Biased Systems:Competing Anisotropies”, Phys. Rev. Lett., vol. 95, no. 5, pp. 057204, 2005.

[156] F. Fettar, L. Cagnon, and N. Rougemaille, “Three dimensional magnetization profile and multiaxes exchange bias in Co antidot arrays”, Appl. Phys. Lett., vol.97, no. 19, pp. 192502, 2010.

[157] L. Torres, L. Lopez-Diaz, O. Alejos and J. Iñiguez, “Micromagnetic study of lithographically defined non-magnetic periodic nanostructures in magnetic thin films”, *Phys. B*, vol. 275, no.1-3, pp. 59, 2000.

[158] A. Scholl, H. Ohldag, F. Nolting, J. Stohr, and H. A. Padmore, “X-ray photoemission electron microscopy, a tool for the investigation of complex magnetic structures”, *Rev. Sci. Instrum*., vol.73, no. 3, pp.1362, 2002.

[159] L.J. Heyderman, S. Czekaj, F. Nolting, D.-H. Kim, P. Fischer. “Cobalt antidot arrays on membranes: Fabrication and investigation with transmission X-ray microscopy”, *J. Magn. Magn. Mater*., vol. 316, no. 2, pp.99, 2007.

[160] F. García-Sánchez, E. Paz, F. Pigazo, O. Chubykalo-Fesenko, F. J. Palomares, J. M. González, F. Cebollada, J. Bartolomé and L. M. García, “Coercivity mechanisms in lithographed antidot arrays”, *EPL*, vol. 84, no.6, pp. 67002, 2008.

[161] J. S. Jiang, J. E. Pearson, Z. Y. Liu, B. Kabius, S. Trasobares, D. J. Miller, S. D. Bader, D. R. Lee, D. Haskel, G. Srajer, and J. P. Liu, “A new approach for improving Exchange-spring magnets”, *J Appl Phys*, vol. 97, no.10, pp.10K311, 2005.

[162] Y. Toga, H. Moriya, H. Tsuchiura, A. Sakuma, “First principles study on interfacial electronic structures in exchange-spring magnets”, *J. Phys.: Conf. Ser.*, vol.266, no.1, pp. 012046, 2011.

[163] I. S. Jiang, E. E. Fullerton, C. H. Sowers, A. Inomata, and S. D. Bader, “Spring Magnets Films”, *IEEE Trans Magn*., vol.35, no. 5, pp. 3229, 1999.

[164] E. F. Kneller and R. Hawig, “The Exchange-Spring Magnet: A New Material Principle for Permanent Magnets”, *IEEE Trans Magn*., vol.27, no.4, pp.3588, 1991.

[165] J. M. D. Coey and R. Skomski, "New Magnets from interstitial intermetallics", *Physica Scripta*, vol. T49, pp, 315, 1993.

[166] R. Skomski and M. D. Coey, "Giant energy product in nanostructured two-phase magnets", *Phys. Rev. B*, vol. 48. no.21, pp. 15812, 1993.

[167] R. Fischer. T. Leinewebber, and H. Kronmüller. "Fundamental magnetization processes in nanoscaled composite permanent magnets", *Phys. Rev. B*, vol. 57, no.17, pp. 10723, 1998.

[168] E. E. Fullerton, J. S. Jiang, S. D. Bader, “Hard/soft magnetic heterostructures: model exchange-spring magnets”, *J. Magn. Magn. Mater*, vol. 200, no.1-3, pp.392, 1999.

[169] R. Coehoorn, D. B. de Mooij, and C. J. De Waard, “Meltspun permanent magnet materials containing Fe3B as the main phase”, *J. Magn Magn Mater*, vol. 80, no. 1, pp. *101*, 1989.

[170] J. Ding, P.G. McCormick and R. Street, “Remanence enhancement in mechanically alloyed isotropic Sm7Fe93-nitride”, *J Magn Magn Mater*., vol.124, no. 1–2, pp. 1, 1993.

[171] L. Withanawasam, G. C. Hadjipanayis, and R. F. Krause, “Enhanced remanence in isotropic Fe-rich melt-spun Nd-Fe-B ribbons”, *J. Appl. Phys*., vol. 75, no.10, pp.6646, 1994.

[172] D. Kumar, A. Gupta, “Evolution of structural and magnetic properties of sputtered nanocrystalline Co thin films with thermal annealing”, *J Magn Magn Mater*., vol. 308, no. 2, pp. 318, 2007

[173] R. Skomski, “Aligned two-phase magnets: Permanent magnetism of the future?”, *J Appl Phys*., vol. **76**, no.10, pp. 7059, 1994.

[174] E. Goto, N. Hayashi, T. Miyashita. And K. Nakagawa, “Magnetization and Switching Characteristics of Composite Thin Magnetic Films”, *J. Appl. Phys*., vol. 36, no.9, pp.2951, 1965.

[175] T. Lieneweber and H. Kronmüller, “Micromagnetic examination of exchange coupled ferromagnetic nanolayers”, *J. Magn. Magn. Mater.*, vol.176, no.2–3, pp. 145, 1997.

[176] T. Schrefl, J. Fidler, H. Kronmüller, “Remanence and coercivity in isotropic nanocrystalline permanent magnets”, *Phys. Rev. B*, vol. 49, no.9, pp. 6100, 1994.

[177] W. Rave,K. RamstoKck, “Micromagnetic calculation of the grain size dependence of remanence and coercivity in nanocrystalline permanent magnets”, *J. Magn. Magn. Mater.*, vol.171, no.1-2, pp.69, 1997.

[178] R. Fischer, H. Kronmüller,, “Static computational micromagnetism of demagnetization processes in nanoscaled permanent magnets”, *Phys. Rev. B*, vol. 54, no.10, pp.7284, 1996.

[179] R. Fischer, T. Schrefl, H. Kronmüller, J. Fidler, “Phase distribution and computed magnetic properties of high-remanent composite magnets”, *J. Magn. Magn. Mater.*, vol.150, no.3-1, pp. 329, 1995.

[180] R.F. Sabiryanov and S.S. Jaswal, “Magnetic properties of hard/soft composites: SmCo5/Co1-*x*Fe*x*”, *Phys. Rev. B*, vol.58, no.18, pp. 12071, 1998.

[181] R.F. Sabiryanov and S.S. Jaswal, “Electronic structure and magnetic properties of hard/soft multilayers”, *J. Magn. Magn. Mater.*, vol.177–181, no. 2, pp. 989, 1998.

[182] D.A. Thompson, Ph. D. Thesis, Carnegie Institute of Technology, Sept. 1965.

[183] C. K. Lo, Y. Liou, C. P. Chang, I. Klik, Y. D. Yao, and J. C. A. Huang, “Structure and magnetic anisotropy of epitaxial fcc-Co(110) and hcp-Co(1100) films”, *Appl. Phys. Lett.,* vol. 68, no. 15, 1996

[184] V. P. Chuang, W. Jung, C. A. Ross, J. Y. Cheng, Oun-Ho Park, and Ho-Cheol Kim, “Multilayer magnetic antidot arrays from block copolymer templates”, *J. Appl. Phys.*, vol. 103, no. 7, pp.074307, 2008.

[185] R. Fermento, D.C. Leitao, J.M. Teixeira, A.M. Pereira, F. Carpinteiro, J. Ventura, J.P. Araujo and J.B. Sousa, “Structural, magnetic and transport properties of ion beam deposited Co thin films”, *Non-Crystalline Solids 9*, vol. 354, no.47–51, pp. 5279, 2008.

[186] W Y. Lee, H.T. Leung, W. Zhang, Y.B. Xu, A. Hirohata, C.C. Yao, B.-Ch. Choi, D.G. Hasko, and J.A,C. Bland, “Magnetization Reversal and Magnetic Anisotropy in Co Networks Nanostructures”, *IEEE Trans Magn.*, vol. 35, no. 5, 1999.

[187] J. A. Barnard, A. Butera, H. Fujiwara, V. R. Inturi, J. D. Jarratt, T. J. Klemmer, T. W. Scharr, and J. L. Weston, “High coercivity nanostructured networks”, *J. Appl. Phys.*, vol.81, no.8, pp. 5467, 1997.

[188] J. M. D. Coey, “Hard Magnetic Materials: A Perspective”, *IEEE Trans Magn*., vol. 47, no. 12, pp. 4671, 2011.